İSTANBUL TECHNICAL UNIVERSITY ★ INSTITUTE OF SCIENCE AND TECHNOLOGY

FINITE ELEMENT ANALYSIS OF RESPONSE OF A FLOATING STRUCTURE TO AN UNDERWATER EXPLOSION

M.Sc. Thesis by
Fatih ARUK, B.Sc.

Department : Mechanical Engineering

Programme : Construction

JUNE 2008

İSTANBUL TECHNICAL UNIVERSITY ★ INSTITUTE OF SCIENCE AND TECHNOLOGY

FINITE ELEMENT ANALYSIS OF RESPONSE OF A FLOATING STRUCTURE TO AN UNDERWATER EXPLOSION

M.Sc. Thesis by
Fatih ARUK
(503051205)

Date of submission : 05 May 2008
Date of defence examination : 09 June 2008

Supervisor (Chairman) : Prof. Dr. Tuncer TOPRAK
Co-Supervisor (Chairman) : Dr. Ergün BOZDAĞ
Members of the Examining Committee : Prof. Dr. Zahit MECİTOĞLU
Prof. Dr. Rüstem ASLAN
Prof. Dr. Ata MUĞAN

JUNE 2008

İSTANBUL TEKNİK ÜNİVERSİTESİ ★ FEN BİLİMLERİ ENSTİTÜSÜ

YÜZEN BİR YAPININ BİR SU ALTI PATLAMASINA CEVABININ SONLU ELEMANLAR YÖNTEMİ İLE ANALİZİ

YÜKSEK LİSANS TEZİ
Fatih ARUK
(503051205)

Tezin Enstitüye Verildiği Tarih : 05 Mayıs 2008
Tezin Savunulduğu Tarih : 09 Haziran 2008

Tez Danışmanı : Prof. Dr. Tuncer TOPRAK
Eş Danışman : Dr. Ergün BOZDAĞ
Diğer Jüri Üyeleri : Prof. Dr. Zahit MECİTOĞLU
Prof. Dr. Rüstem ASLAN
Prof. Dr. Ata MUĞAN

HAZİRAN 2008

ACKNOWLEDGMENTS

I would like to express my gratitude to my advisors, Prof. Dr. Tuncer TOPRAK and Dr. Ergün BOZDAĞ, for giving me the opportunity to work on this project, and for their support and guidance.

I would also like to express my deepest gratitude to Prof. Dr. Ata MUĞAN for his constant suggestions, guidance and support through out the course of the study.

I would like to thank specifically to Mr. Ali ÖGE and Mr. Cemal GÖZEN from A-Z Tech for their technical support on finite element modeling and for their generosity on sharing their deep engineering experience.

Special thanks to my friend Hasan KÖRÜK for his support and synergy. Lastly, it's my deepest pride to thank here my mother and father. This thesis is dedicated to their love.

May 2008 Fatih ARUK

TABLE OF CONTENTS

ABBREVIATIONS

UNDEX : Underwater Explosion
FE : Finite Element
FEM : Finite Element Method
DFT : Discrete Fourier Transform
DAA : Doubly Asymptotic Approximation
CAD : Computer Aided Design

LIST OF TABLES

Page No

LIST OF FIGURES

Page No

LIST OF SYMBOLS

A	: Radius of bubble [m]
A_N	: Area associated with the nth slave node
a_c	: Charge radius [mm]
a_{in}	: Incident wave acceleration
a_{max}	: Maximum bubble radius [m]
c_f	: Speed of sound in fluid [m/s]
c_1, a_1	: Admittance parameters
C_D	: Flow drag parameter
$[C]_f$	: Fluid damping matrix
$[C]_s$	: Structural damping matrix
D	: Charge depth [m]
E	: Young's modulus
f	: Frequency [Hz]
$f_{\max}$	: The maximum frequency of the excitation
$\mathbf{g}$	: Gravitational acceleration
$\mathbf{H}$	: The vector of acoustic interpolation functions
I^N	: Internal force term
$\mathbf{K}$, $\mathbf{k}$	: Charge material constants
K_5, K_6	: Constants specific to charge
K_c	: Adiabatic charge constant
K_f	: Bulk modulus
$[K]_s$	: Structural stiffness matrix
$[K]_f$	: Fluid stiffness matrix
$L_{\max}$	: The maximum internodal interval
m_c	: Mass of the charge [kg]
m_p	: Mass per unit area of the plate [kg/mm^2]
$[M]_f$	: Fluid mass matrix
$[M]_s$	: Structural mass matrix
$\mathbf{N}$	: The vector of structural interpolation functions
$\mathbf{n}$	: Outward normal to the structure
$\mathbf{n}^-$	: Inward normal on the boundary of the acoustic medium
$n_{\min}$	: The minimum number of internodal intervals per wavelength
P	: Pressure [N/mm^2]
P_i	: Incident pressure shock wave [N/mm^2]
P_R	: Reflected Pressure [N/mm^2]
P_r	: Reflected shock wave from the bottom of the plate [N/mm^2]
P_t	: Total Pressure behind the plate [N/mm^2]
P_{max}	: Maximum pressure [N/mm^2]
P_{atm}	: Atmospheric pressure [N/mm^2]
p	: The dynamic pressure in the fluid

p_o : Initial static pressure
p_c : Cavitation pressure
p_v : Pseudo-pressure
$\{p\}$: Fluid pressure vector
$\{p_I\}$: Incident pressure wave vector
$\{p_S\}$: Scattered pressure wave vector
$\{P_f\}$: External incident wave loading on the fluid
$\{P\}_s$: External force acting on the structure
$\mathbf{P}(\mathbf{x}_N)$: The projection of nth slave node onto the master surface
$p(t)$: The incident pressure variation at the stand-off point
$p'(t)$: The incident pressure variation at the image stand-off point
P^J : Applied load vector
P_c, v_c, A, B : Charge material constants
Q : Reflection coefficient
R : Stand-off distance [mm]
S : Acoustic boundary surfaces
S_{fp} : Surface on which the value of the acoustic pressure is prescribed
S_{ft} : Surface where the normal derivative of fluid medium is prescribed
S_{fi} : Radiating acoustic boundary
S_{fs} : Acoustic structural interaction surface
$[S_{fs}]$: The transformation matrix for acoustic-structural interaction
S_t : Surface of the structure where a surface traction is applied
t : Time [s]
T : Gas bubble period [s]
T_c : Explosive time constant [s]
t_c : Cut-off time [s]
t_{cav} : The time at which cavitation occurs [s]
Δt : Time step in explicit time integration
Δt_s : The stable time increment associated with the structure
Δt_f : The stable time increment associated with the fluid
$\mathbf{t}$: Surface traction vector applied to the structure
$T(\mathbf{x})$: Boundary traction term
T_0 : Prescribed normal derivative of the acoustic medium
T_S : The scattered fluid traction
T_{fi} : The boundary traction term associated with radiating boundaries
u : Migration of bubble [m]
$\mathbf{u}^f$: Displacement of the fluid particles
$\dot{\mathbf{u}}^f$: Fluid particle velocity
$\ddot{\mathbf{u}}^f$: Fluid particle acceleration
$\mathbf{u}^m$: Displacement of the structure
u^N : A displacement or rotation component
$\mathbf{U}_i$: Displacement of ith driving node
$\mathbf{U}_{i'}$: Displacement of ith driven node
V : Volume of the bubble
V_c : Volume of the charge
v_i : Fluid particle velocity behind the incident shock wave [m/s]

v_p : Velocity of Taylor Plate [m/s]
v_{pmax} : Maximum plate velocity [m/s]
v_r : Fluid particle velocity behind the reflected shock wave [m/s]
V_f : Volume of the fluid medium
ν : Poisson's ratio
ω_i : Natural frequency associated with the ith mode
$\mathbf{x}_j$: Spatial position of a fluid point in the acoustic medium
$\mathbf{x}_N$: The spatial position of nth slave node
$\mathbf{x}_o$: Spatial position of the stand-off point
$\mathbf{x}_s$: Spatial position of the source
$\mathbf{x}_s'$: Spatial position of the image source
$\mathbf{x}_o'$: Spatial position of the image stand-off point
ρ : Density of the structure
ρ_f : Density of the fluid [kg/m^3]
ρ_c : Density of the charge [kg/m^3]
α_c , β_R : Mass and stiffness proportional damping factors
$\boldsymbol{\beta}^N$: Strain interpolant associated with the nth degree of freedom
γ : Volumetric drag coefficient
γ' : The ratio of specific heats for gas
λ, μ : Lamé's constants
$\delta\varepsilon$: Strain variation in the structure
$\boldsymbol{\sigma}$: Stress tensor
ξ_{max} : Fraction of critical damping in the mode with the highest frequency

FINITE ELEMENT ANALYSIS OF RESPONSE OF A FLOATING STRUCTURE TO AN UNDERWATER EXPLOSION

SUMMARY

All new combatant ships or any new submarine design, or any undersea weapon such as torpedoes, should be designed to survive extreme loading conditions, such as underwater explosions (UNDEX). One can carry UNDEX shock trials to validate design. However, these shock trials require years of planning and preparation and are extremely expensive. The cost involved and the environmental effects require exploration of numerical solution techniques that can analyze the response of any new design subject to various explosions. Computational modeling and response, if perfected, can effectively and accurately replace the experimental procedures used to obtain the UNDEX response. The computational modeling also provides a valuable tool for design validation during early design phase. In this study, some near proximity underwater explosion simulations on a floating shock platform were carried using the finite element package ABAQUS. The effect of fluid mesh size, cavitation and damping on the response of the structure was investigated. Once the method has been validated by experimental results, the same procedure can be reliably used to evaluate the response of any warship or shipboard equipment to underwater explosions.

YÜZEN BİR YAPININ BİR SU ALTI PATLAMASINA CEVABININ SONLU ELEMANLAR YÖNTEMİ İLE ANALİZİ

ÖZET

Bütün yeni savaş gemileri veya yeni bir denizaltı tasarımı, ya da torpido gibi deniz altı silahları, su altı patlamaları gibi aşırı yükleme koşullarına dayanıklı şekilde tasarlanmalıdırlar. Yeni bir tasarımın bu şartlara karşı dayanımını kanıtlamak için şok deneyleri yapılabilir. Ancak böyle bir su altı patlama deneyinin yapılması yıllarca sürebilecek bir planlama ve hazırlık evresi gerektirir ve oldukça pahalıdır. Bu yüksek maliyet ve çevreye verilen olumsuz etkiler, yeni bir tasarımın su altı patlamalarına karşı dayanımını test edebilmek için sayısal çözüm yöntemlerinin araştırılmasını gerek kılmaktadır. Sayısal modelleme, doğru ve eksiksiz yapılırsa, etkin bir şekilde deneysel yöntemlerinin yerini alabilir. Bu sayısal yöntemler henüz tasarım aşamasında iken su altı patlamasına cevabın hesaplanmasını ve tasarımın eksik ya da kusurlu yanlarının ortaya çıkarılmasını sağlayabilirler. Bu çalışmada, yüzen bir şok test platformunun bir su altı patlamasına olan cevabı ABAQUS sonlu elemanlar yazılımı kullanılarak hesaplanmıştır. Denizin akustik bir ortam olarak modellendiği ve yapısal-akustik etkileşimin simüle edildiği analizlerle akustik eleman boyutunun, kavitasyonun ve yapısal sönümün etkisi incelenerek ortaya koyulmuştur. Çalışmada izlenen yöntem ve araçlar, sonuçların deneysel çalışmayla doğrulanması halinde, herhangi bir geminin ya da gemi ekipmanının su altı patlamasına olan cevabının güvenilir bir şekilde hesaplanmasında kullanılabilir.

1. INTRODUCTION

Warships are the most important part of a navy, and should last destructive effects of any near underwater explosion. As a defensive measure against underwater explosions, shipboard systems must be shock hardened to a certain level to ensure combat survivability of both personnel and equipment. So, shock resistance is a major issue that should be considered at early design phase of any new warship or shipboard equipment such as radars, weapons, torpedoes, etc. A major aim in the design of modern warships and shipboard equipment has been to eliminate or at least reduce damage caused by UNDEX.

Over the years the UNDEX response of underwater or floating structures was obtained by doing physical testing. These shock trials, while beneficial in determining the wartime survivability of surface ships, require years of planning and preparation and are extremely expensive. So, numerical simulations have been developed to accurately capture the fluid structure interaction phenomenon involved during an UNDEX event between the structure and the surrounding fluid medium.

As ship and warship design has an increasing interest in our country in recent years, more research and expertise are needed in evaluation of ship-shock response to severe loading conditions such as shock loads caused by UNDEX. The importance of the subject is clear from this point of view.

This study aims to clarify the underwater explosion phenomena and draw a way to simulate the response of any floating structure, such as a shock test platform or a surface ship, to a near underwater explosion using finite element method. First of all, the UNDEX phenomena should be understood in required detail since it is a complex event containing solid-fluid interaction, acoustic fluid modeling, explosion loading, cavitation, etc; the first chapter deals with this, also presenting the required similitude relations for shock loading. Then the theoretical background of UNDEX simulations and UNDEX modeling techniques which are readily available with the finite element package ABAQUS are introduced.

After presenting the UNDEX simulation methodology which was used in this work, the response of a shock test platform that is to be used in shipboard equipment testing, as part of the Turkish Navy Project MİLGEM, was simulated using ABAQUS. The effect of the fluid mesh size, cavitation and structural damping was investigated.

The shock test platform was shock-loaded according to the test parameters as specified in related military specification for high impact shock tests of shipboard machinery, equipment and systems [1]. The acceleration, velocity and displacement results at certain locations were presented. The stresses and plastic strains experienced by the structure were also revealed. The results obtained and the methodology used in this work will provide the basis for the future experimental work.

2. BACKGROUND

In World War II, many warships experienced the highly destructive effects of near underwater explosions from mines and torpedoes. Since this time, extensive work has gone into the research and study of the effects of UNDEX. A major goal in the design of modern warships and shipboard equipment has been to eliminate or at least reduce damage caused by UNDEX.

Over the years the UNDEX response of underwater or floating structures was obtained by doing physical testing. Physical testing of a ship to determine its response to an underwater explosion is an expensive process that can cause damage to the surrounding environment. These shock trials attempt to test the ship under "near combat conditions" by igniting a large charge of HBX-1 underwater at varying distances from the ship. The effect of the shocks to ship systems is observed and the response of the ship is monitored and recorded for each shot. The lead ship of each class, or a ship substantially deviating from other ships of the same class, is required to undergo these trials in order to correct any deficiencies on that ship as well as the follow on ships of the class.

These shock trials, while beneficial in determining the wartime survivability of surface ships, require years of planning and preparation and are extremely expensive. For example, United States Navy spent tens of millions of dollars for the shock trials conducted on ships called USS JOHN PAUL JONES (DDG 53) in 1994 and on USS WINSTON S. CHURCHILL (DDG 81) in 2001 [2]. In addition, these tests present an obvious danger to the crew onboard, the ship itself, and any marine life in the vicinity of the test. Due to this inherent safety risk, shock trials do not test up to the ship's design limits or even the true wartime shock environment. This has raised the question as to whether or not the information gleaned from doing the tests is worth the high cost of conducting them [3]. Moreover these tests are performed after the first ship is already built.

Therefore, the literature [4-9] shows the data collected from expensive experimental tests on simple cylindrical shells and plate structures. The cost involved and the

environmental effects require exploration of numerical solution techniques that can analyze the response of a ship or ship-like structure subject to various explosions. Computational modeling and response, if perfected, can effectively and accurately replace the experimental procedures used to obtain the UNDEX response. Over the years, numerical simulations have been developed to accurately capture the fluid structure interaction phenomenon involved during an UNDEX event between the structure and the surrounding fluid medium [10, 11].

An UNDEX simulation consists of obtaining the response of a finite-sized structure (a shock test platform in this work) subjected to a blast load when immersed or floating in an infinite fluid medium (sea or ocean). Due to the fact that UNDEX simulations use an infinite fluid medium, researchers [12-15] have developed techniques that combine the benefits of both boundary element and finite element methods. In this method, the structure was discritized into finite elements, and the surrounding fluid medium was divided into boundary elements. An approximate boundary integral technique, "Doubly Asymptotic Approximation" (DAA), was used in this kind of incident wave problems and boundary integral programs were developed.

Kwon and Cunningham [12] coupled an explicit finite element analysis code, DYNA3D, and a boundary element code based on DAA, Underwater Shock Analysis (USA), to obtain the dynamic responses of stiffened cylinder and beam elements. Also, during the early 90s Kwon and Fox [13] studied the nonlinear dynamic response of a cylinder subjected to side-on underwater explosion using both the experimental and numerical techniques. Sun and McCoy [14] combined the finite element package ABAQUS and a fluid-structure interaction code based on the DAA to solve an UNDEX analysis of a composite cylinder. Similarly, there have been other researchers [15, 16] that coupled a finite element code with a boundary element code such as DAA to capture the fluid-structure interaction effect. Moreover, Cichocki, Adamczyk, and Ruchwa [17, 18] have performed extensive research to obtain an UNDEX response of simple structures and have implemented entire fluid-structure interaction phenomenon, pressure wave distribution, and the radiation boundary conditions into the commercial finite element package ABAQUS.

Getting the required knowledge and software after above advances in computer aided simulation of UNDEX events, some researches used these tools in simulation of

ships and submarines exposed to shock loading of near proximity explosives. Shin and Santiago conducted a two dimensional shock response analysis of a mid-surface ship in 1998 [19]. Three dimensional ship shock trial simulation of a warship was performed by Shin in 2004 [20]. Shock response of a surface ship subjected to non-contact underwater explosions was conducted by Liang and Tai in 2005 [21].

Figure 2.1 : From Expensive and Dangerous Shock Trials to Virtual UNDEX Environment [20].

3. UNDERWATER EXPLOSION PHENOMENA

3.1 Sequence of Events in UNDEX

An underwater explosion produces a great amount of gas and energy, resulting in a shock wave [22]. It is initiated with the detonation of an explosive, such as TNT or HBX-1. Once the reaction starts, it propagates through the explosive material in the form of a pressure wave. As this pressure wave advances through the explosive, it initiates chemical reactions which create more pressure waves. The detonation event transforms the explosive material from its original solid phase to a gas at very high temperature and pressure (on the order of 3000 ^{o}C and 5000 MPa.). The detonation process occurs rapidly (on the order of nanoseconds) because of the fact that the increase in pressure in the material results in wave velocities that will exceed the acoustic velocity in the explosive material. Therefore, a shock wave exists in the explosive material. The mixture of high heat and high compressive pressure enables the explosion to be a self-propagating process. The resulting shock wave is then transferred to the surrounding fluid on the outer wet surface of the charge.

Though the water is taken to be incompressible in many engineering applications the water surrounding the detonating charge compresses slightly as a result of the extreme shock pressure generated by the explosive. This compression shock wave produced by the sudden increase of pressure in the surrounding water travels radially away from the explosion with a velocity approximately equal to the velocity of sound in water. Despite of the fact that the actual value of the velocity of sound in water slightly changes depending on temperature, pressure and salinity, it can be taken to be approximately 1524 m/s for design and analysis purposes [22].

Once the pressure wave reaches the wet boundary of the gas bubble, an extreme pressure wave and resulting outward motion of the water follows it. The shock wave has a sharp front since the pressure increase is discontinuous. The steep increase is then followed by an exponential decay. As the pressure propagates through the fluid medium (Figure 3.1), the peak value of the pressure front decreases [22].

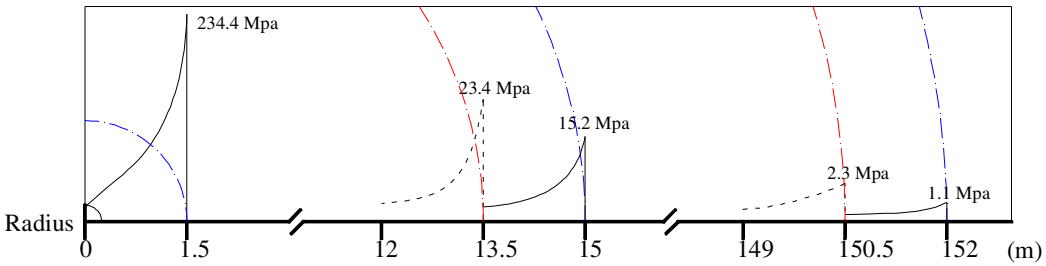

Figure 3.1 : Shock Wave Profiles From a 136 kg TNT Charge [22].

3.2 Similitude Relations (Pressure versus Time)

For UNDEX loading of a structure that is floating or submerged, the pressure versus time history at a certain point in the fluid between the structure and the charge location is needed. This point is called "stand-off point" and the distance between the stand-off point and the charge location (source point) is called "stand-off distance". To save analysis time, the standoff point is typically on or near the solid surface where the incoming incident wave would be first reflected [23].

According to the principle of similarity, if the linear dimensions of a charge and all other lengths are altered in the same ratio for two explosions, the shock waves formed will have the same pressures at corresponding distances scaled by this ratio, if the times at which pressure is measured are also scaled by this same ratio. This principle leads directly to simple predictions of the values of the shock wave parameters at the point of observation based only upon the distance from the charge to the point of observation and the dimensions and type of the charge [24].

Following similitude relations can be used for an accurate representation of the far-field pressure profiles of an explosive [25]:

$$P(R,t) = P_c \left[\frac{a_c}{R} \right]^{1+A} f(\tau) \qquad \textbf{(3.1)}$$

where

$$\tau = \left[\frac{a_c}{R} \right]^{B} \frac{v_c t}{a_c} \qquad \textbf{(3.2)}$$

in which R (stand-off distance) is the distance from the center of the explosive charge with radius a_c, and P_c, v_c, A and B are constants associated with the charge material and t is time. Some recommended values for these constants are shown in Table 3.1 [25]. Two choices for $f(\tau)$ are

$$f(\tau) = e^{-\tau} \qquad \tau \le 1 \qquad \textbf{(3.3)}$$

$$f(\tau) = 0.8251e^{-1.338\tau} + 0.1749e^{-1.805\tau} \qquad \tau \le 7 \qquad \textbf{(3.4)}$$

A comparison of equations (3.3) and (3.4) with a measured pressure profile is shown in Figure 3.2 [25] for the constants of Coles (1946). The double-exponential fit (Eq. 3.4) is in better coherence with measured data up to the time when pressure is down to about 5 % of its peak value. Therefore, the double exponential fit was chosen to be used in this work.

Table 3.1: Material Constants for Similitude Relations.

Material	Source	$P_c(Gpa)$	$v_c(m/s)$	A	B
TNT (1.52 g/cc)	Coles (1946)	1.42	992	0.13	0.18
TNT (1.60 g/cc)	Farley and Snay (1978)	1.45	1240	0.13	0.23
TNT (1.60 g/cc)	Price (1979)	1.67	1010	0.18	0.185
HBX-1 (1.72 g/cc)	Swisdak (1978)	1.71	1470	0.15	0.29
HBX-1 (1.72 g/cc)	Price (1979)	1.58	1170	0.144	0.247
Pentolite (1.71 g/cc)	Thiel (1961)	1.65	1220	0.14	0.23

According to MIL-S-901D [1], HBX-1 charges are to be used in shock testing. A Matlab function plotting the required pressure vs. time history for a user-input mass of HBX-1 charge at a user specified stand off point was written according to the material constants in Table 3.1. The Matlab code used to generate this figure is provided in APPENDIX A. The pressure vs. time history was presented in Figure 3.3 for a 25 kg HBX-1 charge at a stand-off distance of 10 meters. As seen in figure, the

peak pressure prescribed by Swisdak (1974) is slightly higher than Price (1979). Because it is a common engineering intuition, pressure time histories with higher peak pressure values were used in this work.

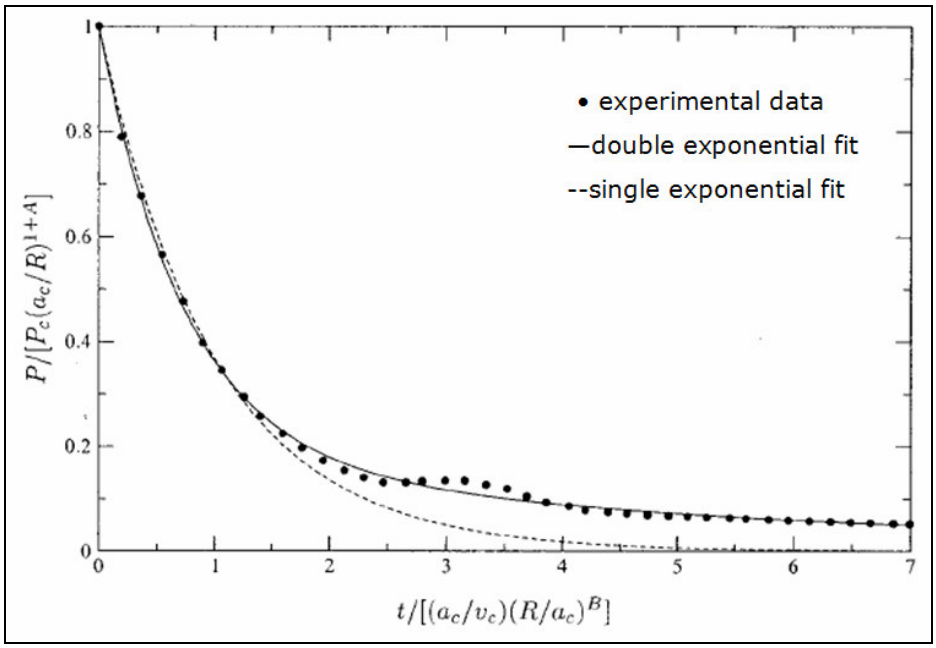

Figure 3.2 : A Comparison of Equations (3.3) and (3.4) With a Measured Pressure Profile [25].

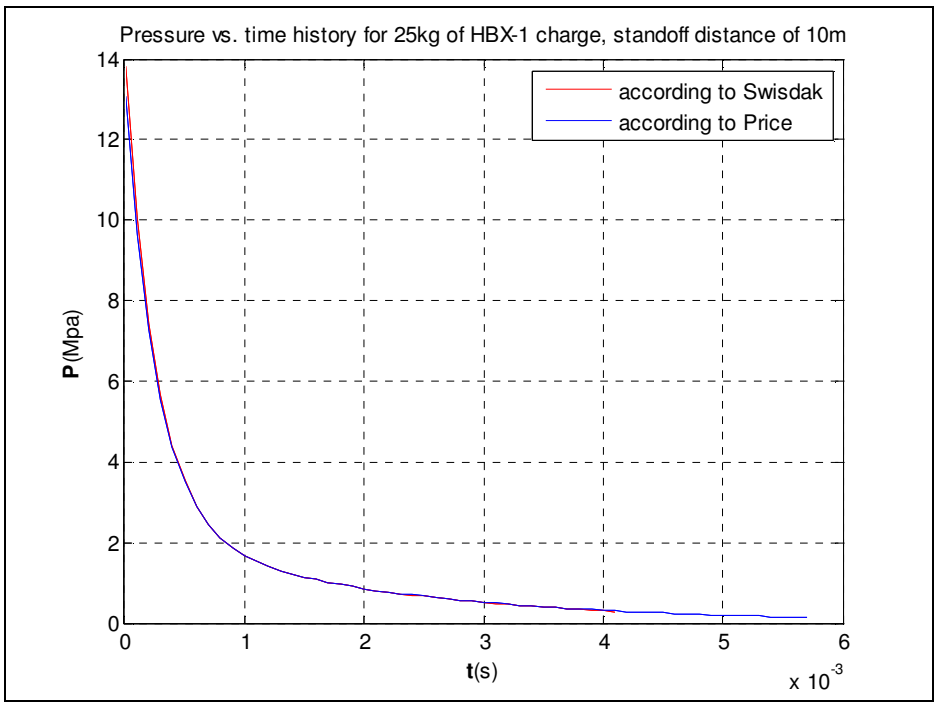

Figure 3.3 : Pressure Versus Time for an HBX-1 Charge.

3.3 Explosive Gas Bubble

As described in previous section, the detonation creates a shock wave for which approximate relations were given. This shock wave leaves highly compressed gases behind. These hot and compressed gases form a bubble. This spherical gaseous bubble continues to expand to relieve its pressure until the internal pressure falls below the surrounding hydrostatic pressure of the water. In this period the bubble actually expands above its equilibrium due to the momentum of the expansion [25]. Equation (3.5) and (3.6) can be used to calculate the gas bubble period and maximum bubble radius [20];

$$T = K_5 \frac{m_c^{\frac{1}{3}}}{(D+10.06)^{\frac{5}{6}}} \ [s] \qquad \textbf{(3.5)}$$

$$a_{\max} = K_6 \frac{m_c^{\frac{1}{3}}}{(D+10.06)^{\frac{1}{3}}} \ [m] \qquad \textbf{(3.6)}$$

where T is gas bubble period in s, $a_{\max}$ is the maximum radius a bubble can reach in meters, m_c is mass of the charge in kg, D is charge depth in meters, K_5 and K_6 are constants specific to the charge type. The values of K_5 and K_6 for HBX-1 are 2.3023 and 3.8196 respectively [20].

Once the bubble reaches its maximum radius, there is a large positive pressure gradient between the bubble and the surrounding fluid. This causes the bubble to collapse upon itself until the volume of the bubble is small enough so that the pressure increase inside the bubble is sufficiently high to stop further collapse. At this point, a negative pressure gradient between the bubble and surrounding fluid exists. The bubble now expands once again to achieve equilibrium, to a size smaller than the initial maximum radius, but still larger than the point of equilibrium. This results in the collapse and expansion process repeating itself again, creating a bubble pulse at each repetition [20]. The first bubble pulse has maximum amplitude of 10-20 % of the initial shock pulse [26].

This oscillatory motion continues until the bubble loses all of its energy due to viscous resistance from the fluid around it or the bubble reaches to the surface of the water [20]. Figure 3.4 shows this expansion and contraction process of the bubble and its normal migration pattern towards the surface of the water [25].

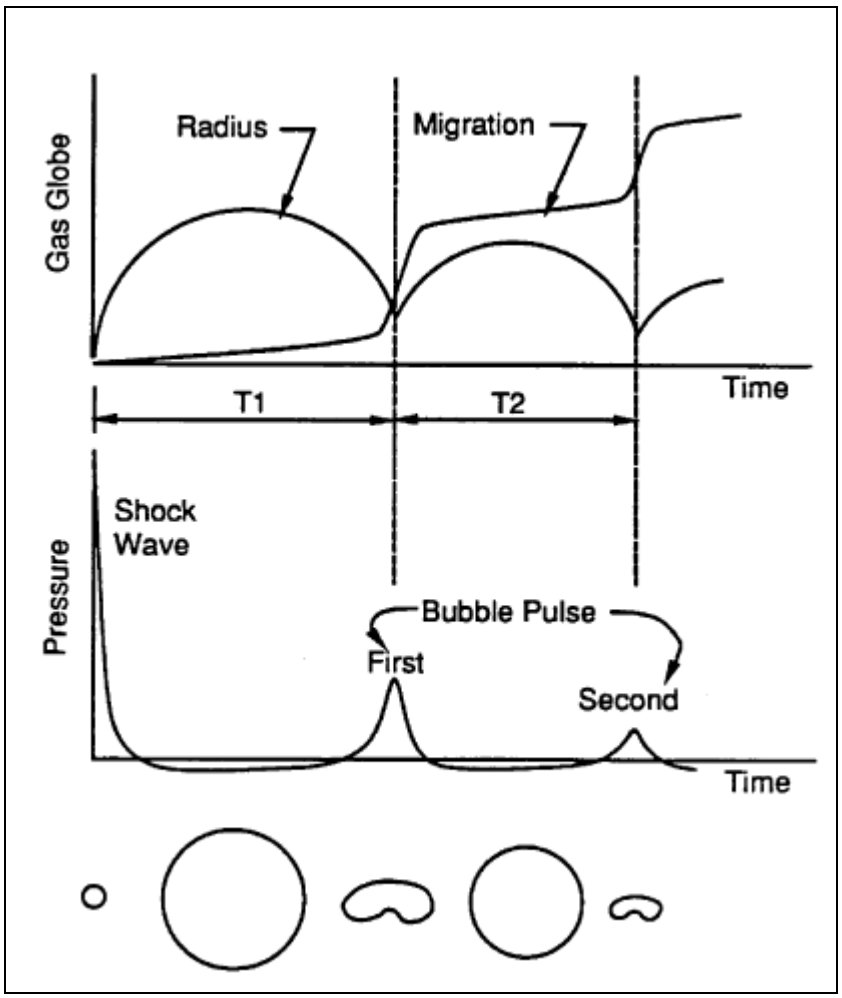

Figure 3.4 : Gas Bubble Growth, Migration and Bubble Pulse [25].

Since the period of the bubble pulses is close to the period of the first bending vibration modes of ships, these loads represent a strong source of excitation for a ship structure [26]. It is especially important for the late time response of the ship. However, in this work the effect of the bubble pulses were neglected due to following reasons; first of all, the first bending mode of the shock test platform whose response was to be calculated is so much above the frequency of the bubble pulses. For example, take a 27.2 kg of HBX-1 charge at a depth of 7.3 m; these values are according to the military specifications [1] which were also used in this work. Using equations (3.5) and (3.6);

$$T = K_5 \frac{m_c^{\frac{1}{3}}}{(D+10.06)^{\frac{5}{6}}} = 2.3023 \frac{27.2^{\frac{1}{3}}}{(7.3+10.06)^{\frac{5}{6}}} = 0.642s \quad \textbf{(3.7)}$$

$$f = \frac{1}{T} = \frac{1}{0.642} \approx 2Hz \quad \textbf{(3.8)}$$

$$a_{\max} = K_6 \frac{m_c^{\frac{1}{3}}}{(D+10.06)^{\frac{1}{3}}} = 3.8196 \frac{27.2^{\frac{1}{3}}}{(7.3+10.06)^{\frac{1}{3}}} = 4.44m \quad \textbf{(3.9)}$$

Here, T is the period of the bubble pulse and f is the frequency of bubble pulse excitation. The first mode of the shock platform is at about 31 Hz (after the first 6 rigid body modes) that is well above the bubble pulse frequency. So the platform will not get in resonance due to bubble pulses.

Also, as it will be explained in detail in next sections, explicit time integration with a time increment of $10^{-6}s$ is not rare in shock analysis. Continuing analysis up to for example 1 second (that is comparable with bubble period of 0.642 s) to evaluate late time response of a ship or a shock test platform is not computationally efficient even with the latest computer technology because it would require 100000 time increments. For instance in this work, a 0.04 second analysis took about four days with an 8 cpus machine. Increasing time increment to speed the analysis would result in unstable and inaccurate results.

3.3.1 Geers-Hunter Model

Geers and Hunter proposed a mathematical model which considers an underwater explosion as a single event consisting of a shockwave phase and a bubble oscillation phase, with the first phase providing initial conditions to the second [25].

According to this model, the volume acceleration of the bubble during the shockwave phase is given by [25];

$$\ddot{V}(t) = \frac{4\pi a_c}{\rho_f} P_c \left[0.8251 \mathrm{e}^{(-1.338t/T_c)} + 0.1749 e^{(-0.1805t/T_c)} \right] \quad \textbf{(3.10)}$$

in which

$$P_c = K(m_c^{1/3}/a_c)^{1+A} \tag{3.11}$$

$$T_c = km_c^{1/3}(a_c/m_c^{1/3})^B \tag{3.12}$$

where K, k are constants for charge material and ρ_f is the density of the fluid.

Initial conditions for shockwave phase are;

$$\dot{V}(0) = 0 \tag{3.13}$$

$$V(0) = \frac{4}{3}\pi a_c^3 . \tag{3.14}$$

Integration of (3.10) with these initial conditions yields;

$$\dot{V}(t) = \frac{4\pi a_c}{\rho_f} P_c \left[1.5857 - 0.6167\,\mathrm{e}^{(-1.338t/T_c)} - 0.9690\,\mathrm{e}^{(-0.1805t/T_c)}\right] T_c \tag{3.15}$$

$$\begin{aligned} V(t) = \frac{4}{3}\pi a_c^3 + \frac{4\pi a_c}{\rho_f} P_c \Big[1.5857\,t/T_c - 5.8293 + 0.4609\,\mathrm{e}^{(-1.338t/T_c)} + \\ +5.3684\,\mathrm{e}^{(-0.1805t/T_c)}\Big] T_c^2 \end{aligned} \tag{3.16}$$

Radial displacement and velocity follow as;

$$a = \left(\frac{3}{4\pi}V\right)^{\frac{1}{3}} \tag{3.17}$$

$$\dot{a} = \frac{1}{4\pi}\dot{V}/a^2 \tag{3.18}$$

These expressions are evaluated at $t_I = 7T_c$ to determine the initial conditions for the subsequent bubble response calculations during the oscillation phase. This choice was validated since, for a single set of charge constants, the initial condition values for values of t_I between $3T_c$ and $7T_c$ produce essentially the same response during the oscillation phase, as demonstrated by Geers and Hunter [25].

The following are the equations of motion for the doubly asymptotic approximation model to describe the evolution of the bubble radius, *a*, and migration, *u*, during the oscillation phase [25]:

$$\dot{a} = -\frac{\phi_{l0}}{a} - \frac{1}{c_f}\left(\dot{\phi}_{l0} - \dot{a}^2 - \frac{1}{3}\dot{u}^2 - \frac{2}{3}\dot{u}\frac{\phi_{l0}}{a}\right) \tag{3.19}$$

$$\dot{u} = -\frac{\phi_{l1}}{a} - \frac{1}{c_f}\left(\dot{\phi}_{l1} - 2\dot{a}\dot{u}\right) \tag{3.20}$$

$$\dot{\phi}_{l0} = \frac{1}{(1+\varsigma)}\left[\left(\frac{1}{2}+\frac{1}{2}\frac{\rho_g}{\rho_f}+\varsigma\right)\left(\dot{a}^2+\frac{1}{3}\dot{u}^2\right) - \frac{\rho_g}{\rho_f}c_g\frac{\phi_{l0}}{a} + \frac{2}{3}(1+\varsigma)\dot{u}\frac{\phi_{l1}}{a} - Z\right] \tag{3.21}$$

$$\dot{\phi}_{l1} = \frac{1}{(1+\varsigma)}\left[\left(1+\frac{\rho_g}{\rho_f}+2\varsigma\right)\dot{a}\dot{u} - \left(1-\frac{\rho_g}{\rho_f}\right)ga - \frac{\rho_g}{\rho_f}c_g\left(2\frac{\phi_{l1}}{a}+\frac{\phi_{g1}}{a}\right) + \frac{3}{8}C_D\dot{u}^2\right] \tag{3.22}$$

$$\dot{\phi}_{g1} = \frac{1}{(1+\varsigma)}\left[\left(2+\frac{c_g}{c_f}+\varsigma\right)\dot{a}\dot{u} - \frac{c_g}{c_f}\left(1-\frac{\rho_g}{\rho_f}\right)ga - c_g\left(2\frac{\phi_{l1}}{a}+\frac{\phi_{g1}}{a}\right) - \frac{c_g}{c_f}\frac{3}{8}C_D\dot{u}^2\right] \tag{3.23}$$

in which

$$\varsigma = \frac{\rho_g c_g}{\rho_f c_f} \tag{3.24}$$

$$Z = \frac{1}{\rho_f}\left(P_g - p_I + \rho_f g u\right) + \frac{1}{3}\left[\left(\frac{\phi_{l1}}{a}\right)^2 - \frac{\rho_g}{\rho_f}\left(\frac{\phi_{g1}}{a}\right)^2\right] \tag{3.25}$$

$$P_g = K_c\left(\frac{V_c}{V}\right)^{\gamma'} \tag{3.26}$$

$$\rho_g = \rho_c\left(\frac{V_c}{V}\right) \tag{3.27}$$

$$c_g = c_c\left(\frac{V_c}{V}\right)^{\frac{1}{2}(\gamma'-1)} \tag{3.28}$$

$$c_c = \sqrt{\frac{\gamma K_c}{\rho_c}} \tag{3.29}$$

In above equations, ρ_c is the charge mass density, c_f is the sound speed in fluid, $(4/3)\pi a^3$ is the current volume of the bubble, K_c is the adiabatic charge constant, V_c is the volume of charge, γ' is the ratio of specific heats for gas, g is the acceleration due to gravity, and $p_I = p_{atm} + \rho_f gD$ (where p_{atm} is the atmospheric pressure and D is the depth of the charge's center). C_D is an empirical flow drag parameter, which impedes the bubble's migration [25].

Seven initial conditions are needed [25]. The first two are $a(t_I) = a_I$, $\dot{a}(t_I) = \dot{a}_I$, the second two are $u(t_I) = 0$, $\dot{u}(t_I) = 0$, the fifth one is $\phi_{l1}(t_I) = 0$, and the remaining two are determined as

$$\phi_{l0}(t_I) = -a_I \dot{a}_I \left[1 - \frac{1}{2}\left(1 - \frac{\rho_{gI}}{\rho_f} \right) \frac{\dot{a}_I}{c_f} + \varsigma_I \right] + \frac{a_I}{c_f} Z_I \tag{3.30}$$

and

$$\phi_{g1}(t_I) = -\varsigma_I^{-1} \left(1 - \frac{\rho_{gI}}{\rho_f} \right) \frac{g}{c_f} a_I^2 \tag{3.31}$$

with

$$Z_I = \rho_f^{-1}\left(P_{gI} - p_I \right) - \frac{1}{3}\left(1 - \frac{\rho_{gI}}{\rho_f} \right)^2 \frac{\rho_f}{\rho_{gI}} \left(\frac{g a_I}{c_{gI}} \right)^2 \tag{3.32}$$

Using above initial conditions, equations (3.19) through (3.23) can be solved by using any suitable method for nonlinear ordinary differential equations.

3.3.2 The Pressure Wave at a Stand-off Point Induced by the Geers-Hunter Bubble Model

The pressure wave induced during the bubble response at a stand of point can be expressed as [27]

$$p_I(\vec{x}_j, t) = p_t(t)\, p_x(\vec{x}_j) \tag{3.33}$$

For the shock wave phase $(t < 7T_c)$;

$$p_t(t) = \frac{\rho_f}{4\pi}\left(\frac{a_c}{R_j}\right)^A \ddot{V}(t) \tag{3.34}$$

with $\ddot{V}$ given by equation (3.10). For the bubble oscillation phase $(t \geq 7T_c)$;

$$p_t(t) = \frac{\rho_f}{4\pi}\ddot{V}(t) = \rho_f\left(a^2\ddot{a} + 2a\dot{a}\right) \tag{3.35}$$

In above equations, $\vec{x}_j$ is the position vector of the stand-off point and R_j is distance from the current charge center, $\vec{x}_s$ to stand-off point, $\vec{x}_j$.

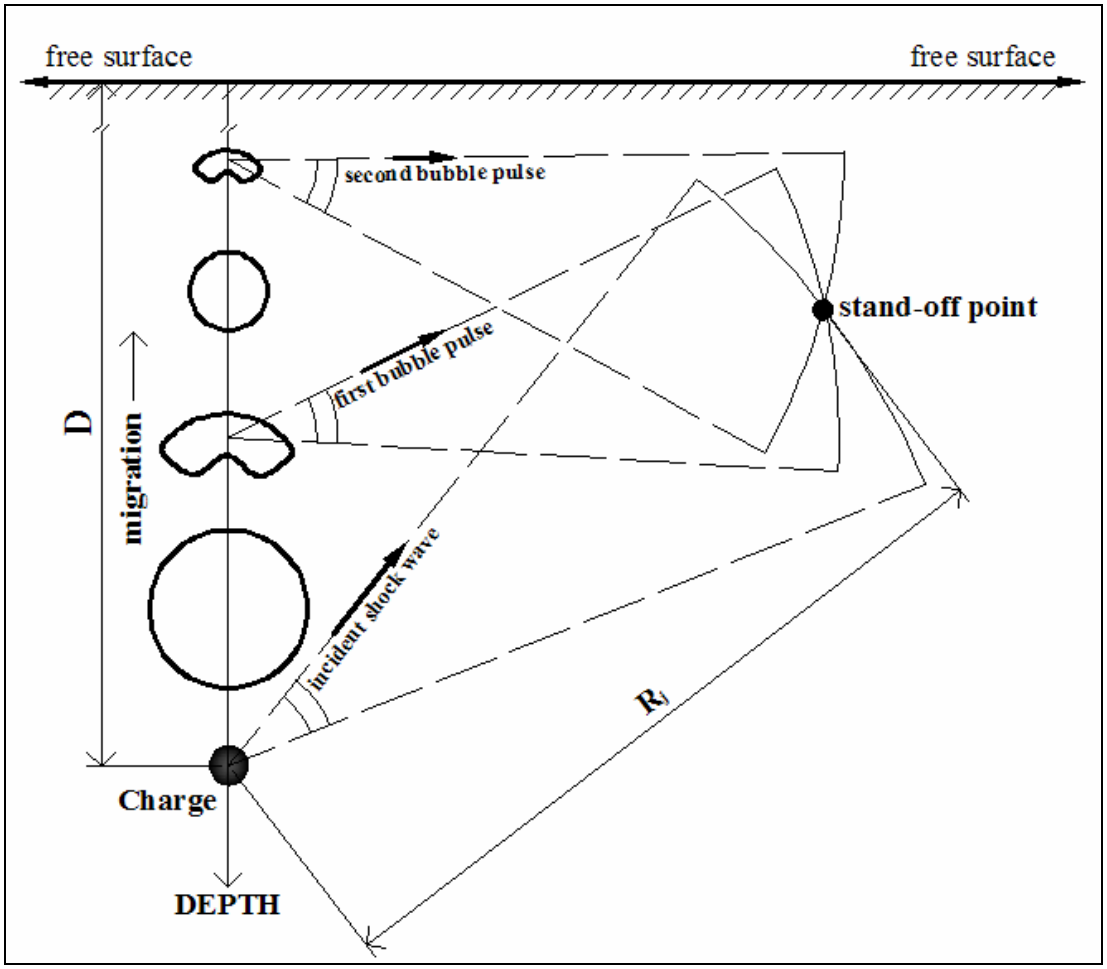

Figure 3.5 : Incident Shock Wave and Following Bubble Pulses at Stand-off Point.

For both shock wave phase and bubble oscillation phase;

$$p_x(\vec{x}_j) = \frac{1}{R_j} \tag{3.36}$$

Here $R_j = \left\| x_s - x_j \right\|$.

3.3.3 Application of Geers and Hunter Model

ABAQUS has an internal mechanical model which uses Geers-Hunter model for UNDEX loading. It uses a fourth-order Runge-Kutta integrator to prescribe the pressure variation at the stand-off point prior to analysis. It then uses this pressure variation in the analysis. To see the effect of the bubble oscillation, this preprocessor can be used.

In section 3.3, the bubble period and maximum radius of the bubble of a 27.2 kg HBX-1 charge located at a depth of 7.3 m was evaluated using the approximate equations in the related section. In this section, the Geers-Hunter model was used to calculate the bubble radius and migration for the same situation as well as the pressure shock profile for the case of most severe loading condition as specified in military specifications [1]. In this most severe loading condition, the shortest distance from the charge to the shock test platform (stand-off distance) is 8.77 m and the pressure profile was evaluated at this distance. The calculations were then repeated this time with changing the explosive depth to 65m. The results were compared with analytical ones.

First of all, we need to input required data to be able to use the equations presented in sections 3.3.1 and 3.3.2. Inputs in Table 3.2 were provided for HBX-1 charge and sea water properties. Values of A and B were taken from Table 3.1. In Table 3.2, the values of K and k were taken from Swisdak [24]. The values of C_D, ρ_c, K_c, γ were provided from Geers and Hunter [25]. For values of ρ_f, c_f, g and p_{atm}, an another source [28] was referenced.

The calculations were carried using ABAQUS preprocessor. Figure 3.6 gives bubble radius change and migration results for m_c = 27.2 kg and D =7.3 meter.

Table 3.2: Input for Bubble Simulation [24, 25, 28].

Bubble Definition Input			
Input	Value	Input	Value
K	56700000	k	0.000084
K_c	1045000000	γ'	1.3
ρ_f	1025	c_f	1500
g	9.81	p_{atm}	101325
ρ_c	1720	C_D	1

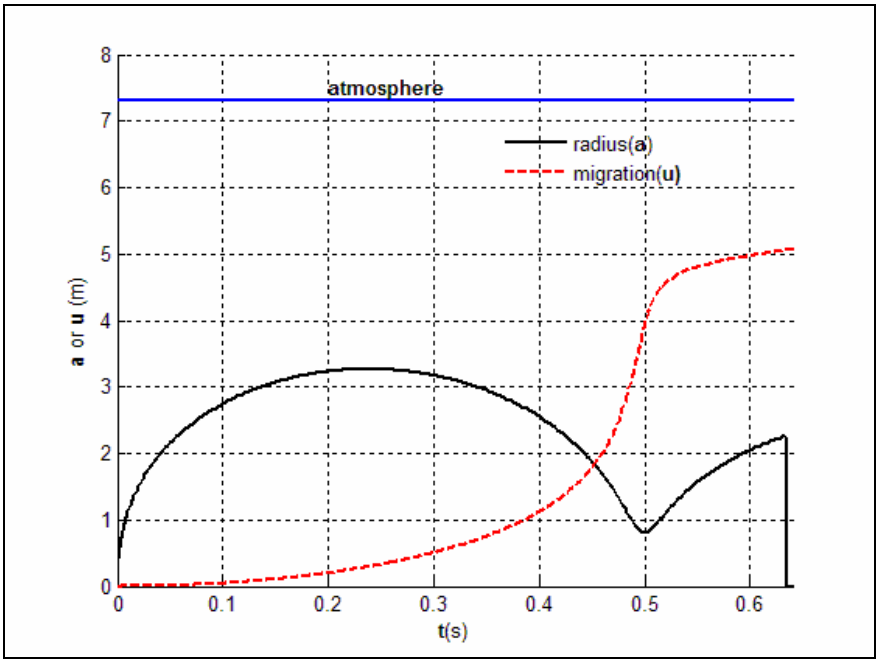

Figure 3.6 : Radius Change and Migration for 27.2 kg HBX-1 Charge at 7.3 m Depth.

As Figure 3.6 reveals, the bubble expansion-contraction process fully repeats only once and it loses all its internal energy before the second period has been completed. This is because that the charge is very near to the free surface. It can be seen from the figure that the bubble period is about 0.5 seconds and the maximum radius that the bubble can reach is 3.25 m. With the approximate equations given in section 3.3, the

bubble period had been found to be 0.6425 s and the maximum bubble radius had been estimated to be 4.44 m. So, equations (3.7) and (3.8) can be said to be roughly in coherence with Geers and Hunter bubble model.

Figure 3.7 gives bubble radius change and migration results for the same charge weight but this time with D = 65 m. Here, the bubble expansion-contraction process repeats many times due to excess hydrostatic pressure.

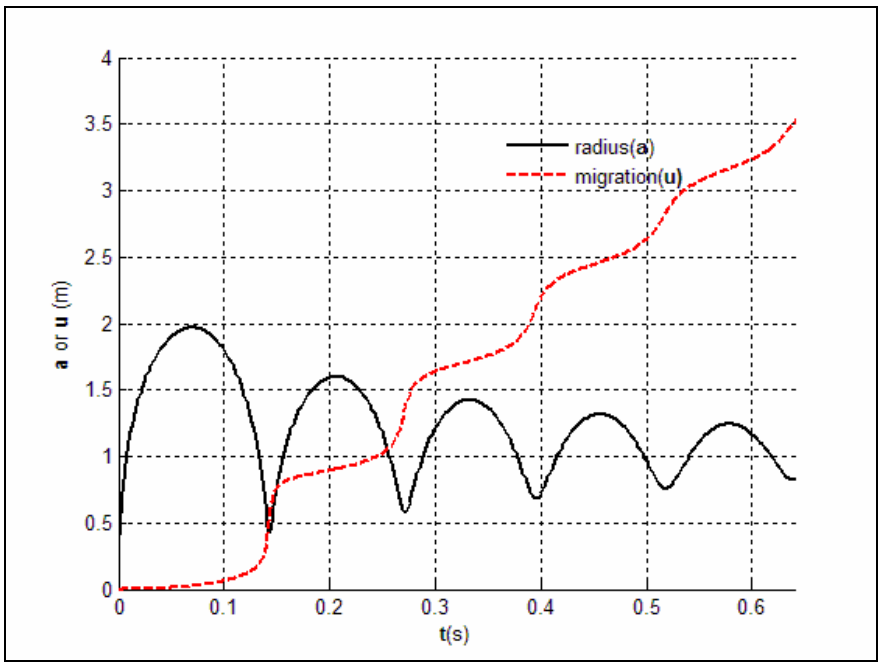

Figure 3.7 : Radius Change and Migration for 27.2 kg HBX-1 Charge at 65 m Depth.

The pressure wave profiles during shock wave and bubble oscillation phases at the stand-off point (8.77 m away from the source) for both D = 7.3m and D = 65 m cases are shown in Figure 3.8. It is seen that in D = 65m case, the bubble oscillation creates shock pulses with a frequency of about 10 Hz. The first bubble pulse amplitude seems to be comparable with the initial shock wave. On the other hand, in D = 7.3 m case, that is also the situation in this work, the bubble creates only one shock pulse with a relatively smaller amplitude compared with D = 65 m case.

Figure 3.9 is a closer look at the bubble oscillation phase. The first bubble pulse created in D = 65 m case is about 3 times the first bubble pulse created in the D = 6.7 m case. Many bubble pulses with decreasing amplitude follows the first bubble pulse in D = 65 m case. On the other hand in shallow water explosion, only one bubble pulse with relatively smaller amplitude is created.

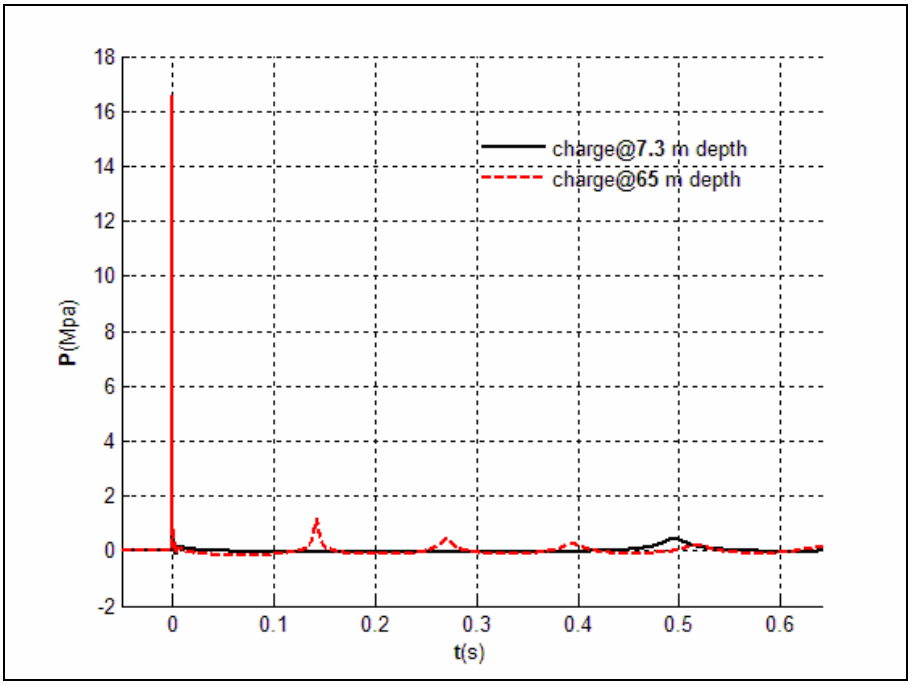

Figure 3.8 : The Pressure Shock Wave Profiles at 8.77 m Away From the Source.

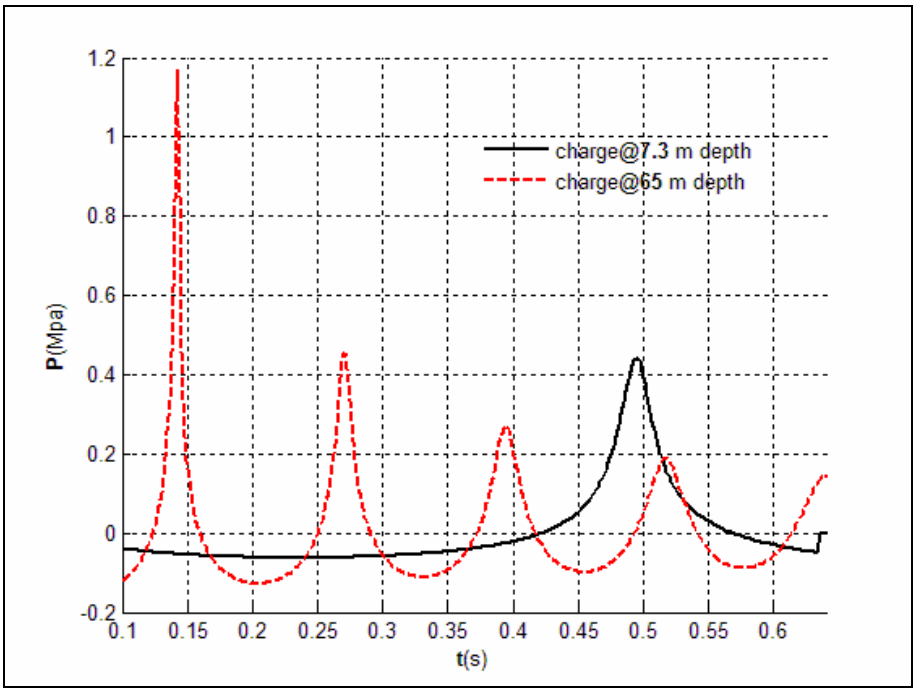

Figure 3.9 : Bubble Pulses at 8.77 m Away From the Source.

The bubble pulse in D = 7.3 m case is only about 2.5 % of the initial shock wave and it does not create a periodic excitation which might result in resonance of any floating structure in late time response. Together with the reasons explained in Section 3.3, the bubble pulses were neglected in this study.

The initial shock wave profiles created by D = 7.3 m and D = 65 m cases are identical. It is also worth noting that since the initial shock wave phase in Geers and Hunter model is based on the similitude equations (3.1) and (3.4), they should both have given the same pressure profiles in that phase. However, as seen in Figure 3.10, the decay rate of the initial shock wave phase for Geers and Hunter model is higher than Equation (3.1) indicates. This difference may be due to numerical integration scheme used in Geers and Hunter Model. The peak pressure values are the same. For convenience, Equation (3.1) was used for the remaining part of the work.

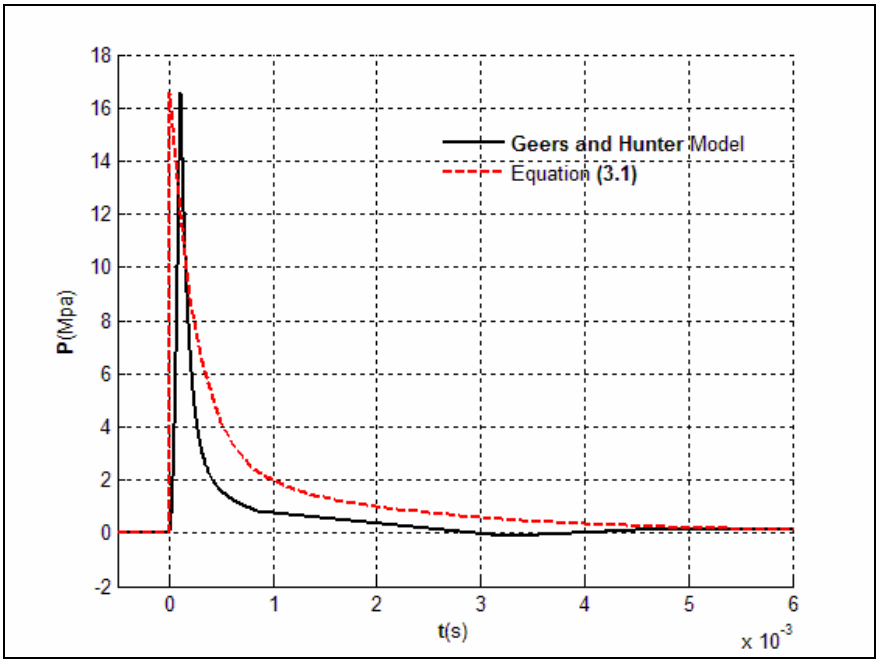

Figure 3.10 : Incident Shock Wave Profiles for 27.2 kg HBX-1 Charge at the Stand-off Point Located 8.77 m Away From the Source.

3.4 Cavitation Effects

Cavitation takes place in water when there is area of near-zero absolute pressure (about 206.8 Pa) [20]. This negative pressure results in a tensile force in the water. Because water can not withstand negative pressure, separation, or cavitation, occurs. Two types of cavitation occur in an UNDEX event; 'bulk' and 'local' cavitations. As the names imply, 'bulk' cavitation is a large volume of low pressure. On the other hand, 'local' cavitation is a small zone of low pressure usually observed at the fluid structure interaction surface. The effect of cavitation on the response of the floating

structures is important and must be properly modeled in order to obtain accurate results.

3.4.1 Bulk Cavitation

When an UNDEX takes place, a three dimensional spherical pressure wave is formed. It propagates outward in all directions away from the charge center. This outward propagation can be explained better by the aid of a two-dimensional model as depicted in Figure 3.11 [29].

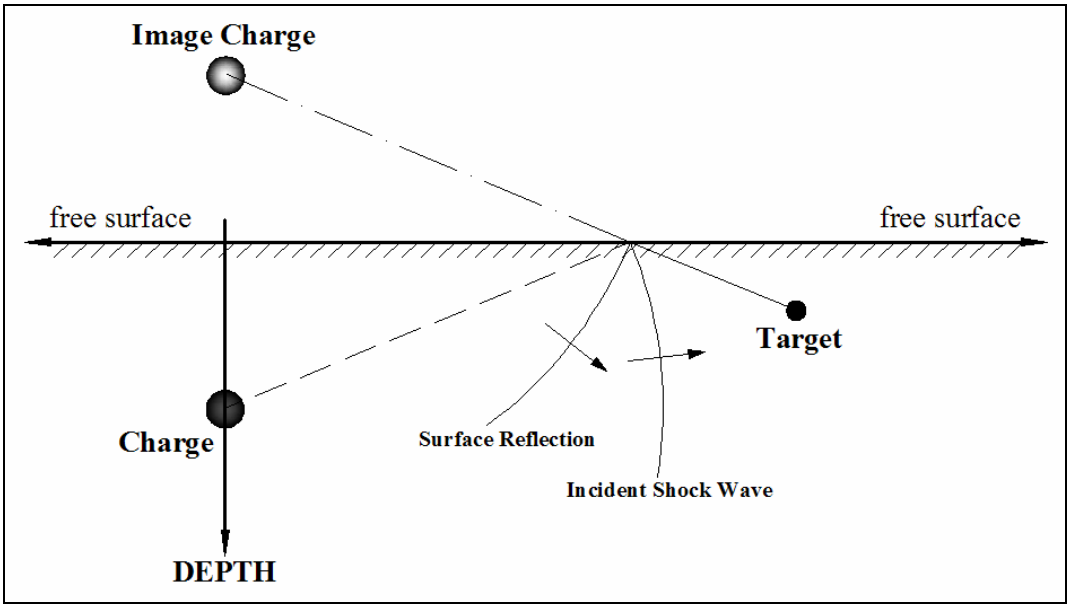

Figure 3.11 : Pressure Waves in UNDEX at a Point in the Fluid Medium.

The incident shock wave emitted from the charge is compressive in nature. It is the strongest wave and it reaches the target first. At free surface, the compressive incident pressure is scattered as a tension pressure since the free surface is soft and total pressure at this region should be zero;

$$P + P_R = 0 \tag{3.37}$$

The free surface reflects the incident pressure as if there is a new source of pressure wave above the free surface which emanates tension pressure; the mass of this image charge is the same of the real charge and its position is determined by taking the symmetry of the real charge according to the free surface. The calculations for the total pressure at target point then can be calculated considering both the charge and image charge, with atmospheric and hydrostatic pressures added.

As shown in Figure 3.12, the incident wave arrives at the target at t_0 followed by the arrival of the image wave, cut-off time (t_c in figure) later than t_0. At this time the incident shock wave has decayed and the arrival of the scattered wave which is tension in nature results in a sharp drop in pressure at the point of interest. Here, cavitation occurs if this sharp drop in pressure is strong enough to reduce the total pressure below the cavitation. For simplicity, the cavitation limit of the sea water was taken to be zero in following discussions.

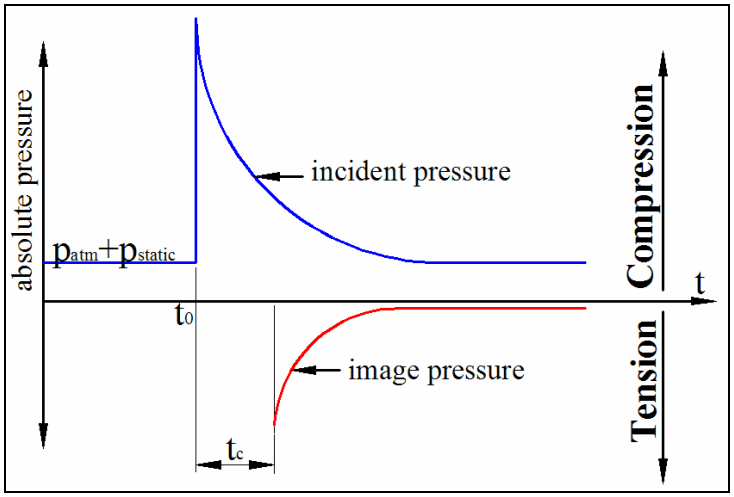

Figure 3.12 : Incident and Reflected Shock Waves; Showing Cut-off [29].

By considering Figure 3.13 and modifying Equations (3.1) and (3.2), the incident pressure profile at a point in fluid can be expressed as;

$$P(R_{j1},t) = P_c \left[\frac{a_c}{R_{j1}}\right]^{1+A} f(\tau) \tag{3.38}$$

$$\tau = \left[\frac{a_c}{R_{j1}}\right]^{B} \frac{v_c(t-t_o)}{a_c} \qquad t \geq t_0 \tag{3.39}$$

Here, R_{j1} is the distance from the charge to the target. Using the single exponential fit (Equation (3.3)) for its simplicity and above two equations;

$$P(R_{j1},t) = P_c \left[\frac{a_c}{R_{j1}}\right]^{1+A} e^{-\tau} \tag{3.40}$$

If we take;

$$\frac{1}{\theta}=\left[\frac{a_c}{R_{j1}}\right]^B\frac{v_c}{a_c} \tag{3.41}$$

$$\tau=\frac{(t-t_o)}{\theta} \qquad t\geq t_0 \tag{3.42}$$

The incident pressure profile can be expressed as;

$$P(R_{j1},t)=P_c\left[\frac{a_c}{R_{j1}}\right]^{1+A}e^{-\frac{(t-t_0)}{\theta}} \qquad t\geq t_0 \tag{3.43}$$

Similarly, the image pressure profile at target can be expressed as;

$$P_R(R_{j2},t)=-P_c\left[\frac{a_c}{R_{j2}}\right]^{1+A}e^{-\frac{(t-t_0-t_c)}{\theta}} \qquad t\geq t_0+t_c \tag{3.44}$$

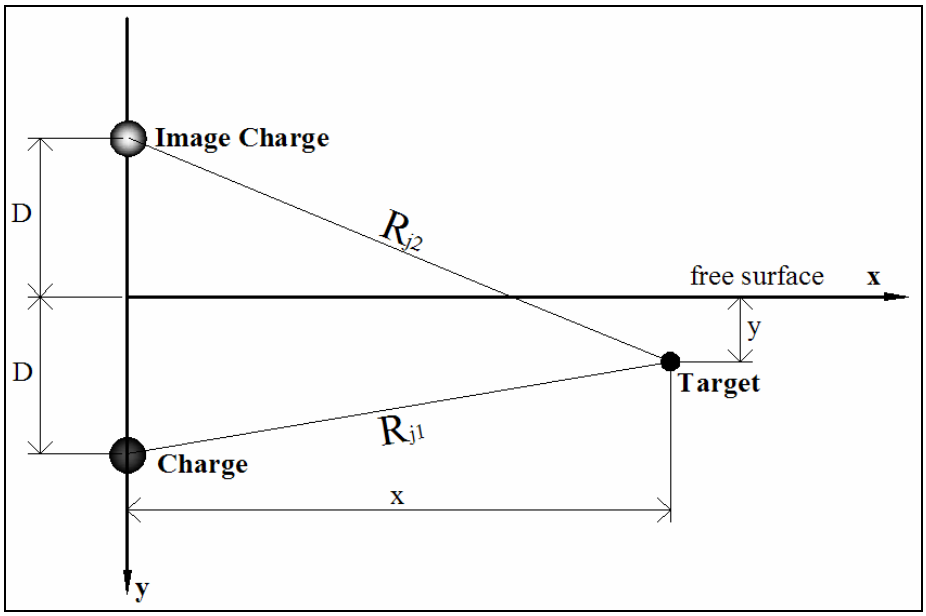

Figure 3.13 : Geometrical Quantities in UNDEX.

Total pressure at target can be expressed as;

$$P_{total}(t)=P+P_R+p_{atm}+\rho_f gD \tag{3.45}$$

$$P_{total}(t) = P_c\left[\frac{a_c}{R_{j1}}\right]^{1+A} e^{-\frac{(t-t_0)}{\theta}} - P_c\left[\frac{a_c}{R_{j2}}\right]^{1+A} e^{-\frac{(t-t_0-t_c)}{\theta}} + p_{atm} + \rho_f gD$$

The most severe instant at which cavitation is likely to occur is at cut-off, when;

$$t = t_0 + t_c \tag{3.46}$$

where from its definition;

$$t_c = \frac{\left(R_{j2} - R_{j1}\right)}{c_f} \tag{3.47}$$

So total pressure at cut-off is;

$$P_{total}(t_0 + t_c) = P_c\left[\frac{a_c}{R_{j1}}\right]^{1+A} e^{-\frac{\left(R_{j2}-R_{j1}\right)}{\theta c_f}} - P_c\left[\frac{a_c}{R_{j2}}\right]^{1+A} + p_{atm} + \rho_f gD \tag{3.48}$$

At upper cavitation boundary, the total pressure at cut-off should be zero [29] ;

$$F(x, y) = P_c\left[\frac{a_c}{R_{j1}}\right]^{1+A} e^{-\frac{\left(R_{j2}-R_{j1}\right)}{\theta c_f}} - P_c\left[\frac{a_c}{R_{j2}}\right]^{1+A} + p_{atm} + \rho_f gD = 0 \tag{3.49}$$

where

$$R_{j1} = \sqrt{(D-y)^2 + x^2} \tag{3.50}$$

$$R_{j2} = \sqrt{(D+y)^2 + x^2} \tag{3.51}$$

To determine the lower cavitation boundary, the decay rates of the reflected wave and absolute pressure should be equated [29];

$$G(x, y) = -\frac{P_i}{\theta c_f}\left[1 + \left[\frac{R_{j2} - 2D\left(\frac{D+y}{R_{j2}}\right)}{R_{j1}}\right]\left[B - \frac{BR_{j2}}{R_{j1}} - 1\right]\right] -$$

$$-\frac{(1+A)P_i}{R_{j1}^2}\left[R_{j2}-2D\left(\frac{D+y}{R_{j2}}\right)\right]+\rho_f g\left(\frac{D+y}{R_{j2}}\right)+\frac{(1+A)}{R_{j2}}\left(P_i+p_{atm}+\rho_f gy\right)=0 \tag{3.51}$$

with P_i is the incident wave at cut-off;

$$P_i=P_c\left[\frac{a_c}{R_{j1}}\right]^{1+A} e^{-\frac{(R_{j2}-R_{j1})}{\theta c_f}} \tag{3.52}$$

A Matlab code can be used to generate a plot of cavitation region in the fluid due to an UNDEX. It is provided in APPENDIX B.

According to MIL-S-901D [1], the shock test platform is to be loaded by the explosion of 27.2 kg HBX-1 charge at 7.31 m depth. The explosion will be repeated for the same charge and depth with four different orientations with respect to the platform. These orientations are to be visualized in Figure 3.14.

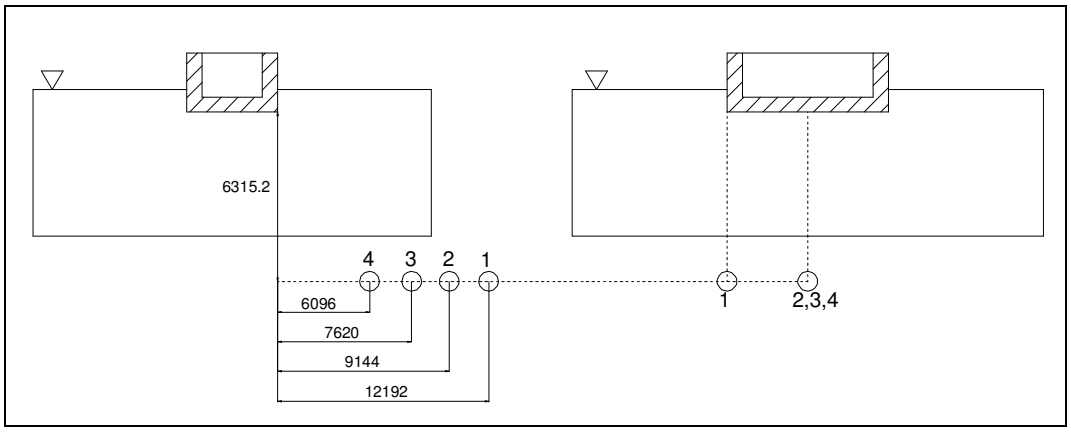

Figure 3.14 : Charge Orientations for Four-Shots Relative to Platform as Specified in MIL-S-901D.

Using Matlab and the code provided in APPENDIX B, the fluid region that is likely to cavitate for four cases shown above was estimated. Figures 3.15 and 3.16 are 2D views of the UNDEX region showing the cavitating area. The figures also show the fluid mesh boundary used in the analysis. In all cases, cavitation is likely to occur in a big region of the fluid mesh shown with green lines. So, cavitation should be considered in simulations.

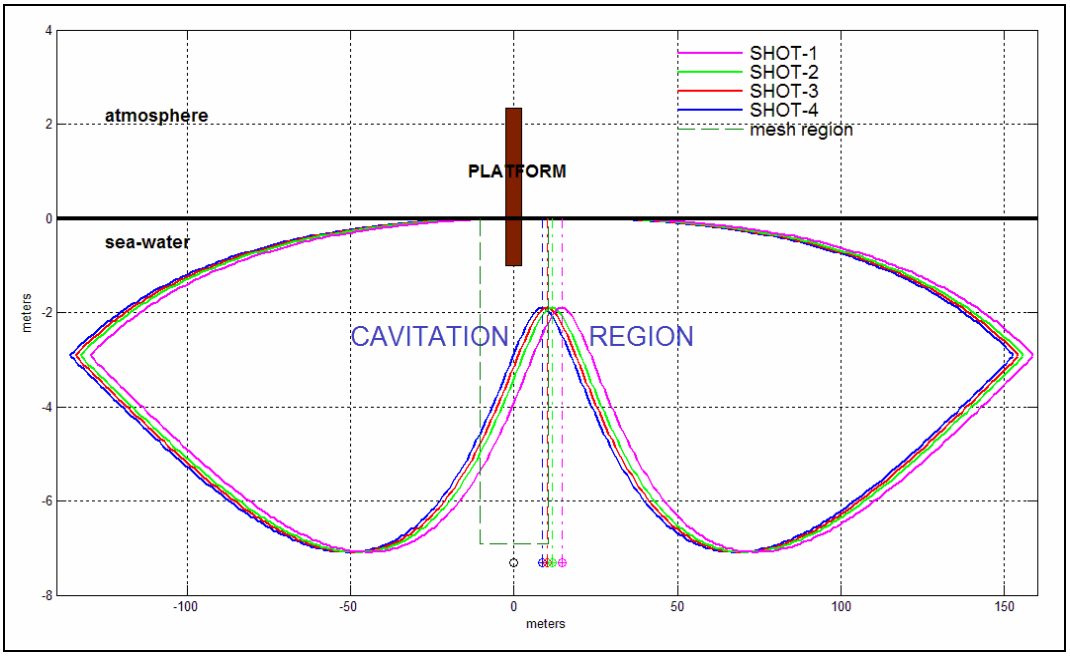

Figure 3.15 : Cavitation Regions for Four UNDEX Cases of 27.2 kg HBX-1 Charge, Rear View.

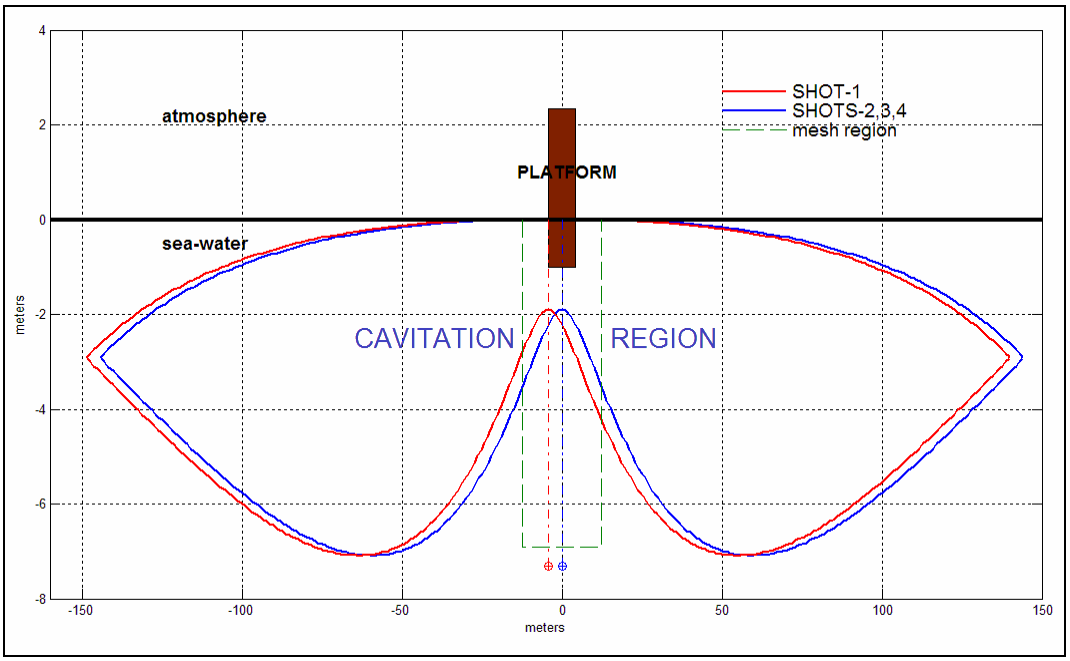

Figure 3.16 : Cavitation Regions for Four UNDEX Cases of 27.2 kg HBX-1 Charge, Front View.

3.4.2 Local Cavitation

As described in previous sections, local cavitation is usually observed at the fluid structure interaction surface. As the fluid-structure interaction takes place, the total pressure along the bottom of the structure becomes negative. Because the water is not able to sustain tension, the water pressure reduces to vapor pressure (about zero

MPa) and cavitation occurs. Taylor plate theory can be used to explain the local cavitation phenomenon assuming that the plate is rigid (Figure 3.17) [8].

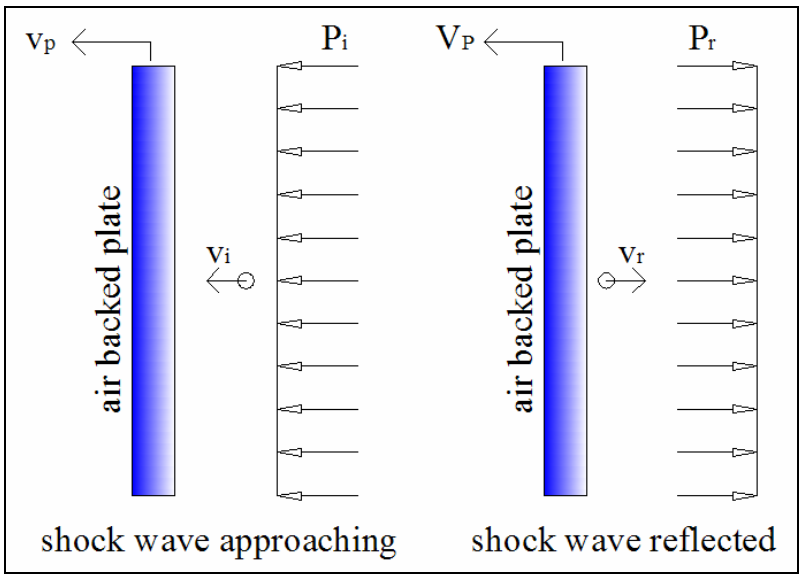

Figure 3.17 : Taylor Plate Subjected to a Plane Wave [29].

The plate is subjected to an incident shock wave $P_i(t)$ which can be taken to be a planar wave away from the explosion source. As this incident wave interacts with the plate, it is reflected as a planar wave $P_r(t)$. If the fluid particle velocities behind the incident and reflected shock wave are $v_i(t)$ and $v_r(t)$ respectively, the velocity of the plate, $v_p(t)$ becomes [21];

$$v_p(t) = v_i(t) - v_r(t) \tag{3.53}$$

Applying Newton's second law of motion to the plate;

$$m_p \frac{dv_p}{dt} = P_t = P_i + P_r \tag{3.54}$$

Here, P_t is the total pressure behind the plate and m_p is the mass per unit area of the plate. For a one-dimensional wave, it can be shown using the D'Alembert solution to the wave equation and the reduced momentum equation for a fluid, that the pressure for the incident and reflected shock waves are defined as [21];

$$P_i(t) = \rho_f c_f v_i(t) \tag{3.55}$$

$$P_r(t) = \rho_f c_f v_r(t) \tag{3.56}$$

Using Equations (3.55) and (3.56) in Equation (3.53), the reflected pressure can be expressed as;

$$P_r(t) = P_i(t) - \rho_f c_f v_p(t) \tag{3.57}$$

Then, the equation of motion (3.54) can be rewritten as;

$$m_p \frac{dv_p}{dt} + \rho_f c_f v_p(t) = 2P_i = 2P_{\max} e^{-t/\theta} \qquad t > 0 \tag{3.58}$$

Here, Equation (3.43) was used together with that retarded time, t_0, was taken to be zero and;

$$P_{\max} = P_c \left[\frac{a_c}{R} \right]^{1+A} \tag{3.59}$$

in which *R* is the stand-off distance from charge center to the center of the plate. The explosive was assumed to be located on the normal line through the center of the plate.

Equation (3.59) is a first-order linear differential equation. Solving the differential equation to obtain the velocity of the plate;

$$v_p(t) = \frac{2P_{\max}\theta}{m_p(1-\beta)} \left[e^{-\beta t/\theta} - e^{-t/\theta} \right] \qquad t > 0 \tag{3.60}$$

$$\beta = \frac{\rho_f c_f \theta}{m_p} \tag{3.61}$$

Using Equation (3.54) and (3.57), total pressure in front of the plate can be found as;

$$P_t(t) = P(t)_i + P_r(t) = 2P(t)_i - \rho_f c_f v_p(t) = \frac{2P_{\max}}{1-\beta} \left[e^{-t/\theta} - \beta e^{-\beta t/\theta} \right] \tag{3.62}$$

As β becomes large (a lightweight plate), the total pressure in Equation (3.62) will become negative very early. Since water cannot sustain tension (i.e. any significant negative pressure), cavitation will occur when the vapor pressure of water is reached. This is known as local cavitation. As cavitation occurs, the plate is actually

separating from the fluid and the velocity of the plate reaches to maximum at the instant cavitation occurs [9].

The time at which cavitation occurs, t_{cav}, can be found by equating the total pressure expression (Equation (3.62)) to vapor pressure of the water which can be taken to be zero [9];

$$t_{cav} = \frac{\ln \beta}{\beta - 1}\theta \tag{3.63}$$

The maximum plate velocity can also be evaluated at that time using Equation 3.60;

$$v_{p\max} = \frac{2P_{\max}}{\rho_f c_f}\beta^{1/(1-\beta)} \tag{3.64}$$

3.4.3 Analytical Velocity Estimation of a Shock Test Platform Subjected to Through-Centerline Underwater Explosion

The Equations (3.60), (3.62) and (3.64) can be used to roughly estimate the vertical velocity, total pressure behind and maximum velocity respectively of a floating shock platform subjected to UNDEX of an HBX-1 explosive located on the normal line through the center of the plate.

In reality, when the total pressure is zero, the atmospheric pressure on the dry side of the platform will slow down the platform. The equation of motion after the cavitation occurs can be written as;

$$m_p \frac{dv_p}{dt} = -P_{atm} \qquad t > t_{cav} \tag{3.65}$$

Solving this simple first order linear differential equation, the velocity of the platform after cavitation can be expressed as;

$$v_p(t) = \frac{-P_{atm}}{m_p}(t - t_{cav}) + v_p(t_{cav}) \qquad t > t_{cav} \tag{3.66}$$

As it is the maximum velocity reached at cavitation time;

$$v_p(t) = \frac{-P_{atm}}{m_p}(t - t_{cav}) + v_{p\max} \qquad t > t_{cav} \tag{3.67}$$

Equation (3.60) together with equation (3.67) can be used to estimate the vertical motion of the platform assuming that it is rigid. A simple Matlab code was provided in APPENDIX C to calculate the vertical velocity of the platform analyzed in this work. Figure 3.18 shows the incident pressure, the total pressure and the vertical velocity of the platform when it is subjected to the through-centerline explosion of a 50 kg HBX-1 charge at a depth of 20 m.

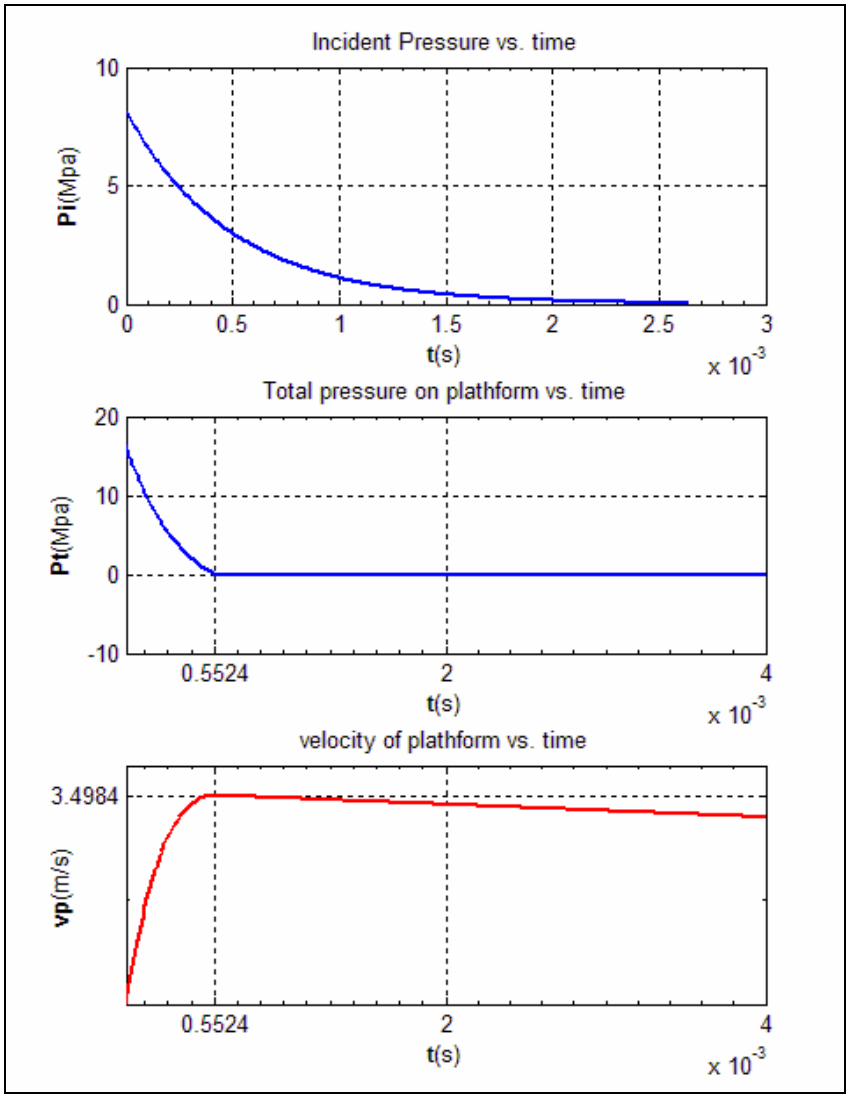

Figure 3.18 : Incident and Total Pressures, and Velocity of Shock Platform Subjected to Through-Centerline UNDEX of 50 kg HBX-1 Charge at 30 m Depth.

4. ELEMENTS OF UNDERWATER EXPLOSION SIMULATION

4.1 Acoustic Equations

Consider a one-dimensional fluid flow through a duct with cross-sectional area *A*, and with velocity v_0. The gross fluid state variables are pressure (P_0) and density (ρ_0). The fluid flow is opposed by a homogeneous, isotropic, volumetric velocity-dependent drag, γ [30]. The net force acting on an elemental volume of fluid of length dx is equal to the time rate of change in its momentum. This is expressed as;

$$A\left(P_0^x - P_0^{x+dx} - \gamma v_0 dx\right) = \frac{\partial}{\partial t}\rho_0 v_0 A dx \qquad \textbf{(4.1)}$$

This can be written as:

$$\frac{\partial}{\partial t}P_0 + \gamma v_0 + \frac{\partial}{\partial t}\rho_0 v_0 = 0 \qquad \textbf{(4.2)}$$

We now consider small perturbations in the fluid where the perturbed variables are $P_0 + p$, $\rho_0 + \rho$, and $v_0 + v$ [30]. Substituting these into the above equation yields;

$$\frac{\partial}{\partial t}\left(P_0 + p\right) + \gamma\left(v_0 + v\right) + \frac{\partial}{\partial t}\left[\left(\rho_0 + \rho\right)\left(v_0 + v\right)\right] = 0 \qquad \textbf{(4.3)}$$

Assuming no changes of the gross variables in time, and neglecting products of small quantities we have:

$$\frac{\partial}{\partial t}P_0 + \frac{\partial}{\partial t}p + \gamma\left(v_0 + v\right) + \rho_0\frac{\partial v}{\partial t} + v_0\frac{\partial \rho}{\partial t} = 0 \qquad \textbf{(4.4)}$$

Also assuming a slow flow in the fluid, we set [30]:

$$\frac{\partial}{\partial t}P_0 = v_0 = 0 \qquad \textbf{(4.5)}$$

This gives us the equilibrium statement for the perturbed acoustic flow:

$$\frac{\partial}{\partial t} p + \gamma v + \rho_0 \frac{\partial v}{\partial t} = 0 \tag{4.6}$$

This equilibrium equation for small motions of a compressible, adiabatic fluid with velocity-dependent momentum loses can be expressed in three dimensions by tensor notation as [27]:

$$\frac{\partial p}{\partial \mathbf{x}} + \gamma \dot{\mathbf{u}}^f + \rho_f \ddot{\mathbf{u}}^f = 0 \tag{4.7}$$

where p is the dynamic pressure in the fluid (the pressure in excess of any initial static pressure), $\mathbf{x}$ is the spatial position of the fluid particle, $\dot{\mathbf{u}}^f$ is the fluid particle velocity, $\ddot{\mathbf{u}}^f$ is the fluid particle acceleration, ρ_f is the density of the fluid, and γ is the "volumetric drag" (force per unit volume per velocity) caused by the fluid flowing through the matrix material. The slow flow assumption is usually considered to be sufficiently accurate for steady fluid velocities up to Mach 0.1 [23].

4.1.1 Derivation of Acoustic Constitutive Equation

In acoustics, the pressure-density relationship is essentially non-linear and given as:

$$P_0 = K' \rho_0^{\gamma} \tag{4.8}$$

where K' is a constant and γ is the ratio of specific heats [30].

Therefore, we have:

$$\frac{dP_0}{d\rho_0} = \gamma K' \rho_0^{\gamma-1} = \frac{\gamma}{\rho_0} K' \rho_0 = \frac{\gamma}{\rho_0} P_0 \tag{4.9}$$

Since the changes in pressure and density have been assumed to be small, we can write:

$$\frac{dP_0}{d\rho_0} = \frac{p}{\rho} \tag{4.10}$$

Where p and ρ are the acoustic pressure and density of the perturbation.

So we have:

$$\frac{p}{\rho} = \frac{\gamma}{\rho_0} P_0 \Rightarrow p = (\gamma P_0)\left(\frac{\rho}{\rho_0}\right) \Rightarrow p = K_f \left(\frac{\rho}{\rho_0}\right) \tag{4.11}$$

where K_f is called the bulk modulus.

Now, consider a fixed mass of gas occupying volume V_0, and undergoing a small volume change ΔV. To satisfy the conservation of mass, we must have;

$$\rho_0 V_0 = (\rho_0 + \rho)(V_0 + \Delta V) \tag{4.12}$$

This gives:

$$\frac{\rho}{\rho_0} = -\frac{\Delta V}{V_0} = -\varepsilon_f \tag{4.13}$$

Hence, we have the constitutive relationship [30];

$$p = -K_f \varepsilon_f \tag{4.14}$$

Here, the fluid is assumed to be inviscid, linear and compressible. In three dimensions:

$$p = -K_f \frac{\partial}{\partial \mathbf{x}} \cdot \mathbf{u}_f \tag{4.15}$$

4.1.2 Acoustic Constitutive Equation for Cavitating Fluid

For an acoustic medium capable of undergoing cavitation, the absolute pressure (sum of the static pressure and the excess dynamic pressure) can not drop below the specified cavitation limit. When the absolute pressure drops to this limit value, the fluid is assumed to undergo free expansion without a corresponding drop in the dynamic pressure. The pressure would rebuild in the acoustic medium once the free expansion that took place during the cavitation is reversed sufficiently to reduce the volumetric strain to the level at the cavitation limit. The constitutive behavior for an acoustic medium capable of undergoing cavitation can be stated as [27] ;

$$p = \max\{p_v, (p_c - p_o)\} \tag{4.16}$$

where a pseudo-pressure p_v, a measure of the volumetric strain, is defined as

$$p_v = -K_f \frac{\partial}{\partial \mathbf{x}} \cdot \mathbf{u}_f \tag{4.17}$$

4.2 Acoustic Boundary Conditions in UNDEX Analysis

Acoustic fields are strongly dependent on the conditions at the boundary of the acoustic medium [27]. Generally, four types of acoustic boundary conditions exist in an UNDEX analysis which are discussed below.

The boundary of an acoustic medium that obeys Equation (4.7) and Equation (4.15) (Equation (4.16) replaces Equation (4.15) in case of cavitating fluid) can be divided into sub regions S as shown in Figure 4.1 on which the following conditions are imposed:

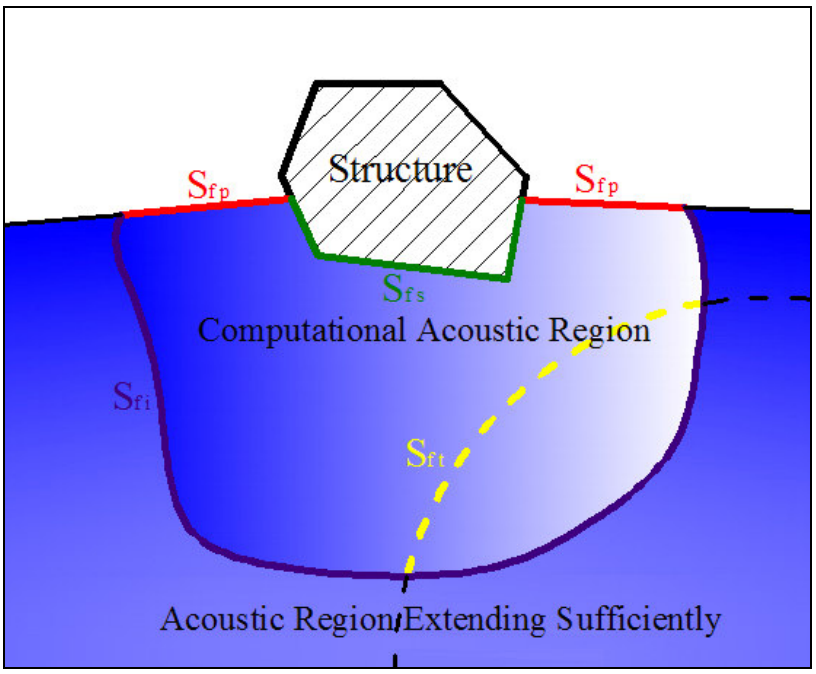

Figure 4.1 : Usual Surfaces of a Fluid Medium, Interacting With a Structure, on Which Various Boundary Conditions Are Imposed in an UNDEX Event.

S_{fp}; It is the surface on which the value of the acoustic pressure p is prescribed. In UNDEX, it is the free surface on which the acoustic pressure is equivalent to atmospheric pressure.

S_{ft}; Where we prescribe the normal derivative of the acoustic medium. This condition also prescribes the motion of the fluid particles and can be used to model acoustic sources, rigid walls (baffles), incident wave fields, and symmetry planes. In UNDEX, it is used to model the spherical shock wave resulting from the explosion of a charge, which is an incident wave field.

S_{fi}; It's the radiating acoustic boundary. As it's the case in UNDEX event, acoustic media extends sufficiently far from the region of interest that they can be modeled as infinite in extent. In such cases it is convenient to truncate the computational region and apply a boundary condition to simulate waves passing exclusively outward from the computational region.

S_{fs}; Where the motion of an acoustic medium is directly coupled to the motion of a solid. On such an acoustic-structural boundary the acoustic and structural media have the same displacement normal to the boundary, but the tangential motions are uncoupled. In UNDEX, it sands for the fluid-structure interaction between the water and any structure on or in the sea, i.e. a surface ship, a submarine or a floating shock platform which is the case in this work.

4.3 Formulation of Direct Integration, Coupled Acoustic-Structural Analysis

4.3.1 Formulation for Acoustic Medium

To derive the partial differential equation used in direct integration transient analysis, we divide Equation (4.7) by ρ_f, take its gradient with respect to $\mathbf{x}$, neglect the gradient of γ/ρ_f, and combine the result with the time derivatives of Equation (4.15) to obtain the equation of motion for the fluid in terms of the fluid pressure [27]:

$$\frac{1}{K_f}\ddot{p}+\frac{\gamma}{\rho_f K_f}\dot{p}-\frac{\partial}{\partial \mathbf{x}}\cdot\left(\frac{1}{\rho_f}\frac{\partial p}{\partial \mathbf{x}}\right)=0 \qquad \textbf{(4.18)}$$

To obtain a single scalar equation over the entire body (weak form), an arbitrary variational field, δp, is introduced and integrated over the fluid;

$$\int_{V_f} \delta p \left(\frac{1}{K_f} \ddot{p} + \frac{\gamma}{\rho_f K_f} \dot{p} - \frac{\partial}{\partial \mathbf{x}} \cdot \left(\frac{1}{\rho_f} \frac{\partial p}{\partial \mathbf{x}} \right) \right) dV = 0 \qquad \textbf{(4.19)}$$

Green's theorem, which converts a volume integral to surface integral, allows Equation (4.19) to be rewritten as [27];

$$\int_{V_f} \left[\delta p \left(\frac{1}{K_f} \ddot{p} + \frac{\gamma}{\rho_f K_f} \dot{p} \right) + \frac{1}{\rho_f} \frac{\partial \delta p}{\partial \mathbf{x}} \cdot \frac{\partial p}{\partial \mathbf{x}} \right] dV + \int_S \delta p \left(\frac{1}{\rho_f} \mathbf{n}^- \cdot \frac{\partial p}{\partial \mathbf{x}} \right) dS = 0 \qquad \textbf{(4.20)}$$

Here, $\mathbf{n}^-$ is the inward normal on the boundary.

Assuming that p is prescribed on S_{fp}, the equilibrium Equation (4.7) is used on the remainder of the boundary to relate the pressure gradient to the motion of the boundary. Scalar product of Equation (4.7) with inward normal:

$$\mathbf{n}^- \cdot \left(\frac{\partial p}{\partial \mathbf{x}} + \gamma \dot{\mathbf{u}}^f + \rho_f \ddot{\mathbf{u}}^f \right) = 0 \qquad \text{on } S - S_{fp} \qquad \textbf{(4.21)}$$

Using this equation, the term $\mathbf{n}^- \cdot \frac{\partial p}{\partial \mathbf{x}}$ can be eliminated from Equation (4.21) to yield:

$$\int_{V_f} \left[\delta p \left(\frac{1}{K_f} \ddot{p} + \frac{\gamma}{\rho_f K_f} \dot{p} \right) + \frac{1}{\rho_f} \frac{\partial \delta p}{\partial \mathbf{x}} \cdot \frac{\partial p}{\partial \mathbf{x}} \right] dV - \int_{S - S_{fp}} \delta p \left(T(\mathbf{x}) \right) dS = 0 \qquad \textbf{(4.22)}$$

In the above equation, the boundary "traction" term

$$T(\mathbf{x}) = \mathbf{n}^- \cdot \left(\ddot{\mathbf{u}}^f + \frac{\gamma}{\rho_f} \dot{\mathbf{u}}^f \right) = -\mathbf{n}^- \cdot \left(\frac{1}{\rho_f} \frac{\partial p}{\partial \mathbf{x}} \right) \qquad \text{on } S - S_{fp} \qquad \textbf{(4.23)}$$

has been introduced [27].

Except for the imposed pressure on S_{fp}, all of the other boundary conditions described in Section 4.2 can be formulated in terms of $T(\mathbf{x})$. This term has dimensions of acceleration; in the absence of volumetric drag this boundary traction is equal to the inward acceleration of the particles of the acoustic medium:

$$T(\mathbf{x}) = \mathbf{n}^{-} \cdot \ddot{\mathbf{u}}^{f} \qquad \text{on } S - S_{fp} \tag{4.24}$$

When volumetric drag is present, the boundary traction is the normal derivative of the pressure field, divided by the true mass density: a force per unit mass of fluid. Consequently, when volumetric drag exists in a transient acoustic model, a unit of $T(\mathbf{x})$ yields a lower local volumetric acceleration, due to drag losses [27].

In direct integration transient dynamics, the acoustic boundary conditions are enforced as follows [23]:

On S_{fp}, p is prescribed and $\delta p = 0$.

On S_{ft}, where we prescribe the normal derivative of the acoustic pressure per unit density:

$$T_{ft}(\mathbf{x}) \equiv T_0 \tag{4.25}$$

In the absence of volumetric drag in the medium, this enforces a value of fluid particle acceleration, $\mathbf{n}^{-} \cdot \ddot{\mathbf{u}}^{f} = T_0 = a_{in}$ where a_{in} is incident wave acceleration. An imposed $T_0 = a_{in}$ can be used to model the oscillations of a rigid plate or body exciting a fluid, for example. A special case of this boundary condition is $a_{in} = 0$ which represents a rigid immobile boundary. As mentioned above, if the medium has nonzero volumetric drag, a unit of T_0 imposed at the boundary will result in a relatively lower imposed particle acceleration. Incident wave fields on a boundary of a fluid are modeled with a T_0 that varies in space and time, corresponding to the effect of the arrival of the wave on the boundary [23]. It is the way the spherically dilating shock wave was modeled in this work and will be further detailed in a subsequent section.

On S_{fi}, the radiating boundary, a boundary condition is applied by specifying the corresponding impedance [27]:

$$T_{fi}(\mathbf{x}) \equiv -\left(\frac{1}{c_1} \dot{p} + \frac{1}{a_1} p \right) \tag{4.26}$$

where the values of the admittance parameters, $1/c_1$ and $1/a_1$, will again be discussed in a further section.

On S_{fs}, the acoustic-structural interface, we apply the acoustic-structural interface condition by equating displacement of the fluid and solid, which enforces the condition [27]:

$$\mathbf{n}^- \cdot \mathbf{u}^f = \mathbf{n}^- \cdot \mathbf{u}^m \tag{4.27}$$

Here, $\mathbf{u}^m$ is the displacement of the structure. In the presence of volumetric drag it follows that the acoustic boundary traction coupling fluid to solid is;

$$T(\mathbf{x}) = \mathbf{n}^- \cdot \left(\ddot{\mathbf{u}}^m + \frac{\gamma}{\rho_f} \dot{\mathbf{u}}^m \right) \tag{4.28}$$

The formulation of the transient coupled problem would be made nonsymmetric by the presence of the term in Equation (4.28) associated with the volumetric drag coefficient, γ [27]. In the great majority of practical applications the acoustic tractions associated with volumetric drag are small compared to those associated with fluid inertia,

$$\ddot{\mathbf{u}}^m \gg \frac{\gamma}{\rho_f} \dot{\mathbf{u}}^m \tag{4.29}$$

so this term is ignored in transient analysis:

$$T_{fs}(\mathbf{x}) = \mathbf{n}^- \cdot \ddot{\mathbf{u}}^m \tag{4.30}$$

These definitions for the boundary traction term, $T(\mathbf{x})$, are introduced into Equation (4.22) to give the final variational statement for the acoustic medium which is the equivalent of the virtual work statement for a structure [27]:

$$\int_{V_f} \left[\delta p \left(\frac{1}{K_f} \ddot{p} + \frac{\gamma}{\rho_f K_f} \dot{p} \right) + \frac{1}{\rho_f} \frac{\partial \delta p}{\partial \mathbf{x}} \cdot \frac{\partial p}{\partial \mathbf{x}} \right] dV - \int_{S_{fs}} \delta p T_0 dS +$$

$$+\int_{S_{fi}} \delta p \left(\frac{1}{c_1} \dot{p} + \frac{1}{a_1} p \right) dS - \int_{S_{fs}} \delta p \mathbf{n}^{-} \cdot \ddot{\mathbf{u}}^{m} dS = 0 \qquad \textbf{(4.31)}$$

4.3.2 Formulation for Structural Behavior

The structural behavior is defined by the virtual work equation [27];

$$\int_V \delta\varepsilon : \boldsymbol{\sigma} dV + \int_V \alpha_c \rho \delta \mathbf{u}^m \cdot \dot{\mathbf{u}}^m dV + \int_V \rho \delta \mathbf{u}^m \cdot \ddot{\mathbf{u}}^m dV +$$

$$+\int_{S_{fs}} p \delta \mathbf{u}^m \cdot \mathbf{n} dS - \int_{S_t} \delta \mathbf{u}^m \cdot \mathbf{t} dS = 0 \qquad \textbf{(4.32)}$$

Here, $\boldsymbol{\sigma}$ is the stress at a point in the structure, p is the pressure acting on the fluid-structural interface, $\mathbf{n}$ is the outward normal to the structure, ρ is the density of the material, α_c is the mass proportional damping factor (part of the Rayleigh damping assumption for the structure), $\ddot{\mathbf{u}}^m$ is the acceleration of a point in the structure, $\mathbf{t}$ is the surface traction applied to the structure, $\delta \mathbf{u}^m$ is a variational displacement field, and $\delta\varepsilon$ is the strain variation that is compatible with $\delta \mathbf{u}^m$. For simplicity, in this equation all other loading terms such, as body forces, except the fluid pressure and surface traction have been neglected.

In Equation (4.31), first term stands for the internal work of the material. The vertical double dot product in above equations means scalar product of two matrices; corresponding conjugate components of the two matrices are multiplied as pairs and the products summed. The second term in the same equation represents material damping while the third one stands for inertia effects. The fourth term is due to fluid-structure interaction and represents the way fluid drives the structure. The last term is associated with the surface tractions applied to the structure, such as a pressure variation directly applied on a surface region of the structure, S_t.

4.3.3 The Discretized Finite Element Equations

Equations (4.31) and (4.32) define the variational problem for the coupled fields $\mathbf{u}^m$ and p. The problem is discretized by introducing interpolation functions. In the fluid:

$$p = H^P p^P \qquad \textbf{(4.33)}$$

$P = 1, 2, ...$ up to the number of pressure nodes [27]. In the structure:

$$\mathbf{u}^m = \mathbf{N}^N u^N \tag{4.34}$$

$N = 1, 2, ...$ up to the number of displacement degrees of freedom [27]. In these and the following equations, it' assumed that summation is over the superscripts that refer to the degrees of freedom of the discretized model. The superscripts *P*, *Q* are used to refer to pressure degrees of freedom in the fluid and *N*, *M* are used to refer to displacement degrees of freedom in the structure. For structural system, Galerkin method is used; the variational field has the same form as the displacement:

$$\delta\mathbf{u}^m = \mathbf{N}^N \delta u^N \tag{4.35}$$

For the fluid;

$$\delta p = \mathbf{H}^P \delta p^P \tag{4.36}$$

Using the Equations (4.33) and (4.36) in Equation (4.31) and using Equations (4.34) and (4.35) in Equation (4.32), the discretized finite element equations of fluid medium and solid medium are obtained respectively as [27];

$$\delta p^P \left\{ M_f^{PQ} \ddot{p}^Q + C_f^{PQ} \dot{p}^Q + \left(K_f^{PQ} + K_{fi}^{PQ} \right) p^Q - S_{fs}^{PM} \ddot{u}^M - P_f^P \right\} = 0 \tag{4.37}$$

$$\delta u^N \left\{ I^N + M^{NM} \ddot{u}^M + C_{(m)}^{NM} \dot{u}^M + \left[S_{fs}^{QN} \right]^T p^Q - P^N \right\} = 0 \tag{4.38}$$

Here;

$$M_f^{PQ} = \int_{V_f} \frac{1}{K_f} H^P H^Q dV \tag{4.39}$$

$$C_f^{PQ} = \int_{V_f} \frac{\gamma}{\rho_f} \frac{1}{K_f} H^P H^Q dV \tag{4.40}$$

$$K_f^{PQ} = \int_{V_f} \frac{1}{\rho_f} \frac{\partial H^P}{\partial \mathbf{x}} \cdot \frac{\partial H^Q}{\partial \mathbf{x}} dV \tag{4.41}$$

$$K_{fi}^{PQ} = \int_{S_{fi}} \frac{1}{a_1} H^P H^Q dS \tag{4.42}$$

$$S_{fs}^{PM} = \int_{S_{fs}} H^P \mathbf{n}^- \cdot \mathbf{N}^M dS \tag{4.43}$$

$$P_f^P = \int_{S_{ft}} H^P T_0 dS \tag{4.44}$$

$$M^{NM} = \int_V \rho \mathbf{N}^N \cdot \mathbf{N}^M dV \tag{4.45}$$

$$C_{(m)}^{NM} = \int_V \alpha_c \rho \mathbf{N}^N \cdot \mathbf{N}^M dV \tag{4.46}$$

$$I^N = \int_V \boldsymbol{\beta}^N : \boldsymbol{\sigma} dV \tag{4.47}$$

$$P^N = \int_{S_t} \mathbf{N}^N \cdot \mathbf{t} dS \tag{4.48}$$

where $\boldsymbol{\beta}^N$ is a matrix called strain interpolator that depends, in general, on the current position, $\mathbf{x}$, of the material point being considered. The matrix $\boldsymbol{\beta}^N$ that defines the strain variation from the variations of the kinematic variables is derivable from the interpolation functions of solid medium [27].

To make Equation (4.37) and Equation (4.38) dimensionally consistent, a Petrov-Galerkin substitution is applied [27];

$$\delta p^P = \frac{d^2}{dt^2}\left(\delta \hat{p}^P\right) \tag{4.49}$$

This new function $\delta \hat{p}^P$ makes the single variational acoustic-structural equation dimensionally consistent; the single variational equation containing both acoustic and structural mediums is obtained using Equation (4.49) in (4.37) and summing with (4.38);

$$-\delta \hat{p}^P \left\{ M_f^{PQ} \ddot{p}^Q + C_f^{PQ} \dot{p}^Q + \left(K_f^{PQ} + K_{fi}^{PQ} \right) p^Q - S_{fs}^{PM} \ddot{u}^M - P_f^P \right\} +$$

$$+\delta u^N \left\{ I^N + M^{NM} \ddot{u}^M + C_{(m)}^{NM} \dot{u}^M + \left[S_{fs}^{QN} \right]^T p^Q - P^N \right\} = 0 \qquad \textbf{(4.50)}$$

This last equation can be thought to be a picture of the UNDEX event; the terms in first line represent fluid inertia effect, fluid damping effect due to velocity dependent drag, the stiffness of the fluid against pressure changes, the mechanism by which the structure drives the fluid, and the pressure loading due to an incident wave such as an underwater explosion respectively. On the other hand, the terms in second line stands for structural internal work due to deformation of the structure, solid inertia effect, energy losses due to structural damping, and the way fluid drives the structure and any other external force applied to the structure respectively.

So before further progress on subject, for convenience, the discretized equations of motion for acoustic and solid mediums can be expressed in an easy to understand matrix form as;

$$\left[M\right]_f \{\ddot{p}\} + \left[C\right]_f \{\dot{p}\} + [K]_f \{p\} = [S_{fs}]\{\ddot{u}\} + \{P\}_f \qquad \textbf{(4.51)}$$

$$\left[M\right]_s \{\ddot{u}\} + \left[C\right]_s \{\dot{u}\} + [K]_s \{u\} = [S_{fs}]^T \{p\} - \{P\}_s \qquad \textbf{(4.52)}$$

In Equation (4.51), $\left[M\right]_f$ is the fluid mass matrix, $\left[C\right]_f$ is the fluid damping matrix, $\left[K\right]_f$ is the fluid stiffness matrix, $[S_{fs}]^T$ is the transformation matrix that builds the mechanism by which fluid and solid regions interact, $\{P_f\}$ is any external incident wave loading on the fluid such as a spherical shock wave due to an explosion. In Equation (4.52), $\left[M\right]_s$ is the structural mass matrix, $\left[C\right]_s$ is the structural damping matrix, $\left[K\right]_s$ is the structural stiffness matrix and $\{P\}_s$ is any external force acting on the structure. $\{p\}$ and $\{u\}$ are fluid pressure and structural displacement vectors respectively. The other terms are time derivatives of these two. Also note that the $\{p\}$ stands for sum of incident pressure and scattered (reflected) pressure waves respectively such that;

$$\{p\} = \{p_I\} + \{p_S\} \qquad \textbf{(4.53)}$$

$\{p_I\}$ results from any incident shock wave loading while $\{p_S\}$ is the reflection of this incident wave from any structure, boundary or reflection plane.

4.4 Surface-Based Acoustic-Structural Interaction Procedure

To obtain the response to an UNDEX of a floating shock test platform or of any other floating structure such as a surface ship, the integration of the structural behavior as well as the integration of its effects on the fluid at the wetted surface and vice versa are needed. When the shock test platform is loaded by a severe shock wave produced by an underwater explosion, the structure deforms and displaces the fluid on the fluid-structure interface. The pressure distribution on the wetted surface is also changed by the rigid body motion of the platform due to the shock wave. This interaction which goes on until the end of the vibration and rigid body motion of the platform must be accurately modeled using coupled fluid-structure equations. A surface-based coupled acoustic-structural interaction analysis procedure can be used to enforce a coupling between the structural surface nodes and the fluid surface nodes and the equation of motion can then be solved by an explicit time integration scheme which is the preferable solution method for high-speed and short-time dynamic events. The interaction should be defined between the fluid mesh and wetted side of the meshed structure. This section deals with explaining details on this enforced surface-based interaction procedure.

In the surface-based method the tractions and volumetric acceleration fluxes are computed between structural and acoustic media. One side (identified as the “slave”) receives point tractions/fluxes based on interpolation with the shape functions from the other (“master”) side. Either the acoustic fluid or the structural solid can be the slave or master. The side with coarser mesh size should be selected as master because that the interaction is based on the projections from the slave side; since the number of projections will be more when the finer mesh side is selected as slave, the accuracy of the interaction will also increase. In this work, fluid side was selected to be slave in the final analysis.

Figure 4.2 shows the surface based interaction procedure [27]. At the start of an analysis, the projections $\mathbf{x}_N$ of slave nodes onto the master surface are found, and the areas A_N and normals $\mathbf{n}^{-}(\mathbf{x}_N)$ associated with the slave nodes are computed. The

projections are points $\mathbf{P}(\mathbf{x}_N)$ on the master surface; master nodes in the vicinity of this projection are identified. Variables at the slave nodes $\mathbf{x}_N$ are then interpolated from variables at the identified master surface nodes near the projection $\mathbf{P}(\mathbf{x}_N)$.

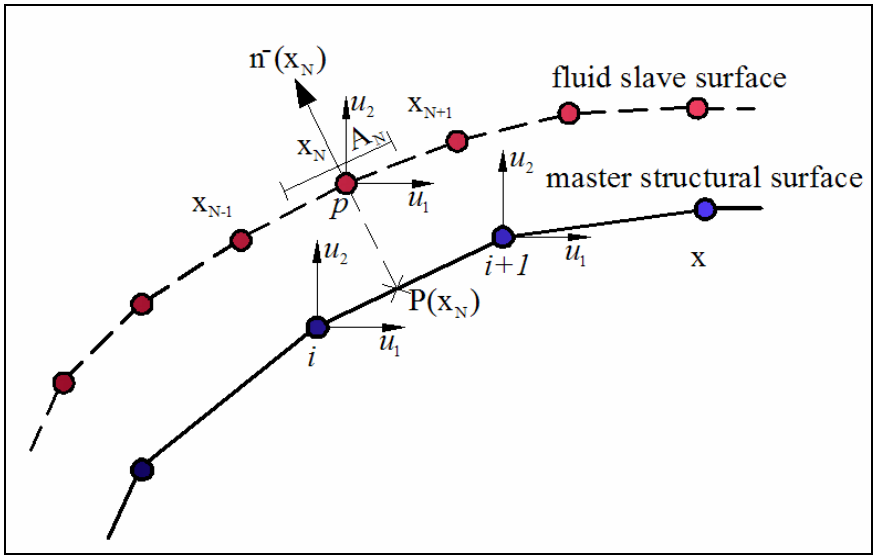

Figure 4.2 : Surface Based Interaction, Fluid as Slave and Structural Surface as Master [23].

If the fluid medium surface is designated as the slave, values at each fluid node are constrained to be an average of the values at the nearby master surface nodes.

From Equation (4.31), the fluid equation coupling term can be expressed alone as;

$$-\int_{S_{fs}} \delta p \mathbf{n}^{-} \cdot \ddot{\mathbf{u}}^{m} dS \qquad \textbf{(4.54)}$$

This term is now approximated at the slave node by the interpolated values of structural displacements at the nearby master nodes times the area of the slave node [23]:

$$\int_{S_{fs}} \delta p \mathbf{n}^{-} \cdot \ddot{\mathbf{u}}^{m} dS \approx A_N \left[\sum_i \mathbf{n}^{-}(\mathbf{x}_N) \cdot N^i(\mathbf{P}(\mathbf{x}_N)) \ddot{\mathbf{u}}_{\mathbf{i}}^{\mathbf{m}} \right] \qquad \textbf{(4.55)}$$

The summation extends over all master nodes i in the vicinity of the slave node projection $\mathbf{P}(\mathbf{x}_N)$. The computation is repeated for each slave node $\mathbf{x}_N$ on the surface S_{fs} and assembled to form the entire coupling matrix.

From equation (4.32), the pressure coupling term in the structural equation can be expressed alone as;

$$\int_{S_{fs}} p\delta\mathbf{u}^m \cdot \mathbf{n} dS \tag{4.56}$$

The contribution to this pressure coupling term due to a slave node is approximated by [23]:

$$\int_{S_{fs}} p\delta\mathbf{u}^m \cdot \mathbf{n} dS \approx p_N A_N \left[\sum_i \mathbf{n}^-(\mathbf{x}_N) \cdot N^i(\mathbf{P}(\mathbf{x}_N)) \right] \tag{4.57}$$

Equation (4.56) and (4.57) for the coupling terms result in matrices that are the transpose of each other.

4.5 Scattering Wave Formulation versus Total Wave Formulation

From the coupled equations of motion of the fluid-solid interaction (Equation (4.37) and Equation (4.38)):

$$M_f^{PQ} \ddot{p}^Q + C_f^{PQ} \dot{p}^Q + \left(K_f^{PQ} + K_{fi}^{PQ} \right) p^Q = + \left[S_{fs}^{PM} \right] T^M + P_f^P \tag{4.58}$$

$$I^N + M^{NM} \ddot{u}^M + C_{(m)}^{NM} \dot{u}^M = - \left[S_{fs}^{QN} \right]^T p^Q + P^N \tag{4.59}$$

The fluid traction:

$$T(\mathbf{x}) = \mathbf{n}^- \cdot \left(\ddot{\mathbf{u}}^f + \frac{\gamma}{\rho_f} \dot{\mathbf{u}}^f \right) = -\mathbf{n}^- \cdot \left(\frac{1}{\rho_f} \frac{\partial p}{\partial \mathbf{x}} \right) \tag{4.60}$$

is a quantity (with dimensions of acceleration) that describes the mechanism by which the solid motion drives the fluid; the fluid drives the solid by the pressure on the solid surface.

The total pressure can be decomposed into the known incident wave component and the unknown scattered component [27]:

$$p = p_I + p_S \tag{4.61}$$

Introducing Equation (4.60) in Equation (4.58) and Equation (4.59), the following equations are obtained:

$$M_f^{PQ}\ddot{p}_S^Q + C_f^{PQ}\dot{p}_S^Q + \left(K_f^{PQ} + K_{fi}^{PQ}\right)p_S^Q = +\left[S_{fs}^{PM}\right]T^M + P_f^P -$$

$$-\left[M_f^{PQ}\ddot{p}_I^Q + C_f^{PQ}\dot{p}_I^Q + \left(K_f^{PQ} + K_{fi}^{PQ}\right)p_I^Q\right] \quad \textbf{(4.62)}$$

For solid:

$$I^N + M^{NM}\ddot{u}^M + C_{(m)}^{NM}\dot{u}^M = -\left[S_{fs}^{QN}\right]^T\left[p_S^Q + p_I^Q\right] + P^N \quad \textbf{(4.63)}$$

It can be seen that the displacements in the solid are driven by the sum of the incident pressure, which forms an applied boundary traction, and the scattered pressure, the unknown pressure field in the fluid.

The incident pressure field is independent of the scattered field by convention. Therefore, it can be shown that it is a solution to the equation [27]:

$$M_f^{PQ}\ddot{p}_I^Q + C_f^{PQ}\dot{p}_I^Q + \left(K_f^{PQ} + K_{fi}^{PQ}\right)p_I^Q = \left[S_{fs}^{PM}\right]T_I^M \quad \textbf{(4.64)}$$

so the fluid domain equation reduces to

$$M_f^{PQ}\ddot{p}_S^Q + C_f^{PQ}\dot{p}_S^Q + \left(K_f^{PQ} + K_{fi}^{PQ}\right)p_S^Q = +\left[S_{fs}^{PM}\right]T_S^M + P_f^P \quad \textbf{(4.65)}$$

The scattered fluid traction, T_S, depends on the incident pressure through the decomposition above and the solid motion at the boundary:

$$T_S = \mathbf{n}^- \cdot \left(\ddot{\mathbf{u}} + \frac{\gamma}{\rho_f}\dot{\mathbf{u}}\right) + \mathbf{n}^- \cdot \left(\frac{1}{\rho_f}\frac{\partial p_I}{\partial \mathbf{x}}\right) \quad \textbf{(4.66)}$$

In UNDEX, incident pressure field, p_I, is due to explosion. In linear analysis where the cavitation of fluid is not included, only the unknown scattered wave Equation (4.65) is solved together with structural Equation (4.63). This is called scattered wave formulation. However, since the cavitation is important in UNDEX analysis and it depends on the total pressure, total wave formulation should be used to include nonlinear fluid behavior.

4.6 Incident Wave Loading

For simulating the incident pressure wave field due to an explosion, the change of pressure at a so called stand-off point is first evaluated from the similitude equations given in Section 3. Then, this incident pressure wave variation is used to calculate the incident pressure wave variation at other fluid points.

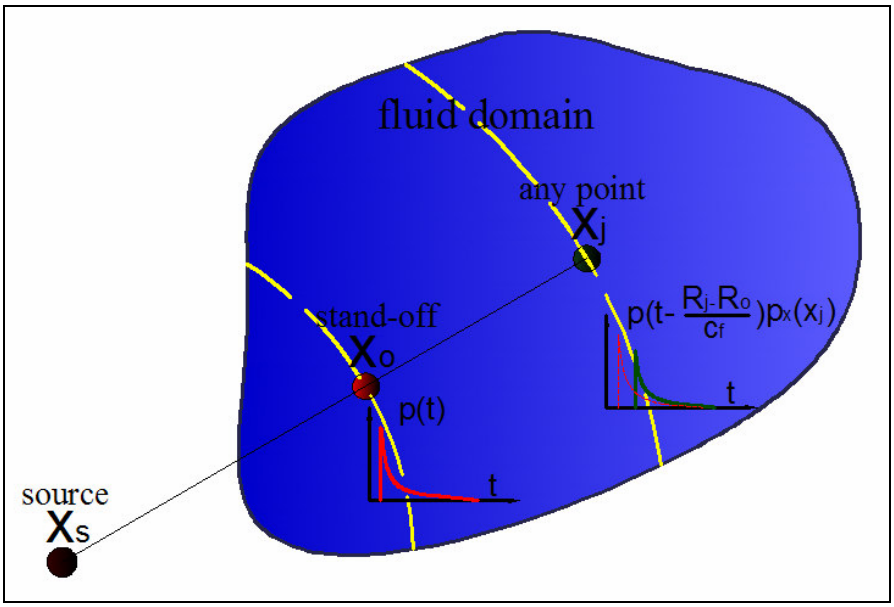

Figure 4.3 : Incident Pressure Wave at Stand-off and Any Other Point in the Fluid Domain.

See Figure 4.3; the incident pressure variation, $p(t)$, at stand-off point, $\mathbf{x}_o$, is calculated from similitude relations. Then the incident pressure variation at a fluid point, $\mathbf{x}_j$, is calculated according to following equation [27]:

$$p_I(\mathbf{x}_j,t) = p\left(t - \frac{R_j - R_o}{c_f}\right) p_x\left(\mathbf{x}_j\right) \tag{4.67}$$

$$R_o = \left\|\mathbf{x}_s - \mathbf{x}_o\right\| \tag{4.68}$$

For spherical waves;

$$R_j = \left\|\mathbf{x}_s - \mathbf{x}_j\right\| \tag{4.69}$$

$$p_x\left(\mathbf{x}_j\right) = \frac{\left\|\mathbf{x}_s - \mathbf{x}_o\right\|}{\left\|\mathbf{x}_s - \mathbf{x}_j\right\|} \tag{4.70}$$

For plane waves:

$$R_j = \frac{\left|\left(\mathbf{x}_j - \mathbf{x}_s\right)\cdot\left(\mathbf{x}_o - \mathbf{x}_s\right)\right|}{\left\|\mathbf{x}_s - \mathbf{x}_o\right\|} \tag{4.71}$$

$$p_x\left(\mathbf{x}_j\right) = 1 \tag{4.72}$$

Note that the source point, $\mathbf{x}_s$, should be located out of the fluid domain. Otherwise, the incident pressure at some fluid region around the source may become infinite according to Equation (4.71) and the results will very likely be inaccurate.

4.7 Reflections From Outside of the Computational Domain

In UNDEX, it's likely that the incident shock wave will be reflected back to the computational domain from any reflection plane, such as from a sea bed. If the reflection plane is far away from the computational domain, the effect can be neglected. However, if the distance of the reflection plane to the source location is comparable with the distance between the source and the structure, then, one should also consider these reflection effects. See Figure 4.4:

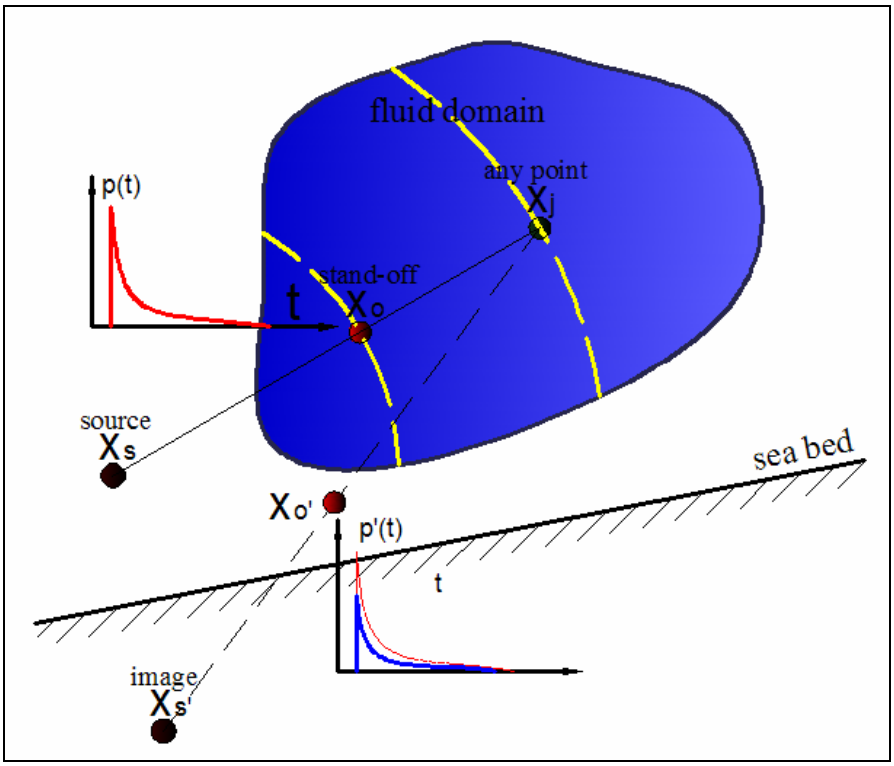

Figure 4.4 : Reflection of Incident Wave From a Sea Bed.

The reflected wave from the seabed can be modeled as if there is another source of incident pressure wave located symmetrically according to the reflection plane. This new source is called the "image" of the real source. The incident pressure wave due to the real source at stand-off point, $\mathbf{x}_o$, is explained in previous section and it is $p(t)$. The pressure wave due to the image wave at a stand-off point distance from the image charge, let's say at point $\mathbf{x}_\mathbf{o}'$, can be evaluated from the equations obtained in previous section.

The distance from the image, $\mathbf{x}_\mathbf{s}'$, to the "image" stand-off point, $\mathbf{x}_\mathbf{o}'$, holds the following equation:

$$\left\|\mathbf{x}_\mathbf{s}' - \mathbf{x}_\mathbf{o}'\right\| = \left\|\mathbf{x}_s - \mathbf{x}_o\right\| \tag{4.73}$$

If the reflection coefficient of the reflection plane is described as the ratio of the reflected pressure wave to the incoming pressure wave, then the incident pressure wave at the image stand-off point, $\mathbf{x}_\mathbf{o}'$, due to the image source can be expressed as;

$$p'(t) = Q \cdot p(t) \tag{4.74}$$

where Q is the reflection coefficient and $p'(t)$ is the reflected pressure wave at $\mathbf{x}_\mathbf{o}'$. Modifying Equations (4.67), (4.68), (4.69) and (4.70):

$$p_I'(\mathbf{x}_j, t) = p'\left(t - \frac{R_j' - R_o'}{c_f}\right) p_x'\left(\mathbf{x}_j\right) \tag{4.75}$$

$$R_o' = \left\|\mathbf{x}_s' - \mathbf{x}_o'\right\| \tag{4.76}$$

For spherical waves;

$$R_j' = \left\|\mathbf{x}_s' - \mathbf{x}_j\right\| \tag{4.77}$$

$$p_x'\left(\mathbf{x}_j\right) = \frac{\left\|\mathbf{x}_s' - \mathbf{x}_o'\right\|}{\left\|\mathbf{x}_s' - \mathbf{x}_j\right\|} \tag{4.78}$$

So Equation (4.75) can be expressed as:

$$p_I'(\mathbf{x}_j,t) = p'\left(t - \frac{\left\|\mathbf{x}_s' - \mathbf{x}_j\right\| - \left\|\mathbf{x}_s' - \mathbf{x}_o'\right\|}{c_f} \right) \frac{\left\|\mathbf{x}_s' - \mathbf{x}_o'\right\|}{\left\|\mathbf{x}_s' - \mathbf{x}_j\right\|} \tag{4.79}$$

Using Equation (4.73) and (4.74):

$$p_I'(\mathbf{x}_j,t) = Qp\left(t - \frac{\left\|\mathbf{x}_s' - \mathbf{x}_j\right\| - \left\|\mathbf{x}_s - \mathbf{x}_o\right\|}{c_f} \right) \frac{\left\|\mathbf{x}_s - \mathbf{x}_o\right\|}{\left\|\mathbf{x}_s' - \mathbf{x}_j\right\|} \tag{4.80}$$

Therefore, the reflected spherical load is similar to the direct load, with magnitude reduced by the reflection impedance effect and by the greater distance traveled.

4.8 Radiating (Nonreflecting) Boundary Conditions

Many of the acoustic studies such as the UNDEX response involve a vibrating structure in an infinite domain. In such cases we model a layer of the acoustic medium using finite elements, to a thickness of 1/3 to a full wavelength, out to a "radiating" boundary surface. We then impose a condition on this surface to allow the acoustic waves to pass through and not reflect back into the computational domain. For radiation boundaries of simple shapes such as planes, spheres etc. simple impedance boundary conditions can represent good approximations to the exact conditions.

The radiation boundary condition is applied by specifying the corresponding boundary traction, given by Equation (4.26):

$$T_{fi}(\mathbf{x}) \equiv -\left(\frac{1}{c_1}\dot{p} + \frac{1}{a_1}p \right) \tag{4.26}$$

$1/c_1$ and $1/a_1$ are admittance parameters which are defined as [27]:

$$\frac{1}{c_1} = \frac{f}{\sqrt{\rho_f}K_f} \tag{4.81}$$

$$\frac{1}{a_1} = f \cdot \left[\frac{\beta}{\rho_f} + \frac{\gamma}{2\rho_f\sqrt{\rho_f}K_f} \right] \tag{4.82}$$

The values of parameters f and β vary with the geometry of the boundary of the radiating surface of the acoustic medium (plane, circular, cylinder etc.).

For simple shapes, the values of admittance parameters are given in Table 4.1.

Table 4.1: Admittance Parameters for Simple Shapes of Radiating Boundary [27].

Geometry	f	β
Plane	1	0
Circle or circular cylinder	1	$\frac{1}{2 \cdot radius}$
Sphere	1	$\frac{1}{radius}$

In this work, plane type radiating boundaries were used.

The radiating boundary conditions are approximate, so that the error in an exterior acoustic analysis is controlled not only by the usual finite element discretization error but also by the error in the approximate radiation condition. The radiation boundary conditions converge to the exact condition in the limit as they become infinitely distant from the radiating structure. In practice, these radiation conditions provide accurate results when the distance between the surface and the structure is at least one-half of the longest characteristic or responsive structural wavelength [23].

4.9 Mesh Refinement

Inadequate mesh refinement is the most common source of difficulties in acoustic and vibration analysis. For reasonable accuracy, at least six representative internodal intervals of the acoustic mesh should fit into the shortest acoustic wavelength present in the analysis. Accuracy improves substantially if eight or more internodal intervals are used at the shortest wavelength [23]. In transient analyses the shortest wavelength present is difficult to determine before an analysis: it is reasonable to estimate this wavelength using the highest frequency present in the loads or prescribed boundary conditions. An “internodal interval” is defined as the distance from a node to its nearest neighbor node in an element; that is, the element size for a linear element or half of the element size for a quadratic element. At a fixed internodal interval, quadratic elements are more accurate than linear elements. However, explicit

analyses require use of linear elements. The level of refinement chosen for the acoustic medium should be reflected in the solid medium as well: the solid mesh should be sufficiently refined to accurately model compressional and shear waves.

If the details of the wave field in the vicinity of the fluid-solid interface are important, the meshes should be of equally high refinement, with the refinement corresponding to the lower wave speed medium.

The acoustic wavelength decreases with increasing frequency, so there is an upper frequency limit for a given mesh. Let $L_{\max}$ represent the maximum internodal interval of an element in a mesh, $n_{\min}$ the number of internodal intervals per acoustic wavelength, $f_{\max}$ is frequency of excitation, and $c_f = \sqrt{K_f / \rho_f}$ the speed of sound. The requirement for maximum linear element length can then be expressed as:

$$L_{\max} \leq \frac{c_f}{n_{\min} f_{\max}} \tag{4.83}$$

So the maximum excitation frequency to be accurately simulated can be expressed as;

$$f_{\max} \leq \frac{c_f}{n_{\min} L_{\max}} \tag{4.84}$$

Because we are interested in the structural response, and the incident pressure wave around the acoustic-structural interface is the driving force, we can use discrete fourier transform, which provides the complex magnitude (the amplitude and phase) of the content of a discrete time varying function, to determine the frequency content of the these loadings. The incident pressure waves around the acoustic-structural interaction for four explosions to be simulated in this work and their frequency domain representation (magnitude versus frequency) are shown in Figure 4.5. The figure also shows the real part of the inverse discrete Fourier transform of the frequency representation of four shots, which is identical to time domain representation given in first plot.

We used an element size of about 50 mm around the acoustic-structural interface. The element size increases up to 150 mm at outer fluid regions. The average maximum element size through the whole acoustic region is 135 mm. The speed of

sound in the fluid can be found by setting $K_f = 2306.35$ Mpa and $\rho_f = 1.025 \cdot 10^{-9}$ tonne/mm^3 which are commonly used values for sea water [28].

$$c_f = \sqrt{\frac{K_f}{\rho_f}} = \sqrt{\frac{2306.35}{1.025 \cdot 10^{-9}}} = 1500032.52\, mm/s \approx 1500\, m/s \quad \textbf{(4.85)}$$

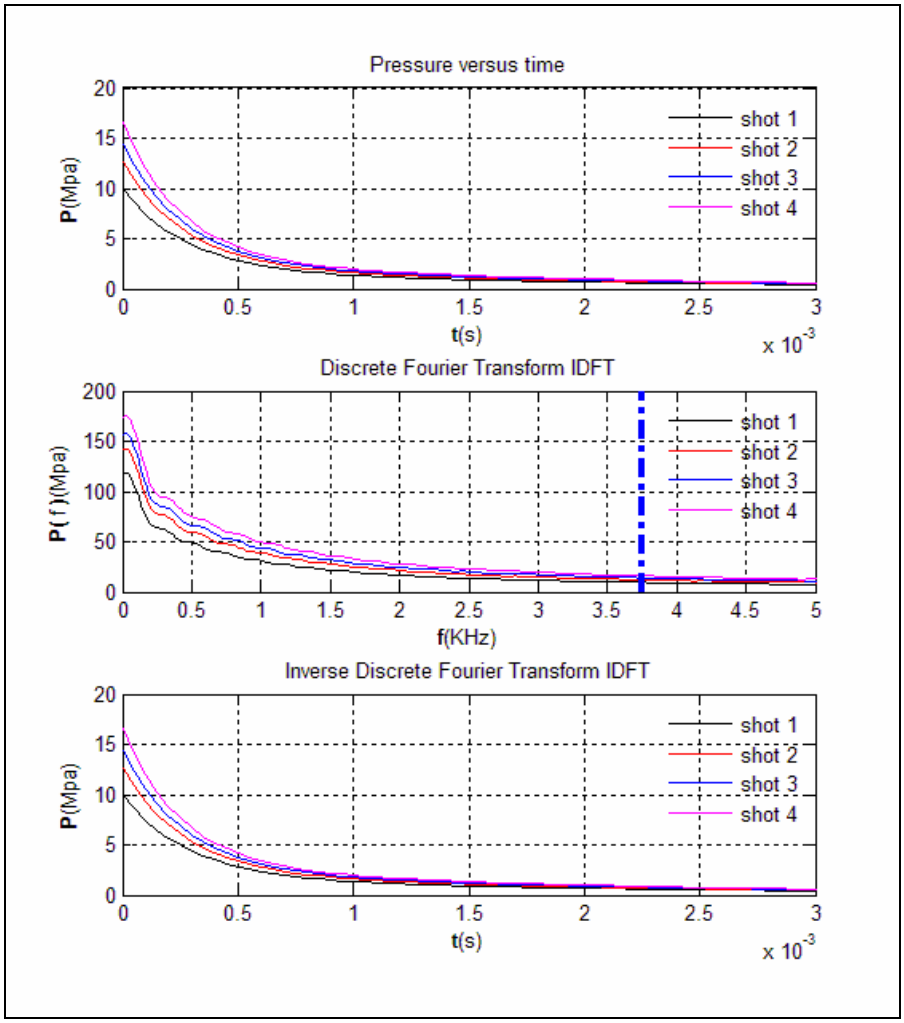

Figure 4.5 : DFT of Incident Shock Wave Profiles.

Setting $n_{\min} = 8$ and Using Equation (4.84), the maximum frequency which can be simulated accurately can be found;

$$f_{\max} \leq \frac{1500\, m/s}{8 \cdot 0.05m} = 3750Hz \quad \textbf{(4.86)}$$

The second plot in Figure 4.5 also shows the frequency content limit up to which the loading will be accurately simulated, by setting the number of internodal intervals

per acoustic wavelength to eight, to have substantially accurate results around the acoustic-structural interface. However, refining mesh to such degree through the whole acoustic region would require about eighteen million elements, which is computationally insufficient. Instead of using Equation (4.84) to determine the overall fluid element size, we carried a mesh convergence study, presented in Section 5, to determine the overall element size for fluid medium. Then the mesh size around the acoustic-structural interface was refined to 50 mm to improve accuracy.

4.10 Explicit Time Integration

The explicit dynamics procedure performs a large number of small time increments efficiently. An explicit central-difference time integration rule is used; each increment is relatively inexpensive because there is no solution for a set of simultaneous equations. The explicit central-difference operator satisfies the dynamic equilibrium equations at the beginning of the increment, *t*; the accelerations calculated at time *t* are used to advance the velocity solution to time $t+\Delta t$ and the displacement solution to time $t+\Delta t$.

4.10.1 Numerical Implementation

The explicit dynamics analysis procedure is based on the implementation of an explicit integration rule together with the use of diagonal ("lumped") element mass matrices. The equations of motion for the body are integrated using the explicit central-difference integration rule [23];

$$\dot{u}^N_{(i+\frac{1}{2})} = \dot{u}^N_{(i-\frac{1}{2})} + \frac{\Delta t_{(i+1)} + \Delta t_{(i)}}{2} \ddot{u}^N_{(i)} \qquad \textbf{(4.87)}$$

$$u^N_{(i+1)} = u^N_{(i)} + \Delta t_{(i+1)} \dot{u}^N_{(i+\frac{1}{2})} \qquad \textbf{(4.88)}$$

where u^N is a degree of freedom (a displacement or rotation component) and the subscript i refers to the increment number in an explicit dynamics analysis. The central-difference integration operator is explicit in the sense that the kinematic state is advanced using known values of $\dot{u}^N_{(i-1/2)}$ and $\ddot{u}^N_i$ from the previous increment. Here it is assumed that the acceleration is constant in between $i-1/2$ and $i+1/2$. This

method integrates constant accelerations exactly. For the method to produce accurate results, the time increments must be quite small so that the accelerations are nearly constant during an increment [31].

The key to the computational efficiency of the explicit procedure is the use of diagonal element mass matrices because the accelerations at the beginning of the increment are computed by [23]:

$$\ddot{u}_{(i)}^{N} = \left(M^{NJ}\right)^{-1}\left(P_{(i)}^{J} - I_{(i)}^{J}\right) \qquad \textbf{(4.89)}$$

where M^{NJ} is the mass matrix, P^{J} is the applied load vector, and I^{J} is the internal force vector. A lumped mass matrix is used because its inverse is simple to compute and because the vector multiplication of the mass inverse by the inertial force requires only n operations, where n is the number of degrees of freedom in the model. The explicit procedure requires no iterations and no tangent stiffness matrix. The internal force vector, I^{J}, is assembled from contributions from the individual elements such that a global stiffness matrix need not be formed [23].

4.10.2 Comparison of Implicit and Explicit Time Integration Procedures

For both the implicit and the explicit time integration procedures, equilibrium is defined in terms of the external applied forces and the internal element forces and the nodal accelerations [31]:

$$M\ddot{u} = P - I \qquad \textbf{(4.90)}$$

Both procedures solve for nodal accelerations and use the same element calculations to determine the internal element forces. The biggest difference between the two procedures lies in the manner in which the nodal accelerations are computed. In the implicit procedure a set of linear equations is solved by a direct solution method. The computational cost of solving this set of equations is high when compared to the relatively low cost of the nodal calculations with the explicit method.

Each iteration in an implicit analysis requires solving a large system of linear equations, a procedure that requires considerable computation, disk space, and memory. For large problems these equation solver requirements are dominant over the requirements of the element and material calculations, which are similar for an

explicit analysis. As the problem size increases, the equation solver requirements grow rapidly so that, in practice, the maximum size of an implicit analysis that can be solved on a given machine often is dictated by the amount of disk space and memory available on the machine rather than by the required computation time.

4.10.3 Advantages of the Explicit Time Integration Method

The explicit method is especially well-suited to solving high-speed dynamic events that require many small increments to obtain a high-resolution solution. If the duration of the event is short, the solution can be obtained efficiently [31].

The most striking feature of the explicit method is the absence of a global tangent stiffness matrix, which is required with implicit methods. Since the state of the model is advanced explicitly, iterations and tolerances are not required [31].

4.10.4 Stability

Explicit time integration is conditionally stable and the stability limit is given in terms of the highest frequency of the system [23]:

$$\Delta t \leq \frac{2}{\omega_{\max}} \tag{4.91}$$

where $\omega_{\max}$ is the highest frequency in the system. With damping, the stable time increment is given by [23]:

$$\Delta t \leq \frac{2}{\omega_{\max}}\left(\sqrt{1+\xi_{\max}^2}-\xi_{\max}\right) \tag{4.92}$$

where $\xi_{\max}$ is the fraction of critical damping in the mode with the highest frequency. Contrary to our usual engineering intuition, introducing damping to the solution reduces the stable time increment.

4.10.5 The Stable Time Increment Estimation

An approximation to the stability limit is often written as the time needed for a dilatational wave to pass across the smallest element dimension in the mesh [23]:

$$\Delta t \approx \frac{L_{\min}}{c} \tag{4.93}$$

where $L_{\min}$ is the smallest element size in the model and c is dilatational wave speed.

For an isotropic, linear elastic material, the dilatational wave speed in structure can be expressed as [23]:

$$c_s = \sqrt{\frac{\lambda + 2\mu}{\rho}} \tag{4.94}$$

where ρ is the density of the material and λ and μ are Lamé's constants which can be expressed in terms of Young's modulus, E, and Poisson's ratio, v:

$$\lambda = \frac{Ev}{(1+v)(1-2v)} \tag{4.95}$$

$$\mu = \frac{E}{2(1+v)} \tag{4.96}$$

In this work, the floating structure to be shock-loaded is made of St44, which has a Young's Modulus of 210000 MPa, and Poisson's ratio of 0.3, together with a density which is equal to $7.85 \cdot 10^{-9}$ tonne/mm^3. So, Lamé's constants are:

$$\lambda = \frac{210000 \cdot 0.3}{(1+0.3)(1-2 \cdot 0.3)} = 121153.8 MPa \tag{4.97}$$

$$\mu = \frac{210000}{2(1+0.3)} = 80769.2 MPa \tag{4.98}$$

So, the speed of dilatational wave in the structure is;

$$c_s = \sqrt{\frac{121153.8 + 2 \cdot 80769.2}{7.85 \cdot 10^{-9}}} = 6000979\, mm/s \approx 6000\, m/s \tag{4.99}$$

In Section 4.9 we had found that the dilatational wave speed in the fluid medium, c_f, is 1500 m/s. The smallest element size in the fluid domain is 50 mm while it's 40 mm for the structure. Using Equation (4.93) we can estimate the stable time increment according to both fluid and structural meshes:

$$\Delta t_s \approx \frac{0.04m}{6000\,m/s} = 6.67 \cdot 10^{-6}\,s \quad \textbf{(4.100)}$$

$$\Delta t_f \approx \frac{0.05m}{1500\,m/s} = 3.33 \cdot 10^{-5}\,s \quad \textbf{(4.101)}$$

The coupled problem will be solved with the smallest time increment calculated; so the structural mesh governs the maximum allowable time increment, thus the number of time increments per analysis. On the other hand, the fluid side governs the maximum allowable mesh size as discussed in Section 4.9, thus the overall size of the problem.

4.11 Structural Damping

In direct integration analysis, one can include material damping effect by use of Rayleigh damping model. This type of damping is also known as "proportional damping" since that damping is proportional to a linear combination of mass and stiffness matrices of the structure as follows [32]:

$$[C]_s = \alpha_R [M]_s + \beta_R [K]_s \quad \textbf{(4.102)}$$

where $[C]_s$, $[M]_s$ and $[K]_s$ are damping, mass and stiffness matrices of the structure respectively, and α_R, β_R are mass and stiffness proportional damping factors. In names of the natural frequencies of the structure, the following relation holds [32]:

$$\xi_i = \frac{\alpha_R}{2\omega_i} + \frac{\beta_R \omega_i}{2} \quad \textbf{(4.103)}$$

where ω_i is the *i* the natural frequency of the structure. This equation implies that, generally the mass proportional Rayleigh damping, α_R, damps the lower frequencies and the stiffness proportional Rayleigh damping, β_R, damps the higher frequencies [23].

To calculate the so-called damping factors, two sets of data is required. Let's say that a multidegree of freedom system has first mode at 30 Hz and second mode at 50 Hz;

we want to add 0.4 % critical damping fraction to the system at these modes. Putting these values into Equation (4.102) for each mode and solving the obtained two equations to obtain the damping factors would yield $\alpha_R = 1.5915 \cdot 10^{-5}$ and $\beta_R = 0.9425$. Using these values in Equation (4.103), the change of critical damping fraction along a specified frequency range can be plotted as seen in Figure 4.6:

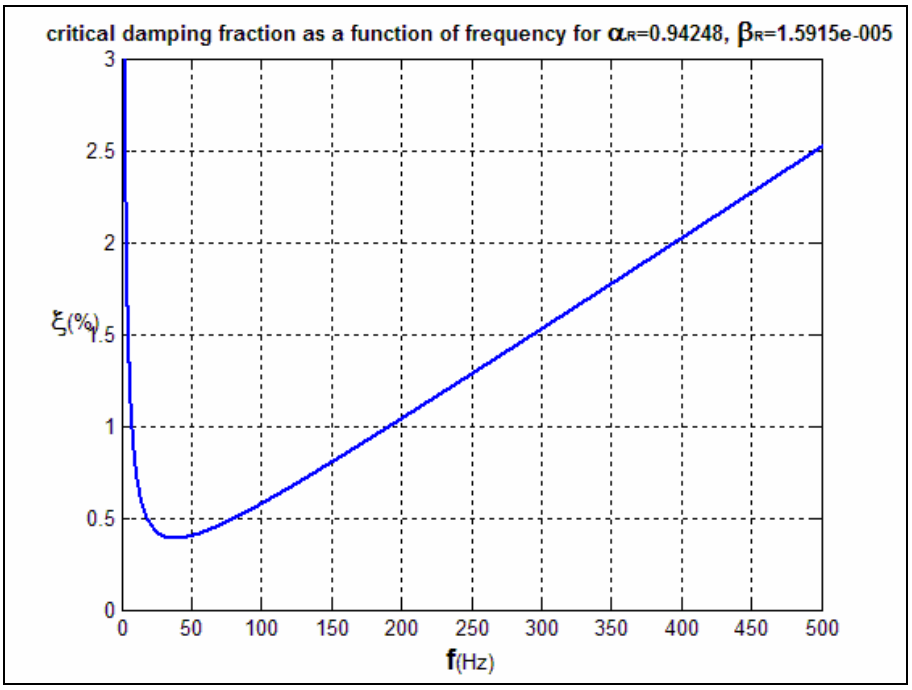

Figure 4.6 : Rayleigh Damping as a Function of Frequency.

4.11.1 Effect of Damping on the Stable Time Increment

For convenience, Equation (4.92) is repeated here:

$$\Delta t \le \frac{2}{\omega_{\max}} \left(\sqrt{1+\xi_{\max}^2} - \xi_{\max} \right) \qquad \textbf{(4.92)}$$

Substituting $\omega_{\max}$ in Equation (4.103) yields:

$$\xi_{\max} = \frac{\alpha_R}{2\omega_{\max}} + \frac{\beta_R \omega_{\max}}{2} \qquad \textbf{(4.104)}$$

These equations indicate a tendency for stiffness proportional damping to have a greater effect on the stable time increment than mass proportional damping. Generally, the effect of the mass proportional damping on stable time increment is negligible [23].

It is generally preferable to damp out low frequency response with mass proportional damping rather than stiffness proportional damping [23]. However, mass proportional damping can significantly affect rigid body motion, so large α_R is often undesirable. To avoid a dramatic drop in the stable time increment, the stiffness proportional damping factor, β_R, should be less than or of the same order of magnitude as the initial stable time increment without damping.

In next sections, the effect of damping on stable time increment will again be discussed with application to floating shock platform.

5. UNDEX METHODOLOGY

5.1 UNDEX Analysis Methodology

Basically, UNDEX analysis consists of 3D CAD modeling of the floating structure, meshing the structure and preparing the fluid domain mesh, obtaining the pressure shock wave profile from the similitude equations and then solving coupled acoustic-structural equations using an explicit finite element package to get the transient response of the floating shock test platform under shock loadings. Post processing follows the analysis. However, before doing an accurate analysis, the whole above process or any component of it may be needed to repeat several or many times. This is especially true if the capabilities of the explicit solver to be used are not known beforehand. Running a 0.04 second simulation of the optimized Finite Element Model requires about four days getting the results. Because the optimized model is still so big, the result files are huge so that post processing also takes days of time. So, preparing a relatively fine mesh and repeating the analysis to see the effect of any UNDEX parameter is inefficient.

The way we behaved in this work is completely different. Figure 5.1 shows the methodology followed in this study. First of all, the 3D CAD model of the shock test platform was constructed based on the 2D drawing using CATIA. Using ABAQUS CAE and the obtained 3D CAD model, a relatively fine mesh of the shock test platform was built up. It was meshed relatively fine because we are interested in stress waves in the structure as well as the velocity and accelerations experienced by the structure. This relatively fine mesh was inefficient for the fluid mesh convergence studies and for the analyses which we run to explore the capabilities of the explicit solver used. This fine mesh of the structure was then coarsened based on the fine mesh using HYPERMESH. We used HYPERMESH because it has many flexible commands to coarsen or refine a finite element model. Then using ABAQUS/ STANDARD, the eigen frequencies and mode shapes of the fine and coarsened structural meshes were obtained and they were compared to make a judgment of whether or not the reduced model was representative of the fine model.

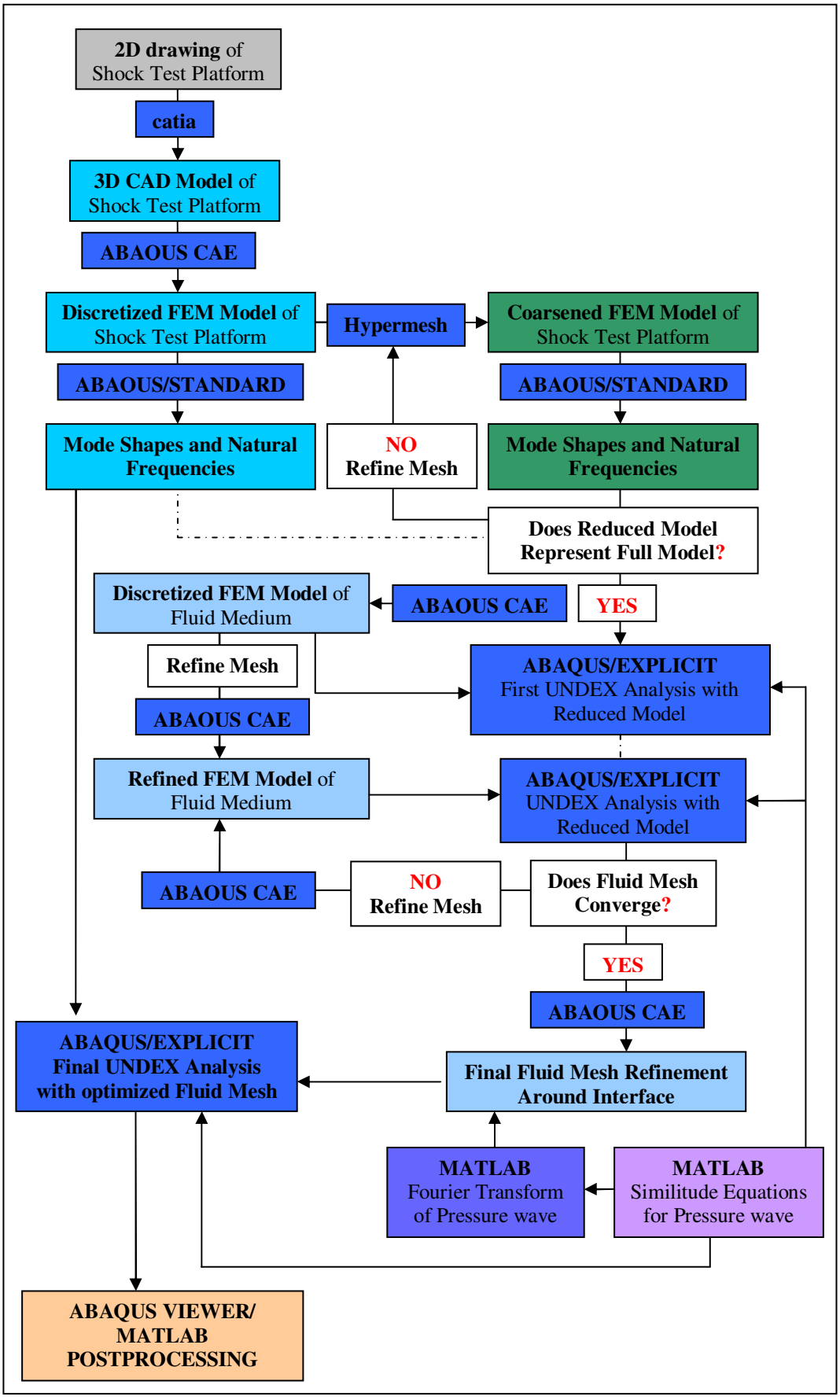

Figure 5.1 : UNDEX Analysis Methodology.

Once the reduced mesh was found to be adequate having compared its natural frequencies and modes with base model, it was ready for use in fluid mesh convergence analysis and any other parametric studies. It was also a cheap tool to be used in the analyses which were run to explore the capabilities of the FE package to be used.

A relatively coarse mesh of the fluid medium was than constructed using ABAQUS CAE. Together with the reduced mesh of the platform, the first coupled UNDEX analysis was run using double precision ABAQUS/EXPLICIT FE package. Incident pressure shock wave profiles were obtained from similitude equations using MATLAB. Then the analyses were repeated by a finer mesh of the fluid medium until the velocity, acceleration and pressure profiles converged. With this optimized fluid mesh, the effect of structural damping and cavitation was also investigated.

A final mesh refinement of the fluid medium around the acoustic-structural interface was carried by the knowledge of the frequency content of the incident shock wave profiles around this region. This knowledge of the frequency content of the incident shock waves was obtained by means of Discrete Fourier Transform using MATLAB.

The final analyses were run by use of this optimized fluid mesh and the relatively fine mesh of the platform. The velocity, acceleration and displacement response of the platform as well as the fluid pressure profiles in the vicinity of the acoustic-structural interface were revealed.

5.1.1 Submodeling Analysis

To obtain converged stress-strain results on the structure, some so-called submodeling analyses were run based on the results of the final coupled acoustic-structural analyses. To understand the submodeling technique, see the simple illustration in Figure 5.2.

The displacement field at the so-called driving nodes is obtained from the global coupled acoustic structural analysis. The submodel region, which includes the point of interest where converged stress-strain results are desired, is refined. Then the displacements at the driving nodes are used to drive the so-called driven nodes on the submodel region during a subsequent submodel analysis.

If the coordinates of the driving nodes on the submodel region in the global analysis are identical to the coordinates of the driven nodes in the subsequent submodel analysis, the driving and driven displacements will also be identical:

$$\mathbf{U}_i = \mathbf{U}_{i'} \qquad \textbf{(5.1)}$$

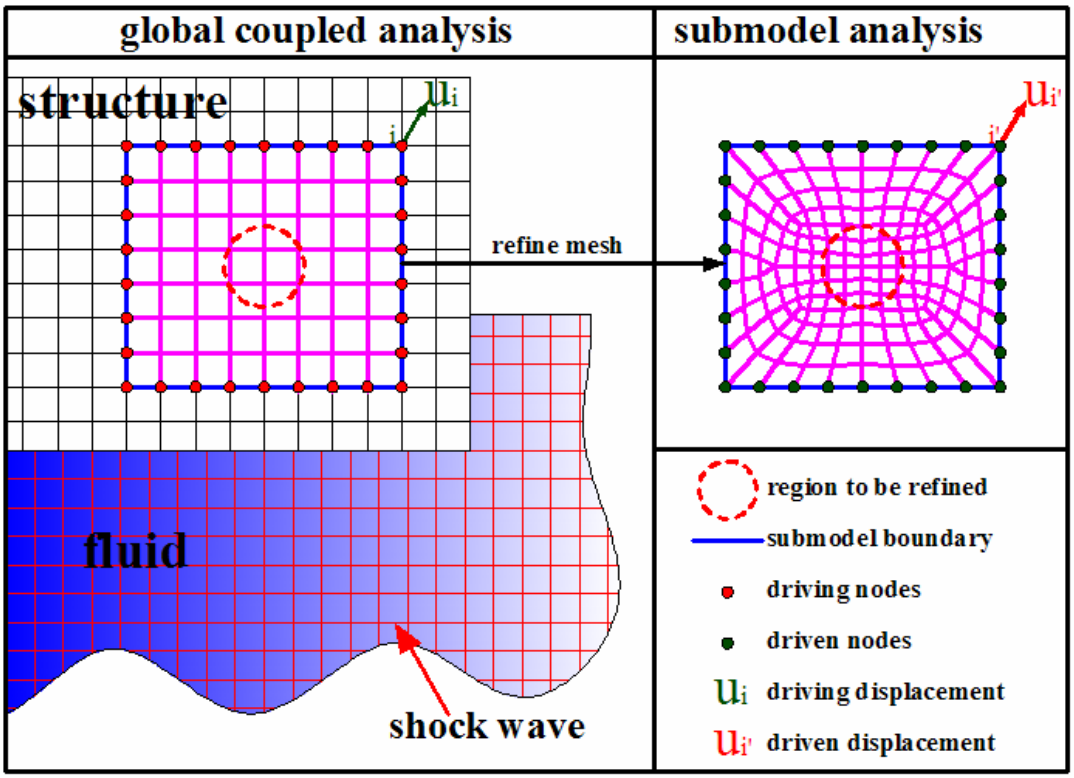

Figure 5.2 : Submodeling Procedure.

This procedure can be used to obtain converged stress-strain results. The point of interest should be relatively far from the submodeling region. Also, the displacements of driving nodes in the global analysis should be written to the global analysis result file in double precision format so that the submodel region will be driven with sufficient accuracy in subsequent submodeling analysis.

5.2 UNDEX Correlation Methodology

The correlation of UNDEX responses, obtained from the finite element analyses, with UNDEX test results is a must to validate the UNDEX methodology before it can be used for any design purposes. The UNDEX analyses require many parameters such as seabed reflection coefficient, Rayleigh damping parameters, etc. These

parameters should be modified according to test results because it is not always possible to prescribe these parameters without experimental knowledge. The finite element model might also need to be modified. Moreover, the validation of numerical code with test results is a must to prove its reliability. Figure 5.3 presents the UNDEX correlation methodology for this work based on a previously published study on subject [33].

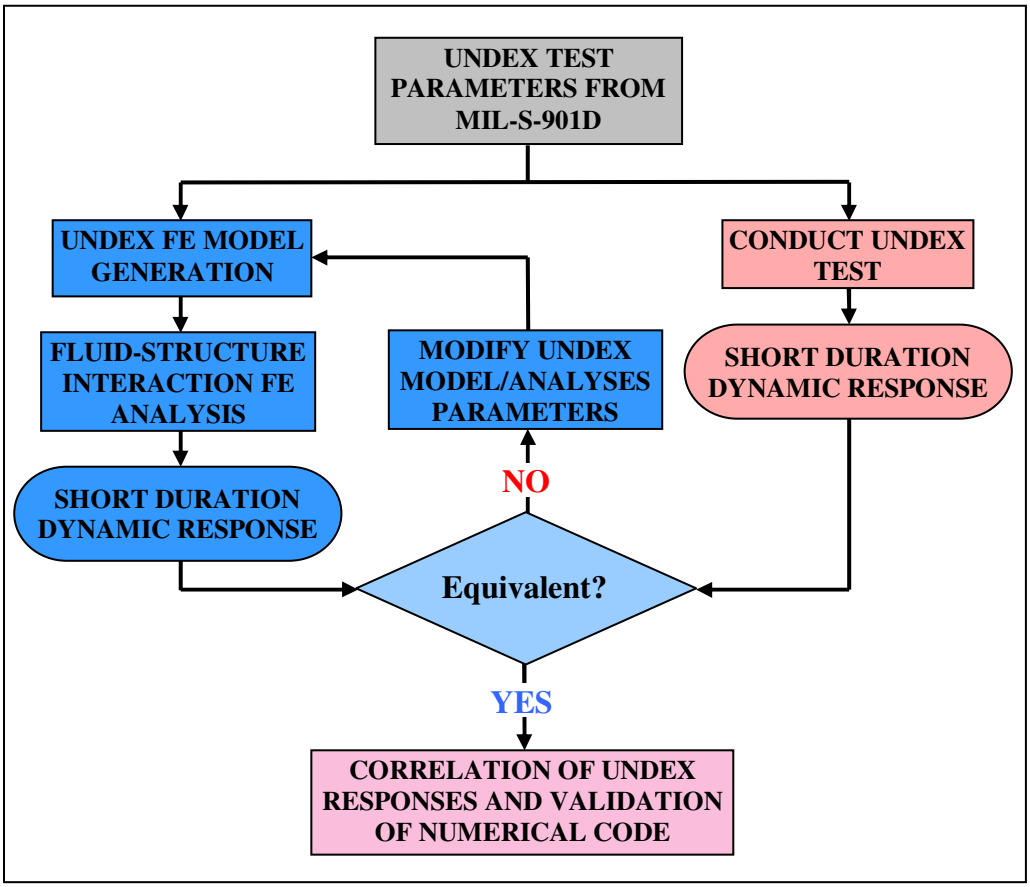

Figure 5.3 : UNDEX Correlation.

5.3 UNDEX Test Parameters From MIL-S-901D

MIL-S-901D is the military specification which covers shock testing requirements for ship board machinery, equipment, system and structures [1]. The shock test platform to be simulated in this work is for heavyweight shock testing of test items whose weight and center of gravity limitations are described in the specification. The dimensional specifications for this so-called standard floating shock test platform are shown in Figure 5.4.

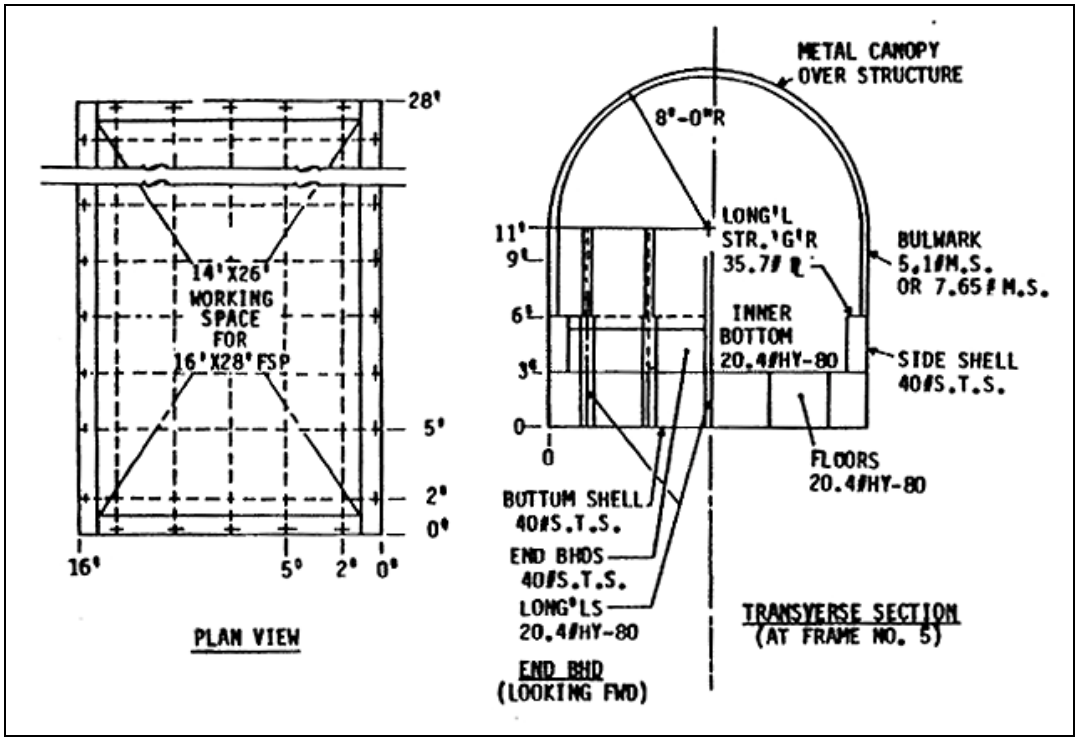

Figure 5.4 : Standard Shock Test Platform as Specified in MIL-S-901D [1].

The specification also describes the weight and type of the charge to be used in tests, as well as its location with respect to sea level and shock test platform. The weight and type of the charge to be used is 27.2 kg HBX-1 and the explosion is to be repeated four times with the same weight of the HBX-1 charge, at varying locations. The location of charge for each shot is shown in Figure 5.5.

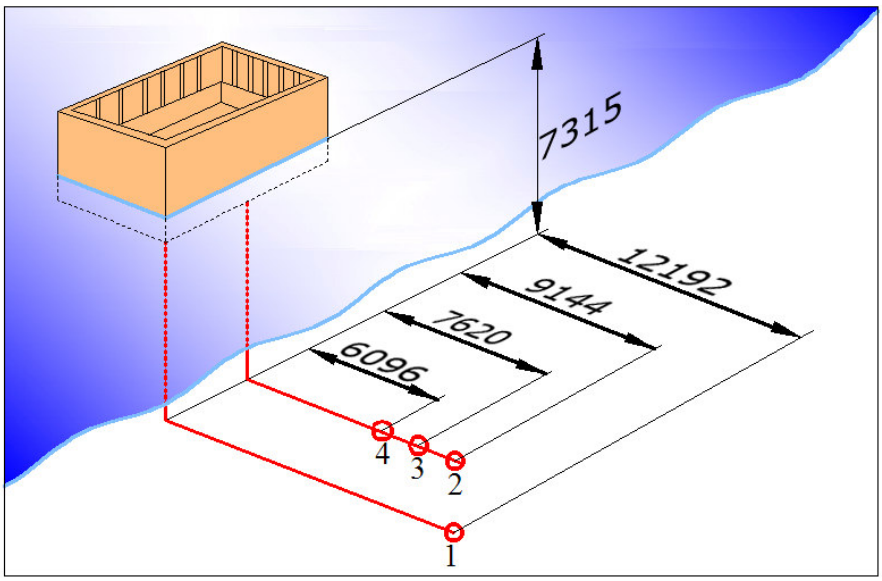

Figure 5.5 : Charge Locations as Specified in MIL-S-901D (Dimensions in mm).

6. MODELLING AND ANALYSIS

6.1 3D CAD Modeling and Generation of Finite Element Models

The shock test platform to be used in the analysis is readily available in Tuzla Military Shipyard. Figure 6.1 shows the general view and details of the shock test platform.

Figure 6.1 : The Shock Test Platform.

The general dimensions of the shock test platform are shown in Figure 6.2.

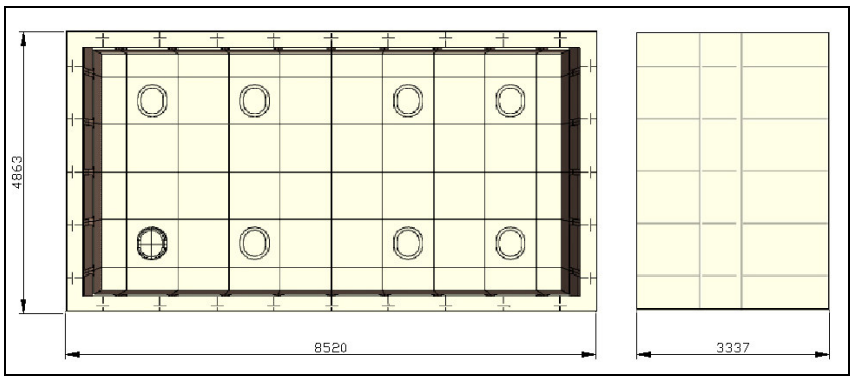

Figure 6.2 : The Outer Dimensions of the Platform.

The 3D geometry of the shock test platform was constructed using Catia. All geometric details were included. Figure 6.3 shows the constructed CAD geometry and some details on it.

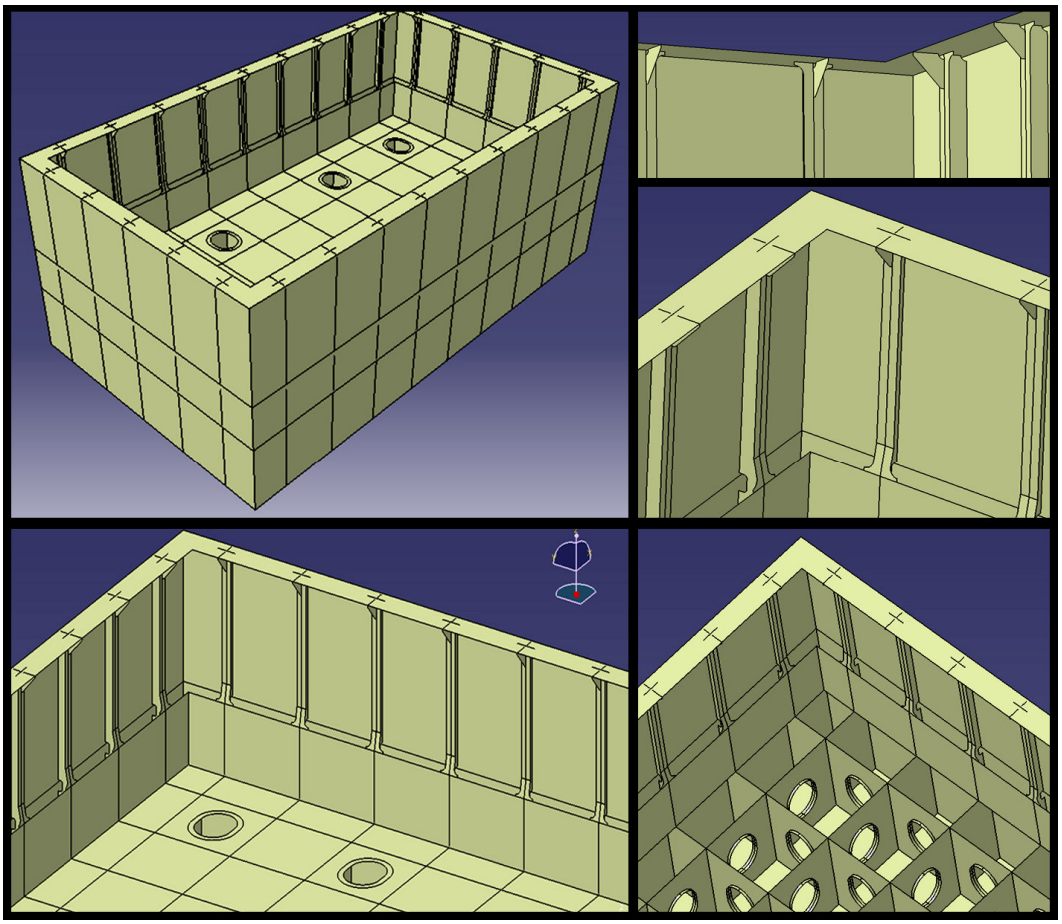

Figure 6.3 : 3D CAD Model of the Platform.

The finite element model of the shock test platform was generated using ABAQUS CAE. Reduced integration linear quadrilateral shell elements were used for discretization. The total number of nodes used in the finite element model is 140316. The number of elements is 142327.

Figure 6.4 shows a general view of the finite element model and some details on it. The connections between the covers and the platform were provided by use of kinematic couplings which are equivalent to rigid links.

A relatively reduced finite element model of the shock test platform was also constructed based on the main finite element model shown in Figure 6.4. Though it is coarse, it is a good representative model of the shock test platform. To judge whether

or not the coarse model is representative of the main model, some modal analysis were run as presented in next section and the main modes of vibration and corresponding natural frequencies were compared.

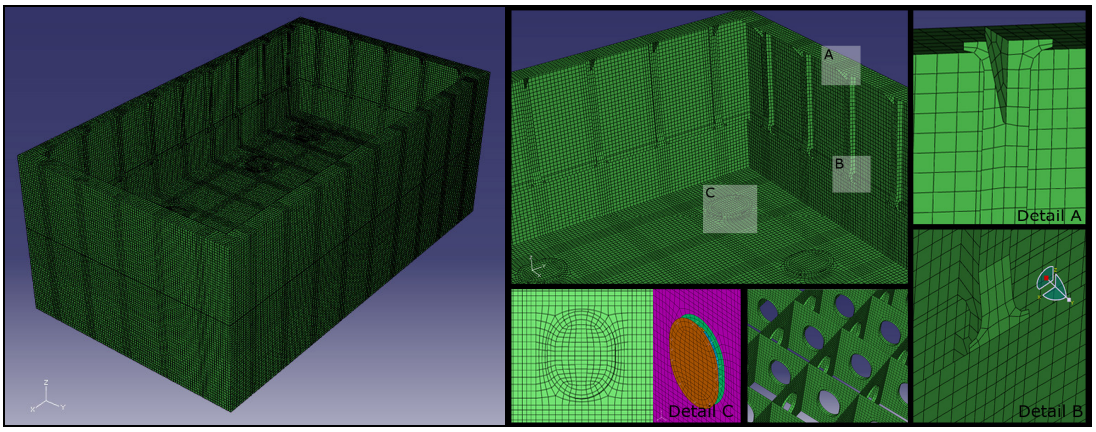

Figure 6.4 : Finite Element Model of the Platform.

Figure 6.5 shows the reduced finite element model and some details on it. The number of nodes used in the model is 7858. The numbers of reduced integration linear quadrilateral and triangular elements used are 8229 and 538 respectively.

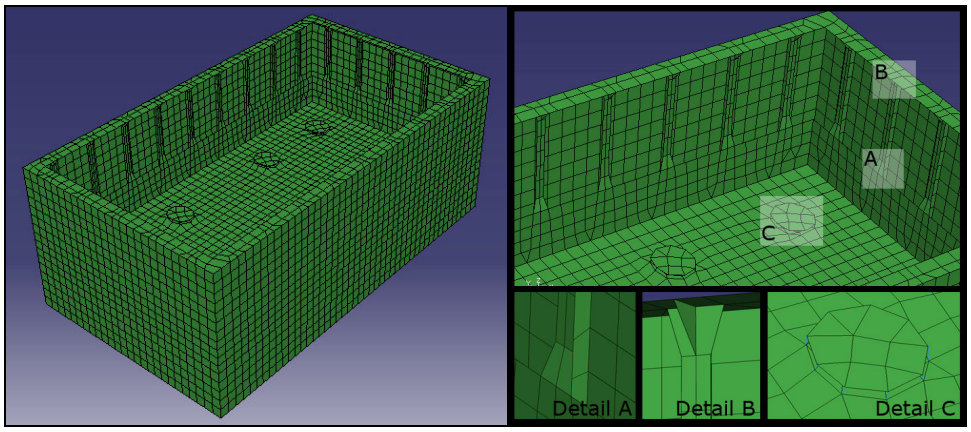

Figure 6.5 : Reduced Finite Element Model of the Platform.

Following material properties were used for steel (St44) structure: The modulus of elasticity was taken to be 210000 N/mm^2. The density of the steel was taken to be 7850 kg/m^3 and the Poisson's ratio was set to 0.3 [34].

6.2 Modal Analysis

To ensure that the prepared finite element model of a structure works accurately, it is a must to run a modal analysis and to evaluate its modes and natural frequencies.

Here, the modal analysis were run for both the finely meshed model which is to be used in final explosion analysis and coarsely meshed model which is to be used in tryout analysis and fluid mesh convergence studies.

Figure 6.6 shows a comparison of the first two and other important modes of two FE models. It can be seen that the mode shapes and natural frequencies of the coarse model is in good coherence with the modes and natural frequencies of the fine model. The negligible shift in natural frequencies is due to the increased stiffness of the platform resulting from the coarsened discretization.

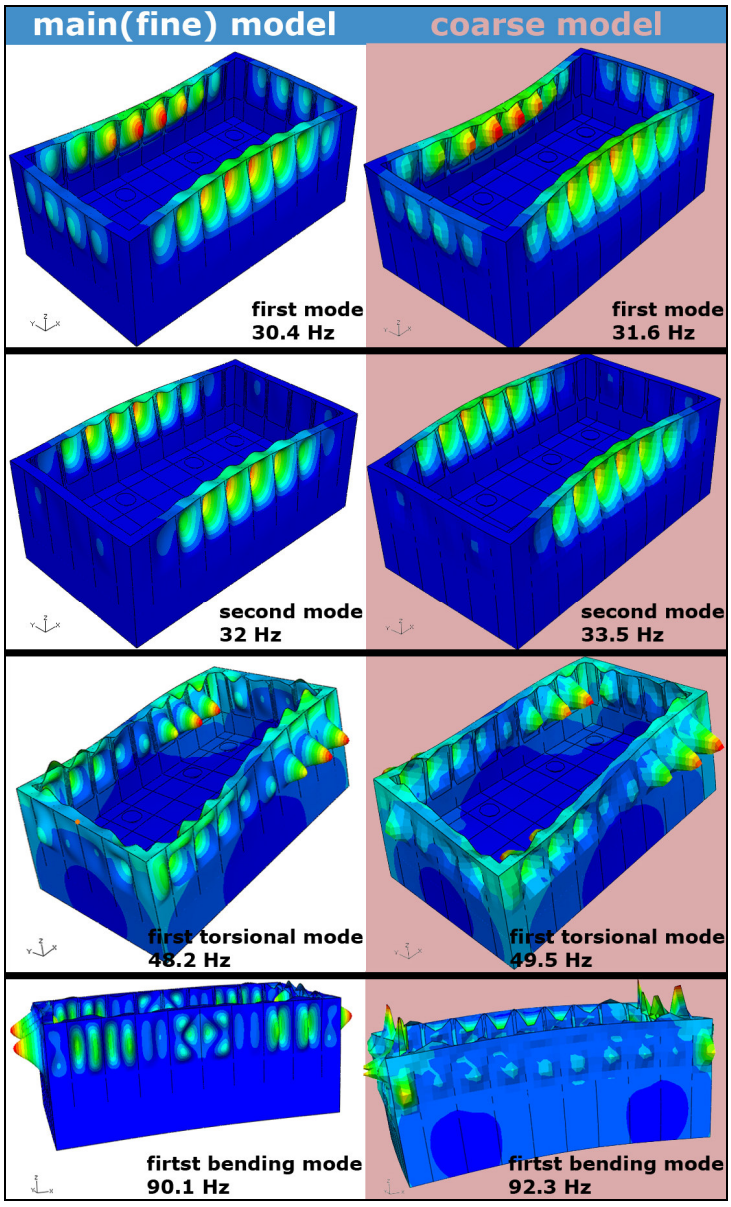

Figure 6.6 : Fundamental Modes of Coarse and Fine FE Models.

6.3 UNDEX Analysis with Reduced FE Model

The reduced (coarse) FE model can be used to roughly estimate the response of the shock test platform to an underwater explosion. The reduced model is an easy-to-use tool for analysis because the modeling and analysis time decreases significantly so that the first tryout analysis can be run quickly. It can also be used to make fluid mesh size convergence analysis as discussed in the next chapters.

For UNDEX analysis, the fluid domain was modeled. The fluid domain was truncated at 8.5 m distance from the shock test platform as seen in Figure 6.6. The depth of the fluid domain is limited by the charge depth since including the charge location in the fluid mesh might result in inaccurate results [23]. So the fluid domain was truncated at 7.2 m depth. The main dimensions of the fluid domain according to the shock test platform are shown in Figure 6.7. The elements used in the fluid domain are reduced integration linear hexahedral acoustic elements

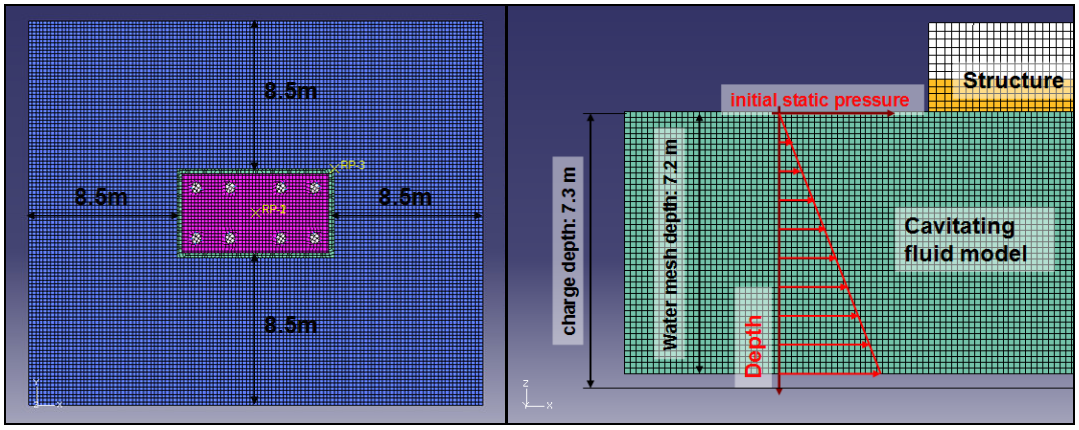

Figure 6.7 : Dimensions of the Fluid Medium and Distribution of Initial Acoustic Static Pressure.

The fluid is capable of going cavitation. At the free surface, the pressure is zero relative to the atmospheric pressure. The cavitation limit of the sea water is about 1.3 kPa absolute at 10 C^0, which is -0.100025 Mpa relative to the atmospheric pressure [35]. Since the cavitation is included in the analysis, the hydrostatic pressure present due to the water is also important and it was applied as an initial static pressure on the whole fluid domain as shown in Figure 6.7.

Zero pressure boundary condition was applied to the free surface as shown in Figure 6.8. The figure also shows the planar nonreflecting boundary condition applied to the exterior fluid surfaces except the free surface. The acoustic-structural interaction

between the wet surfaces of the platform and the acoustic interaction surfaces was implemented by use of a surface-based "tie" constraint as shown in the same figure.

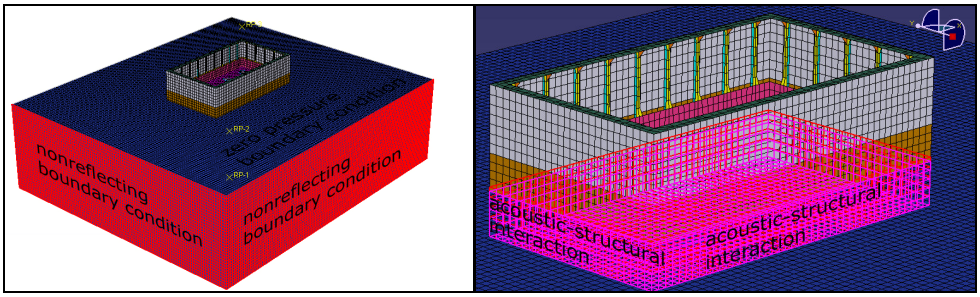

Figure 6.8 : Acoustic Boundary Conditions and the Acoustic-Structural Interaction.

In the UNDEX analysis with the coarse FE model of the platform, the explosive was assumed to be located through the centerline of the platform. The depth from the free surface and the weight of the explosive were taken to be 7315.2 mm and 27.22 kg as described in the related military specification [1]. The stand-off point was taken at 4000 mm away from the source point as shown in Figure 6.9. The pressure profile at the stand-off point due to the explosion was obtained by use of the similitude equations as shown in the same figure. Note that the source point is located outside of the fluid domain.

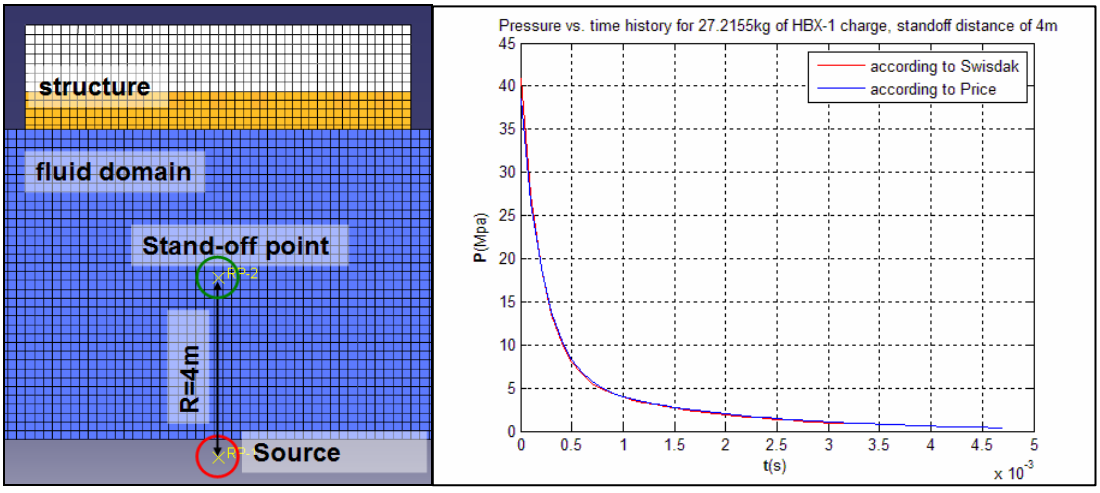

Figure 6.9 : Source (Explosive) and Stand-off Point, and the Pressure Profile at the Stand-off.

The material properties needed for the acoustic fluid domain are its bulk modulus and density. Here, commonly accepted values for the sea water were used [28]: The bulk modulus was taken to be 2306.35 Mpa and the density of the sea-water was taken to be 1025 kg/m^3.

6.3.1 Fluid Mesh Size Convergence Study

As discussed in previous sections, the mesh size used in the fluid domain is critical for the accuracy of the analysis. Here, some fluid mesh size convergence analyses were carried. The platform was assumed to be rigid so that the maximum displacement, velocity and acceleration results in the vertical direction corresponding to each mesh size can be compared easily. The analysis were repeated for four mesh sizes of the fluid domain; 500 mm, 250 mm, 200 mm and 150 mm. Figure 6.10 shows the FE models for various mesh sizes of fluid domain.

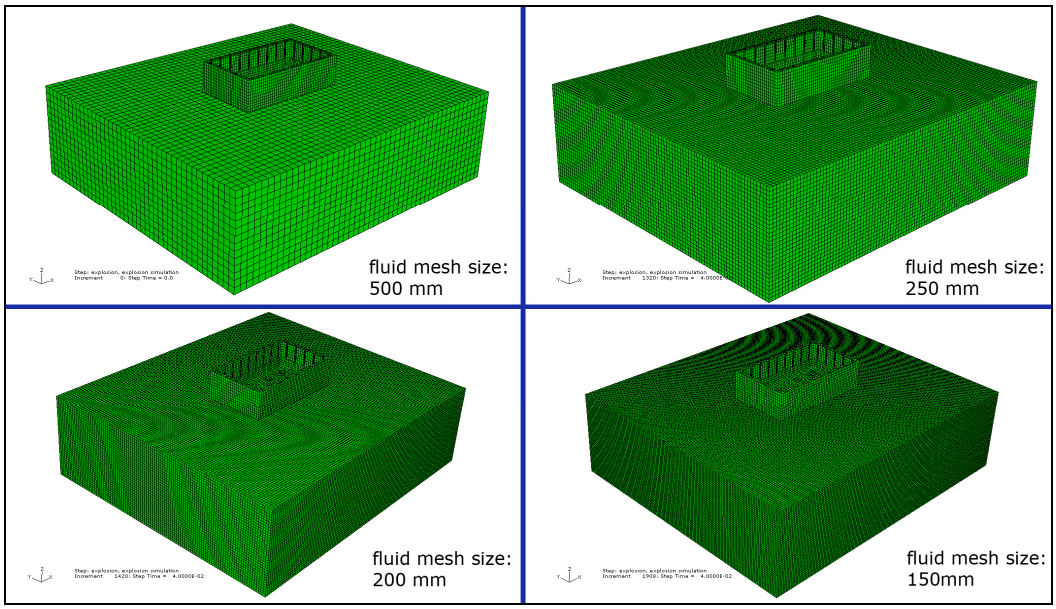

Figure 6.10 : FE Models for Various Mesh Sizes of the Fluid Domain.

The vertical displacement, velocity and acceleration profiles of the center of mass of the rigid platform as well as the absolute acoustic pressure under the keel, through the centerline of the platform are presented in Figure 6.11 for various mesh sizes. The analysis was converged for a fluid mesh size of 150 mm. The shock wave due to the explosion results in a steep increase in the velocity, acceleration and pressure profiles.

Figure 6.11 shows how the peak values of the output variables converge. Comparing the results of the analyses with 150 mm and 200 mm mesh sizes, the difference in the peak values of the output variables is less than 0.8 %. Thus the analysis was said to be converged for a fluid mesh size of 150 mm.

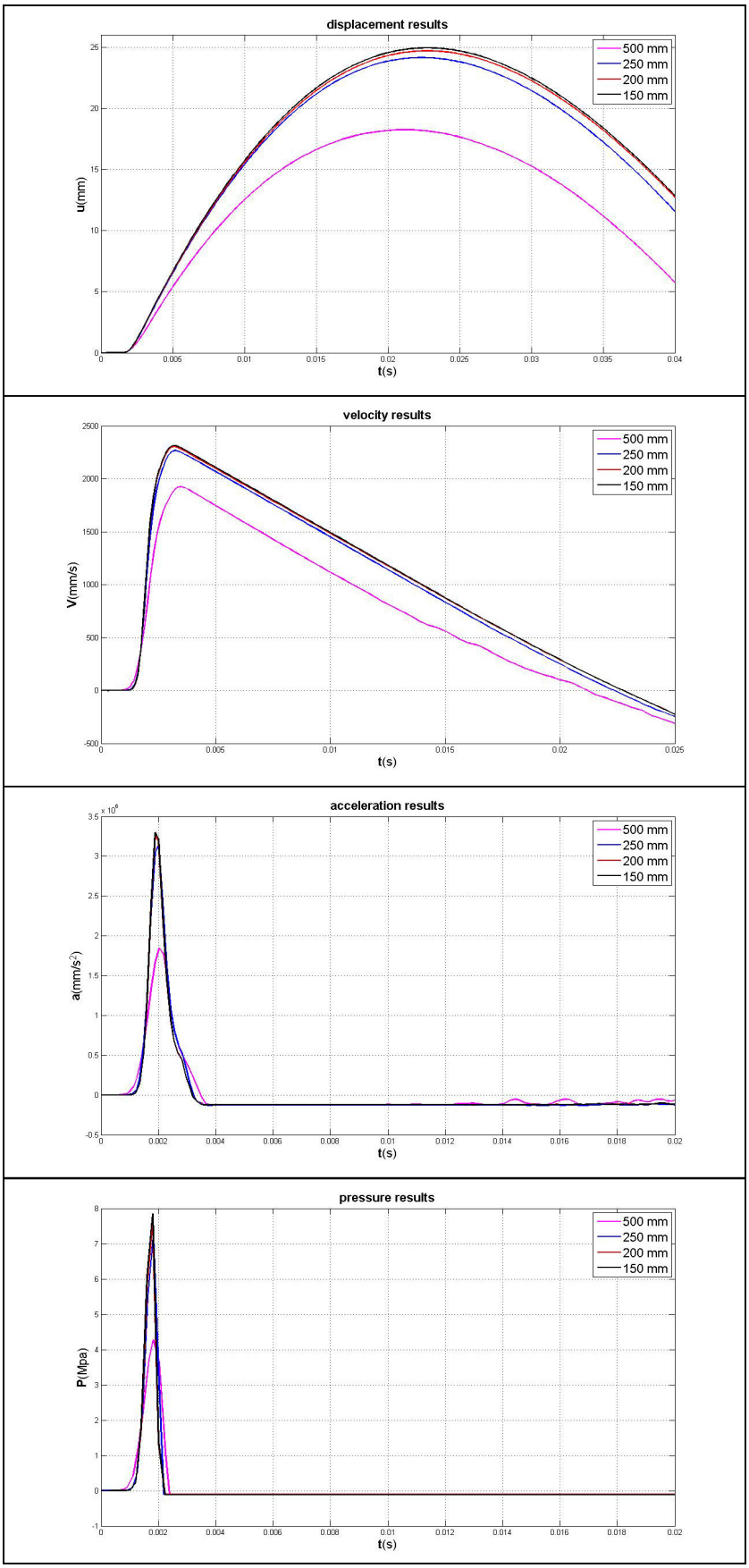

Figure 6.11 : Output Profiles for Various Mesh Sizes of Fluid Domain.

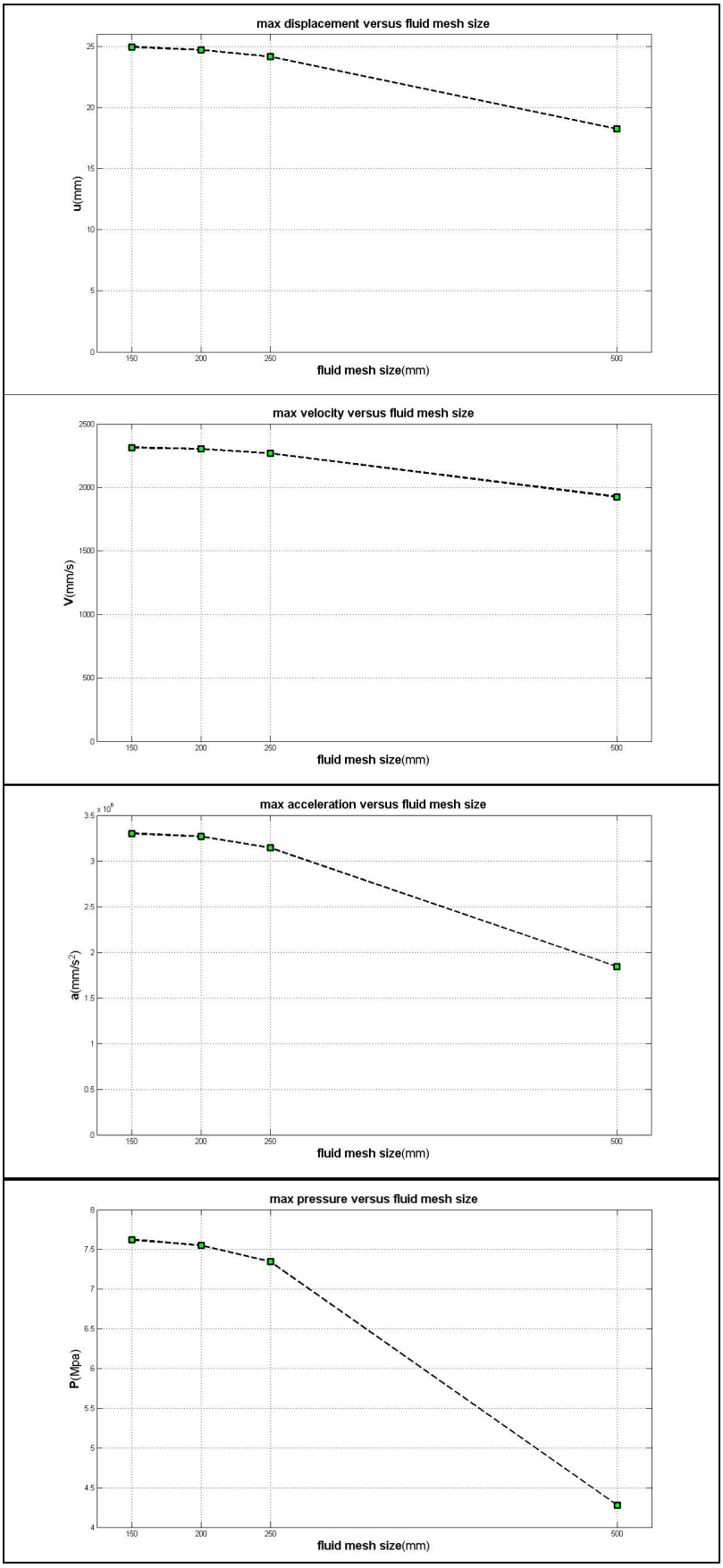

Figure 6.12 : Convergence of the Peak Values of the Response.

Though the results with a fluid mesh size of 150 mm seems to be satisfactory, a final mesh refinement around the acoustic structural interaction will be applied to the fluid domain before the final analysis in the next chapters. The fluid model with 150 mm mesh size has 1059260 nodes through 1021956 elements. After the final mesh refinement, the number of elements will be increased to 4229600.

Figure 6.13 shows the spherical propagation of the pressure shock wave through the fluid medium and the vertical motion of the rigid platform.

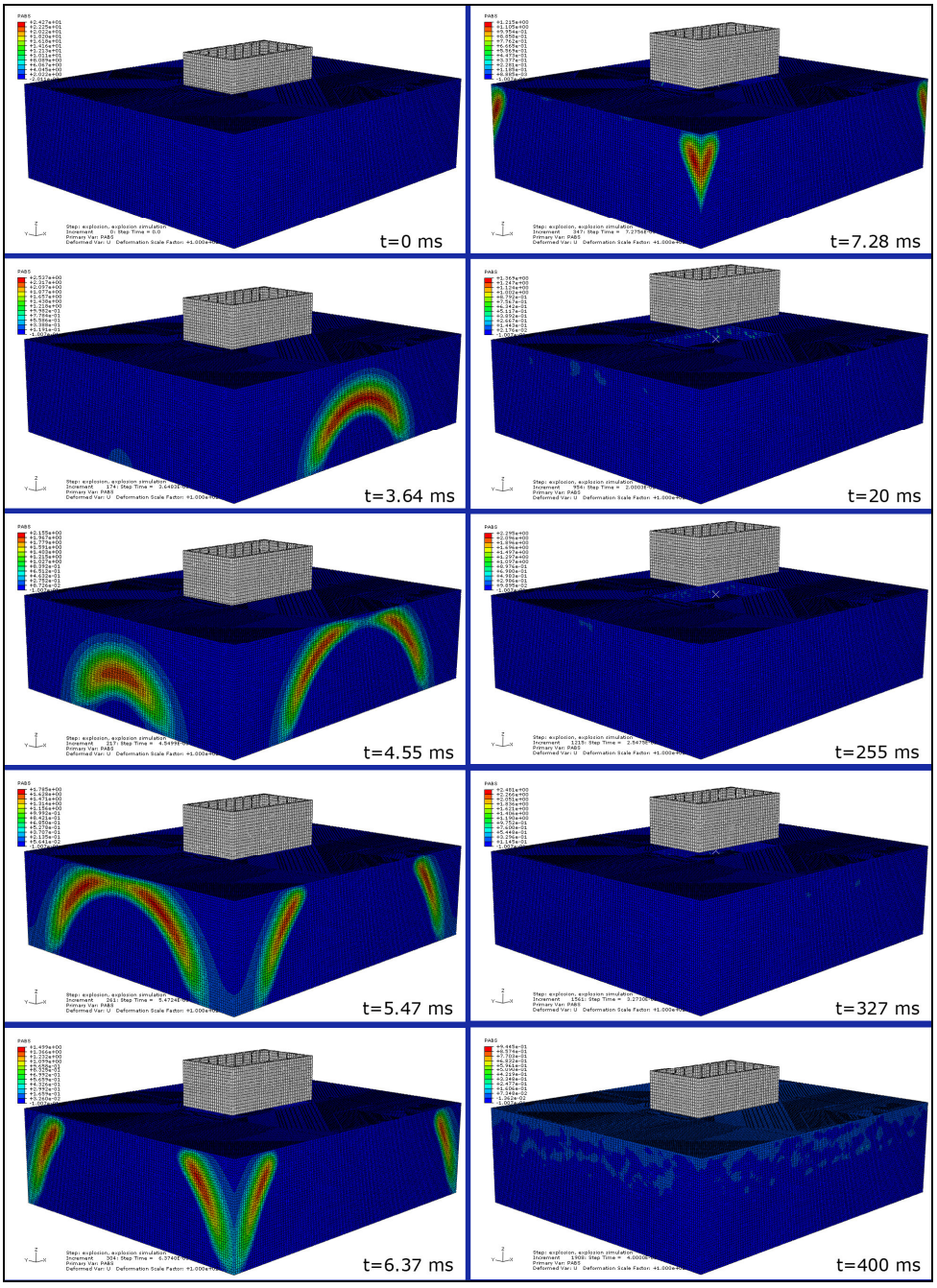

Figure 6.13 : Propagation of the Shock Wave and the Motion of the Platform.

6.3.2 UNDEX Analyses with Deformable Platform and Effect of Damping

Using the converged fluid model with 150 mm mesh size, the same analysis of the previous section was repeated, this time with deformable platform. The analysis was also repeated with Rayleigh damping added to the platform and the results were compared. The Rayleigh damping coefficients α_R and β_R were set to 1.5 and $0.5*10^{-6}$ respectively. These damping coefficients provide about 0.4 % critical damping fraction, ξ, for the first two modes. For the first torsional and bending modes, the critical damping fractions are 0.25 % and 0.15 % respectively. Since the excitation forces acting on the platform have considerable frequency content up to 3500 Hz, the modes of the platform up to very high frequencies will be excited. Thus care should be taken when selecting the Rayleigh damping coefficients so that the critical damping fraction is not undesirably high at high frequencies. Figure 6.14 shows the critical damping fraction as a function of frequency with the selected Rayleigh damping coefficients. It is seen that the critical damping fraction is below 0.6 % up to 3500 Hz.

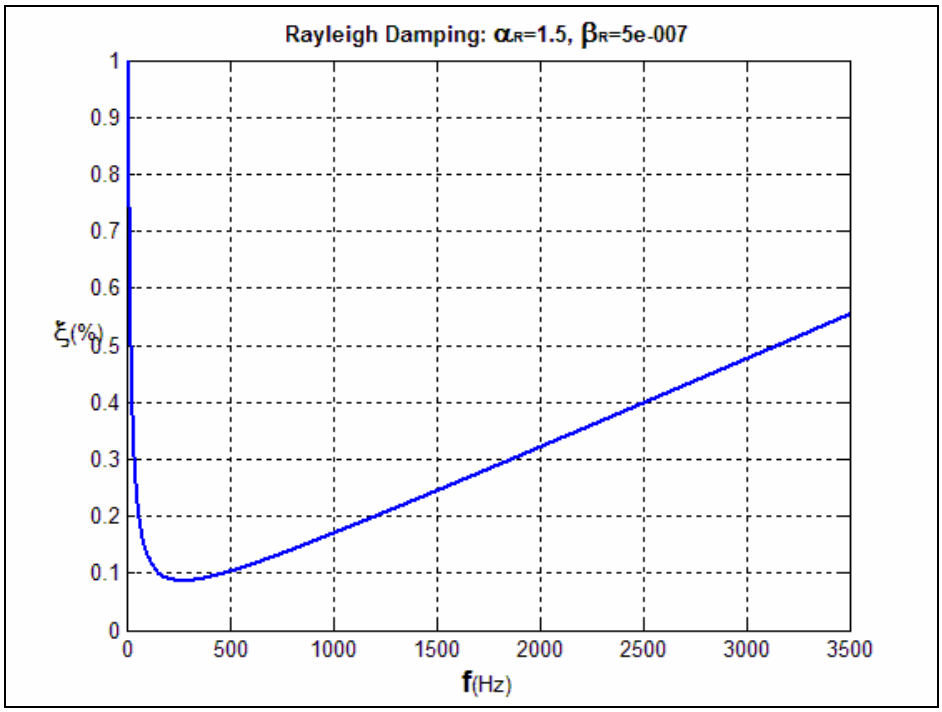

Figure 6.14 : Critical Damping Fraction as a Function of Frequency.

The effect of damping on stable time increment is considerable. Without damping, the stable time increment is $6.93*10^{-6}$. With the above values of the Rayleigh coefficients, $\beta_R=0.5*10^{-6}$, the stable time increment is reduced to $6.46*10^{-6}$. So the

effect of damping in this case is negligible. Increasing β_R to $1.5*10^{-5}$, the stable time increment reduces to $1.54*10^{-6}$, which means that the time needed to complete the analysis will be 4.5 times the time needed for the undamped case. Thus selecting the Rayleigh damping coefficient β_R is also critical for the cost of the analysis. The effect of α_R on the stable time increment is negligible since it damps out low frequencies and the stable time increment is calculated based on the maximum frequency in the system.

Figure 6.15 shows the propagation of the shock wave and the deformation of the platform for the undamped case. Addition of the damping does not considerably change the general view of the event, so it is not shown here. As seen in the figure, the keel of the platform experiences a bending-like deformation.

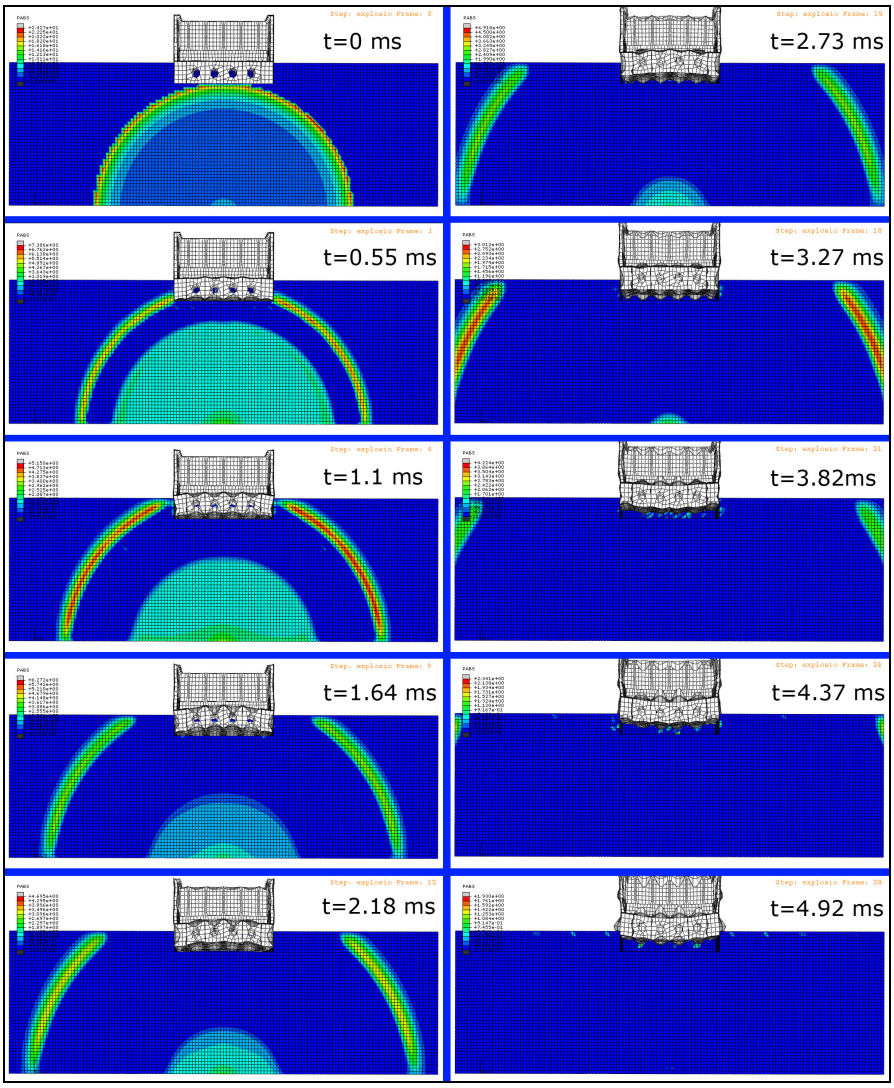

Figure 6.15 : Pressure Wave Propagation and Deformation of the Platform: Def. Scale Factor: 100.

Figure 6.16 shows the deformation of the platform for the undamped case. It is clear that the platform vibrates in its first bending mode. Local modes through the whole platform are also excited. Deformation is very similar for the damped case.

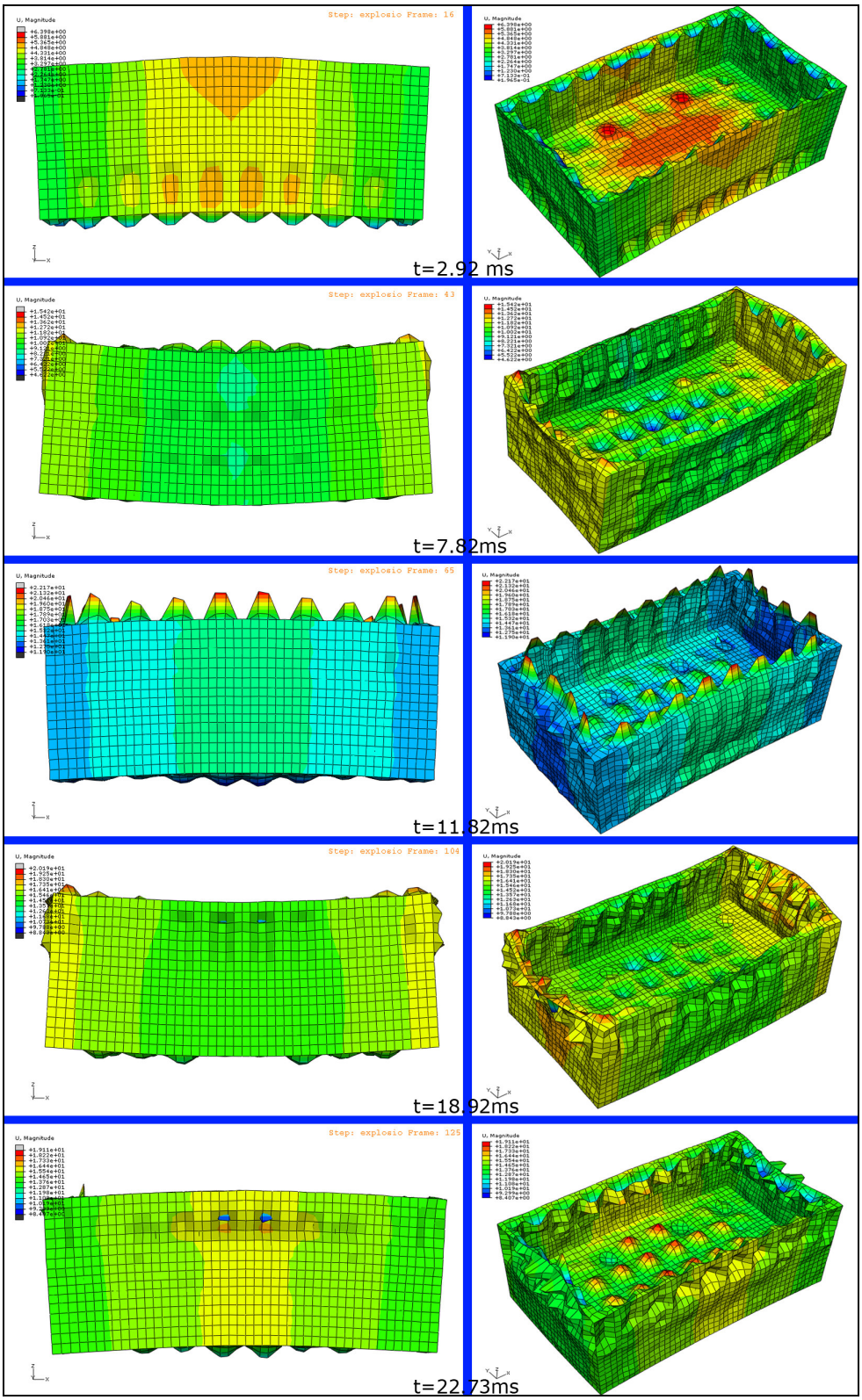

Figure 6.16 : Deformation of the Platform: Def. Scale Factor: 100.

The velocity and acceleration results for some selected nodes on the platform are presented in APPENDIX D. The selected nodes are shown in Figure 6.17.

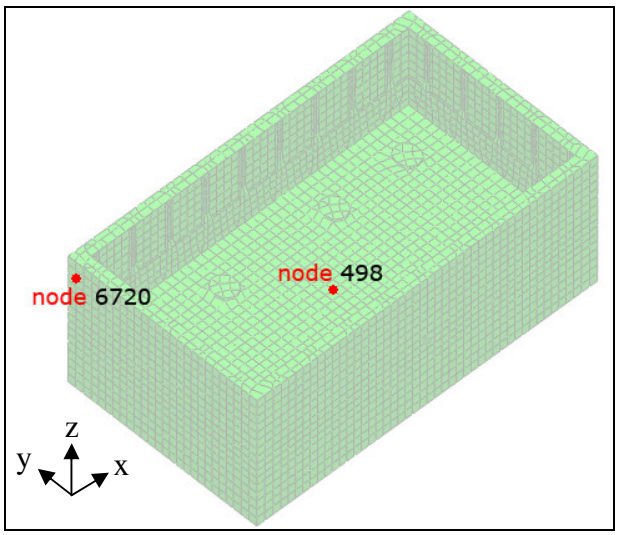

Figure 6.17 : The Nodes for Which Results are Presented.

Node 498 is on the keel of the platform which is the stiffest region on the structure. So, it represents the rigid body motion of the platform. The maximum vertical velocity node 498 experienced is about 6 m/s as shown in Figure D.1. The damping does not have considerable effect on the very early response of the structure. However as the time passes, the effect of the damping is more distinct since the system has no any other damping mechanism. The acceleration profile at this node is shown in Figure D.2. The effect of the damping in acceleration is more relevant and it effects the peak acceleration considerably. As the shock wave passes from the node, it experiences very high acceleration magnitudes and then reduces considerably.

Figure D.3 and D.4 shows the x direction velocity and acceleration profiles at this node. Since the explosion is through the centerline of the platform, the orders of velocity and acceleration magnitudes in horizontal directions are so much less than vertical direction magnitudes. The effect of damping is even more relevant in the response of the node in x direction than vertical response.

The vertical velocity and acceleration plots at node 6720 are shown in Figure D.5 and Figure D.6. The acceleration plot shows how damping is important in the late time response of the node. The peak values of acceleration decreases significantly with the effect of damping. Figure D.7 and Figure D.8 give the x direction velocity

and acceleration responses at the same node. The effect of damping is again significant in the late time response of the platform.

Figure D.9 is the pressure profile at node 101795 of the fluid medium under keel through the centerline of the platform. Since damping slows the motion of the platform, the platform responses to the shock wave slower and the peak value of pressure increases significantly compared with undamped case. In both cases, the pressure under the keel decreases to the cavitation limit very quickly, which is an indicator of local cavitation in acoustic-structural interaction.

6.4 Final UNDEX Analysis with the Main (Refined) FE Model of the Platform

The analyses with the reduced FE model of the platform provided us with the knowledge of the abilities of the explicit solver that was used and it was used to find a converged mesh size of the fluid medium. The coarse model was very useful since that the stable time increment used in the analyses would have been so small to make tryout and fluid mesh size convergence analyses if a relatively finer mesh had been used. It also reduced the time needed to run and post process analyses due to the fact that the number of degrees of freedom had also been reduced.

In this section, all analyses will be carried with the UNDEX parameters as specified in MIL-S 901D; the depth from the free surface and the weight of the explosive are 7315.2 mm and 27.22 kg. The location of the charge according to the platform is for the severest one of the loading conditions specified in MIL-S 901D. It is the shot 4 which is nearest to the platform. The geometry of the shot is shown in Figure 5.5 of the previous section.

Figure 6.18 shows the nodes and elements for which analyses results will be presented.

6.4.1 The Effect of Mesh Refinement Around the Acoustic-Structural Interaction Region

Now, the finely meshed main FE model of the platform can be used with the converged fluid FE model. However, a final mesh refinement of the fluid medium around the acoustic-structural interaction region was carried according to the DFT analysis of Section 4.9. The fluid mesh size around the interaction surfaces was set to

50 mm and it reaches to the value (150 mm) obtained by the convergence analysis of the previous section at the outer surfaces of the fluid domain. Figure 6.19 shows the final mesh refinement around the interaction region.

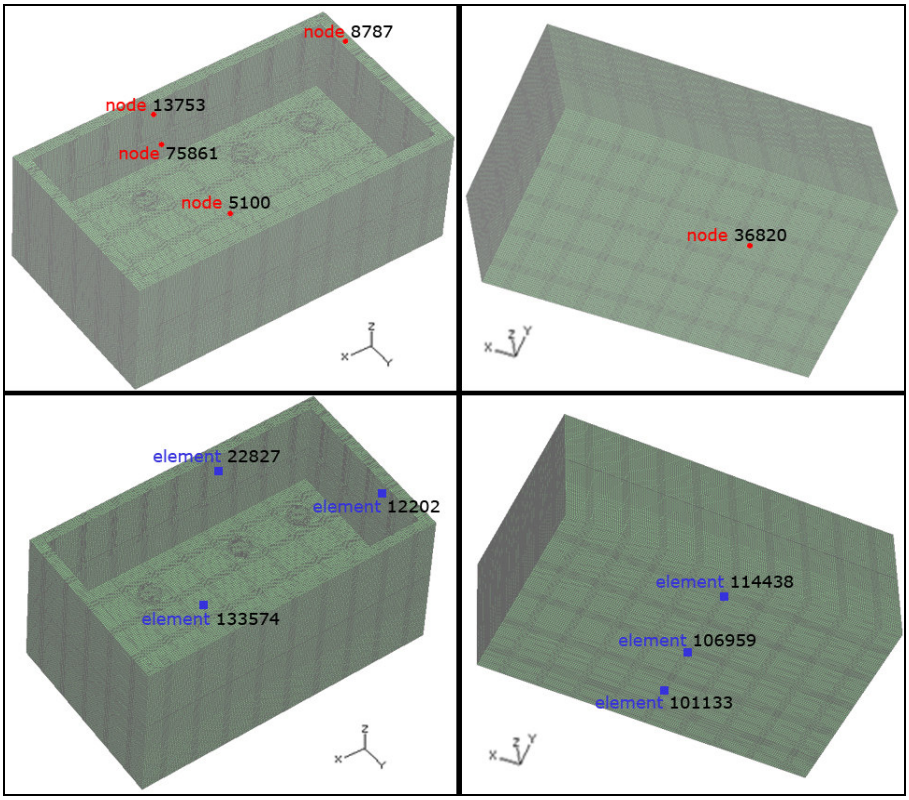

Figure 6.18 : Locations of the Nodes and Elements for Which Results are Presented.

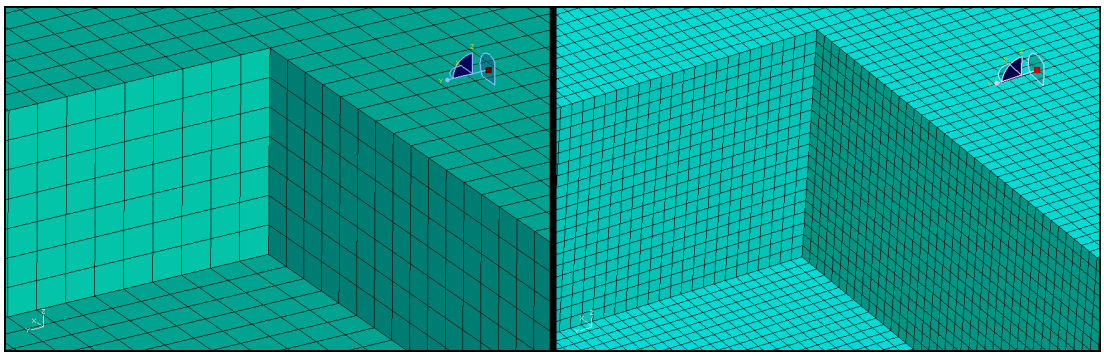

Figure 6.19 : Final Mesh Refinement Around the Interaction Region.

The refinement around the acoustic structural interaction increases the acoustic degrees of freedom by a factor of 4; the number of nodes increases from 1059260 to 4198257. The number of acoustic elements changes from 1021956 to 4229600. Here, the analysis is repeated for the base coarse (left one in Figure 6.19) and the refined (at right in Figure 6.18) FE models of fluid medium and the effect of this costly mesh refinement is revealed.

The results and comparison of the analyses with the coarse and refined meshes of fluid medium are represented in Appendix E. The velocity and acceleration time histories in three global directions at node 5100 and at node 13753 as well as Von Mises equivalent stress results at integration points of element 114438 and element 12202 are given. The pressure profile at node 230527 of the fluid medium which is located under the platform through the center line is also illustrated.

Due to the geometry of the loading, the velocity and acceleration time histories in global x direction at output nodes have relatively lower magnitudes than those which are for y and z directions. However, if the response in x direction is important, it is seen that the results with coarse fluid mesh estimates lower peak values of velocity and acceleration than the results with refined fluid mesh. At node 5100, the maximum peak acceleration is about 60 g with refined mesh while it is 40g for coarse mesh. The velocity and acceleration profiles are similar at very early times for two meshes; however they differ significantly in the remaining part of the analysis for Node 5100. The velocity and acceleration patterns in x direction for node 13753 are very similar for two meshes. However, the peak values of response changes significantly with mesh refinement; the maximum peak value of acceleration for refined mesh is about 150 g while it is about 100 g for coarse mesh.

The results for global y direction shows that the velocity and acceleration time histories at output nodes follows the same pattern for two cases; however the peak values are underestimated in the case of coarse fluid. The peak acceleration values at node 5100 are about 220 g and 160 g for the refined and coarse meshes of the fluid medium respectively. For node 13753, the estimated peaks are about 95 g for coarse fluid case and 110 g for refined mesh. It is also worth noting that the response with refined fluid mesh is noisy since that mesh refinement results in higher frequencies of loading to be simulated and transmitted to the platform. This results in higher frequency modes of vibration of platform to be excited and take part in the response.

The situation for the results in global z direction is very similar. The velocity and acceleration responses at each output node follow very similar pattern for two cases except that the peak values are underestimated with the coarse model and the responses with the refined fluid mesh are noisy. The maximum peak velocities at node 5100 are 1600 mm/s and 1400 mm/s for the refined and coarse meshes of the fluid medium respectively. The peak accelerations are about 350 g and 250 g for two

cases. At node 13753, the peak values of velocity are about 1400 mm/s and 1200 mm/s and the peak values of acceleration are about 300 g and 180 g for refined and coarse cases of fluid medium.

The time histories of equivalent Von Mises stress at integration points of elements 114438 and 12202 follow very similar pattern for two analyses; however, the peak values of Mises stress are lower for the coarse fluid case. At element 114438, the peak values of Mises stress are about 70 Mpa and 50 Mpa for the base and refined fluid meshes respectively. The peak values of responses are about 135 Mpa and 115 Mpa at element 12202 for the same analyses.

The pressure responses under the keel through the centerline of the platform have similar pattern up to 5 ms for both cases. However, the peak value of pressure is underestimated in coarse fluid case. Later, the patterns of pressure responses differ very significantly; the peaks are denser and higher for refined fluid case.

To sum up, the effect of mesh refinement which was carried according to the DFT analysis of the loadings seems to have important effect on the structural response. Especially, the peak values of responses are increased by the refinement. This should be due to the fact that as the internodal interval in the fluid domain decreases with the mesh refinement, the content of loading which is simulated and transferred to the platform is increased. As higher frequency content of loading is simulated, higher structural modes are excited and the peak values of velocity, acceleration and stress components are increased accordingly.

Figure 6.20 shows a sectional view of the pressure shock wave propagation through the fluid medium and deformation of the platform, for the refined fluid case. The transition of energy and momentum to the platform lasts very short, about 3 ms. Transferred shock and energy is then spreads on the platform as a stress wave and deforms it. The speed of shock wave in the structure is even faster than the speed of the pressure wave in the fluid medium. This is the cause why the event is sometimes called “short duration dynamics”. The maximum peak values of output variables such as acceleration and stress occurs during a very short time and it is enough to run the analysis only for a very short period such as 40-50 ms. Otherwise, obtaining the results might require weeks of time if a 1 s analysis would be run. Post processing might not also be possible in some cases due to very high frequency output.

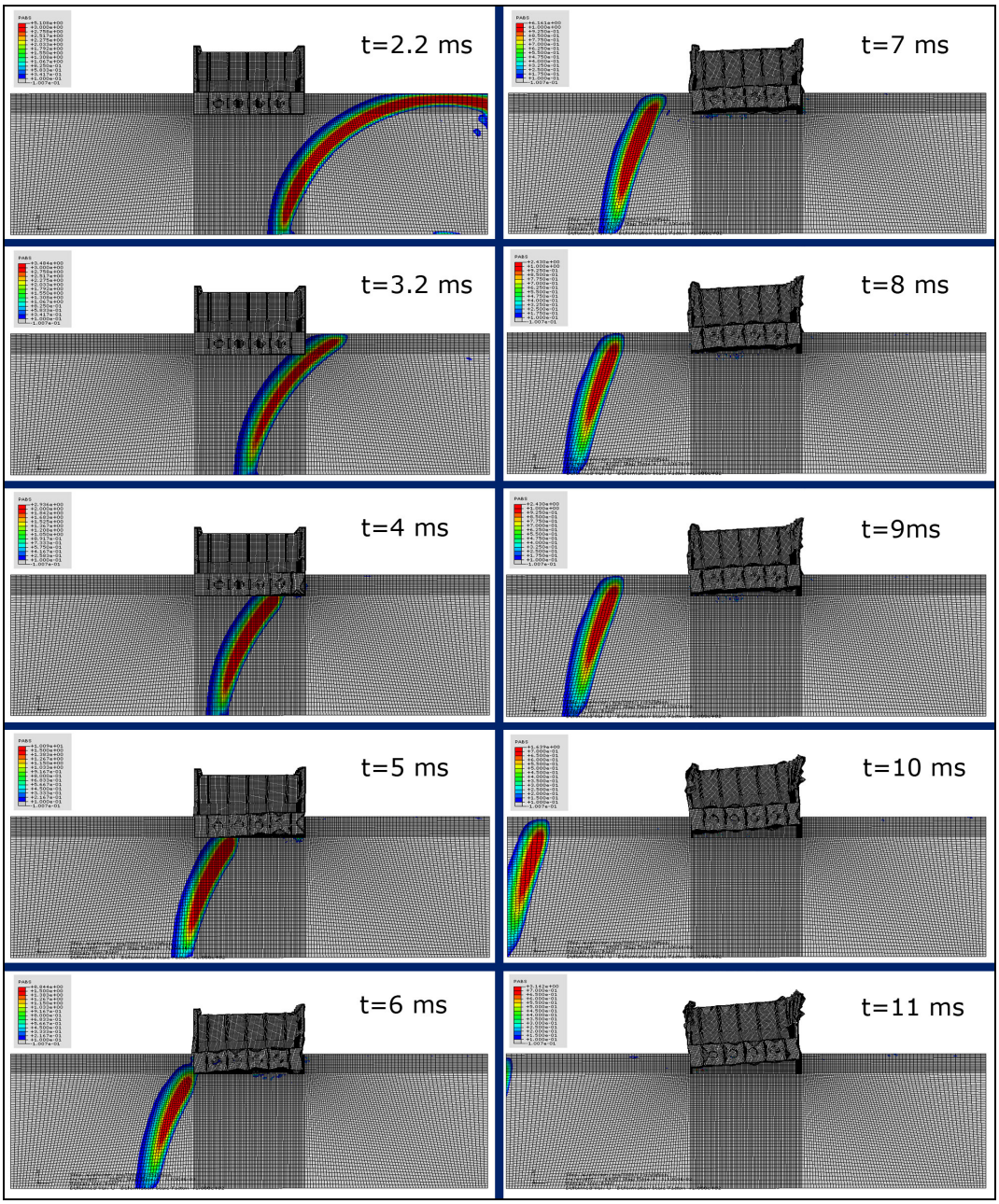

Figure 6.20 : Pressure Wave Propagation and Deformation of the Platform: Def. Scale Factor: 100.

Figure 6.21 shows the pressure change under the platform as the explosion proceeds. Magenta shows the places where the local cavitation occurs. As the shock wave passes and deforms the platform, local cavitation arises and it covers the whole interaction region of the fluid medium. The occurrence of cavitation on small regions is due to the local deformations on the bottom of the platform. The spread of cavitation to the whole interaction region is due to the rigid body motion of the platform. Thus a lighter platform would result in a faster spread of the cavitation around the acoustic-structural interaction region.

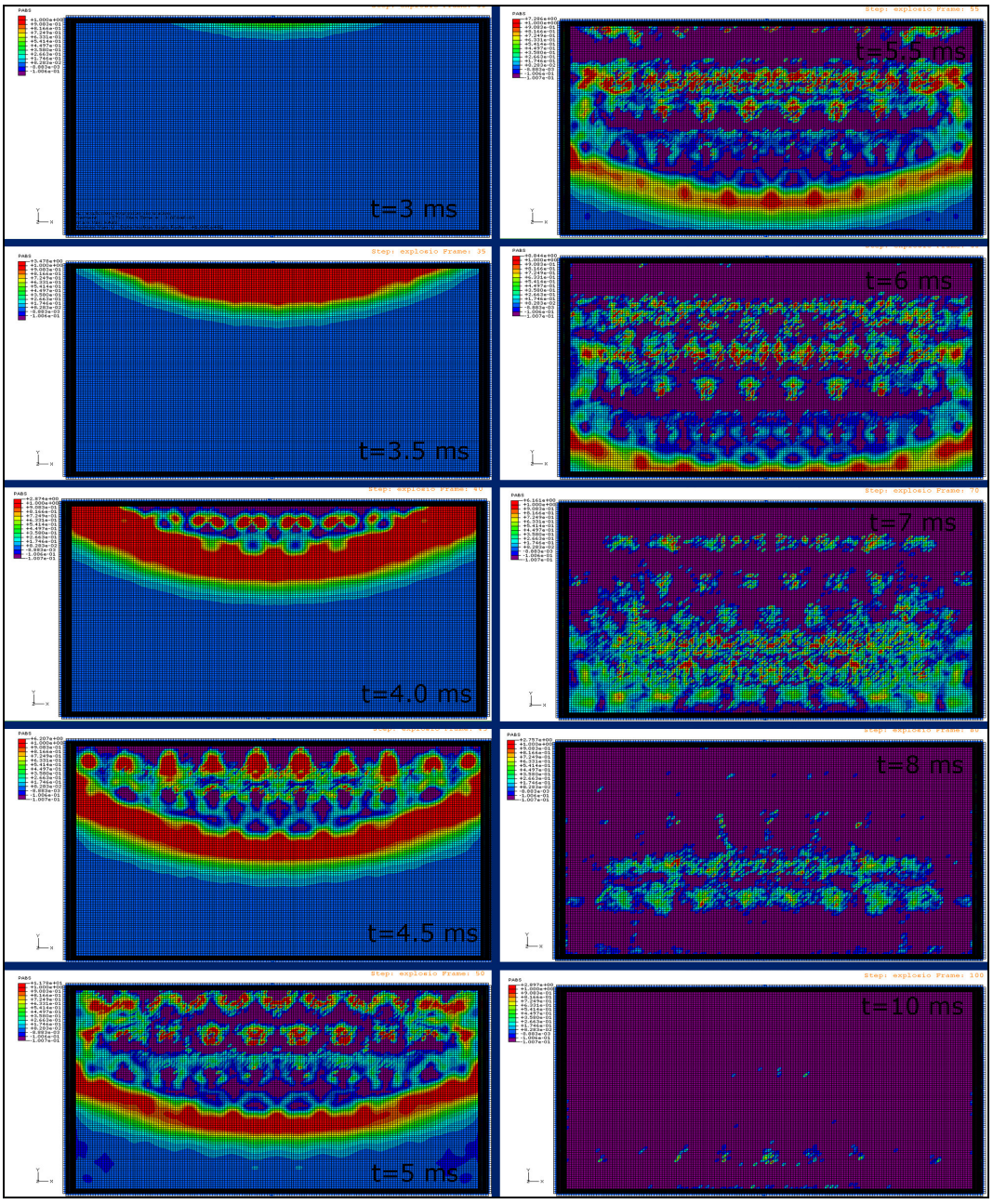

Figure 6.21 : The Change of Pressure Under the Platform and Occurrence of Cavitation.

Figure 6.22 shows the deformation contour of the platform as the shock wave propagates. It can be seen from the figure that local high frequency modes of vibration are excited as the shock wave proceeds as well as fundamental modes of vibration. The platform has a rigid body motion as well as local and global deformations. In explicit dynamic analyses, the acceleration and velocity output for center of mass of the structure is not available in ABAQUS. So we can not present it here.

Figure 6.23 shows the propagation of Mises stress wave.

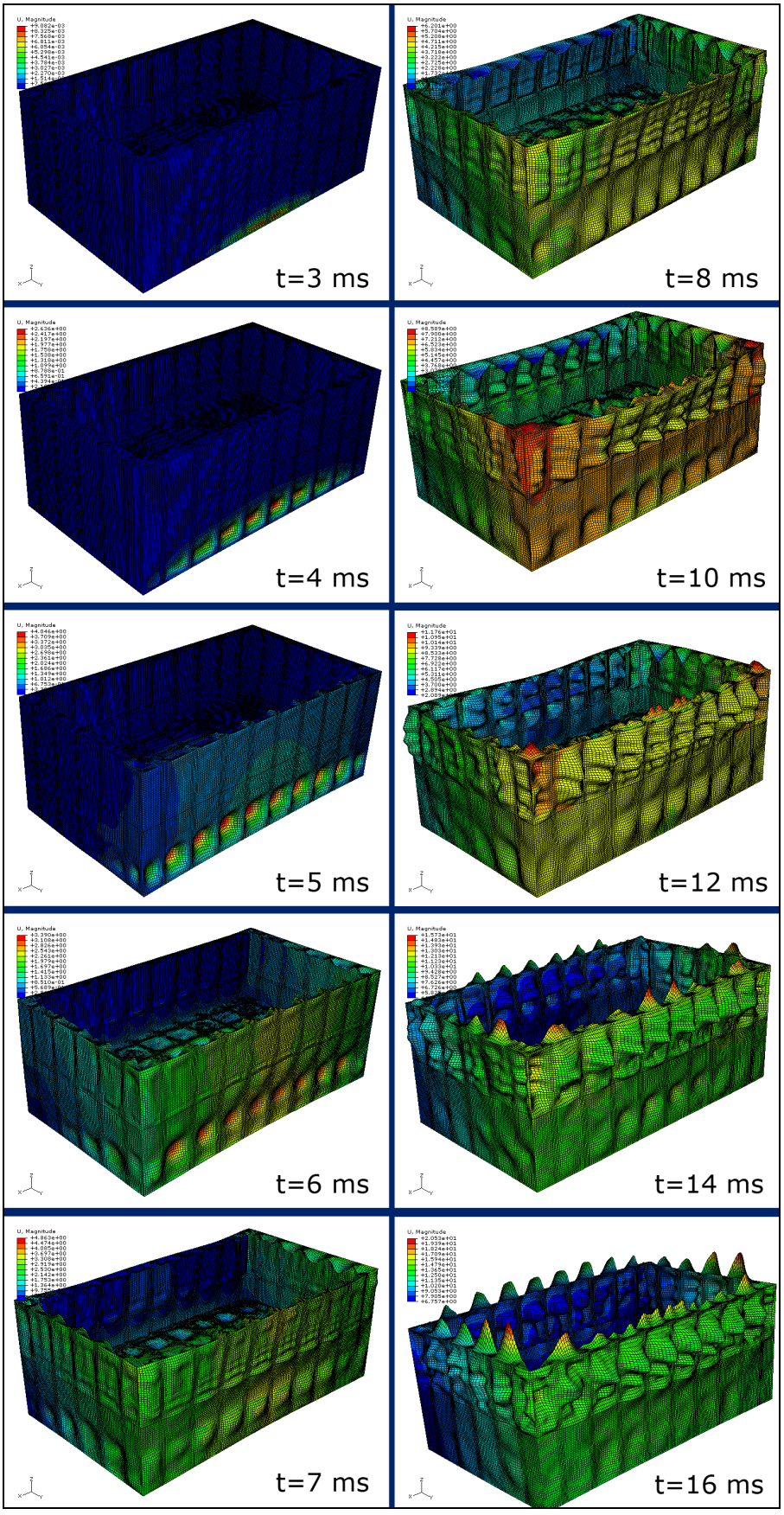

Figure 6.22 : Deformation of the Platform: Def. Scale Factor: 100.

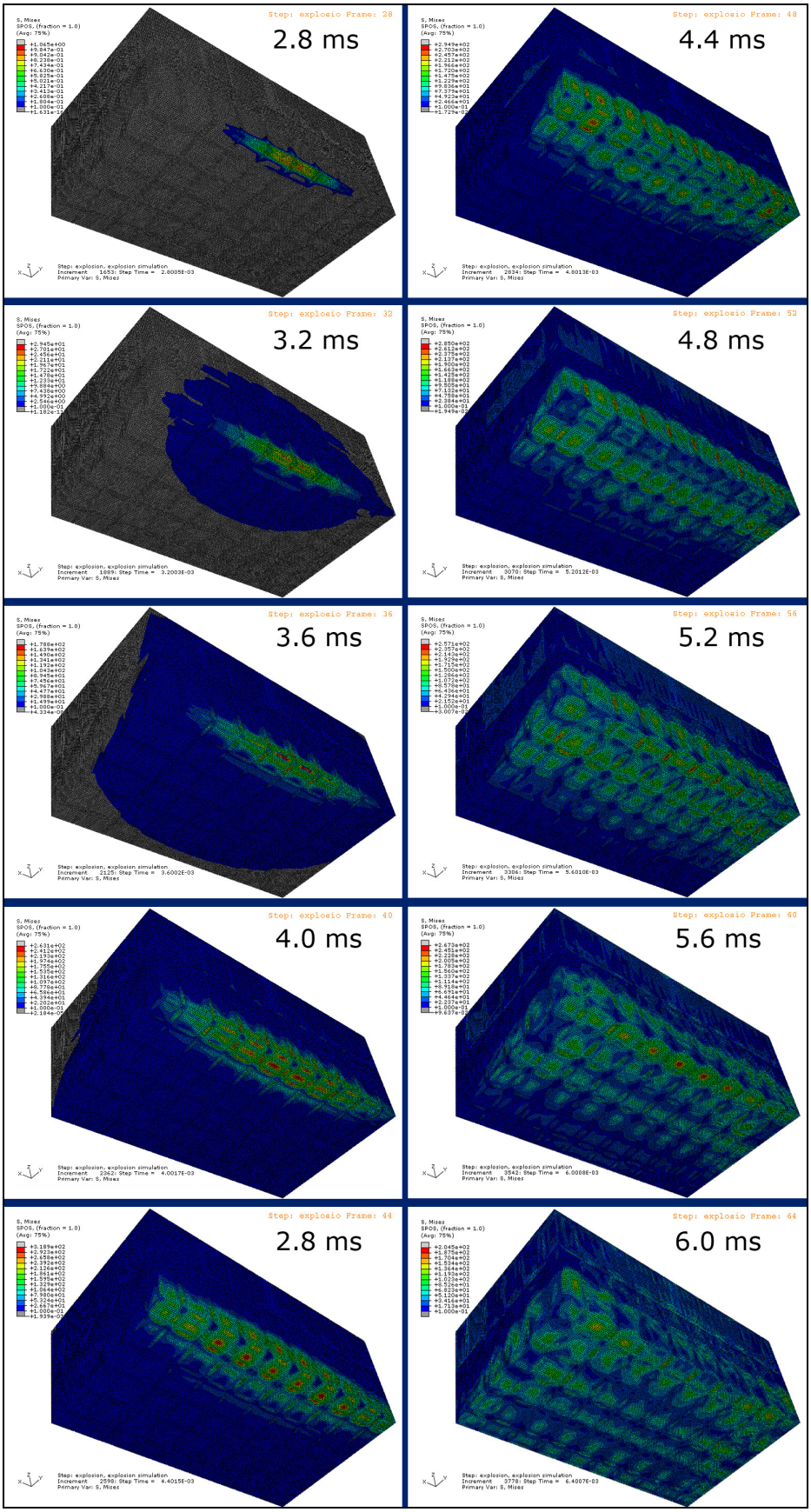

Figure 6.23 : Propagation of Equivalent Von Mises Stress.

The maximum peak accelerations experienced by the structure are of great importance. Figure 6.24 shows a contour plot of the maximum peaks of acceleration magnitudes experienced during the whole event. It does not represent the acceleration field at a certain instant of time, but instead uses all time points to find and plot the maximum peak accelerations. It shows that up to 3790 g acceleration magnitudes are experienced by the structure. However, setting the maximum contour limit to 500 g as shown in Figure 6.25 it's seen that the main framework of the structure experiences accelerations at most up to about 300-400 g. The excess values of acceleration magnitudes occur at the thin sheet sections due to local modes of vibration.

Figure 6.26 is a contour plot of the maximum equivalent Mises stress experienced by the structure during the whole event. A linear elastic-perfectly plastic (with no hardening) material behavior was used; the yield strength of the material was set to 350 Mpa. Figure 6.26 shows that some regions on the loaded side of the platform experience Mises stress values up to 350 Mpa and yielding occurs. Figure 6.26 shows a contour plot of the equivalent plastic strain in uniaxial compression. Up to about 0.2 % equivalent plastic strain arises on some small regions of the platform, especially on the transition regions where the shell thickness changes significantly.

6.4.2 The Effect of Cavitation

Up to that point, all analyses were carried by considering cavitation. Addition of cavitation changes the acoustic constitutive equation from linear to nonlinear as discussed in Section 4.1.2, which adds cost to the solution of the problem. To see the effect of the cavitation on results, the FE model of the previous section with refined fluid medium was run without cavitation and the results were compared with the cavitating case.

The velocity and acceleration time histories for node 75861, equivalent Mises stress profile for element 133574 and absolute acoustic pressure change under keel through the centerline of the platform are given in APPENDIX F. In all outputs, the results are completely different for nonlinear (cavitating) and linear (without cavitation) behaviors of fluid medium. The analysis for which cavitation was neglected results in so much higher velocity and acceleration magnitudes than the analysis with cavitating fluid medium.

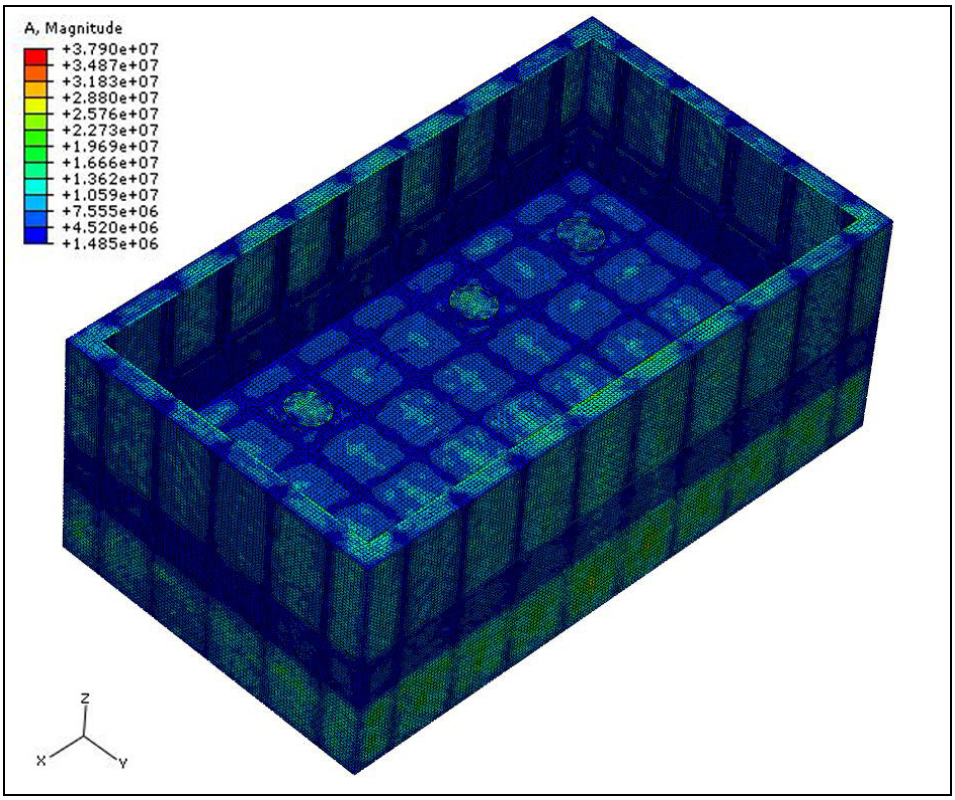

Figure 6.24 : Contour Plot of Max. Acceleration Magnitudes Experienced During the Whole Event.

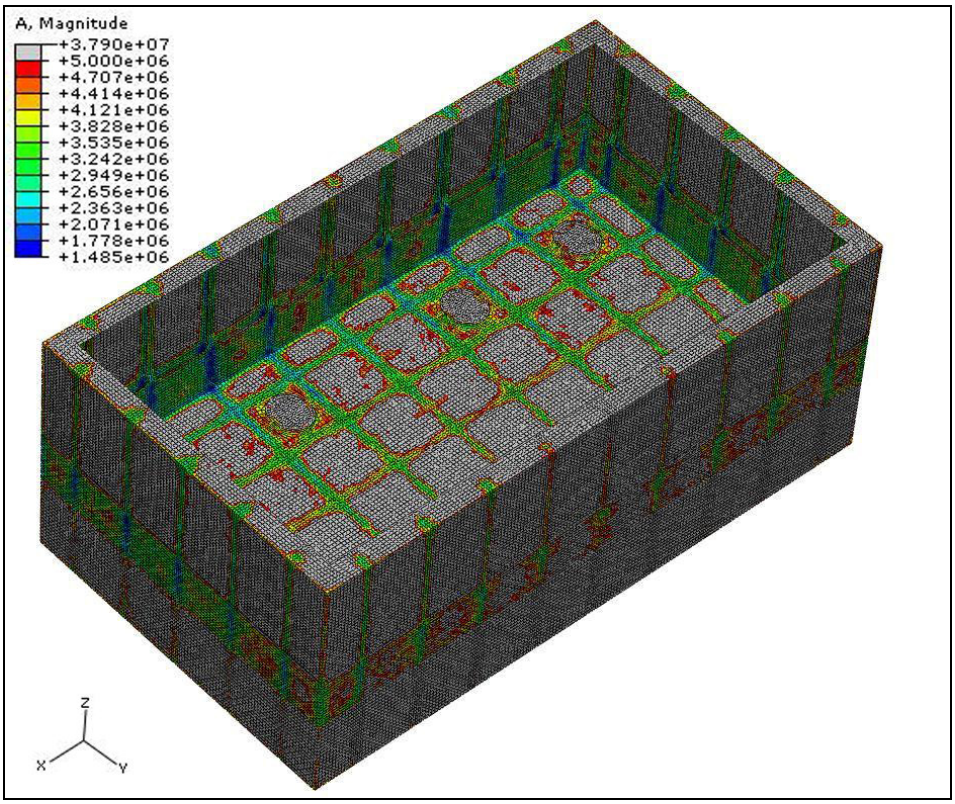

Figure 6.25 : Contour Plot of Max. Acceleration Magnitudes, Maximum Contour Limit Set to 500 g.

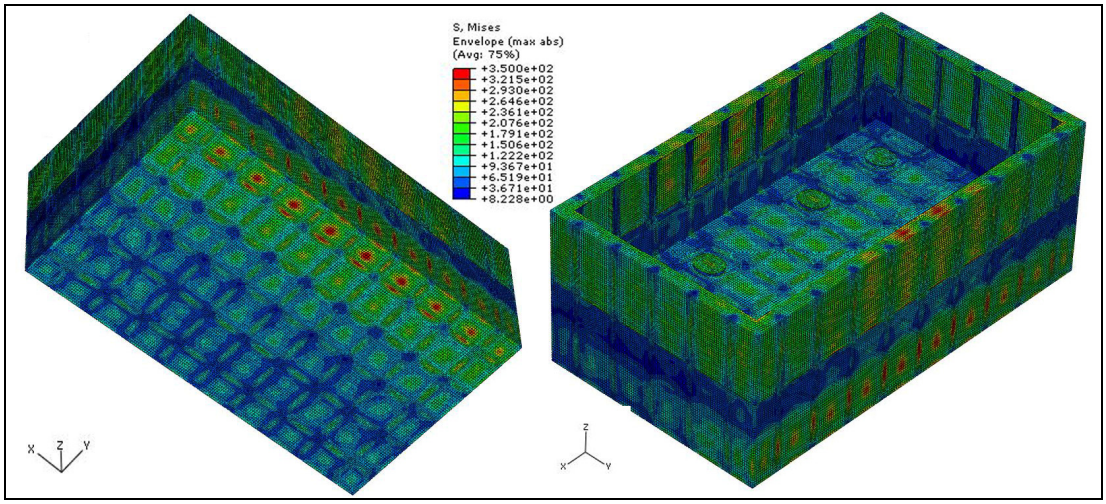

Figure 6.26 : Contour Plot of Max. Equivalent Mises Stress Experienced During the Whole Event.

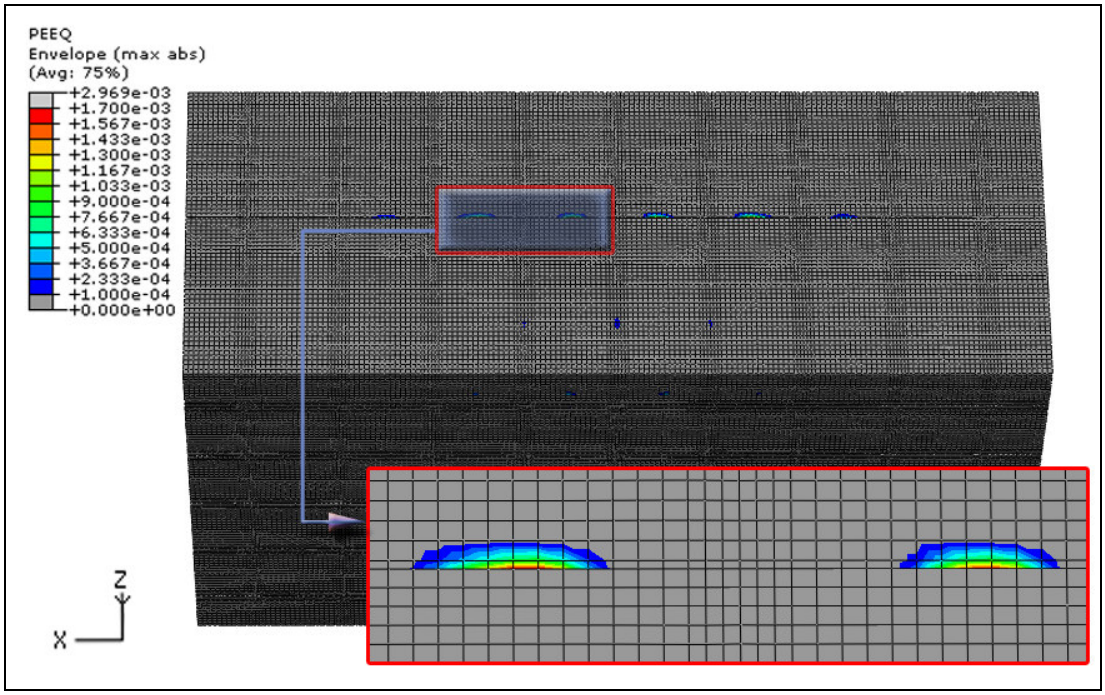

Figure 6.27 : Contour Plot of Equivalent Plastic Strain.

The velocities in y and z directions for linear fluid case have maximum peaks of about 5400 mm/ s and about 7000 mm/s respectively while they are about 1000 mm/s and about 1400 mm/s for cavitating fluid case. The peak accelerations in the specified directions are about 600 g and about 500 g for linear fluid case while they are 380 g and 270 g for cavitating fluid case.

The Mises stress output at element 101133 shows that the peaks with linear fluid case are up to 350 Mpa which indicates yielding while the peaks of Mises stress are well below the yield strength of the material for cavitating fluid case.

The pressure time histories at element 230527 under keel through the centerline of the platform show that the reflected negative pressure waves from the platform and the free surface result in the absolute acoustic pressure to have very low negative magnitudes for the linear fluid case. The peaks of positive and negative pressures also increase accordingly. However, for the cavitating fluid case, the absolute pressure has some smaller positive peaks up to 0.01 ms and then reduces to cavitation limit of the fluid medium. The fluid makes free expansion since that moment until the so-called pseudo-pressure increases above the cavitation limit.

As seen from the above discussion, the effect of cavitation is crucial for UNDEX simulations and including the cavitating fluid behavior is a must to get physically realistic results.

6.4.3 The Effect of Damping

A one more analysis with the refined, cavitating fluid medium of previous section was run by addition of damping to the structure and the results are compared here with the undamped case. The same Rayleigh damping coefficients of Section 6.3.2 were used; α_R and β_R were set to 1.5 and $0.5*10^{-6}$ respectively.

The effect of damping on stable time increment is considerable. Without damping, the stable time increment is $1.69x10^{-6}$. With the above values of the Rayleigh coefficients, the stable time increment is reduced to $1.29x10^{-6}$. The stable time increment is reduced by a factor of 24 % in the damped case, thus increasing the analysis time with the same amount.

The velocity and acceleration time histories for node 36820 and node 8787, equivalent Mises stress time histories for element 106959 and element 22827, and absolute acoustic pressure change under keel through the centerline of the platform at node 230527 of the fluid medium are given in APPENDIX G.

The velocity results at node 36820 in global x direction shows that in the first 6 ms, the effect of damping is not apparent. Later, the addition of damping decreases peak velocity values slightly, following the same pattern with the undamped case. The noise in the undamped case is removed and a smoother response is obtained by the addition of damping. For the velocity in global y direction, the responses are again the same up to 6 ms, later peaks are slightly decreased. The effect of damping on the

velocity response in global z direction is the same with the effect in global y direction.

At node 8787, the effect of damping on velocity responses is similar with the effect of damping on the velocity responses of node 36820. Up to 10 ms, the responses are the same for all three directions. Later the peak values of velocity responses are slightly decreased, but following exactly the same pattern with the undamped case.

For acceleration responses, the effect of damping is more apparent. At node 36820, the effect of damping is negligible up to about 5ms for all three directions. Later, addition of damping results in a smoother response with reduced peak values. The patterns of acceleration time histories are still similar. The peak values of acceleration in global x direction are about 130 g and 80 g for the undamped and damped cases. In y direction, the peaks are about 150 g and 130 g for two cases. However, in global z direction, the maximum peak value of acceleration response occurs at the same time with the same magnitude for damped and undamped cases; it's about 700 g. The peaks are decreased significantly at some other time points.

The equivalent Von Mises stress results at element 106959 reveals that the responses have the same pattern for damped undamped cases and they are the same up to 6 ms for damped and undamped cases. Later, the peak values of responses are decreased slightly. However, at some time points, the decrease in the Mises stress results due to damping is significant. At element 22827, the stress time histories are the same for damped and undamped cases up to 6 ms. The peak values of response later decreases slightly in the damped case.

The pressure time histories for damped and undamped cases at element 230527 under keel through the centerline of the platform shows that the responses are identical up to 7 ms. Later, the response changes significantly but still similar. At about 9 ms, cavitation occurs and free expansion of the fluid goes on until the end of the analysis for both damped and undamped cases.

According to above discussions, it is seen that the effect of damping is slight in the velocity response. However, the peak values of acceleration time histories are decreased significantly by the addition of damping. Damping is especially effective in the late time response of the platform after the initial shock wave has arrived. The effect of damping on Von Mises stress results is also significant at some region. So,

the proper determination of Rayleigh damping coefficients will result in more accurate results. Care should be taken selecting the Rayleigh damping coefficients to ensure that the stable time increment is not decreased dramatically.

6.5 Submodeling Analyses

Once the analyses were carried in full scale including acoustic medium, structure and acoustic structural interaction, some so-called submodeling analyses can be carried to obtain converged stress, strain results at some point included in a submodel region of the structure by use of the displacement field obtained in the full scale global analysis. See Section 5.1.1 for a discussion and illustration of the submodeling analyses.

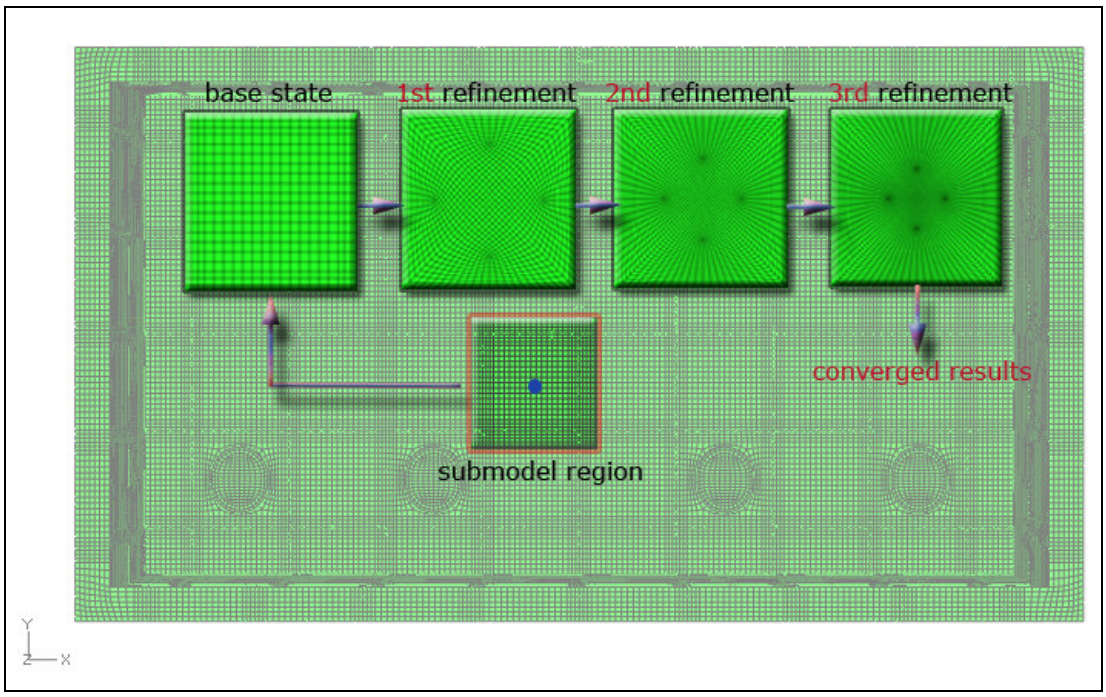

Figure 6.28 : Submodeling Region and Sequential Mesh Refinements.

The fluid mesh size around the interested region was 40 mm in the base state. Then this mesh size was set to 20 mm, 10 mm and 5 mm in the interested region and sequential submodel analyses were run for each refinement using the result files of the global UNDEX analysis which had been run in the previous section. The comparison of equivalent Von Mises stresses for each refinement and convergence of stress is plotted and shown in Figure 6.29.

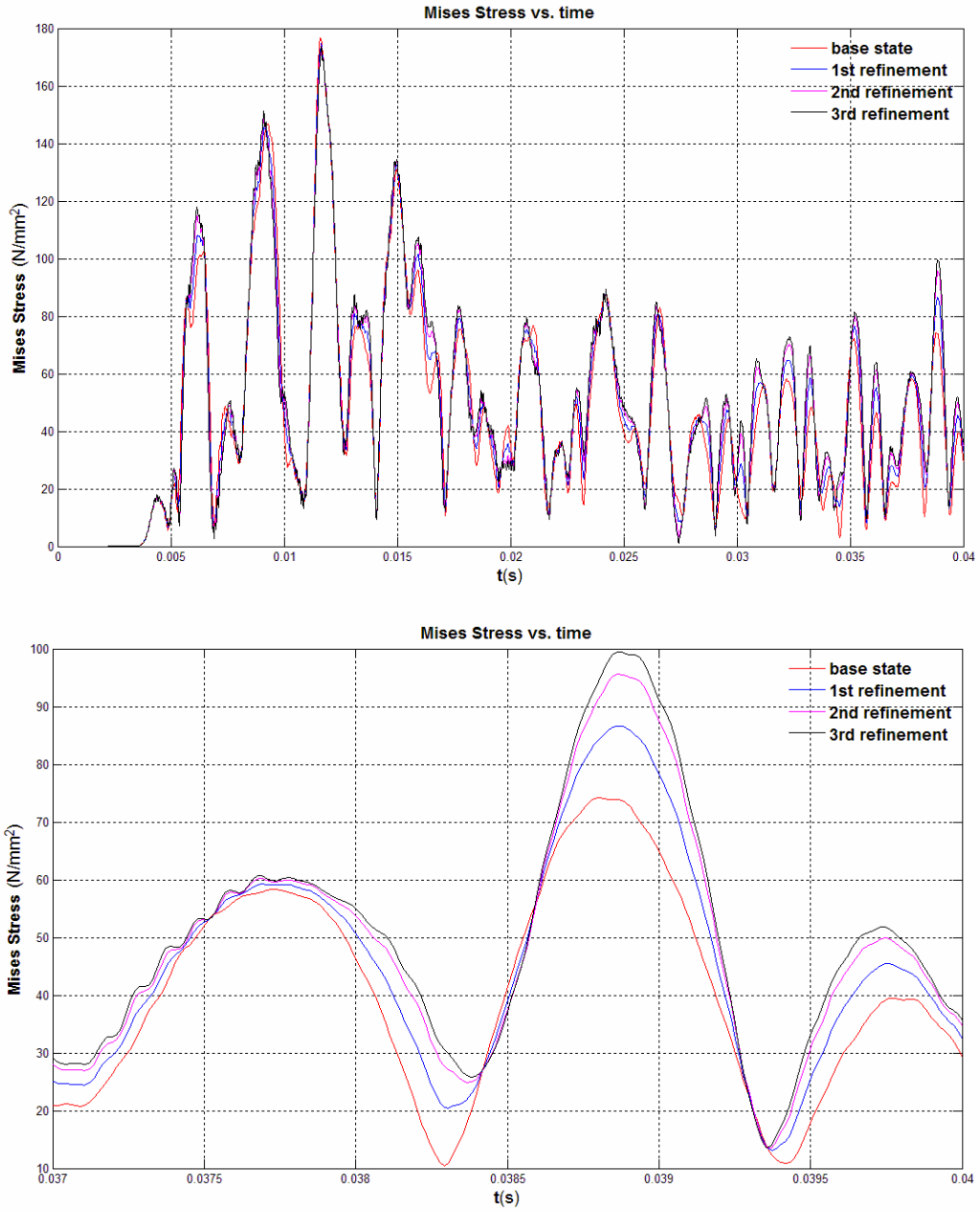

Figure 6.29 : Equivalent Mises Stress for Each Mesh Refinement.

The same convergence tendency is valid for stress and strain components as well. So, submodeling analyses can be used to obtain converged stress-strain results.

7. CONCLUSION

Building a proper FE model for UNDEX simulations and running analyses is a long and though process. The work done in this study can guide the future works on this subject.

The fluid mesh density has an important effect on the outputs and special attention is needed in determining a proper mesh size for the fluid medium. An initial mesh convergence analyses were run in this work to roughly estimate the required fluid element size with the assumption that the structure was rigid. The following DFT analyses of the pressure shock wave time histories around the interaction region provided us with the knowledge of the frequency content of the loadings and the required element size to properly simulate these loadings. With this knowledge, a final mesh refinement around the acoustic-structural region was carried. This approach can be used to estimate a proper mesh density distribution through the fluid medium for UNDEX simulations.

The effect of cavitation in UNDEX simulations was shown to be very important. Though it requires a nonlinear fluid behavior which adds to the cost of the analyses, including cavitation is a must to obtain physically meaningful results.

The effect of damping was also shown to be important, especially in peak acceleration estimation. Since the system has no any other damping mechanism, the effect of damping is apparent in all analyses outputs, especially in the late time response after the shock wave hits the structure. The proper determination of Rayleigh damping coefficients is important to get accurate results. Addition of damping also adds to the cost of the analyses since it decreases the stable time increment.

The analyses results obtained from the global UNDEX simulations can be used to obtain converged stress-strain results at some sub region of the structure. Running the full scale analyses with a local mesh refinement would result in the stable time increment to decrease dramatically because of the fact that the stable time increment

depends on the minimum element size in the model. However, special attention is needed in determining the submodeling region boundaries, and the output from the global analyses should be of enough frequency and precision to properly recreate the displacement field at submodel boundaries.

It's also worth noting that care should be taken in determining the frequency of output because increasing the output frequency increases the analysis time dramatically. To obtain smooth animations of contour plots of output variables, it is enough to take output at each 0.1 ms. For plotting purposes, however, the output frequency used was about 66 kHz. This high frequency output was only demanded for some selected nodes and elements.

Since the fluid domain has millions of degrees of freedom, it is not efficient to get the pressure contour plots for whole fluid medium. Instead, the pressure output can be taken for only elements which are defined on a cutting plane of the fluid medium for visualization. This will fasten the analyses very significantly.

Experimental work is a must for the validation of the numerical code used and of the analysis procedure followed in this work. The same methodology and tools can then be used to reliably estimate the response of any floating structure, such as a surface ship, to underwater explosion.

REFERENCES

[1] **MIL-S-901D**, 1989. Shock Tests, High Impact Shipboard Machinery, Equipment and Systems, Requirements for, *Naval Publications and Forms Center,* Philadelphia.

[2] *Simulated Ship Shock Tests/Trials?* 2003. [online] [Accessed 9th may 2007]. Available from World Wide Web: <http://www.dote.osd.mil/1fte/SSS>

[3] **Jarema, L., Didoszak, M., Shin, Y.S. and Lewis, D.H.,** 2004. Shock Trial Simulation for Naval Ships, *ASNE Day,* Virginia, USA, June 28-29.

[4] **Rajendran, R. and Narsimhan, K.**, 2001. Linear Elastic Shock Response of Plane Plates Subjected to Underwater Explosion, *International Journal of Impact Engineering,* **25,** 493-506.

[5] **Burch, I.A. and Mouritz, A.P.**, 1999. Analysis of Responses of a Small Shock Platform Subjected to Underwater Explosions, *DSTO Report,* **DSTO-TR-089,** Australia.

[6] **Rajendran, R. and Narsimhan, K.**, 2001. Damage Prediction of Clamped Circular Plates Subjected to Contact Underwater Explosion, *International Journal of Impact Engineering,* **25,** 373-386.

[7] **Rajendran, R. and Narsimhan, K.**, 2006. Deformation and fracture behavior of plate specimens subjected to underwater explosion—a review, *International Journal of Impact Engineering,* **32,** 1945-1963.

[8] **Rajendran, R. and Narsimhan, K.**, 2004. Deformation and rupture of thin rectangular plates subjected to underwater shock, *International Journal of Impact Engineering,* **30,** 699-719.

[9] **Hugh, C.F., Hsu, P.Y. and Hwang-Fuu, J.J.**, 2005. Elastic shock response of an air-backed plate to underwater explosion, *International Journal of Impact Engineering,* **31,** 151-168.

[10] **Felippa, C.A.**, 1980. The Top-Down Derivation of The Doubly Asymptotic Approximations for Structure-Fluid Interaction Analysis, in

Innovative Numerical Analysis for the Engineering Sciences, pp. 79-88, University Press of Virginia, Virginia.

[11] **Geers, T.L.**, 1978. Doubly Asymptotic Approximations for Transient Motions of Submerged Structures, *Journal of Acoustical Society of America,* **64,** 1500-1508.

[12] **Kwon, Y.W. and Cunningham, R.E.**, 1998. Comparison of USA-Dyna Finite Element Models for a Stiffened Shell Subject to Underwater Shock, *Computers and Structures,* **66,** 127-144.

[13] **Kwon, Y.W. and Fox, P.K.**, 1993. Underwater Shock Response of a Cylinder Subjected to a Side-on Explosion, *Computers and Structures,* **48,** 637-646.

[14] **McCoy, R.W. and Sun, C.T.**, 1997. Fluid-Structure Interaction Analysis of a Thick Section Composite Cylinder Subjected to Underwater Blast Loading, *Composite Structures,* **37,** 45-55.

[15] **Shin, Y.S. and Hooker, D.T.**, 1996. Damage Response of Submerged Imperfect Cylindrical Structures to Underwater Explosion, *Computers and Structures,* **60,** 683-693.

[16] **Arden, K.E.**, 1995. Use of MSC/NASTRAN in Predicting Structural Response to an Underwater Explosion*, MSC 1995 World Users' Conference Proceedings*, California, May 1995, 51.

[17] **Adamczyk, R. and Cichocki, K.**, 1997. Analysis of the Shock Response of an Underwater Structure Subjected to a Far-Field Explosion*, Proceedings of ABAQUS Users' Conference*, Milan, ITALY, June 1997, 73-87.

[18] **Cichocki, K.**, 1994. Computer Analysis of Dynamic Response due to Underwater Explosion on Hybrid Structure*, Proceedings of ABAQUS Users' Conference*, Newport, June 1994, 207-220.

[19] **Shin Y.S. and Santiago, L.D.**, 1998. Surface ship shock modeling and simulation: two-dimensional analysis, *Journal of Shock and Vibration,* **5,** 129-137.

[20] **Shin Y.S.**, 2004. Ship Shock Modeling and Simulation for Far-Field Underwater Explosion, *Computers and Structures,* **82,** 2211-2219.

[21] **Liang C.C. and Tai Y.S.**, 2006. Shock responses of a surface ship subjected to non-contact underwater explosions, *Ocean Engineering,* **33,** 748-772.

[22] **Coles, R.H.,** 1948. Underwater Explosions, Princeton University Press, Princeton.

[23] Abaqus, 2006. Version 6.6.1, Analysis User Manual.

[24] **Swisdak, M.M.**, 1978. Explosion effects and properties: Part II-Explosion effects in water, *Naval Surface Weapons Center Report,* **NSWC/WOL/TR-77-116,** Naval Surface Weapons Center, Virginia.

[25] **Geers, T.L. and Hunter, L.S.**, 2002. An Integrated Wave-Effects Model for an Underwater Explosion Bubble, *Journal of Acoustical Society of America,* **111,** 1548-1601.

[26] **Kaminski, M.L., Besnier, F., Du, S., Ergin, A., and others**, 2006. Committee II.2; Dynamic Response*, 16th International Ship and Offshore Structures Congress*, Southampton, UK, August 2006, 301-302.

[27] Abaqus, 2006. Version 6.6.1, Theory Manual.

[28] Abaqus, 2006. Version 6.6.1, Example Problems Manual.

[29] **Didoszak, J.M.**, 2004. Parametric Studies of DDG-81 Ship Shock Trial Simulations, *Master of Science Thesis,* Naval Postgraduate School, Monterey, California.

[30] Abaqus, 2006. Version 6.6.1, Structural-Acoustic Analysis using ABAQUS lecture notes.

[31] Abaqus, 2006. Version 6.6.1, Getting Started with ABAQUS.

[32] **Rao, S.S.,** 2004. Mechanical Vibrations, Pearson Prentice Hall, New Jersey.

[33] **O'Daniel, J.L., Krauthammer, T. and Koudela, K.**, 1999. Undex Response Validation by Numerical Simulations and Precision Impact Testing, *9th International Symposium on Interaction of the Effects of Munitions with Structures,* Berlin, USA, May 3-7.

[34] *Material Properties.* 2007. [online] [Accessed 7th may 2007]. Available from World Wide Web: <http://www.matweb.com/search/DataSheet.aspx?MatID=6805&ckck>

[35] *Fluids Data Chart.* 2007. [online] [Accessed 15th June 2007]. Available from World Wide Web: <http://www.engineersedge.com/fluid_flow/fluid_data.htm>

APPENDIX

A. Pressure-Time History Program

```
function [P1,P2] = pressure_pulse(m,R)
% This function calculates the UNDEX pressure-time (P,t) history of a point at a user
% specified distance (R in m) from an HBX-1 charge whose mass (m in kg) is input
% by user. The output values P1 and P2 are pressure time histories according to the
% charge constants by Swisdak (1978) and Price (1979) respectively.
% Written by Fatih ARUK @ 2007: fatih.aruk@gmail.com
Pc=[1.71 1.58]';              % Gpa [Swisdak(1978) Price(1979)]
Vc=[1470 1170]';              % m/s [Swisdak(1978) Price(1979)]
A=[0.15 0.144]';              % dimensionless [Swisdak(1978) Price(1979)]
B=[0.29 0.247]';              % dimensionless [Swisdak(1978) Price(1979)]
d=1720;                       % kg/m^3 Density of HBX-1.72 g/cc
r=(3/4/pi/d*m)^(1/3);         % radius of explosive in meters (m)
Pmsw=Pc(1)*(r/R)^(1+A(1)); % Maksimum pressure at standoff point  (Gpa)
Pmpr=Pc(2)*(r/R)^(1+A(2));
To=((r/R).^B).*Vc/r;
ii=(0:100)';
t=0.0001*ii;
Totsw=To(1)*t;
Totpr=To(2)*t;
fsw=0.8251*exp(-1.338*Totsw)+0.1749*exp(-0.1805*Totsw);
fswr=1/fsw(1)*fsw<0.02;
fsw(fswr)=[];
fpr=0.8251*exp(-1.338*Totpr)+0.1749*exp(-0.1805*Totpr);
fprr=1/fpr(1)*fpr<0.01;
fpr(fprr)=[];
Psw=1000*Pmsw*fsw;  %Mpa
Ppr=1000*Pmpr*fpr;  %Mpa
tsw=t(~fswr);
tpr=t(~fprr);
plot(tsw,Psw,'r-');
hold on;
plot(tpr,Ppr,'b-');
grid on;
ylabel('\bf{P}\rm(Mpa)');
xlabel('\bf{t}\rm(s)');
```

```
legend('according to Swisdak', 'according to Price');

ttl=['Pressure vs. time history for ' num2str(m)  'kg of HBX-1 charge, standoff distance of ' num2str(R) 'm'];

Title(ttl);

P1=[tsw Psw];

P2=[tpr Ppr];

end
```

B. Bulk Cavitation Program

```
% This program will calculate the upper and lower cavitation boundaries due to the
% undex explosion of a user input weight HBX-1 charge at a user input depth from
% the sea surface.
% Written by Fatih ARUK @ 2008: fatih.aruk@gmail.com
Pa = 101325;                    % (pa) atmospheric pressure at sea level.
C = 1502.54;                    % (m/s) speed of sound in sea water
K1 = 56.7*10^6;                 % (pa) explosive pressure constant
K2 = 0.083;                     % explosive time constant
A1 = 1.18;                      % explosive pressure constant
A2 = -0.29;                     % explosive time constant
gamma= 10104.3; % kg/m^2/s^2
W = 27.2;
D = 7.3152;
data_u=[];
data_l=[];
for x = 0:500
for y = 0:0.02:20
r1 = sqrt((D-y)^2+x^2);
r2 = sqrt((D+y)^2+x^2);
theta = K2*W^(1/3)*(W^(1/3)/r1)^A2/1000;                    % seconds
F =(K1*(W^(1/3)/r1)^A1*exp(-(r2-r1)/(C*theta)))+Pa+(gamma*y)-
(K1*(W^(1/3)/r2)^A1);
if F <= 0
data_u =[data_u;x -(y)];
break
end
end
end
for x = 0:(length(data_u)-1)
for y = 0:0.03:20
r1 = sqrt((D-y)^2+x^2);
r2 = sqrt((D+y)^2+x^2);
theta = K2*W^(1/3)*(W^(1/3)/r1)^A2/1000;
Pi = K1*(W^(1/3)/r1)^A1*exp(-(r2-r1)/(C*theta));
```

```
G = -(Pi/(C*theta))*(1+(((r2-(2*D*(D+y)/r2))/r1)*(((A2*r2)/r1)-A2-1)))-
((A1*Pi)/r1^2)*(r2-
2*D*((D+y)/r2))+(gamma)*((D+y)/r2)+(A1/r2)*(Pi+Pa+(gamma*y));
if G >= 0 %Test for cavitation
data_l=[data_l;x -(y)];
break
end
end
end
index_u = data_u(:,2)<data_l(:,2);
data_u(index_u,:)=[];
data_l(index_u,:)=[];
orient tall;
figure(1)
%-------------------------------------------------------
data_u_1=data_u(:,1)+8.526;
data_l_1=data_l(:,1)+8.526;
data_u_1_2=-1*data_u(:,1)+8.526;
data_l_1_2=-1*data_l(:,1)+8.526;
hold on
plot(data_u_1,data_u(:,2),'-b','LineWidth',2);
plot(data_l_1,data_l(:,2),'-b','LineWidth',2);
plot(data_u_1_2,data_u(:,2),'-b','LineWidth',2);
plot(data_l_1_2,data_l(:,2),'-b','LineWidth',2);
plot([data_u_1(end) data_l_1(end)],[data_u(end,2) data_l(end,2)],'-b','LineWidth',2);
plot([data_u_1_2(end) data_l_1_2(end)],[data_u(end,2) data_l(end,2)],'-
b','LineWidth',2);
plot(8.526,-D,'b+');
plot(8.526,-D,'bo');
%figure(2)
%plot(x_axis,y_axis);
%W_text = num2str(W);
%D_text = num2str(D);
%-------------------------------------------------------
data_u_1=data_u(:,1)+10.05;
data_l_1=data_l(:,1)+10.05;
```

```
data_u_1_2=-1*data_u(:,1)+10.05;
data_l_1_2=-1*data_l(:,1)+10.05;
hold on
plot(data_u_1,data_u(:,2),'-r','LineWidth',2);
plot(data_l_1,data_l(:,2),'-r','LineWidth',2);
plot(data_u_1_2,data_u(:,2),'-r','LineWidth',2);
plot(data_l_1_2,data_l(:,2),'-r','LineWidth',2);
plot([data_u_1(end) data_l_1(end)],[data_u(end,2) data_l(end,2)],'-r','LineWidth',2);
plot([data_u_1_2(end) data_l_1_2(end)],[data_u(end,2) data_l(end,2)],'-
r','LineWidth',2);
plot(10.05,-D,'r+');
plot(10.05,-D,'ro');
%-------------------------------------------
data_u_1=data_u(:,1)+11.574;
data_l_1=data_l(:,1)+11.574;
data_u_1_2=-1*data_u(:,1)+11.574;
data_l_1_2=-1*data_l(:,1)+11.574;
hold on
plot(data_u_1,data_u(:,2),'-g','LineWidth',2);
plot(data_l_1,data_l(:,2),'-g','LineWidth',2);
plot(data_u_1_2,data_u(:,2),'-g','LineWidth',2);
plot(data_l_1_2,data_l(:,2),'-g','LineWidth',2);
plot([data_u_1(end) data_l_1(end)],[data_u(end,2) data_l(end,2)],'-g','LineWidth',2);
plot([data_u_1_2(end) data_l_1_2(end)],[data_u(end,2) data_l(end,2)],'-
g','LineWidth',2);
plot(11.574,-D,'g+');
plot(11.574,-D,'go');
%-------------------------------------------
data_u_1=data_u(:,1)+14.622;
data_l_1=data_l(:,1)+14.622;
data_u_1_2=-1*data_u(:,1)+14.622;
data_l_1_2=-1*data_l(:,1)+14.622;
hold on
plot(data_u_1,data_u(:,2),'-m','LineWidth',2);
plot(data_l_1,data_l(:,2),'-m','LineWidth',2);
plot(data_u_1_2,data_u(:,2),'-m','LineWidth',2);
```

```
plot(data_l_1_2,data_l(:,2),'-m','LineWidth',2);
plot([data_u_1(end) data_l_1(end)],[data_u(end,2) data_l(end,2)],'-m','LineWidth',2);
plot([data_u_1_2(end) data_l_1_2(end)],[data_u(end,2) data_l(end,2)],'-
m','LineWidth',2);
plot(14.622,-D,'m+');
plot(14.622,-D,'mo');
%-------------------------------------------
xlabel('meters'); ylabel('meters');
hold on
plot(0,-D,'ko');
%-------------------------------------------------
%x_s=[2.43 2.43 -2.43 -2.43 2.43];
%y_s=[2.34 -1.0 -1.0 2.34 2.34];
hold on
%plot(x_s,y_s,'-k','LineWidth',2)
h=rectangle('Position',[-2.43,-1.0,4.86,3.34]);
set(h,'FaceColor',[0.555, 0.125, 0]);
%-------------------------------------------------
plot([-1000 1000],[0 0],'-k','LineWidth',3);
%-------------------------------------------------
plot([8.526 8.526],[-7.3152 0],'-.b','LineWidth',1);
plot([10.05 10.05],[-7.3152 0],'-.r','LineWidth',1);
plot([11.574 11.574],[-7.3152 0],'-.g','LineWidth',1);
plot([14.622 14.622],[-7.3152 0],'-.m','LineWidth',1);
%-------------------------------------------------
text(-125,2.2,'\bf{atmosphere}','FontSize',14);
text(-125,-0.5,'\bf{sea-water}','FontSize',14);
ss=text(-14,1,'\bf{PLATFORM}','FontSize',14);
set(ss,'Color','k');
ss=text(-50,-2.5,'\rmCAVITATION','FontSize',20);
set(ss,'Color',[0.2, 0.2, 1.0]);
ss=text(23,-2.5,'\rmREGION','FontSize',20);
set(ss,'Color',[0.2, 0.2, 1.0]);
%-------------------------------------------------
line([50 70]',[3.5 3.5]','Color','m','LineWidth',2)
```

```
line([50 70]',[3.1 3.1]','Color','g','LineWidth',2)
line([50 70]',[2.7 2.7]','Color','r','LineWidth',2)
line([50 70]',[2.3 2.3]','Color','b','LineWidth',2)
text(72,3.5,'\rm{SHOT-1}','FontSize',14);
text(72,3.1,'\rm{SHOT-2}','FontSize',14);
text(72,2.7,'\rm{SHOT-3}','FontSize',14);
text(72,2.3,'\rm{SHOT-4}','FontSize',14);
%-------------------------------------------------
ss=line([-10.43 -10.43 10.43 10.43]',[0.0 -6.915 -6.915 0.0]','Color',[0.0 0.5
0.0],'LineWidth',1);
set(ss,'LineStyle','--');
%-------------------------------------------------
line([50 70]',[1.9 1.9]','Color',[0.0 0.5 0.0],'LineWidth',1,'LineStyle','--')
text(72,1.9,'\rm{mesh region}','FontSize',14);
%-------------------------------------------------
xlim([-140 160])
ylim([-8 4])
box on
grid;
```

C. Kick-off Velocity Estimation Program

```
% This program estimates the velocity of the shock test platform due to  the
% explosion of an HBX-1 charge in underwater, that is located at "r" meters depth.
% The explosive was assumed to be located on the normal line through the center of
% the plate. The platform is assumed to be rigid and the shock wave was assumed
% to be a plane wave.
% Written by Fatih ARUK @ 2008: fatih.aruk@gmail.com
% inputs
clear all
close all
ms=39000;       % mass of the platform in 'kg'
a=8.520;        %length of the platform 'm'
b=4.863;        % width of the platform 'm'
As=a*b;         % bottom area of the platform in 'm^2'
mp=ms/As;       % mass per unit area of the platform 'kg/m^2'
R=6.3152;       % vertical distance between the bottom of the platform and the
center of explosive in 'm'
m=27.2155;      % mass of the explosive in 'kg'
Pc=1.71;        % Gpa [Swisdak(1978)]
Vc=1470;        % m/s [Swisdak(1978)]
A=0.15;         % dimensionless [Swisdak(1978)]
B=0.29;         % dimensionless [Swisdak(1978)]
d=1720;         % kg/m^3 Density of HBX-1.72 g/cc
%----------------------incident pressure calculation----------------------
r=(3/4/pi/d*m)^(1/3);           % radius of explosive in meters(m)
Pmsw=Pc(1)*(r/R)^(1+A);    % Maksimum incident pressure at standoff point (Gpa)
To=((r/R).^B).*Vc/r;           % explosive time constant in 's^-1'
ii=(0:1000)';
t=0.00001*ii;
Totsw=To*t;
fsw=exp(-Totsw);
fswr=1/fsw(1)*fsw<0.005;
fsw(fswr)=[];
Psw=1000*Pmsw*fsw;         % incident pressure at stand-off (Mpa)
tsw=t(~fswr);
%------------------------------------------------------------------------
```

```
theta=1/To;                    % explosive time constant in 's'
Pmax=10^9*Pmsw;                % Peak value of incident pressure wave at plate (Pa)
c=1500;                        % speed of velocity in water (m/s^2)
dw=1025;                       % density of the seawater in kg/m^3
Beta=dw*c*theta/mp;
%----------------------cavitation instant------------------------------
tcav=log(Beta)/(Beta-1)*theta; % 's'
%----------------------calculation of total pressure in front of the plate
Pt=10^-6*2*Pmax/(1-Beta)*(exp(-t/theta)-Beta*exp(-Beta*t/theta)); % 'Mpa'
cavitation=t>tcav;
Pt(cavitation)=-0.1;
%----------------------maximum velocity calculation---------------------
vpmax=2*Pmax/dw/c*Beta^(1/(1-Beta));                                % 'm/s'
%----------------------velocity calculation-----------------------------
vp=2*Pmax*theta/mp/(1-Beta)*(exp(-Beta*t/theta)-exp(-t/theta));     %velocity of
plate in 'm/s'
vp(cavitation)=vpmax-100000/mp*(t(cavitation)-tcav);
%----------------------plotting-----------------------------------------
figure(1)
subplot(3,1,1)
%----------------------plotting incident pressure-------------------------
plot(tsw,Psw,'b-');
grid on;
ylabel('\bf{Pi}\rm(Mpa)');
xlabel('\bf{t}\rm(s)');
legend('Incident Pressure versus time');
ttl=['Incident Pressure vs. time for ' num2str(m)  'kg of HBX-1 charge, standoff
distance of ' num2str(R) 'm'];
Title(ttl);
set(gca,'XMinorGrid','off')
set(gca,'XMinorTick','on')
set(gca,'XTick',tcav)
%----------------------plotting total pressure in front of the plate-------
subplot(3,1,2)
plot(t,Pt,'b-');
```

```
grid on;
ylabel('\bf{Pt}\rm(Mpa)');
xlabel('\bf{t}\rm(s)');
legend('Total Pressure versus time');
ttl=['Total pressure on platform vs. time for ' num2str(m)  'kg of HBX-1 charge,
standoff distance of ' num2str(R) 'm'];
Title(ttl);
set(gca,'XMinorGrid','off')
set(gca,'XMinorTick','on')
set(gca,'XTick',tcav)
%------------------------plotting platform velocity----------------------
subplot(3,1,3)
plot(t,vp,'r-');
grid on;
ylabel('\bf{vp}\rm(m/s)');
xlabel('\bf{t}\rm(s)');
legend('Platform velocity versus time');
ttl=['velocity of platform vs. time for ' num2str(m)  'kg of HBX-1 charge, standoff
distance of ' num2str(R) 'm'];
Title(ttl);
set(gca,'XMinorGrid','off')
set(gca,'XMinorTick','on')
set(gca,'XTick',tcav)
```

D. Response Comparison of Damped and Undamped Cases of Coarsened Structural Model

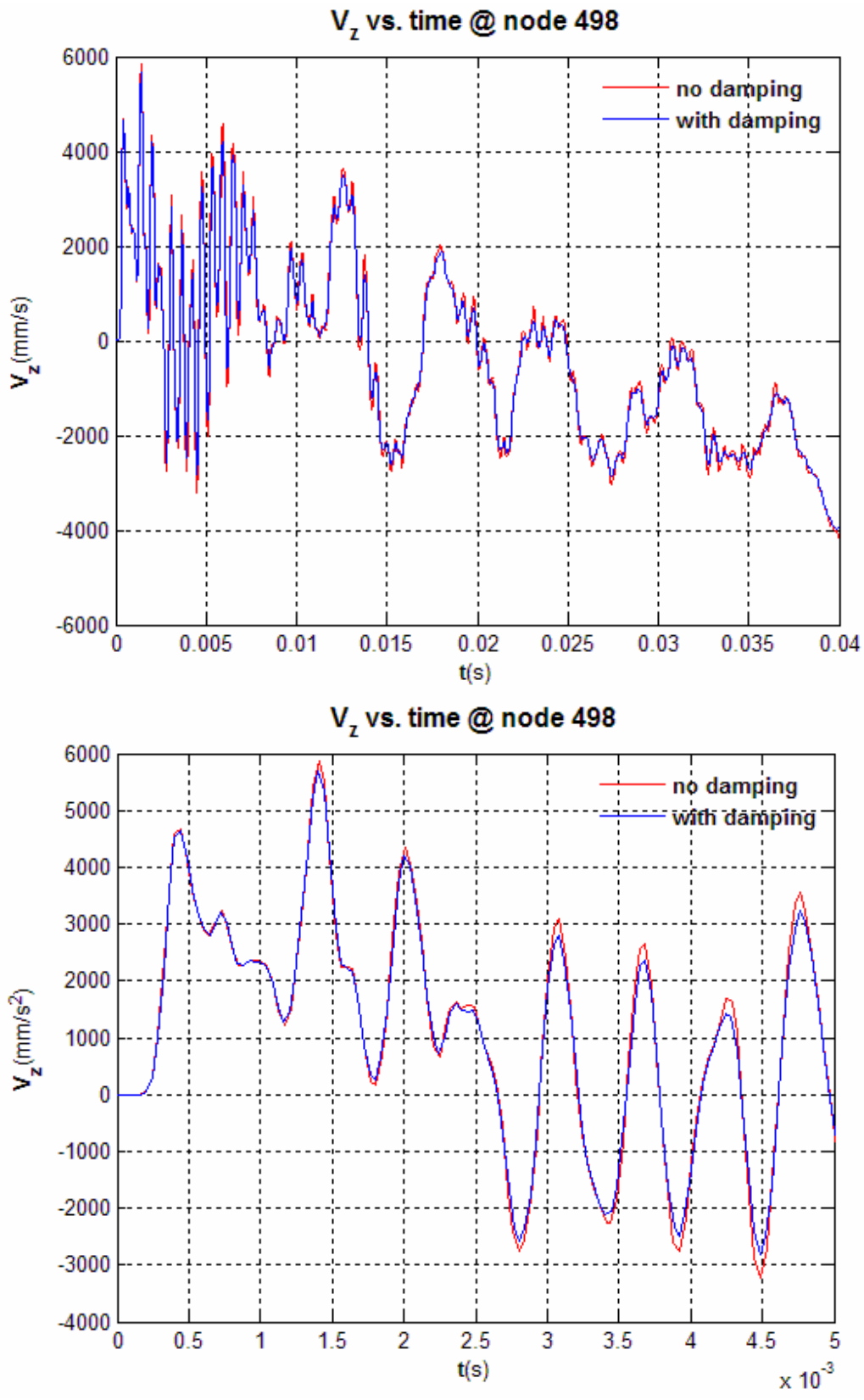

Figure D.1 : Vertical (Z Direction) Velocity at Node 498.

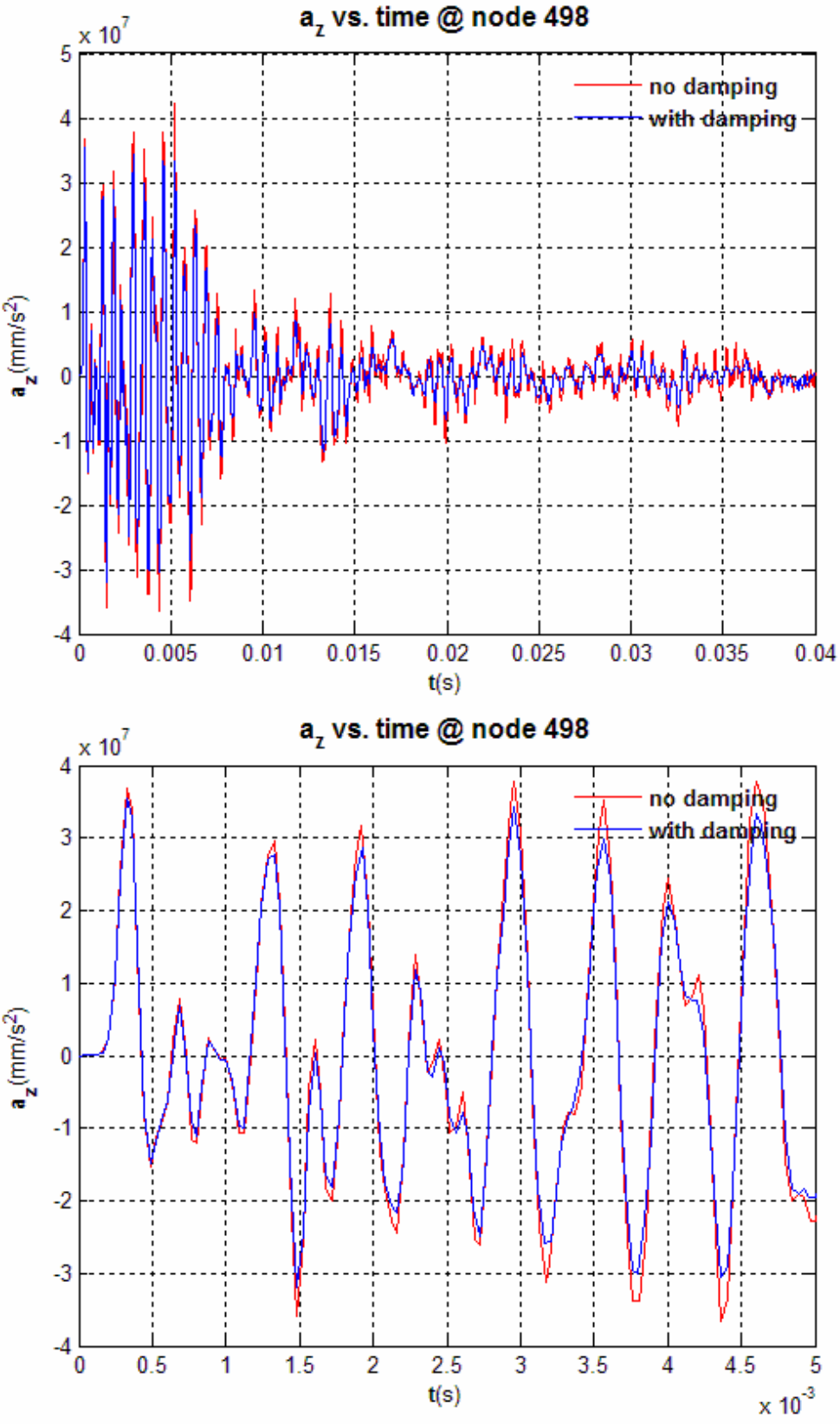

Figure D.2 : Vertical (Z Direction) Acceleration at Node 498.

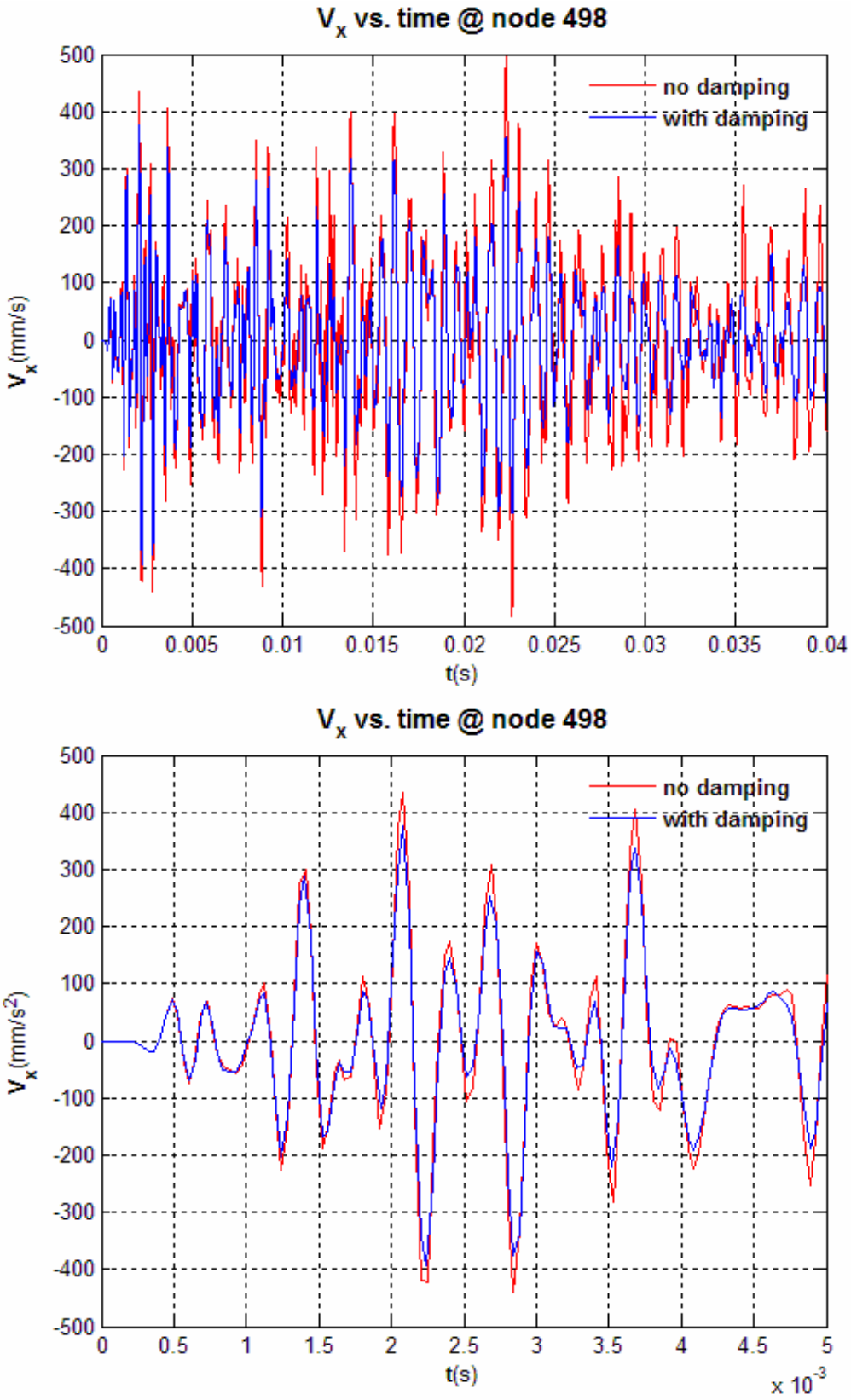

Figure D.3 : X Direction Velocity at Node 498.

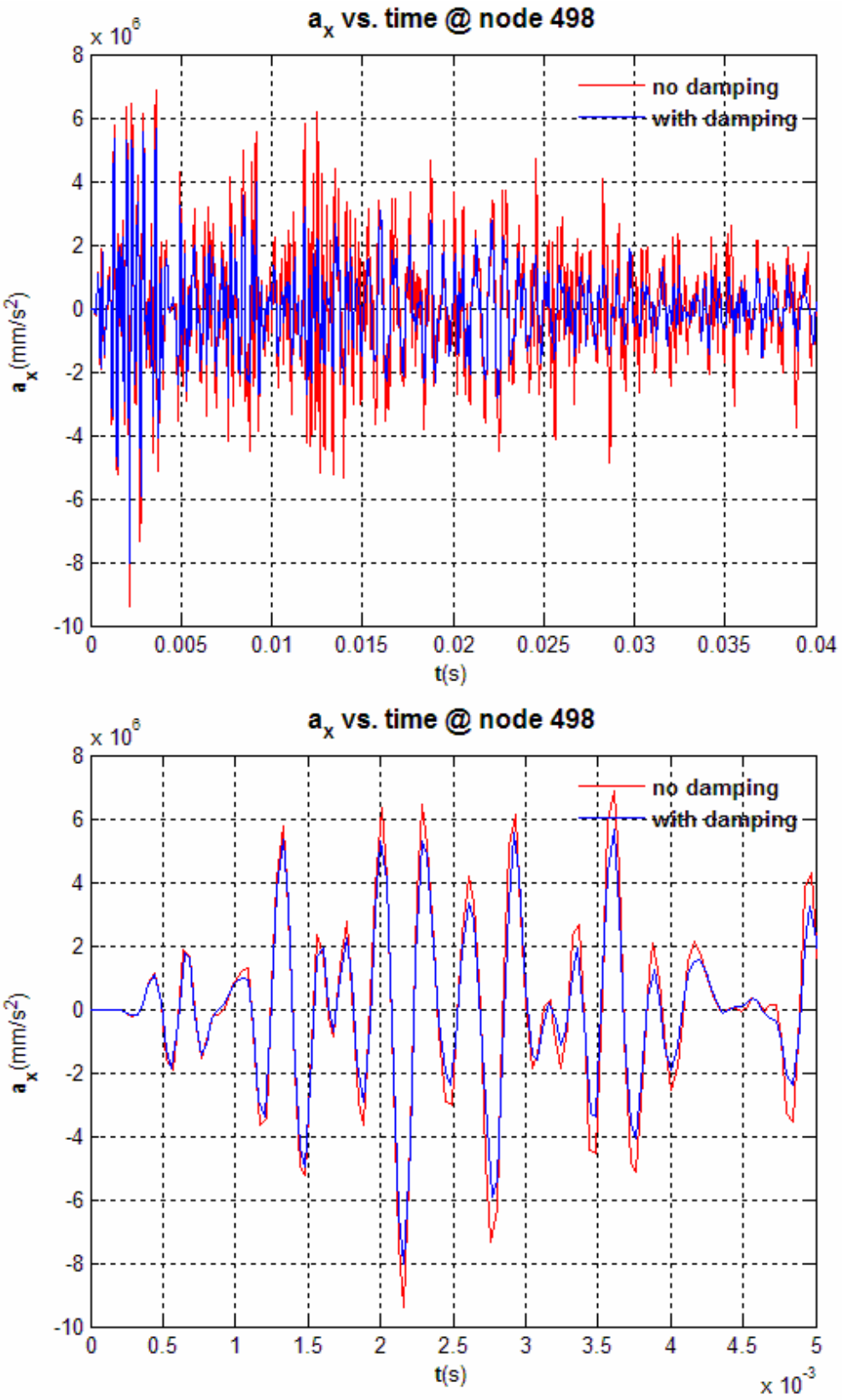

Figure D.4 : X Direction Acceleration at Node 498.

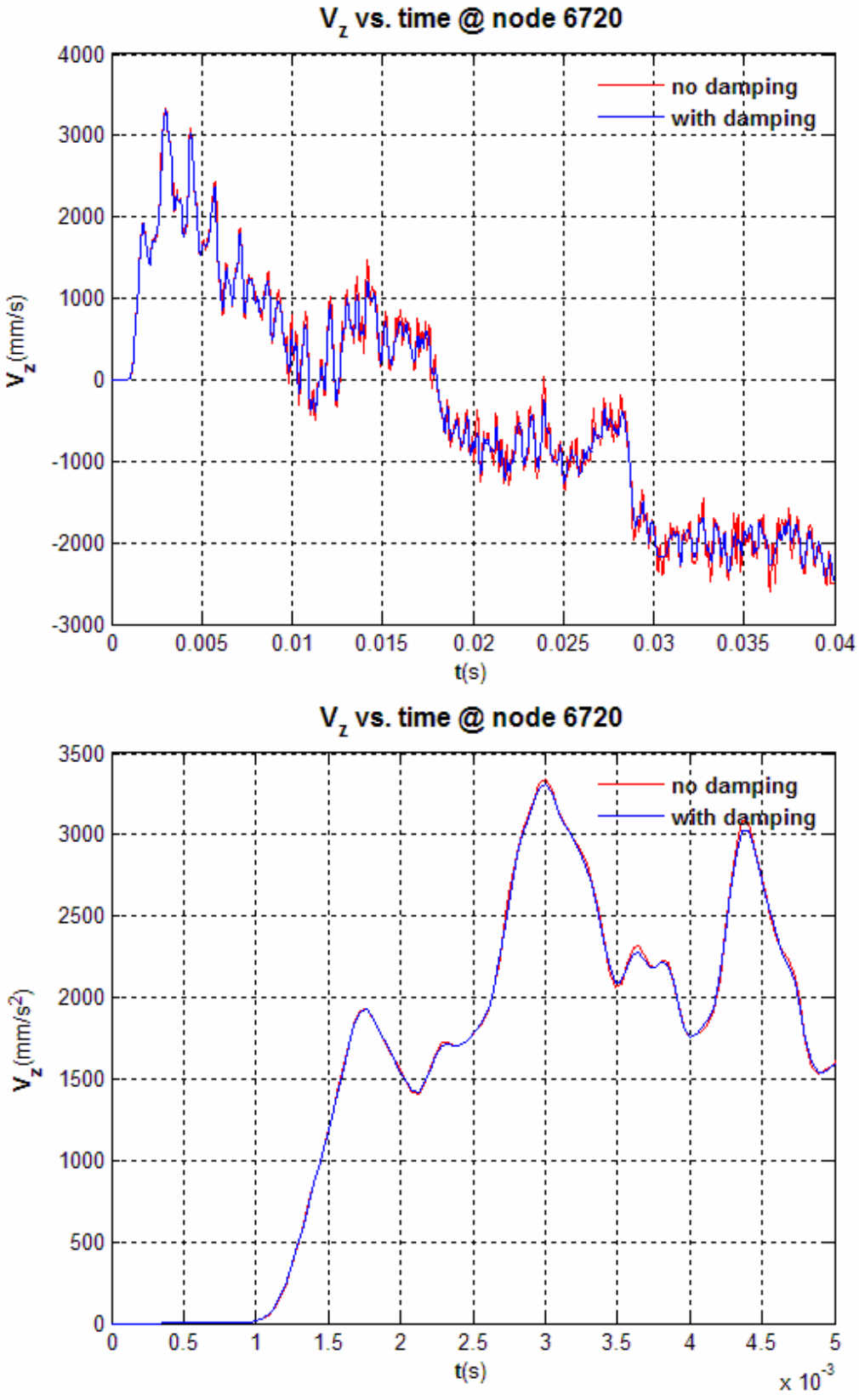

Figure D.5 : Vertical (Z Direction) Velocity at Node 6720.

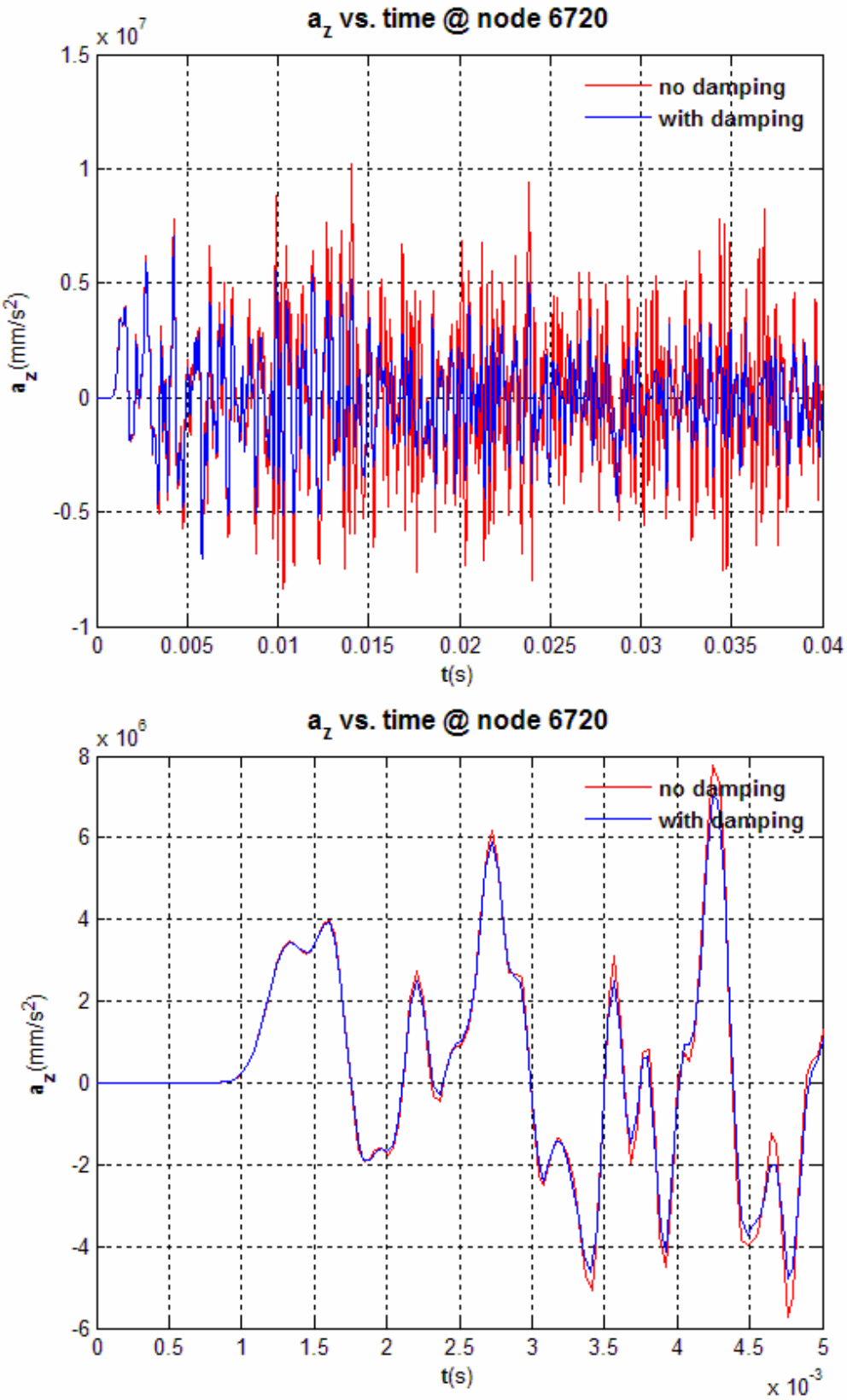

Figure D.6 : Vertical (Z Direction) Acceleration at Node 6720.

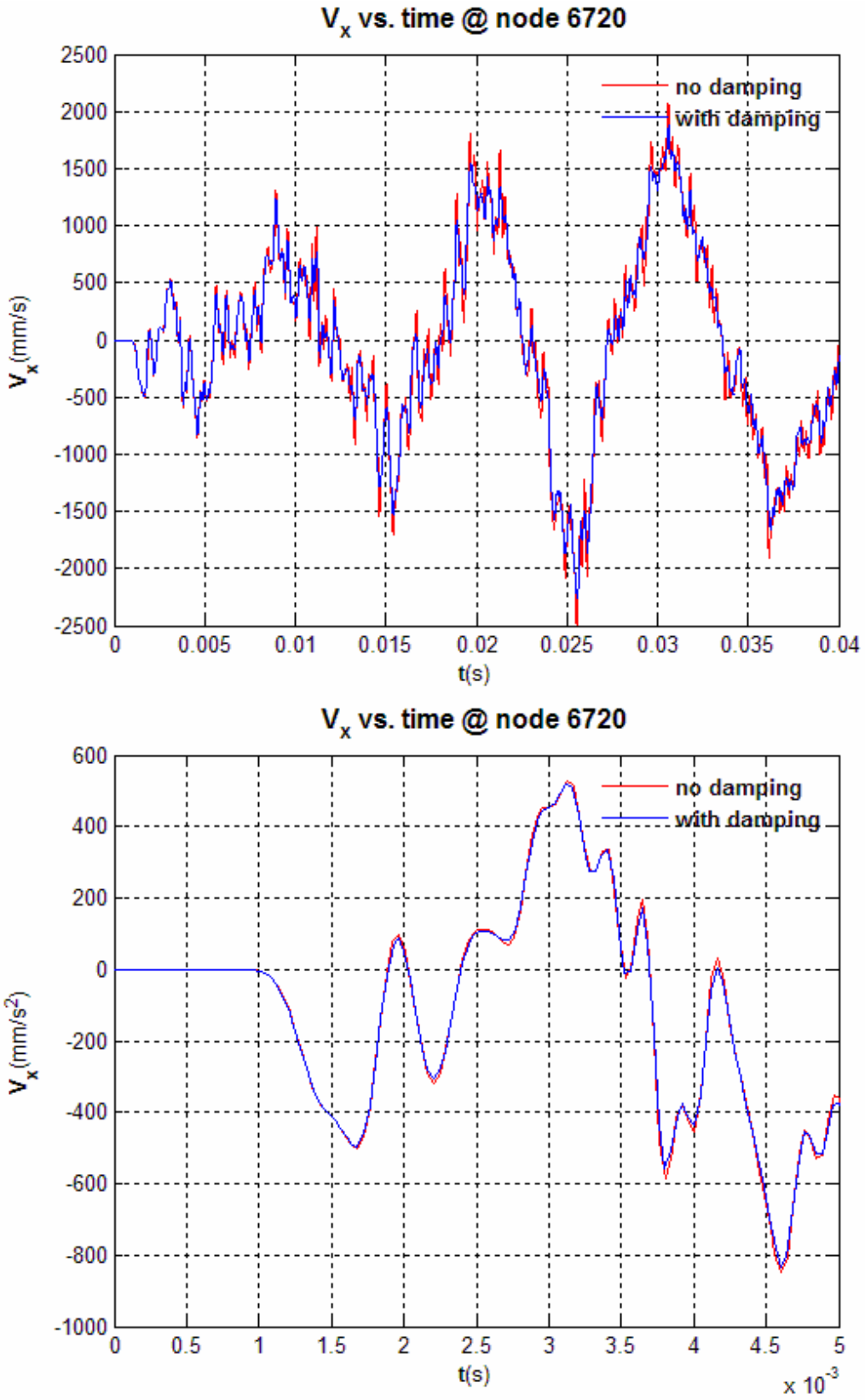

Figure D.7 : X Direction Velocity at Node 6720.

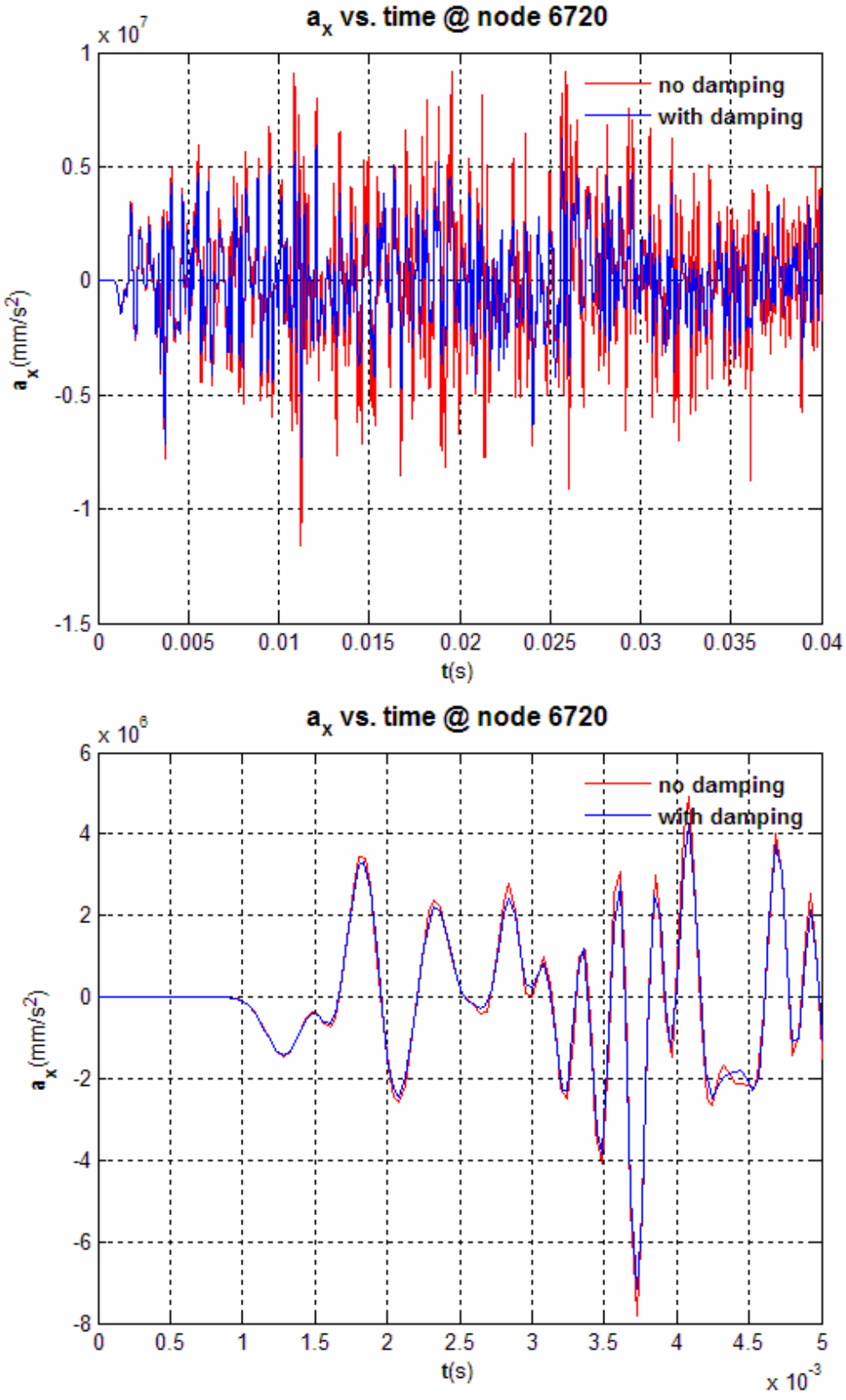

Figure D.8 : X Direction Acceleration at Node 6720.

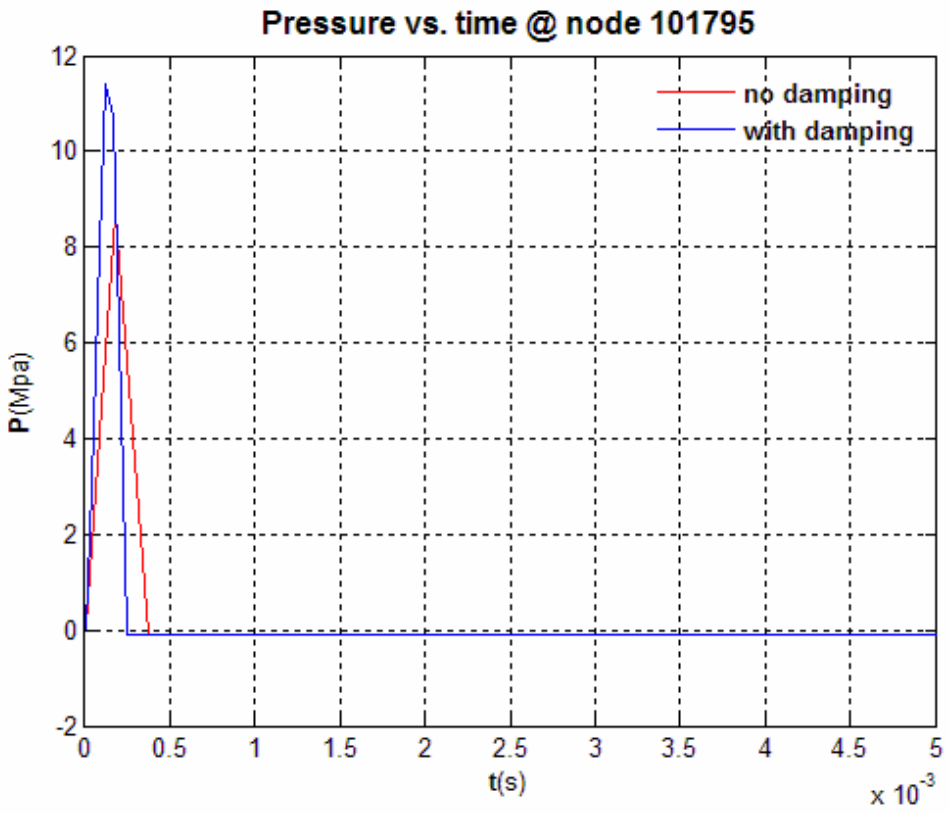

Figure D.9 : Pressure vs. Time Under Keel at Node 101795.

E. Response Comparison of Refined and Coarse Fluid Models

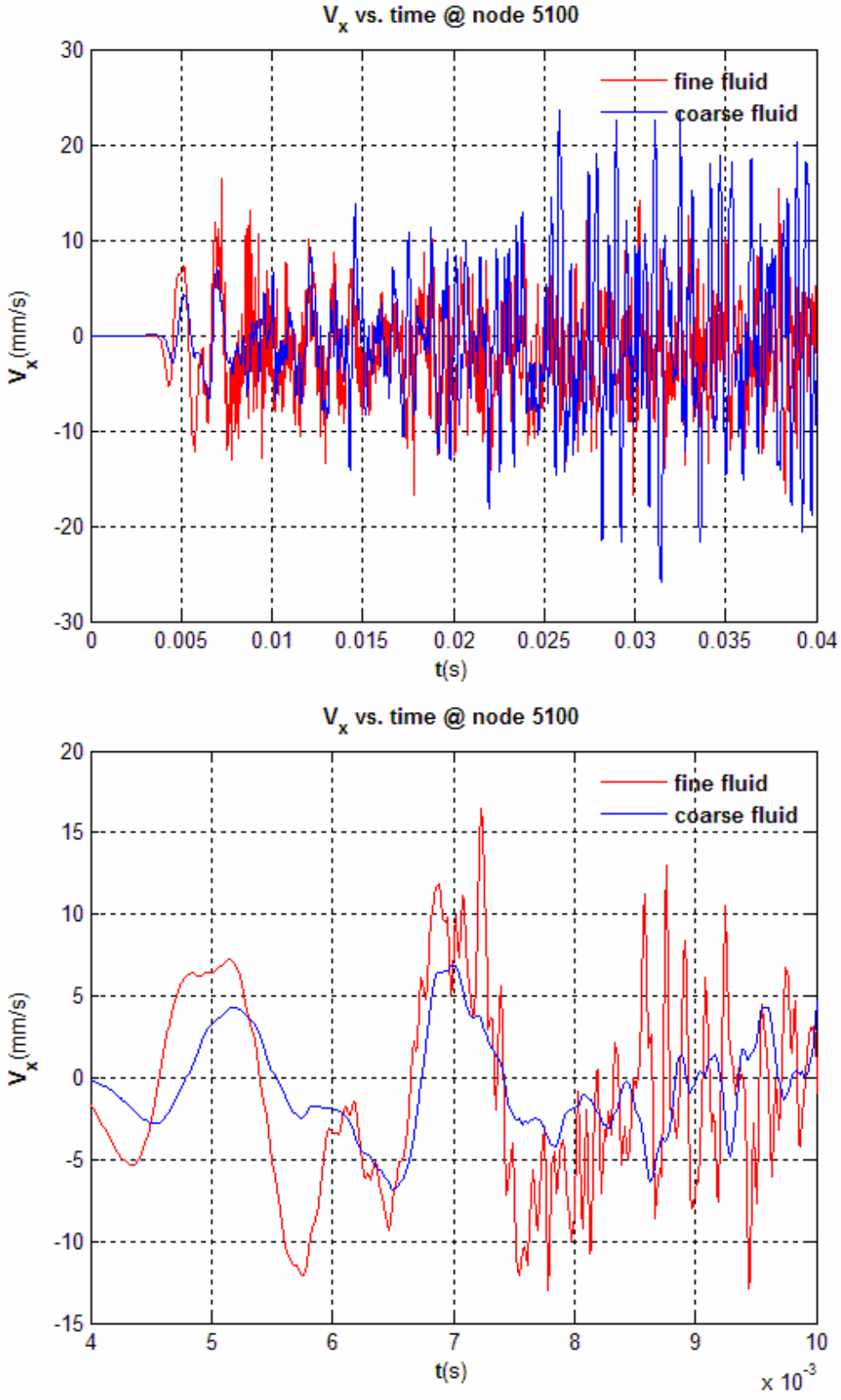

Figure E.1 : X Direction Velocity at Node 5100.

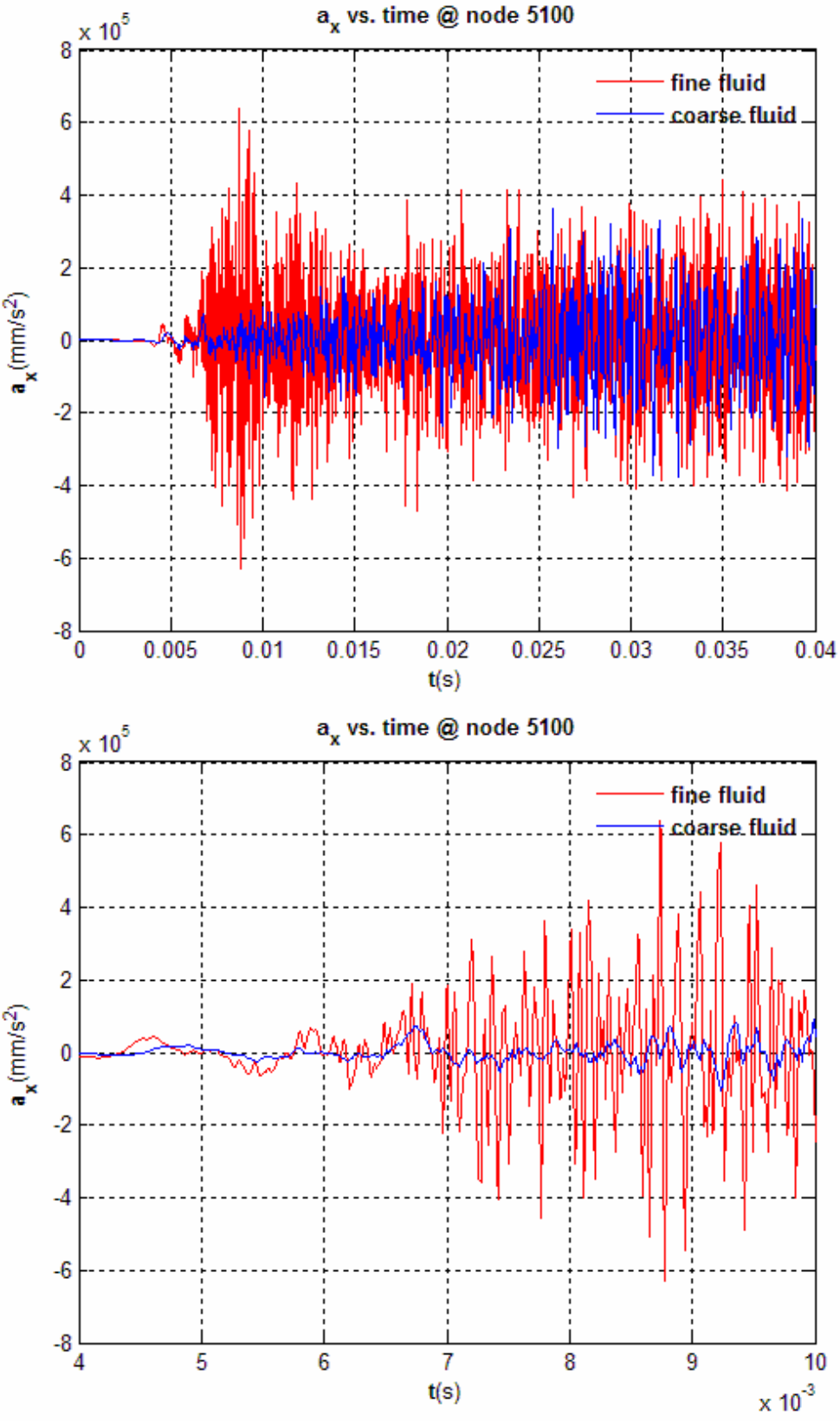

Figure E.2 : X Direction Acceleration at Node 5100.

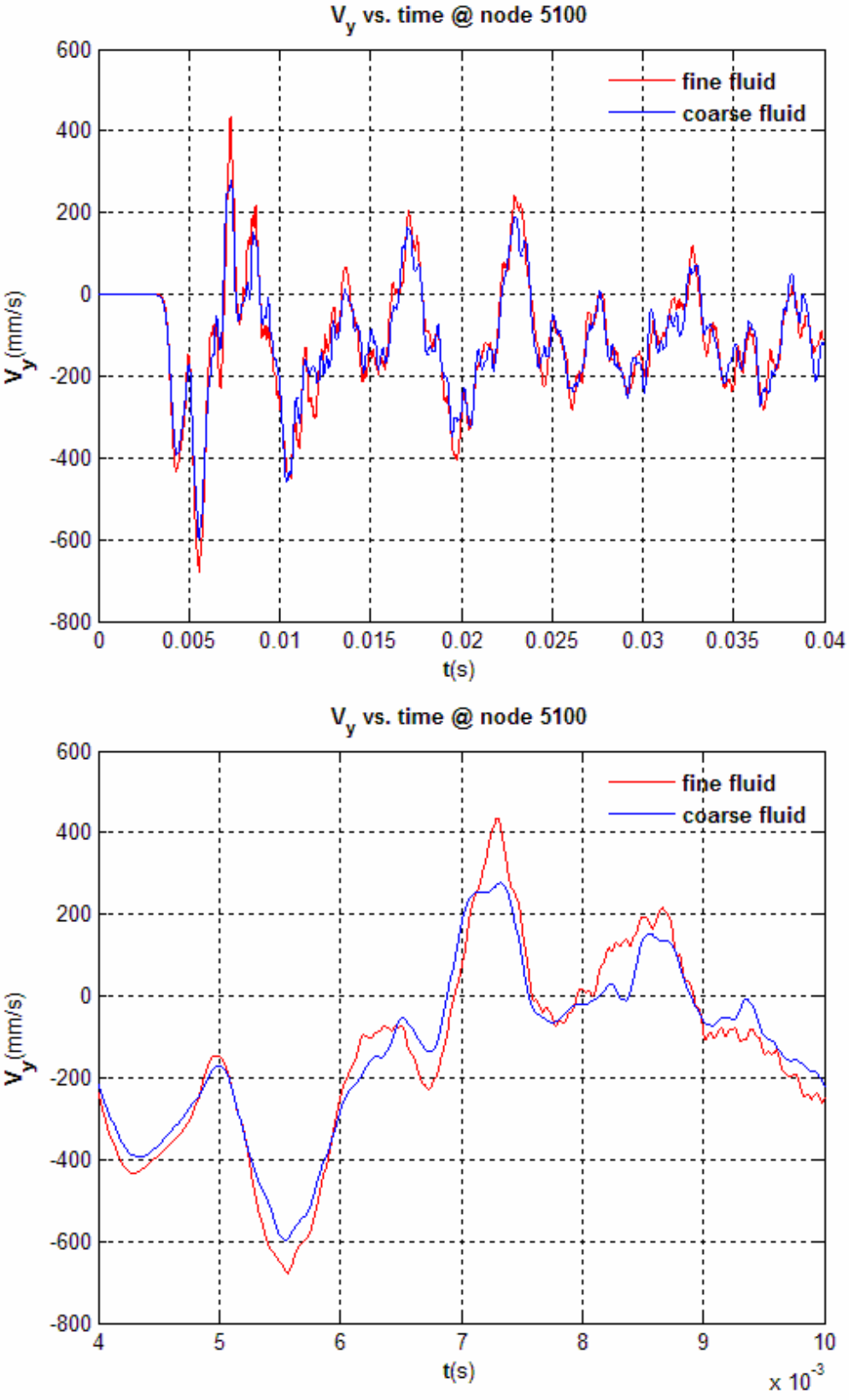

Figure E.3 : Y Direction Velocity at Node 5100.

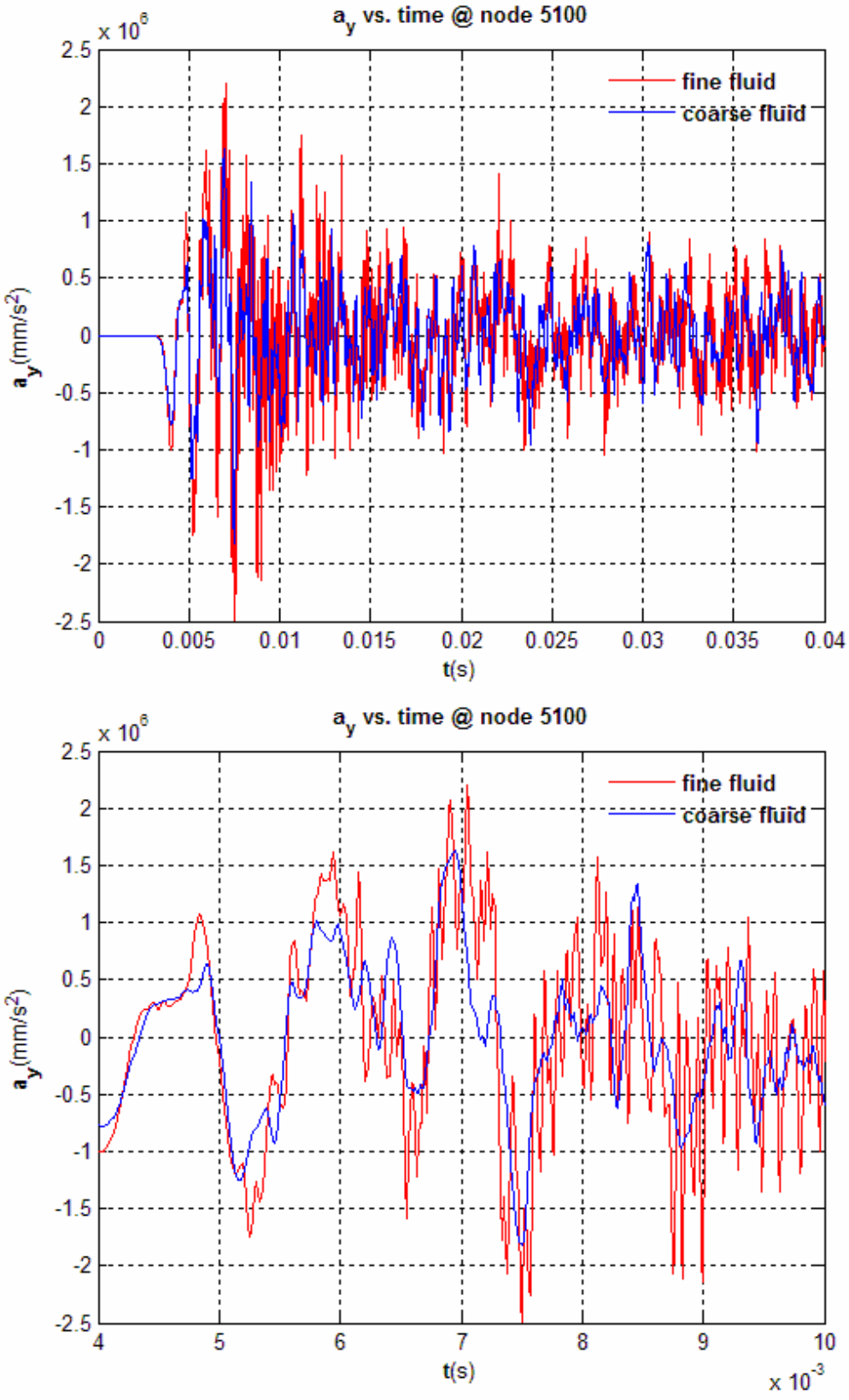

Figure E.4 : Y Direction Acceleration at Node 5100.

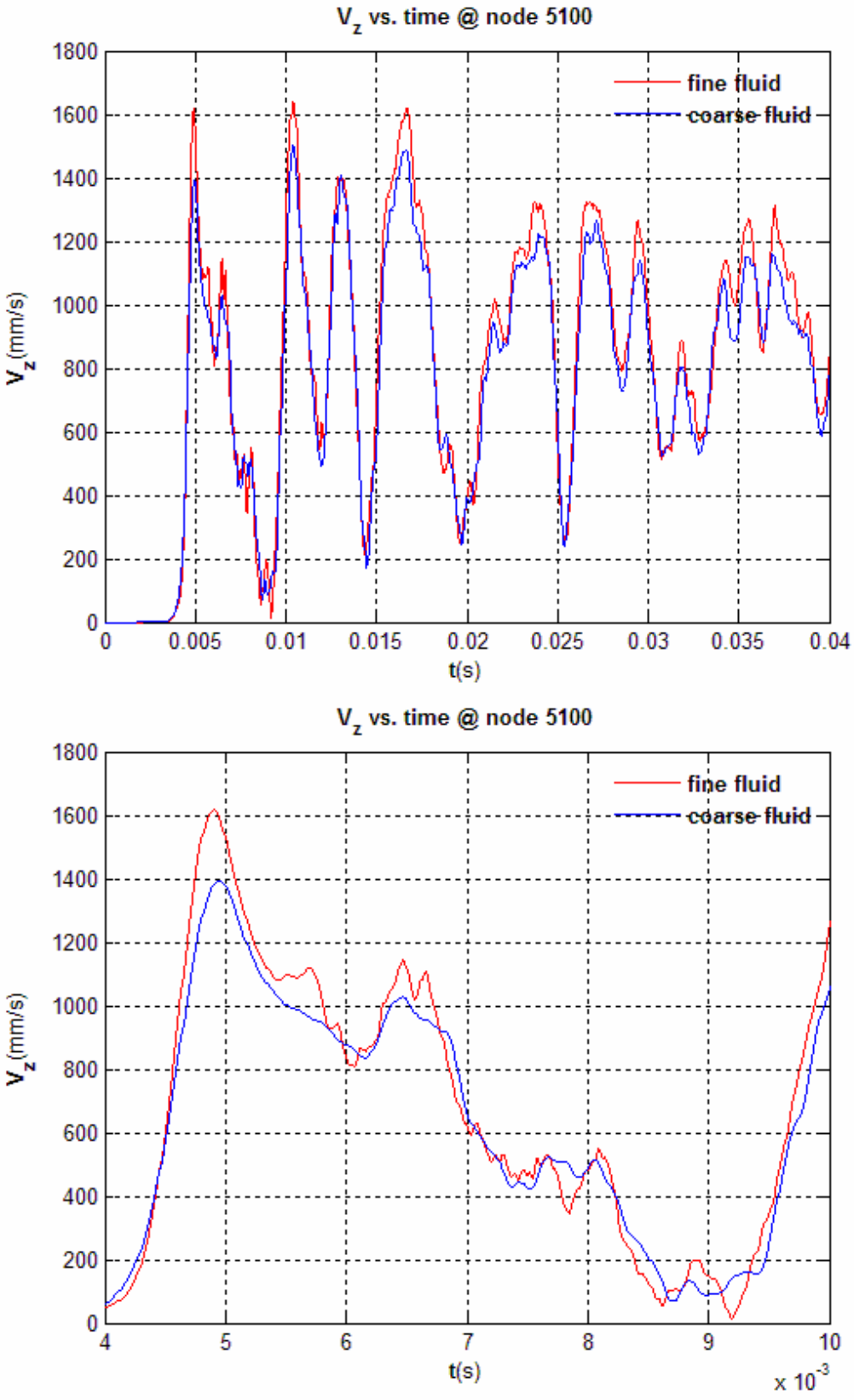

Figure E.5 : Vertical (Z Direction) Velocity at Node 5100.

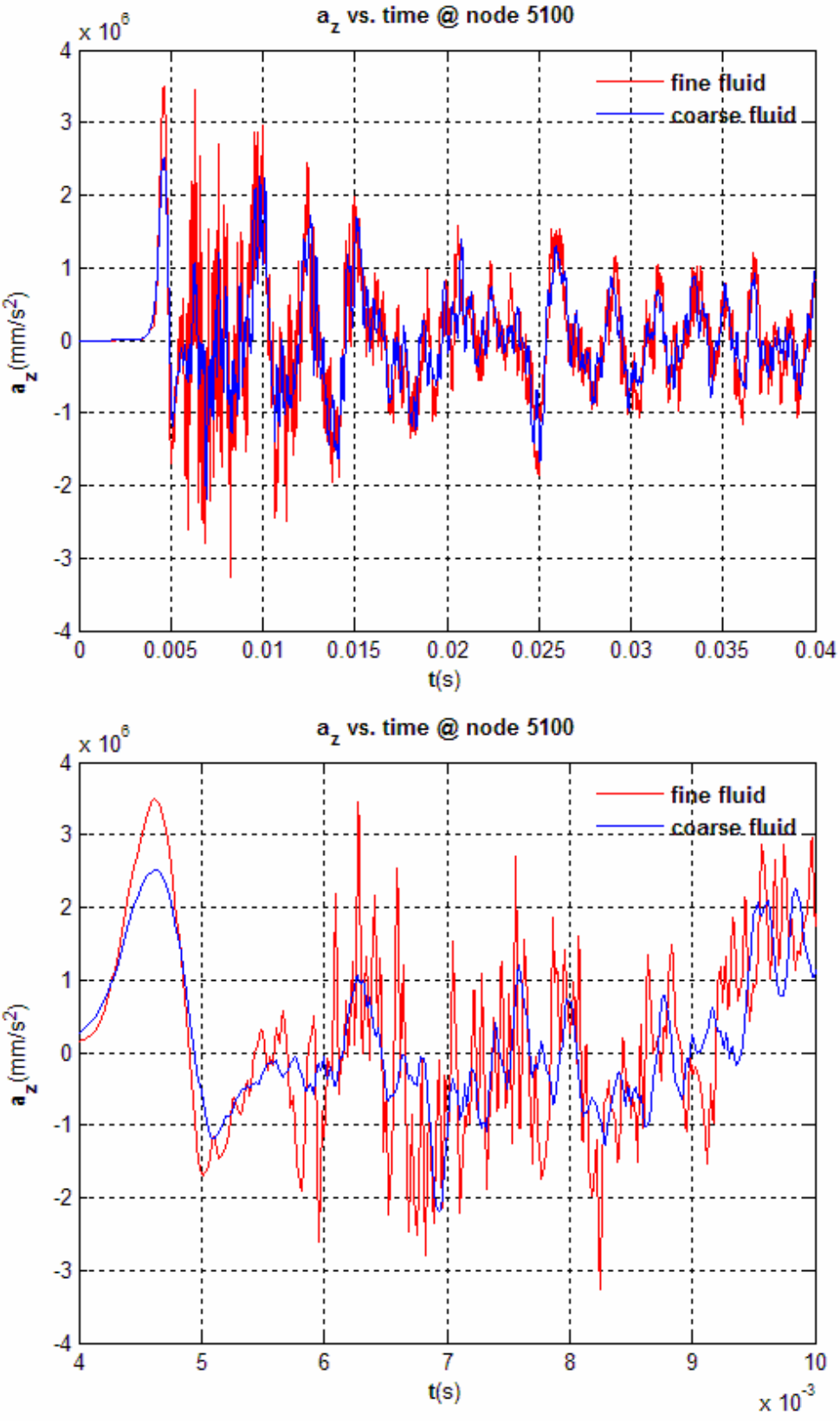

Figure E.6 : Vertical (Z Direction) Acceleration at Node 5100.

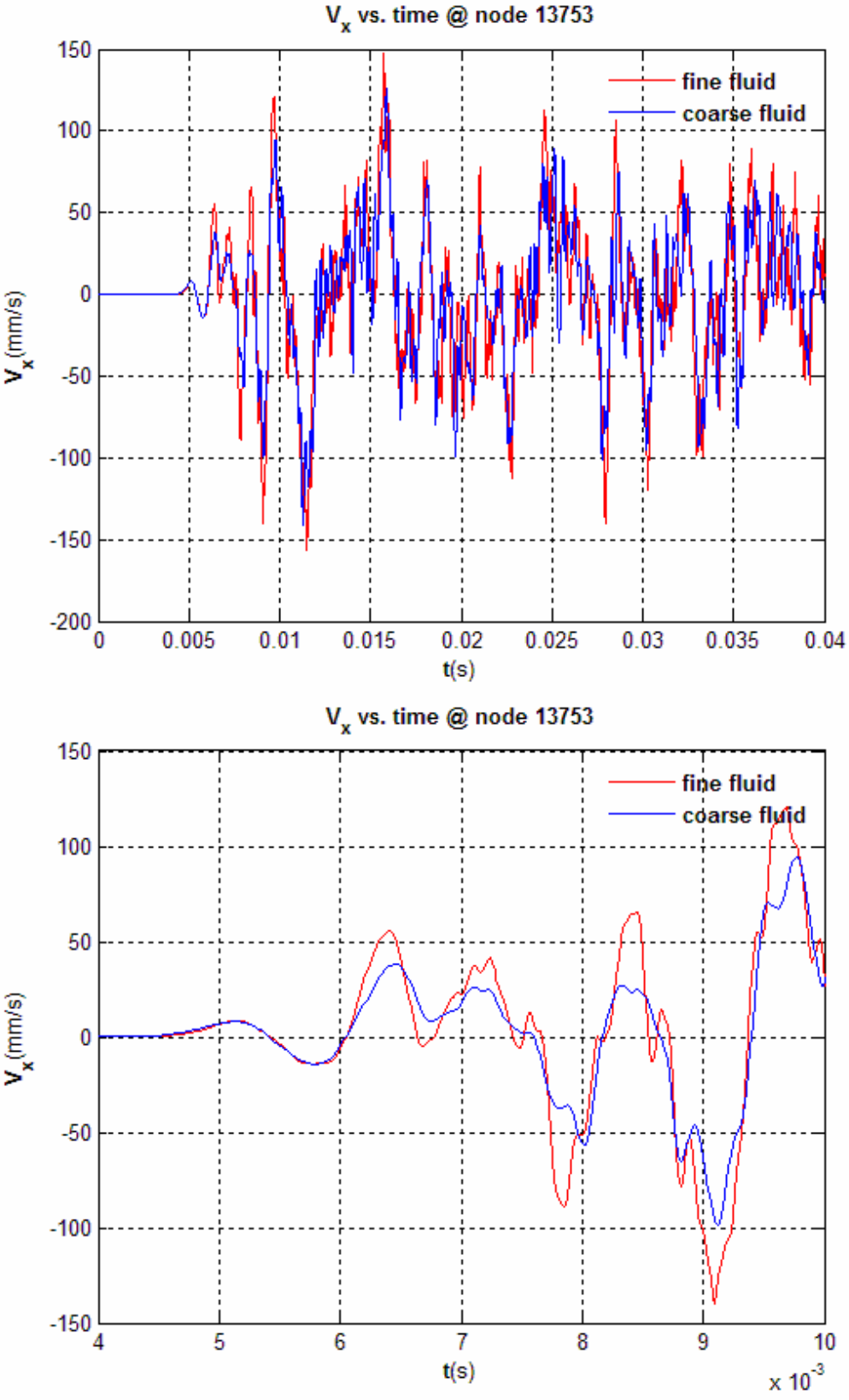

Figure E.7 : X Direction Velocity at Node 13753.

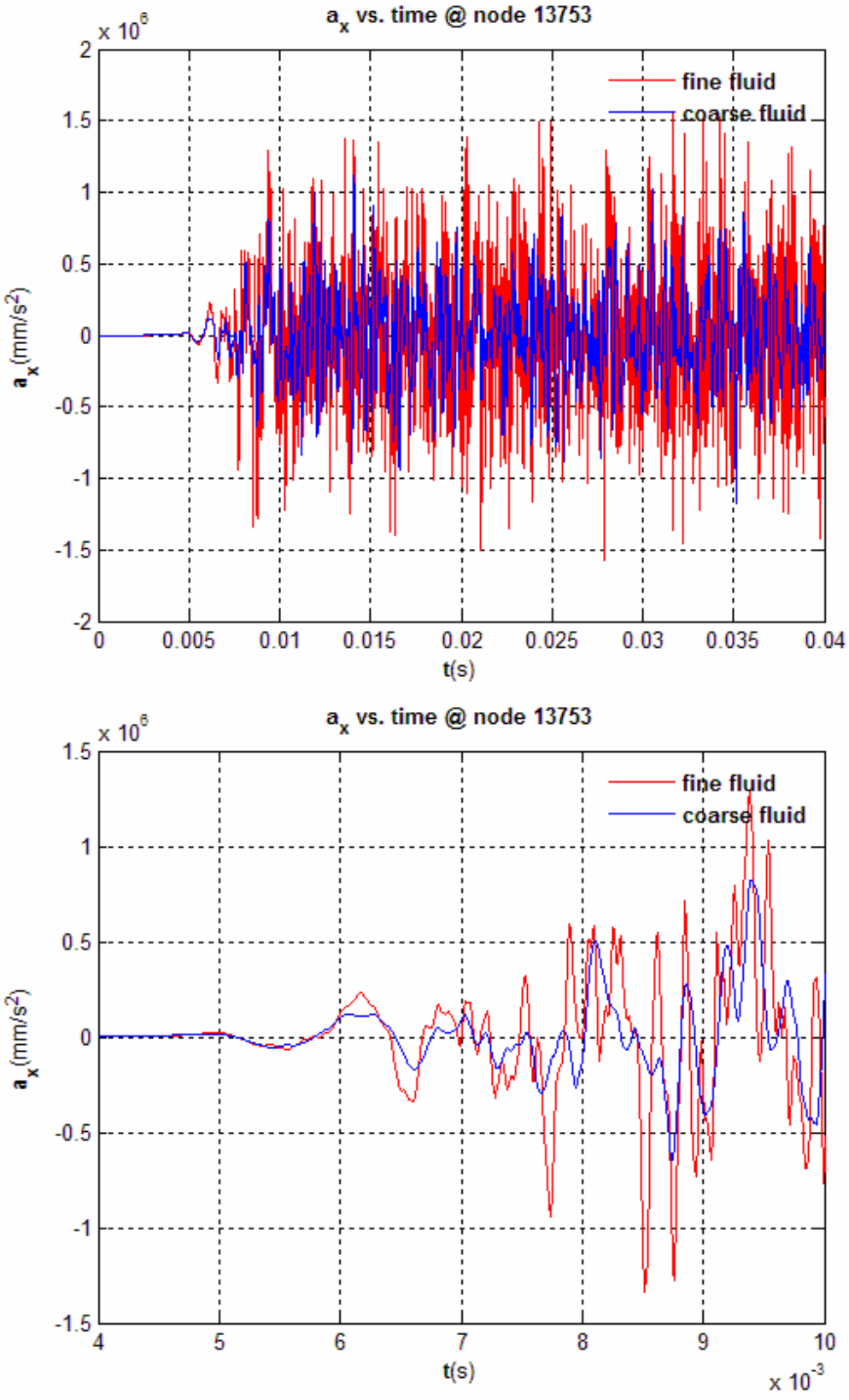

Figure E.8 : X Direction Acceleration at Node 13753.

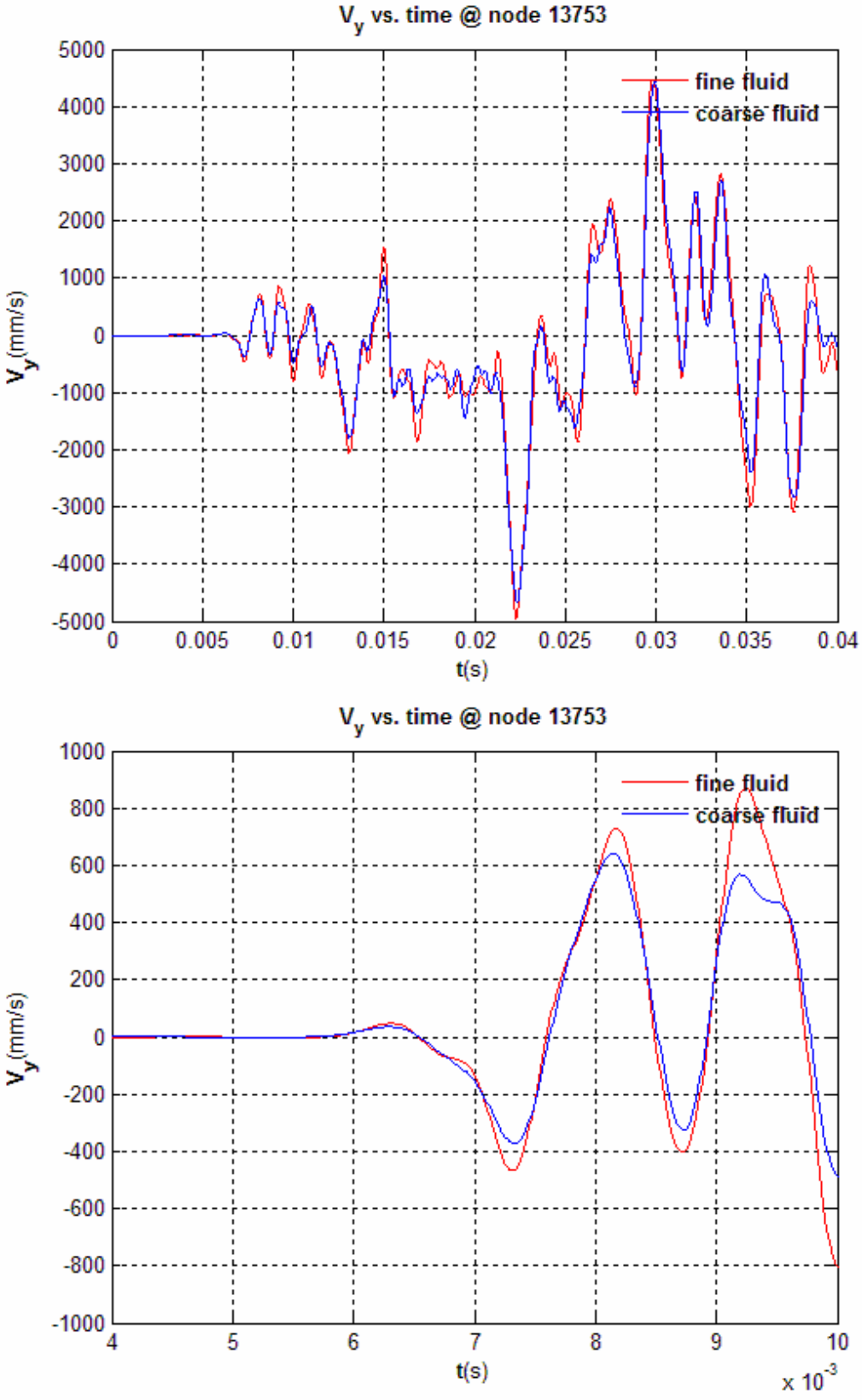

Figure E.9 : Y Direction Velocity at Node 13753.

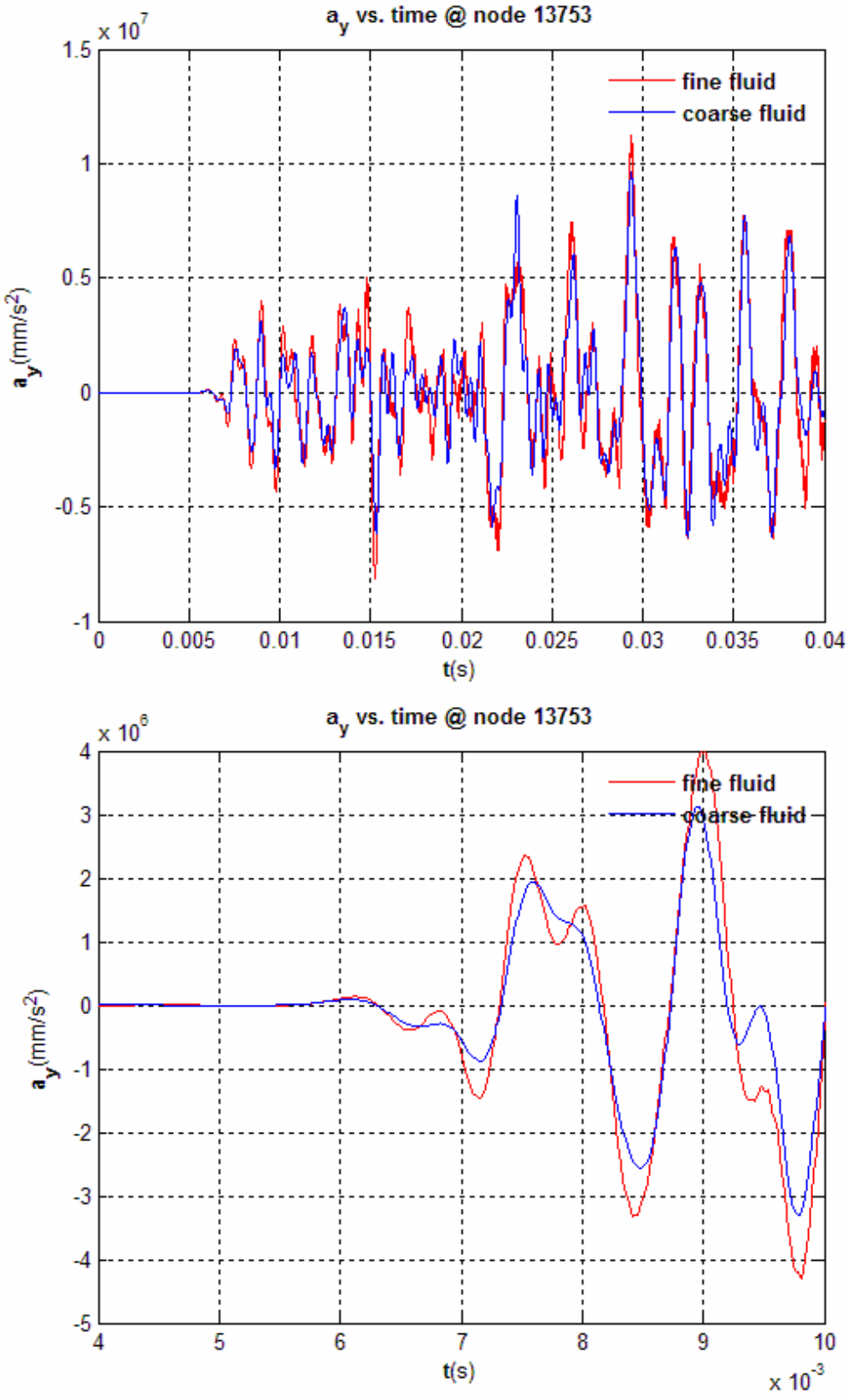

Figure E.10 : Y Direction Acceleration at Node 13753.

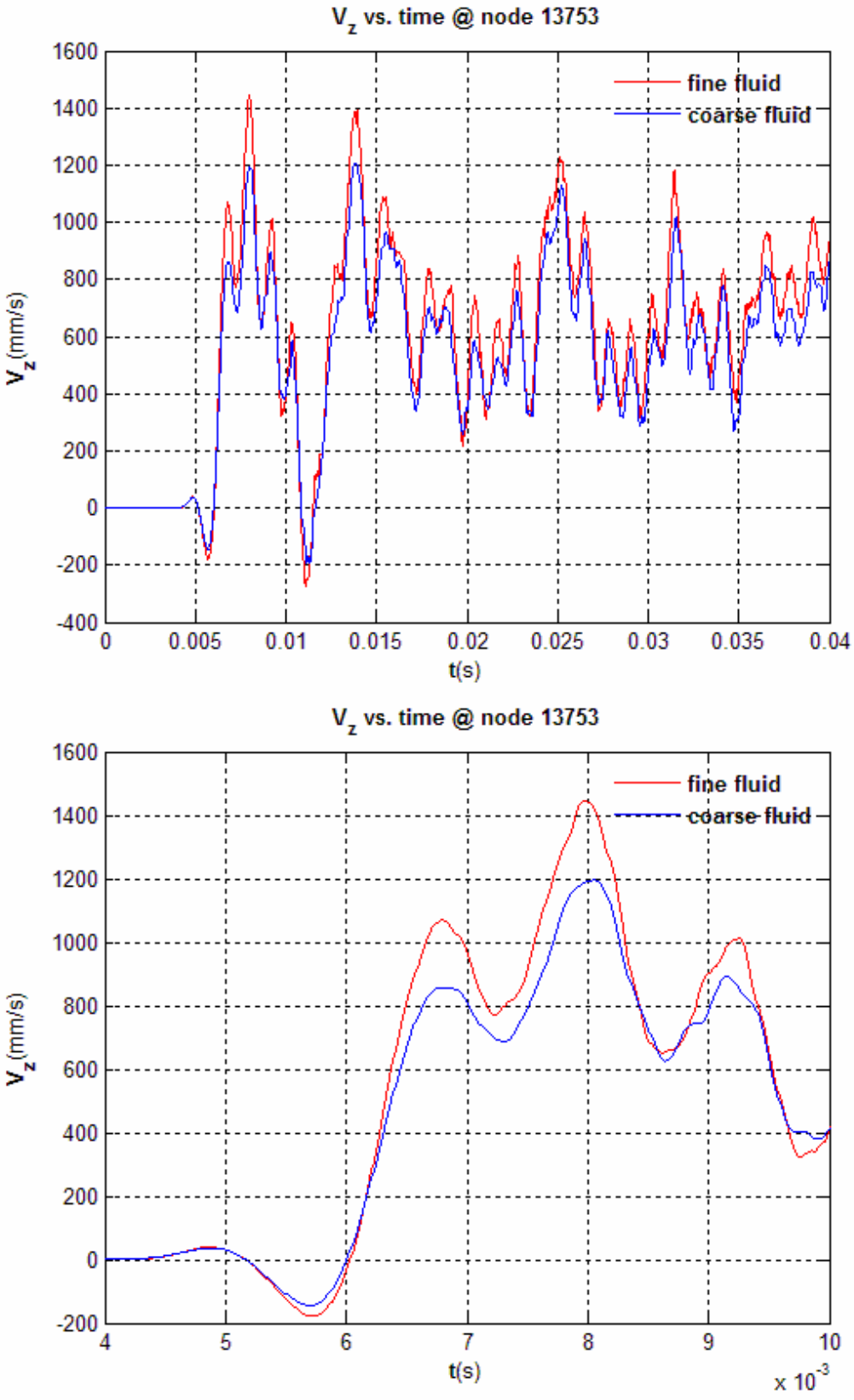

Figure E.11 : Z Direction Velocity at Node 13753.

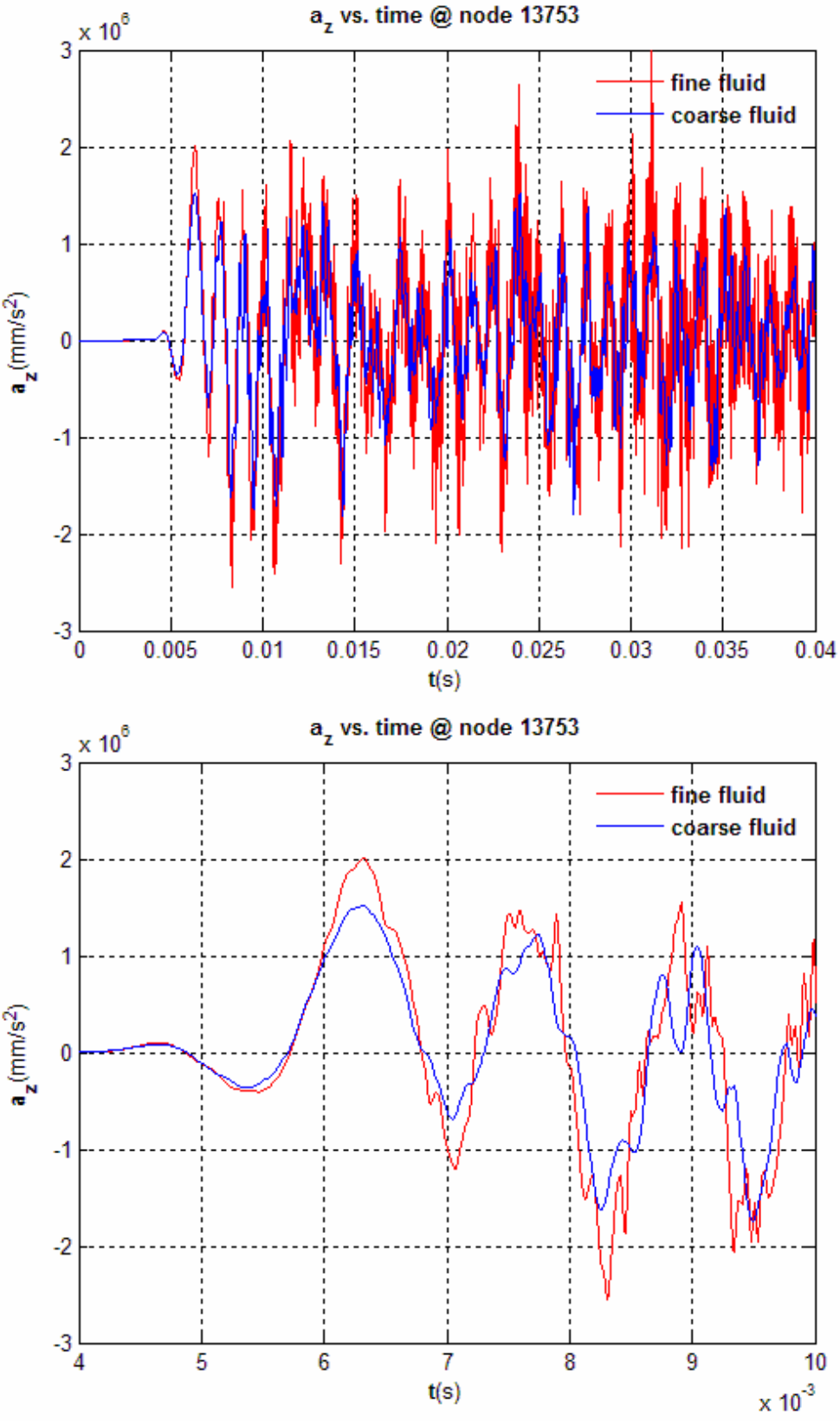

Figure E.12 : Z Direction Acceleration at Node 13753.

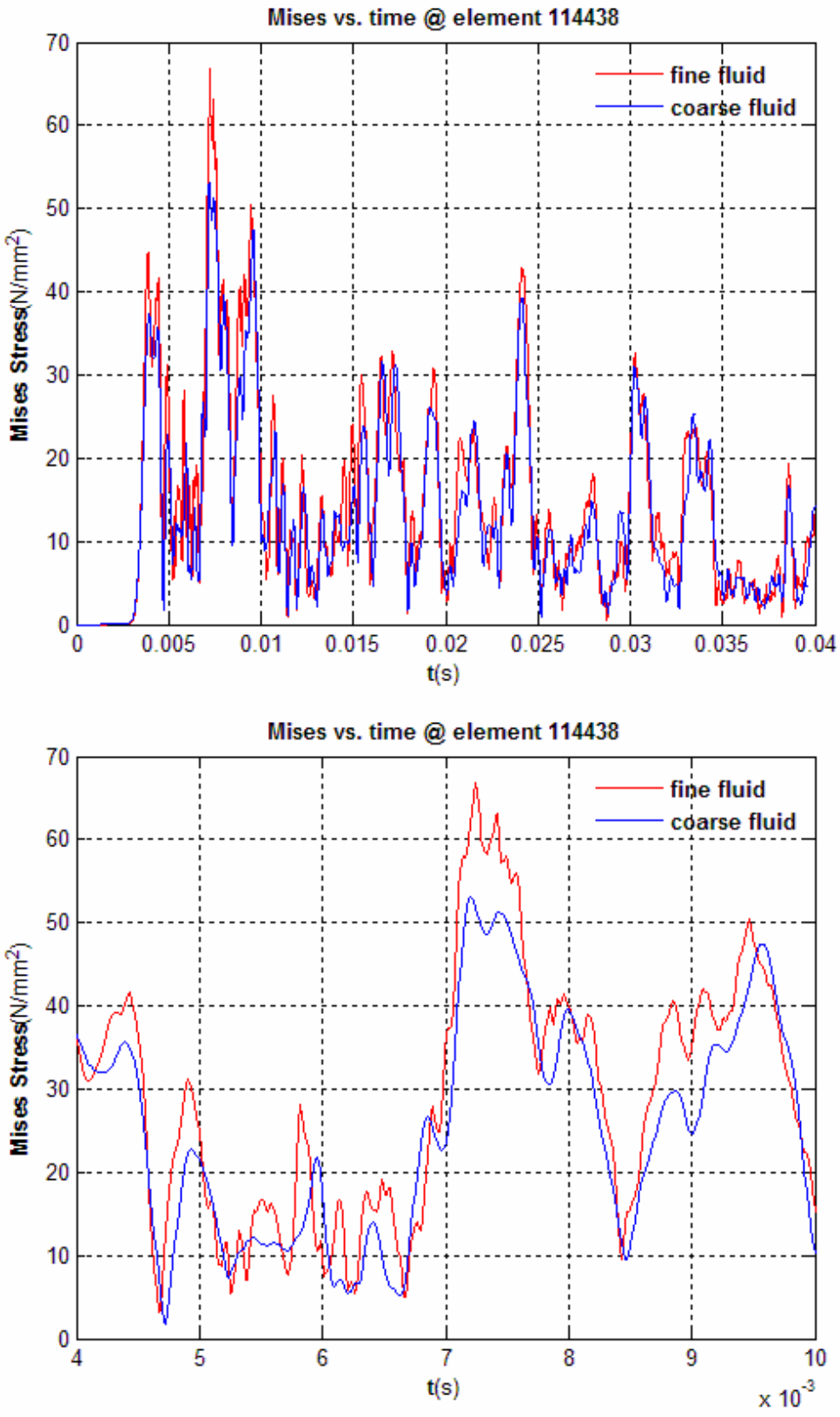

Figure E.13 : Equivalent Von Mises Stress at Element 114438.

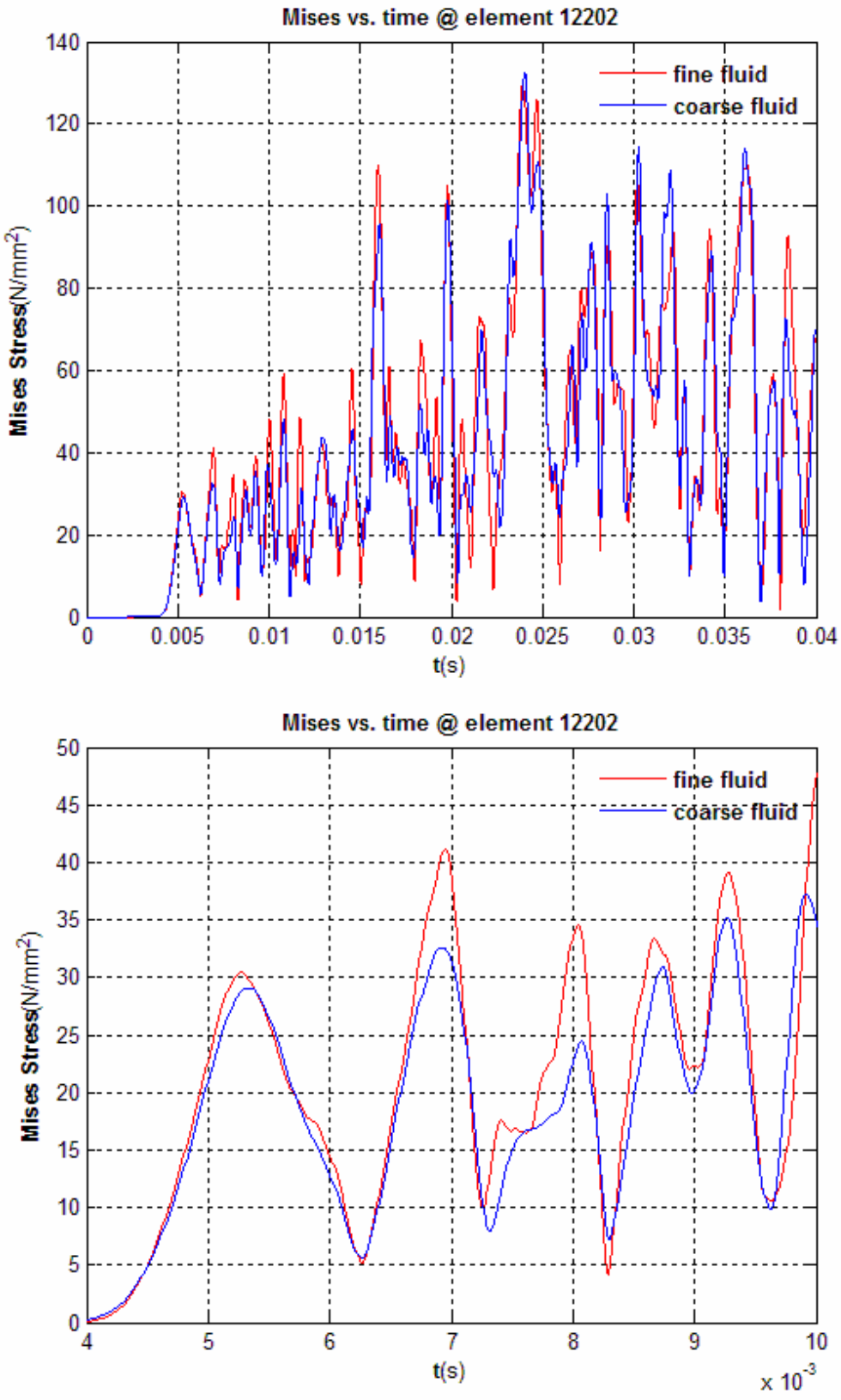

Figure E.14 : Equivalent Von Mises Stress at Element 12202.

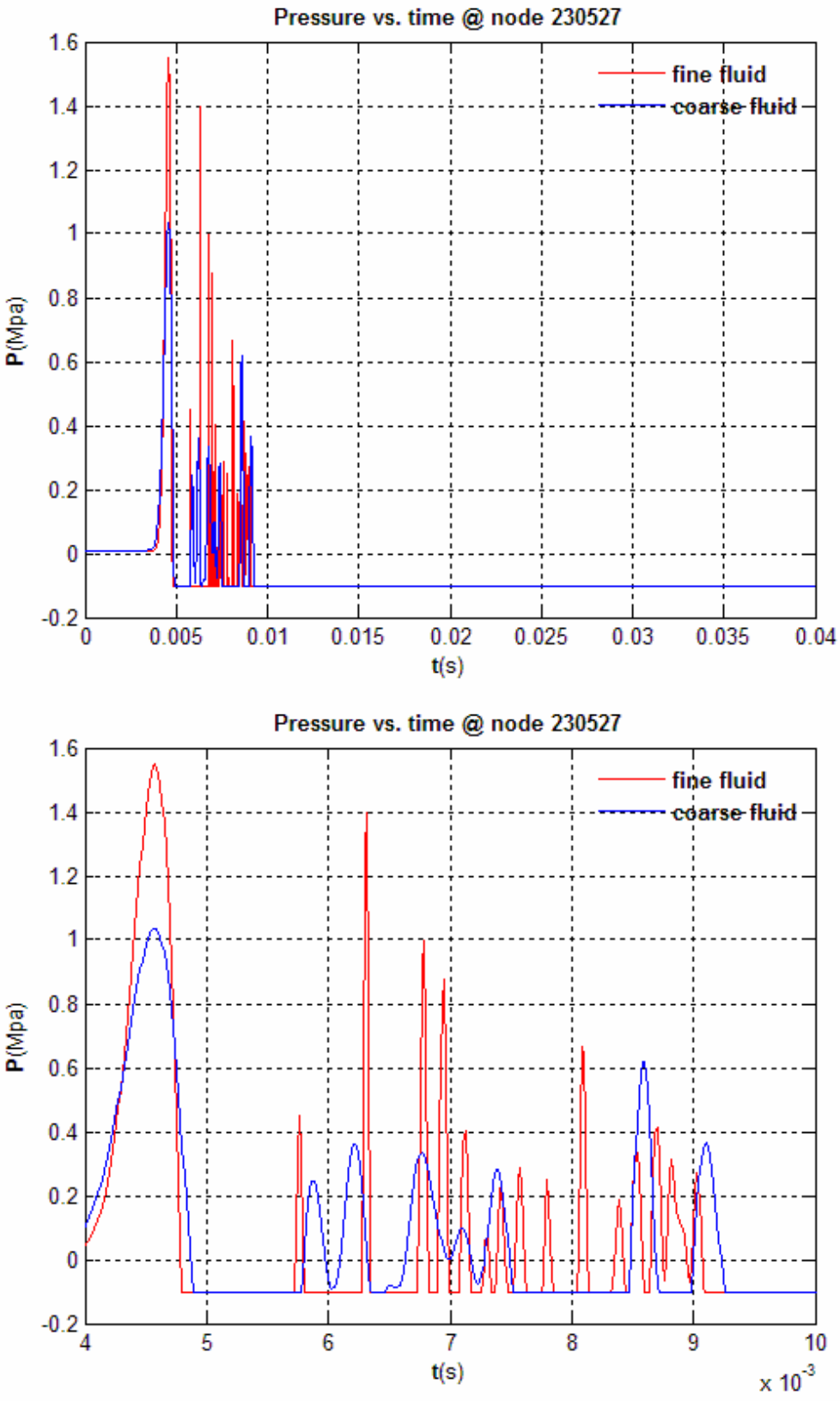

Figure E.15 : Pressure vs. Time Under Keel at Node 230527.

F. Response Comparison of Linear and Nonlinear (Cavitating) Fluids

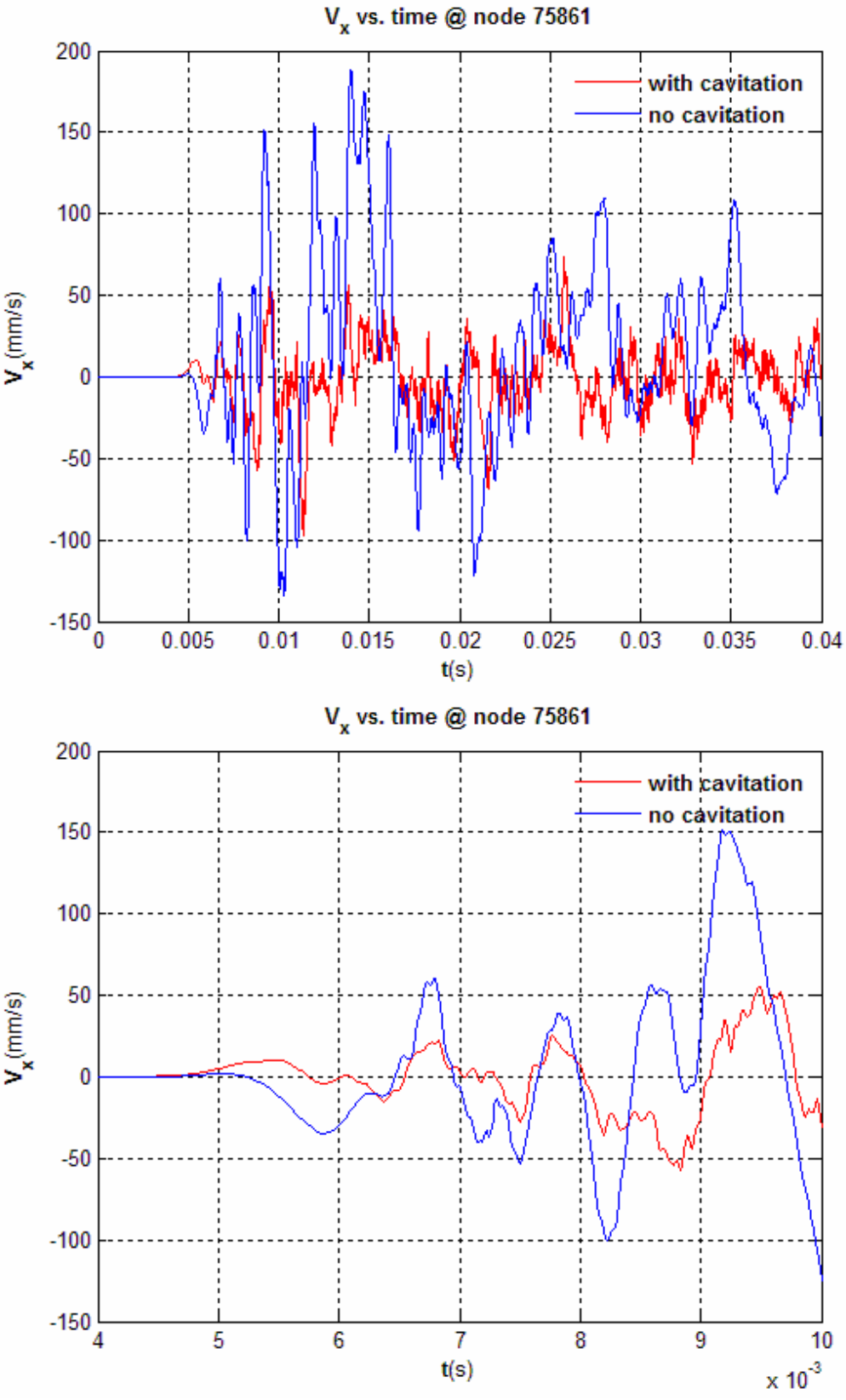

Figure F.1 : X Direction Velocity at Node 75861.

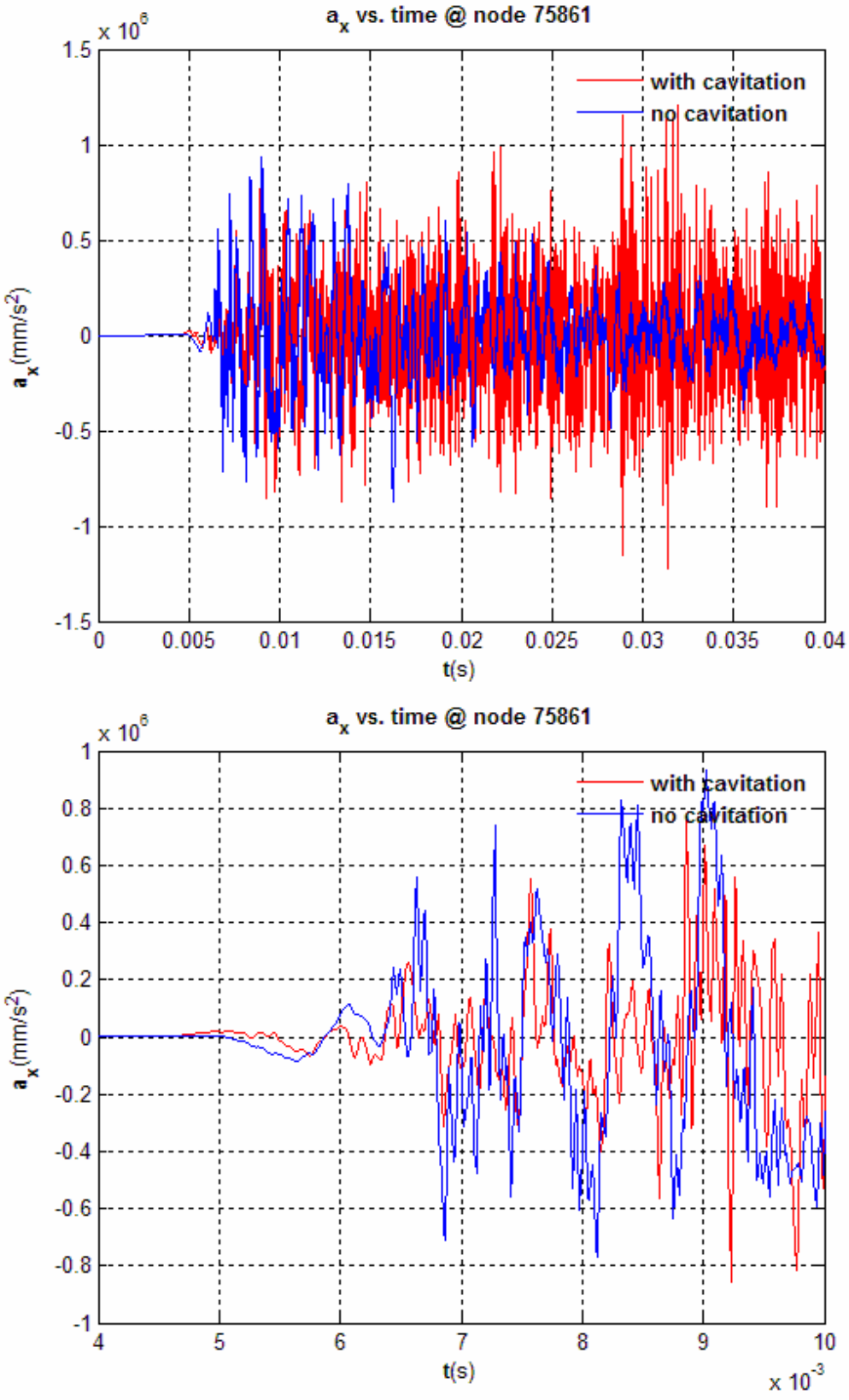

Figure F.2 : X Direction Acceleration at Node 75861.

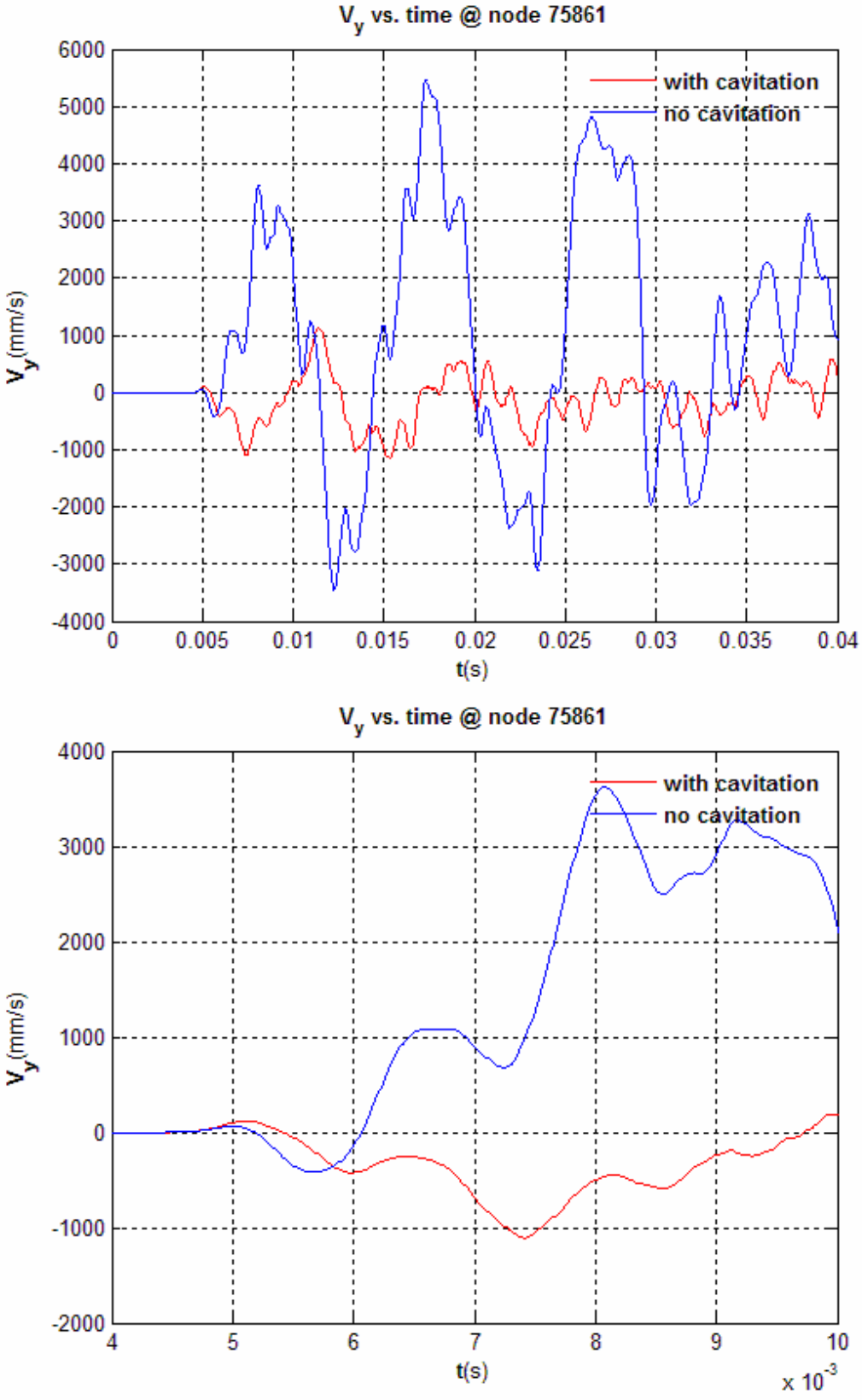

Figure F.3 : Y Direction Velocity at Node 75861.

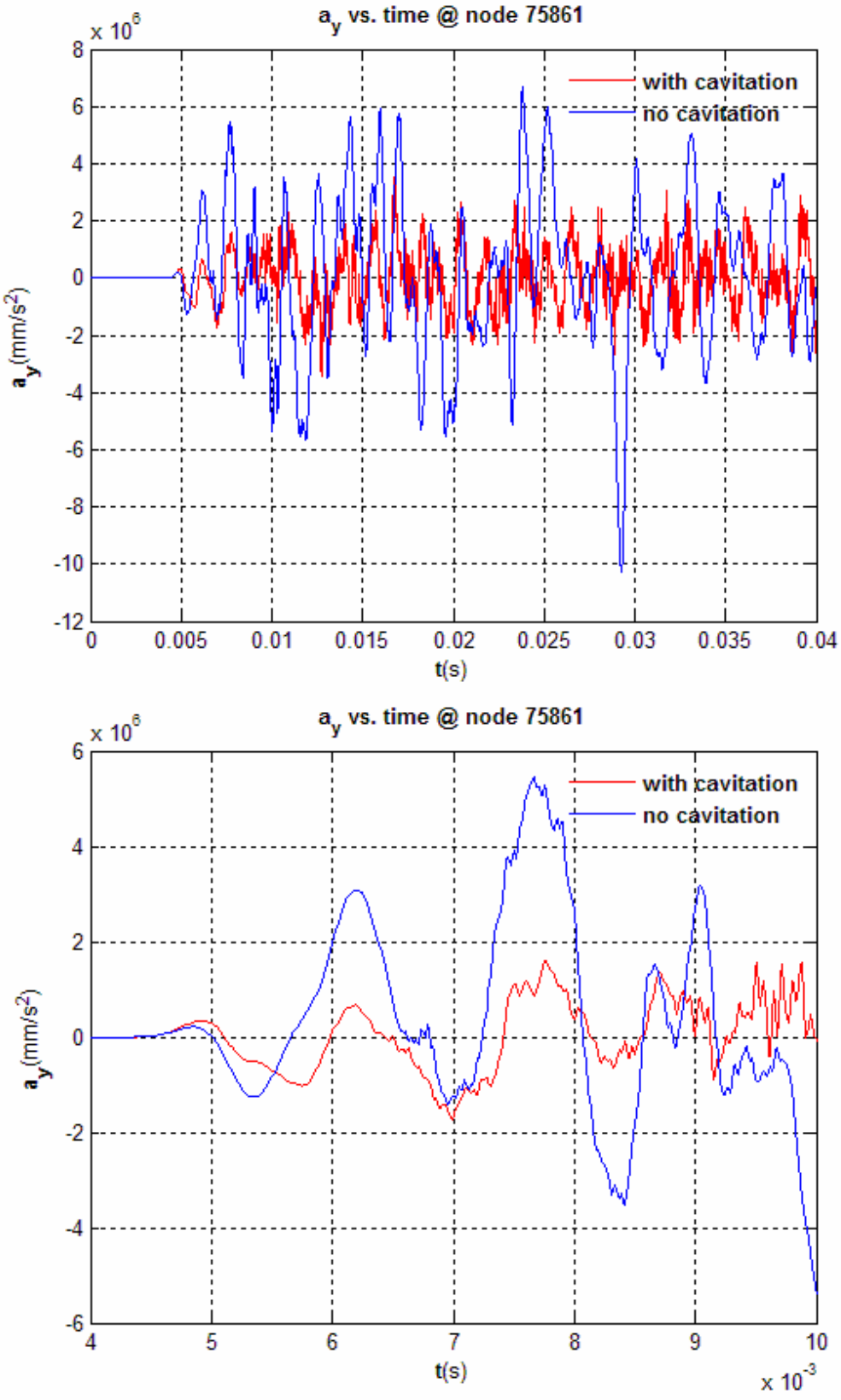

Figure F.4 : Y Direction Acceleration at Node 75861.

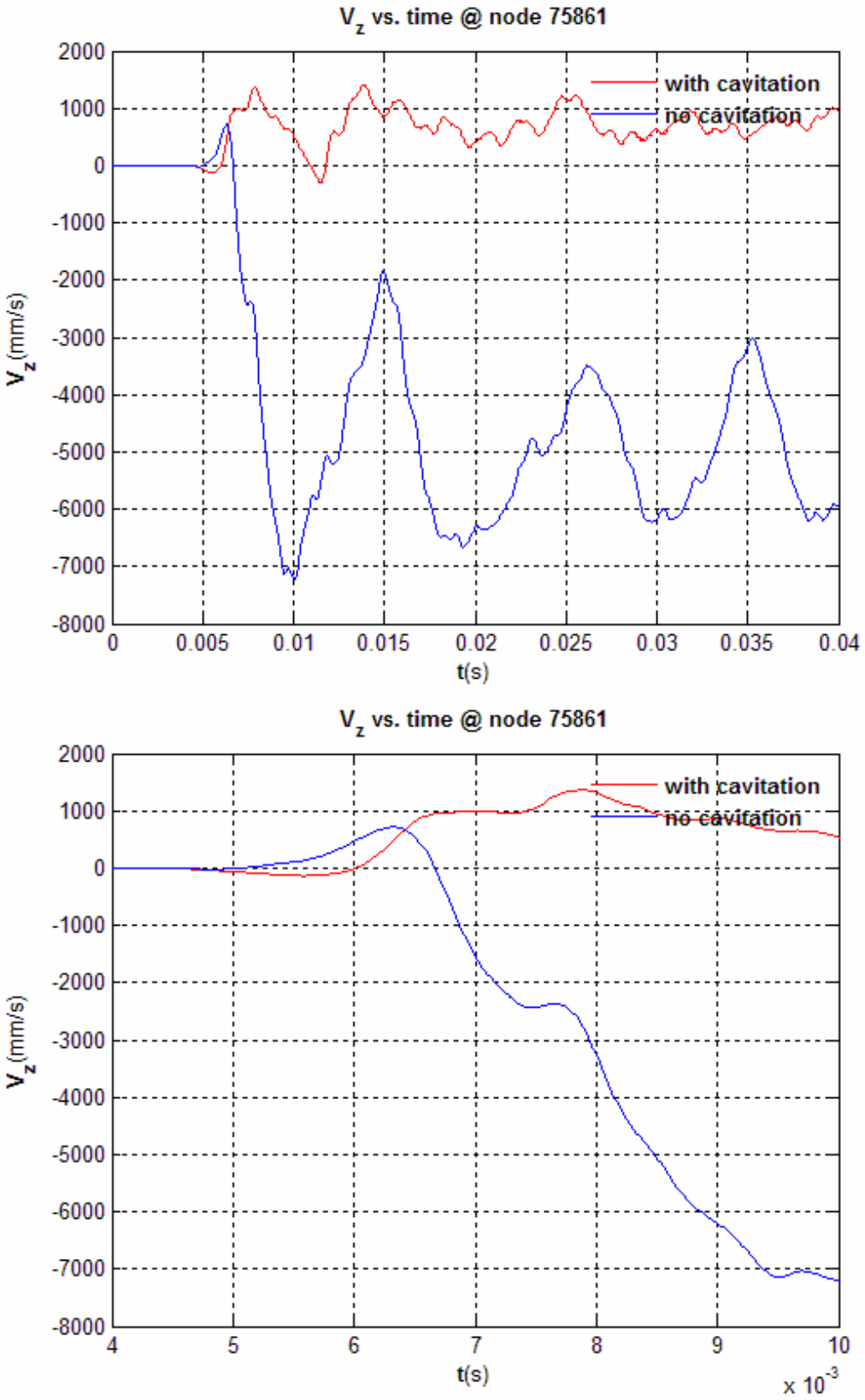

Figure F.5 : Z Direction Velocity at Node 75861.

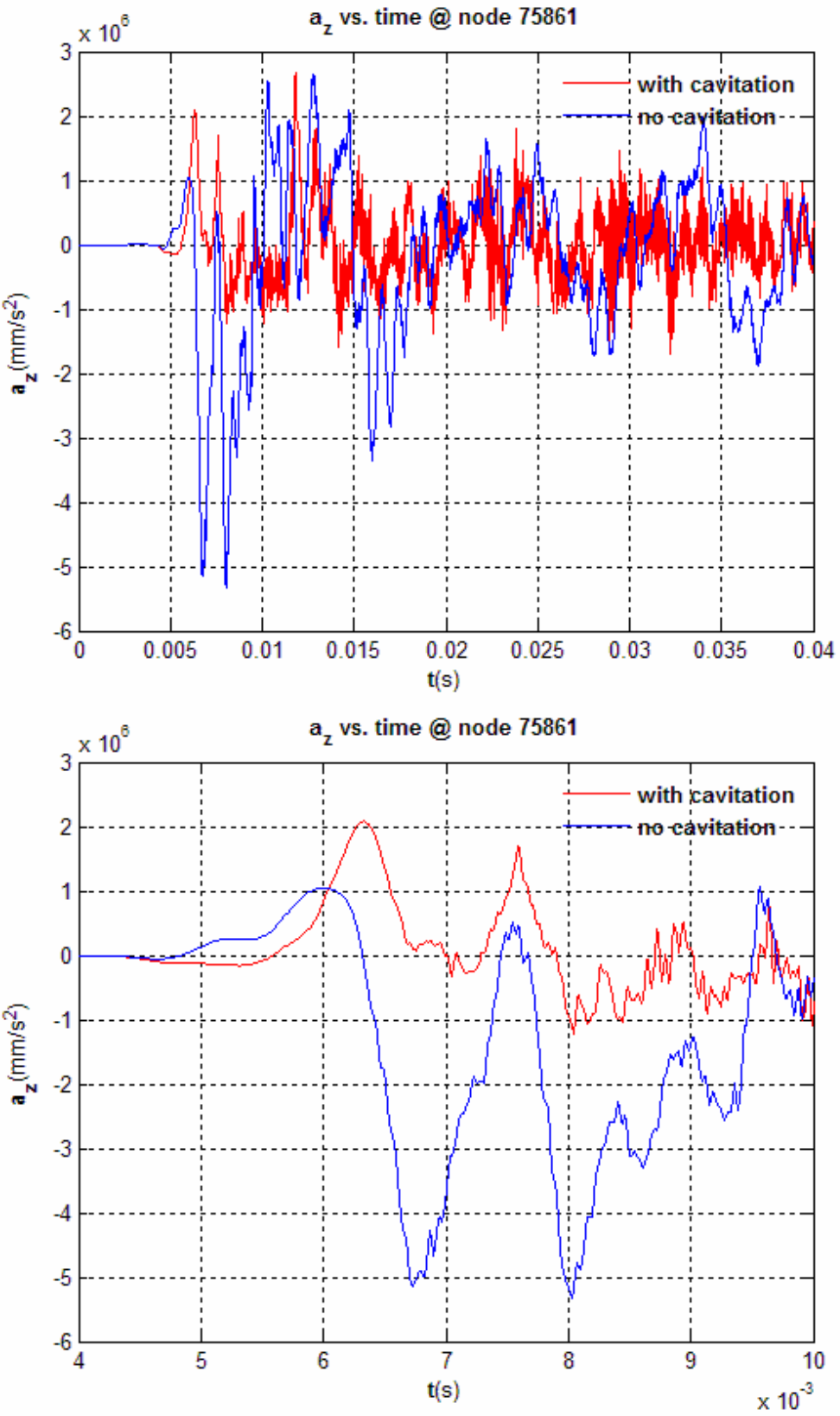

Figure F.6 : Z Direction Acceleration at Node 75861.

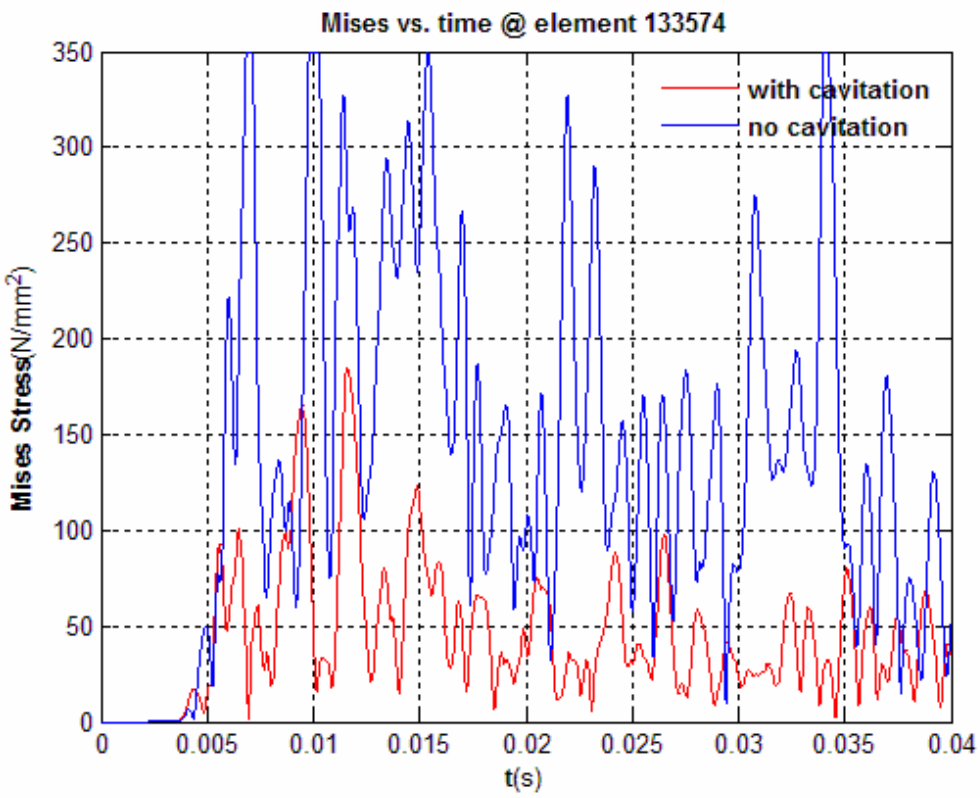

Figure F.7 : Equivalent Von Mises Stress at Element 133574.

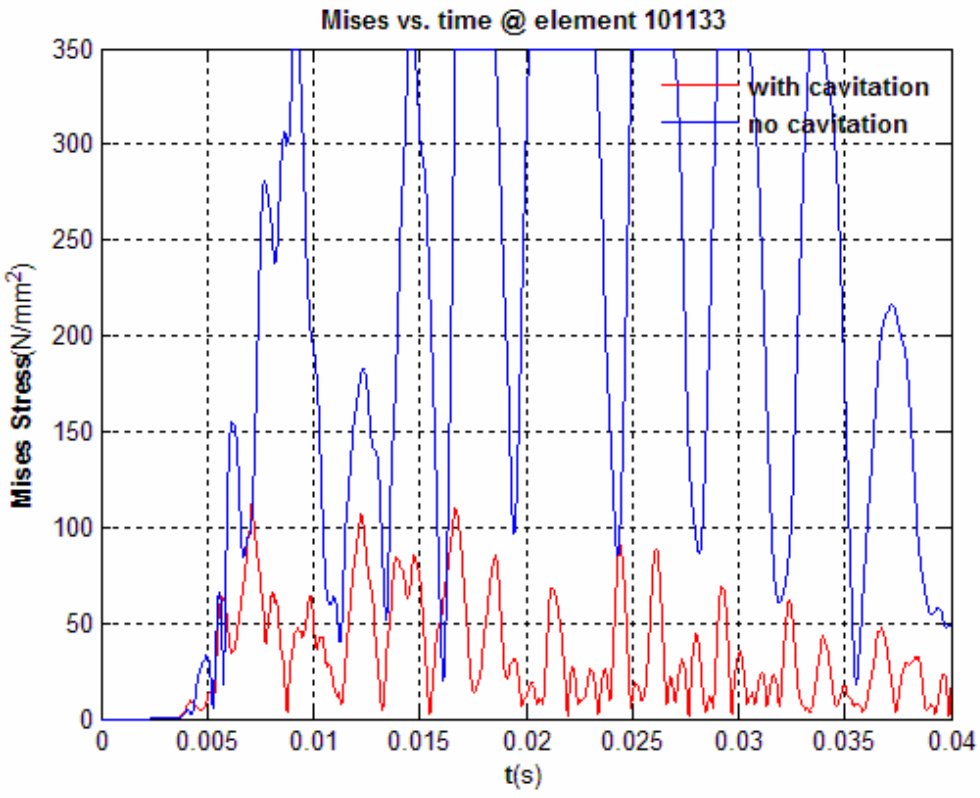

Figure F.8 : Equivalent Von Mises Stress at Element 101133.

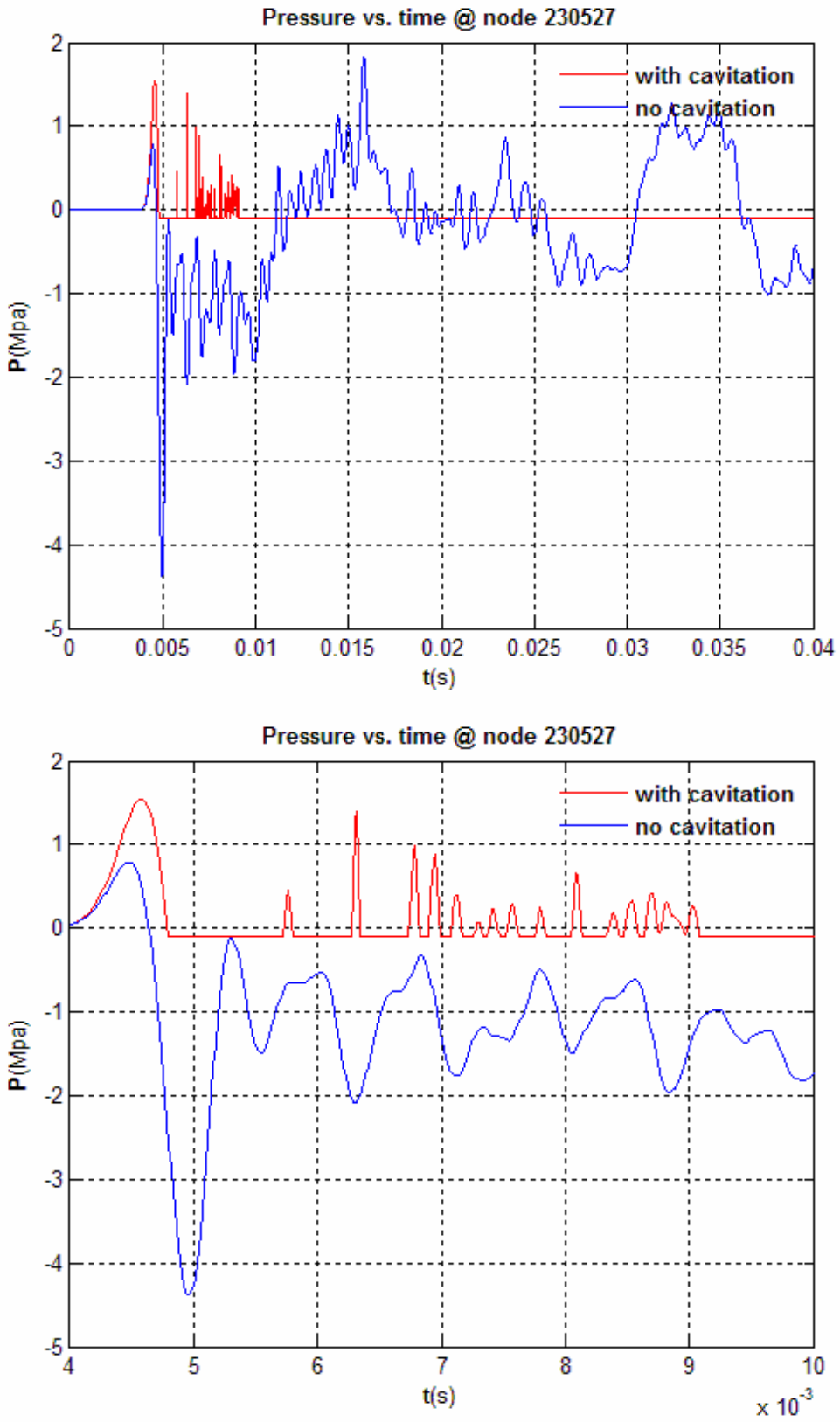

Figure F.9 : Pressure vs. Time Under Keel at Node 230527.

G. Response Comparison of Damped and Undamped Cases of Refined Structural Model

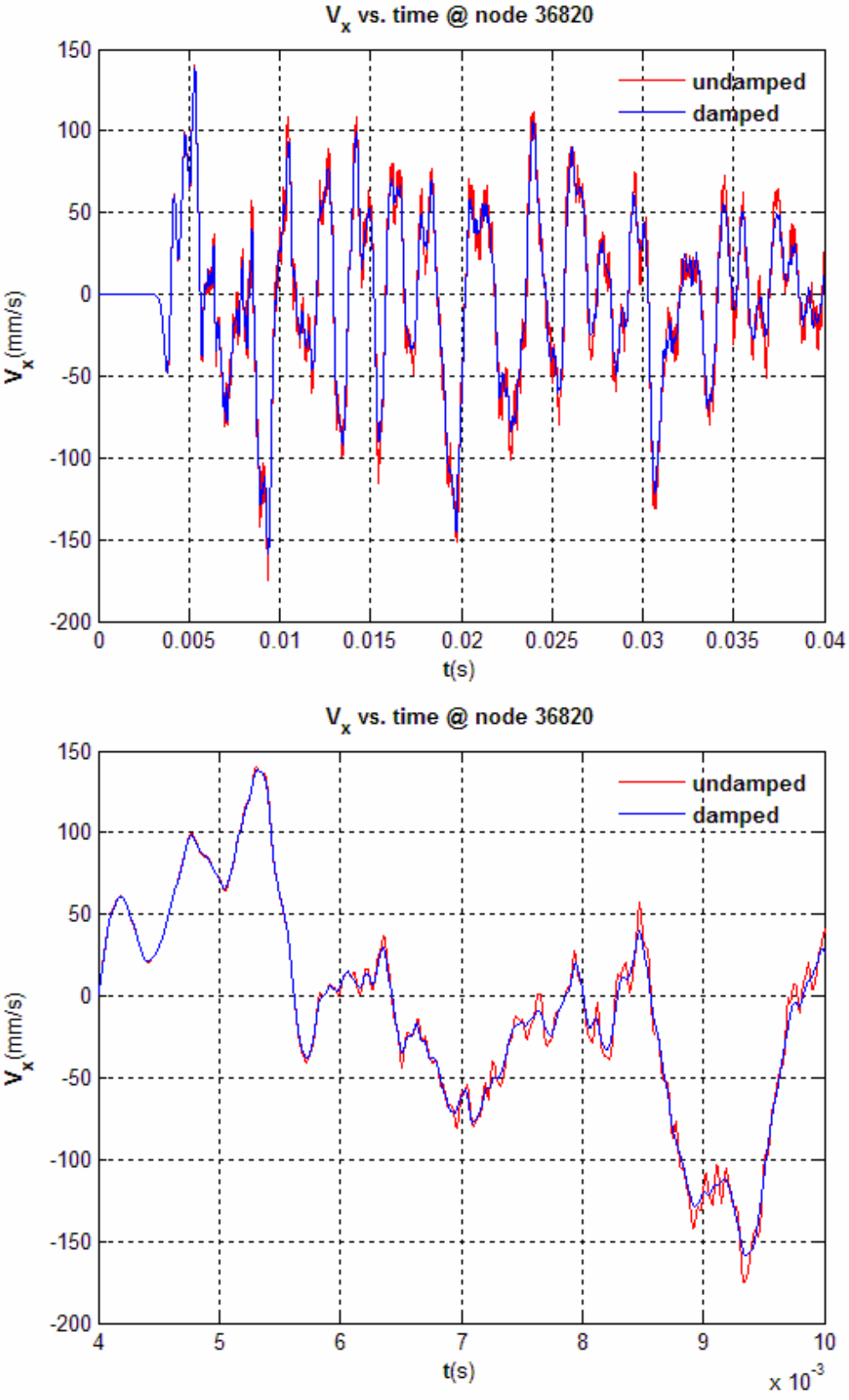

Figure G.1 : X Direction Velocity at Node 36820.

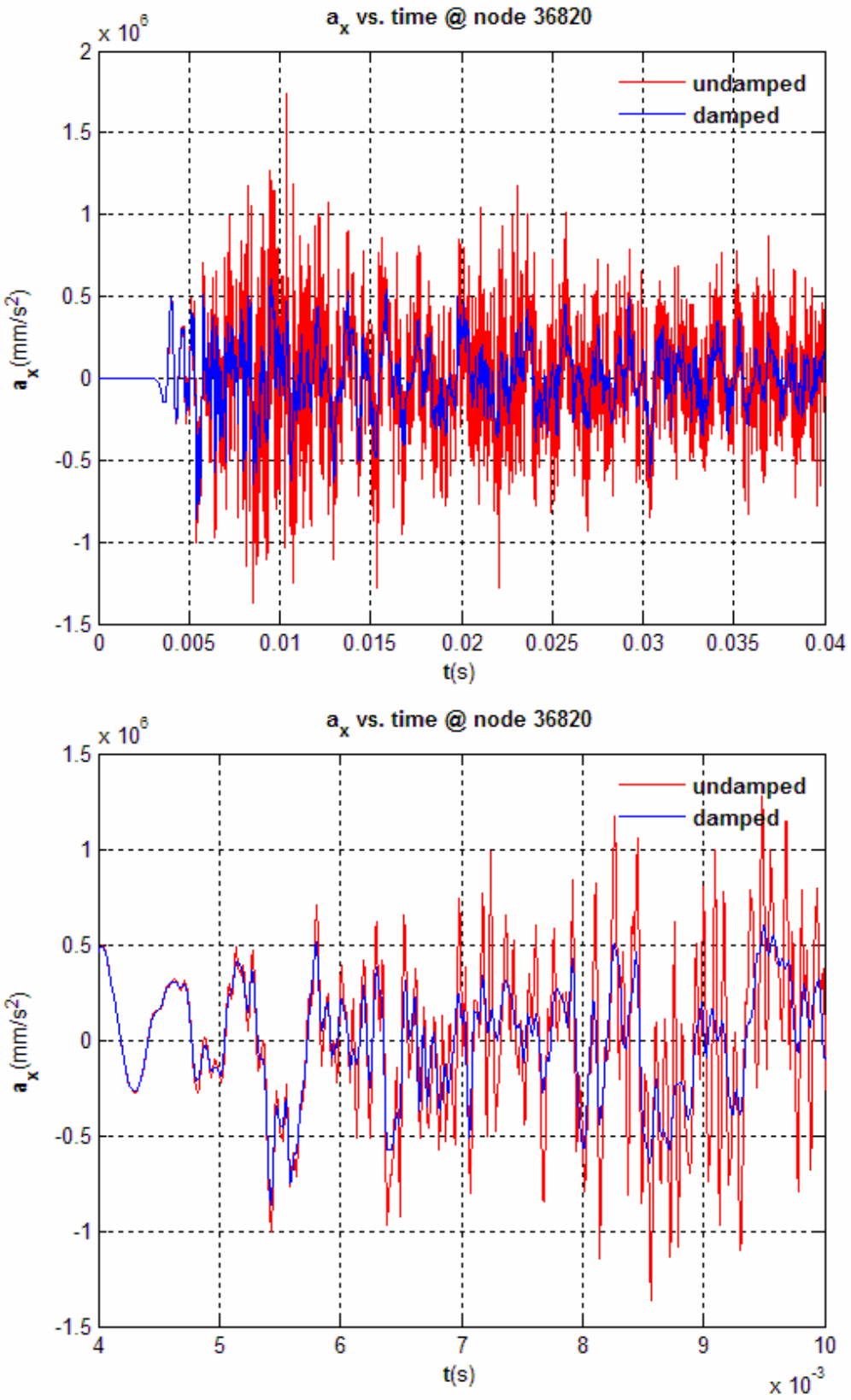

Figure G.2 : X Direction Acceleration at Node 36820.

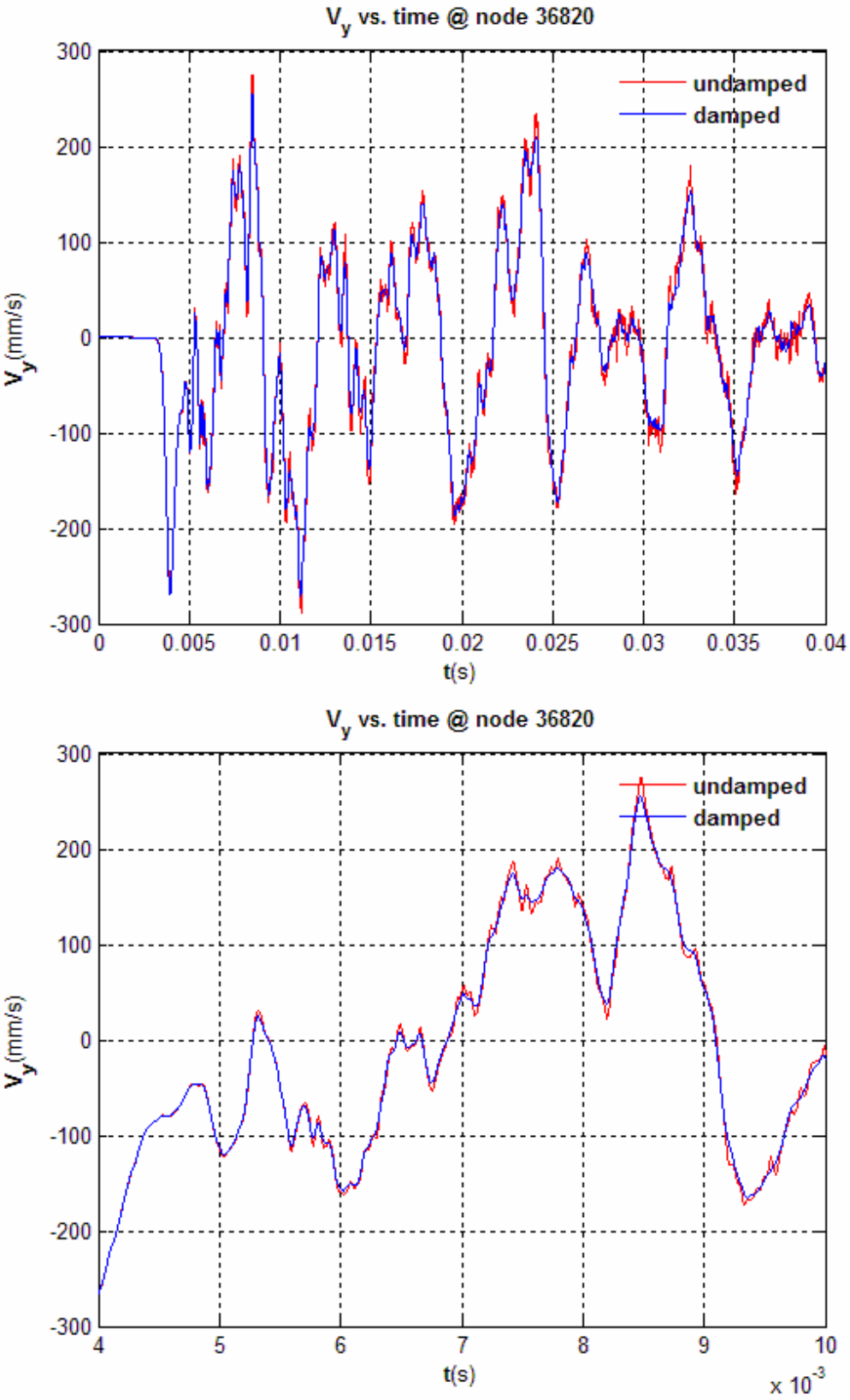

Figure G.3 : Y Direction Velocity at Node 36820.

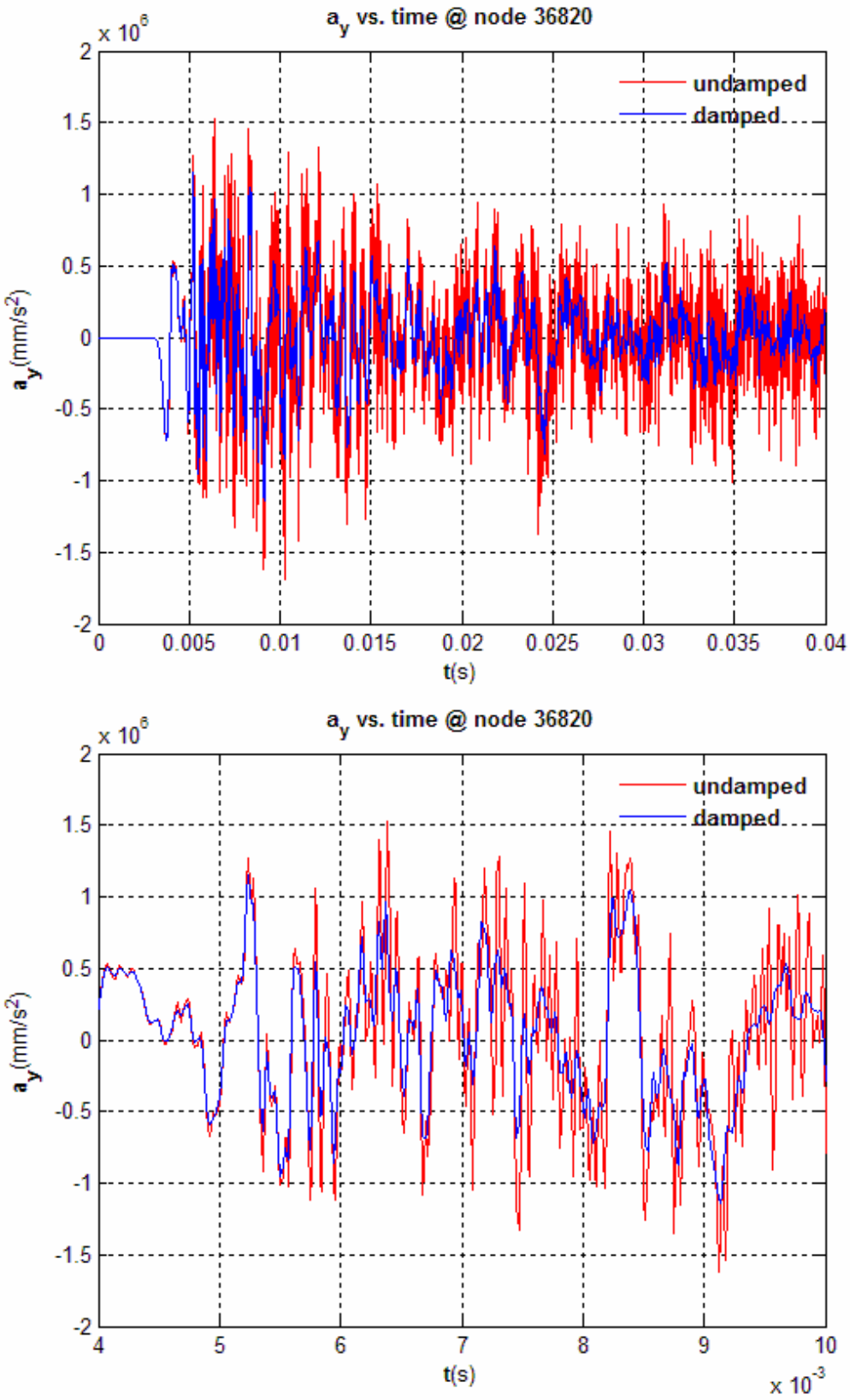

Figure G.4 : Y Direction Acceleration at Node 36820.

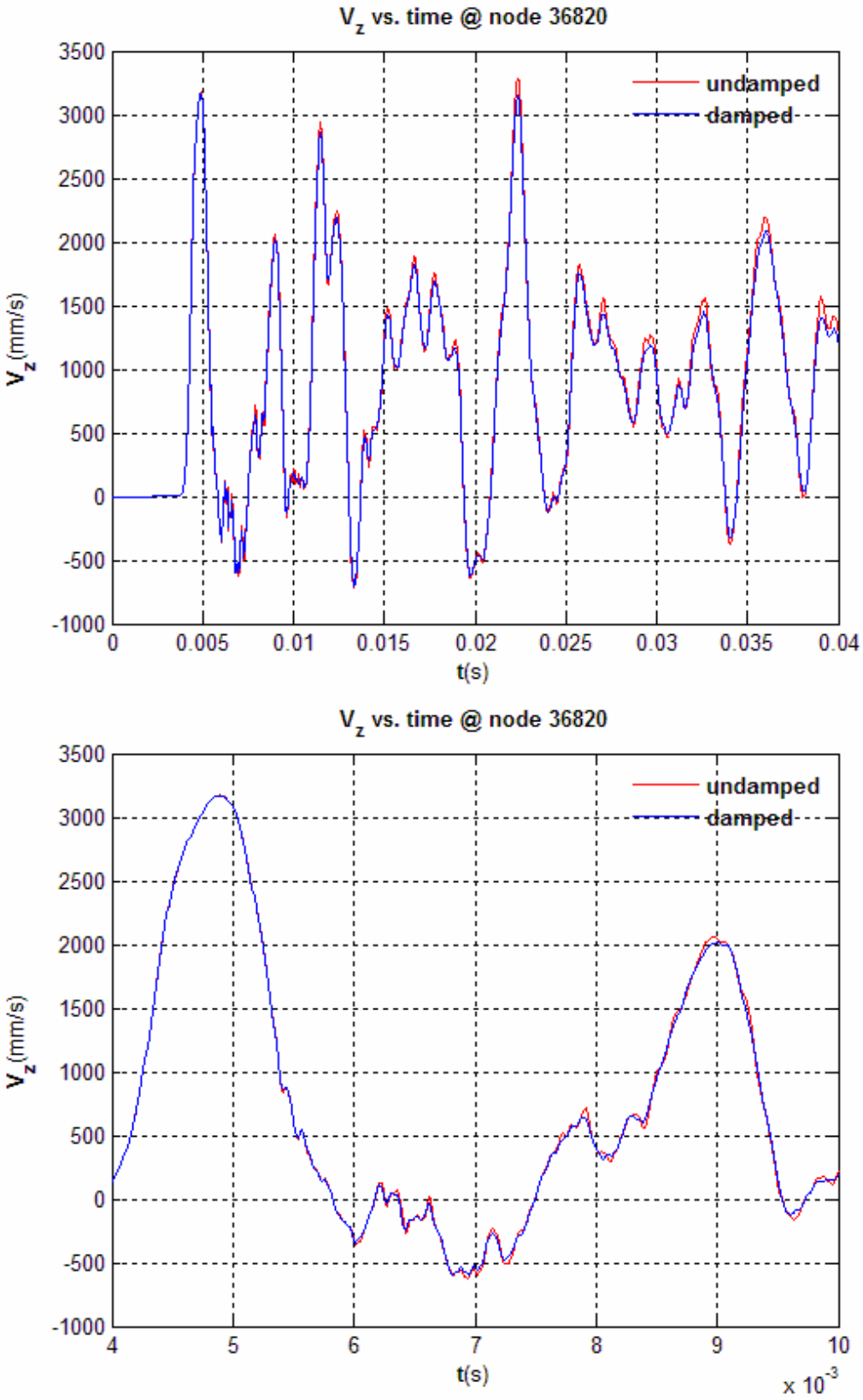

Figure G.5 : Z Direction Velocity at Node 36820.

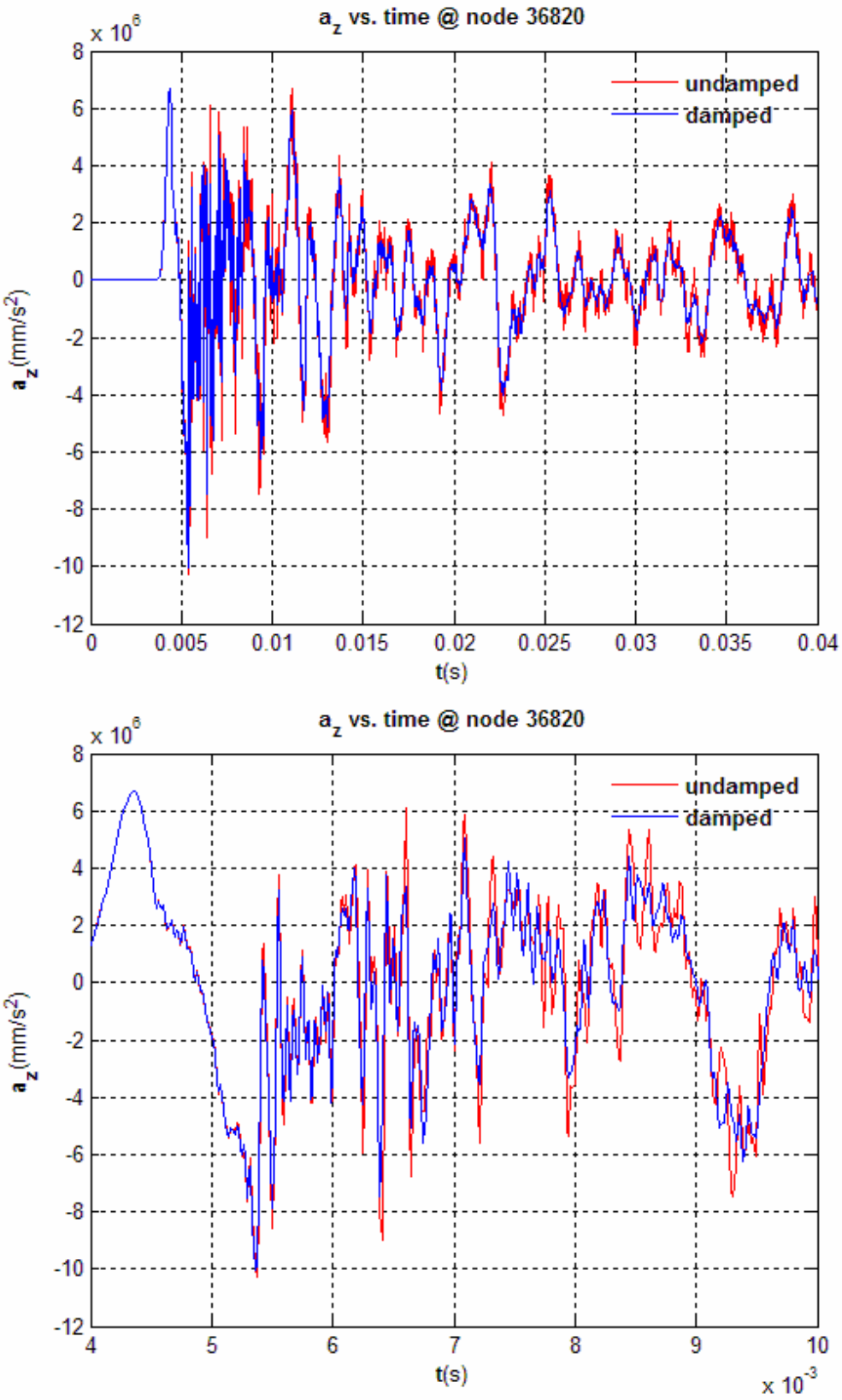

Figure G.6 : Z Direction Acceleration at Node 36820.

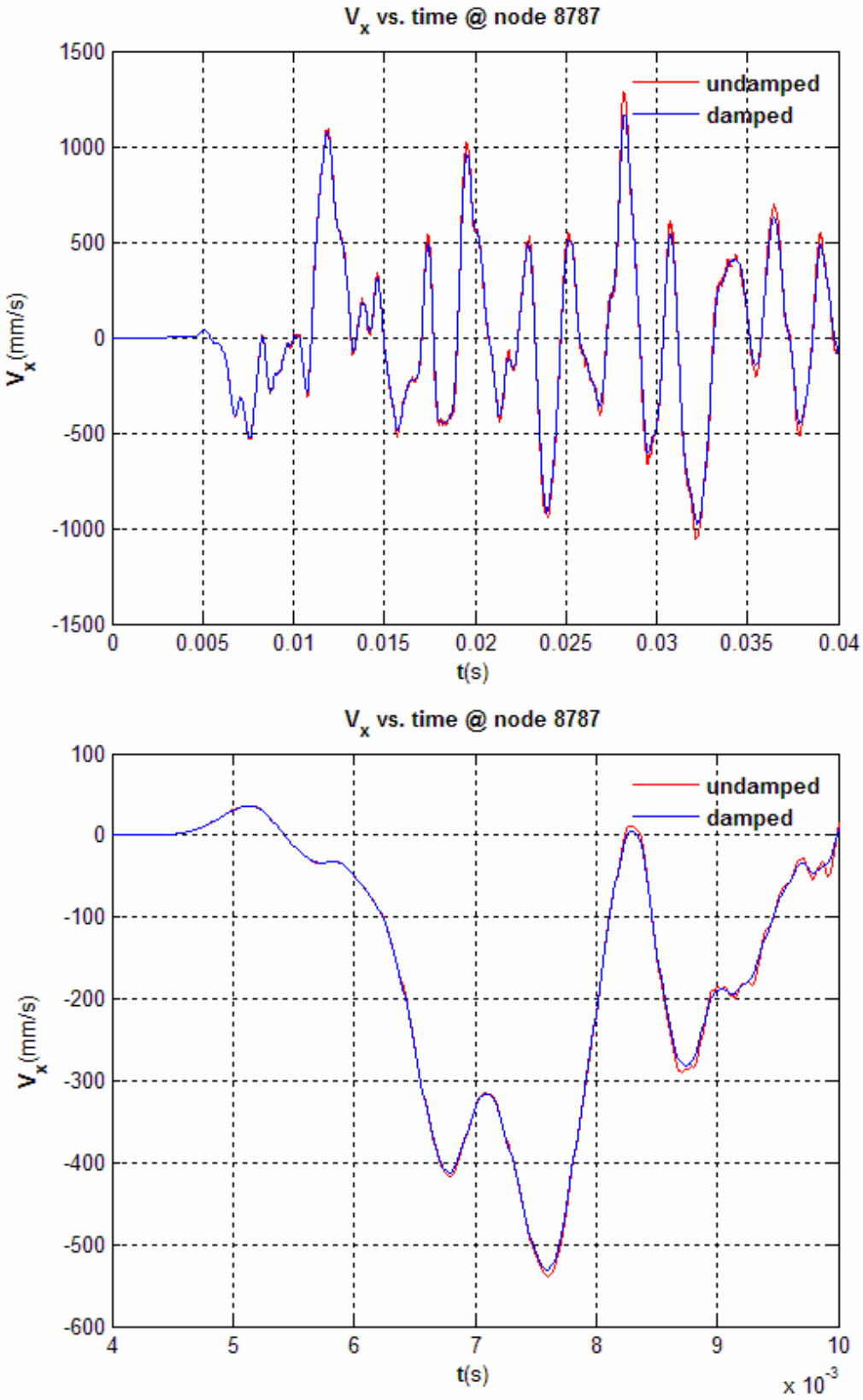

Figure G.7 : X Direction Velocity at Node 8787.

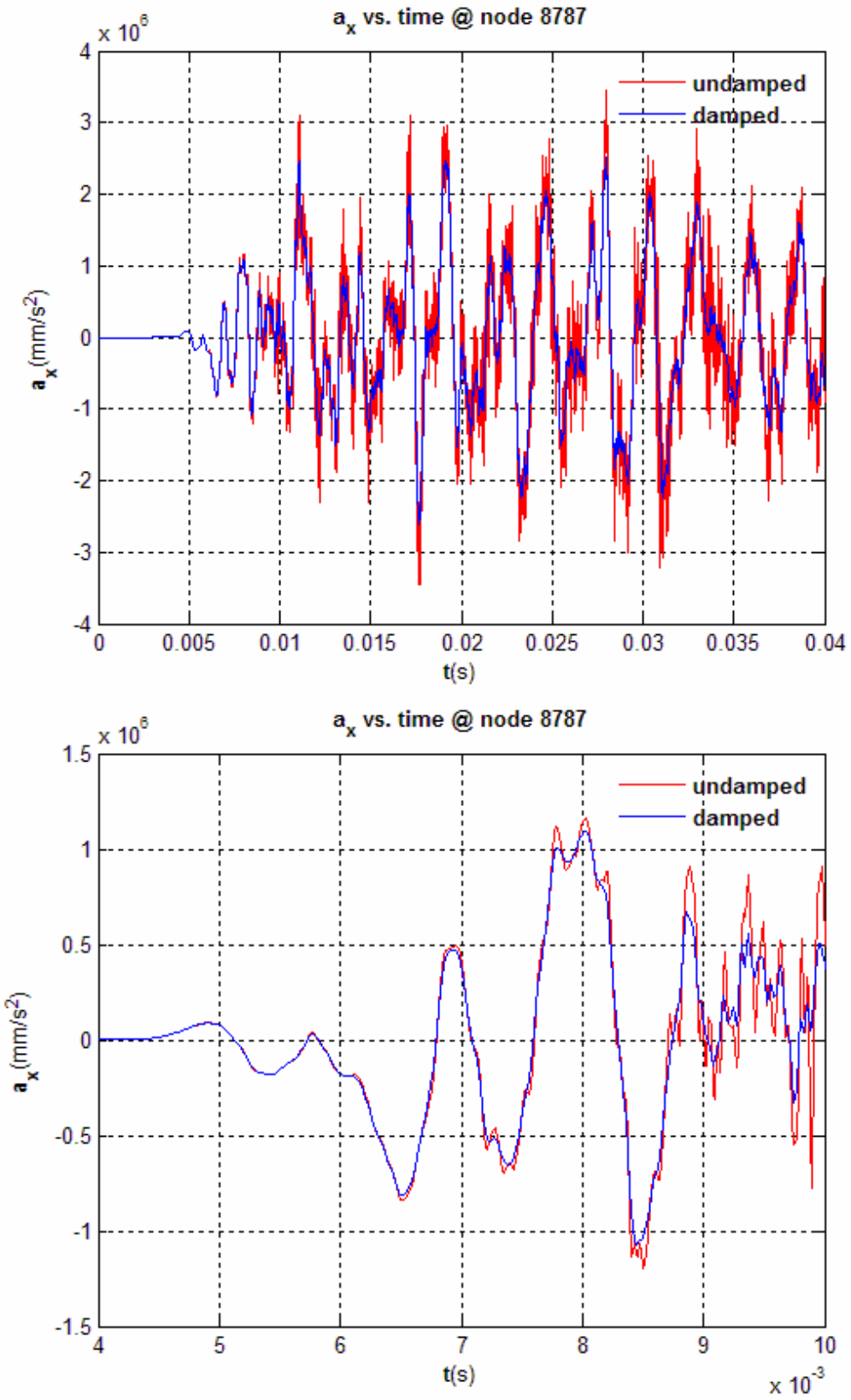

Figure G.8 : X Direction Acceleration at Node 8787.

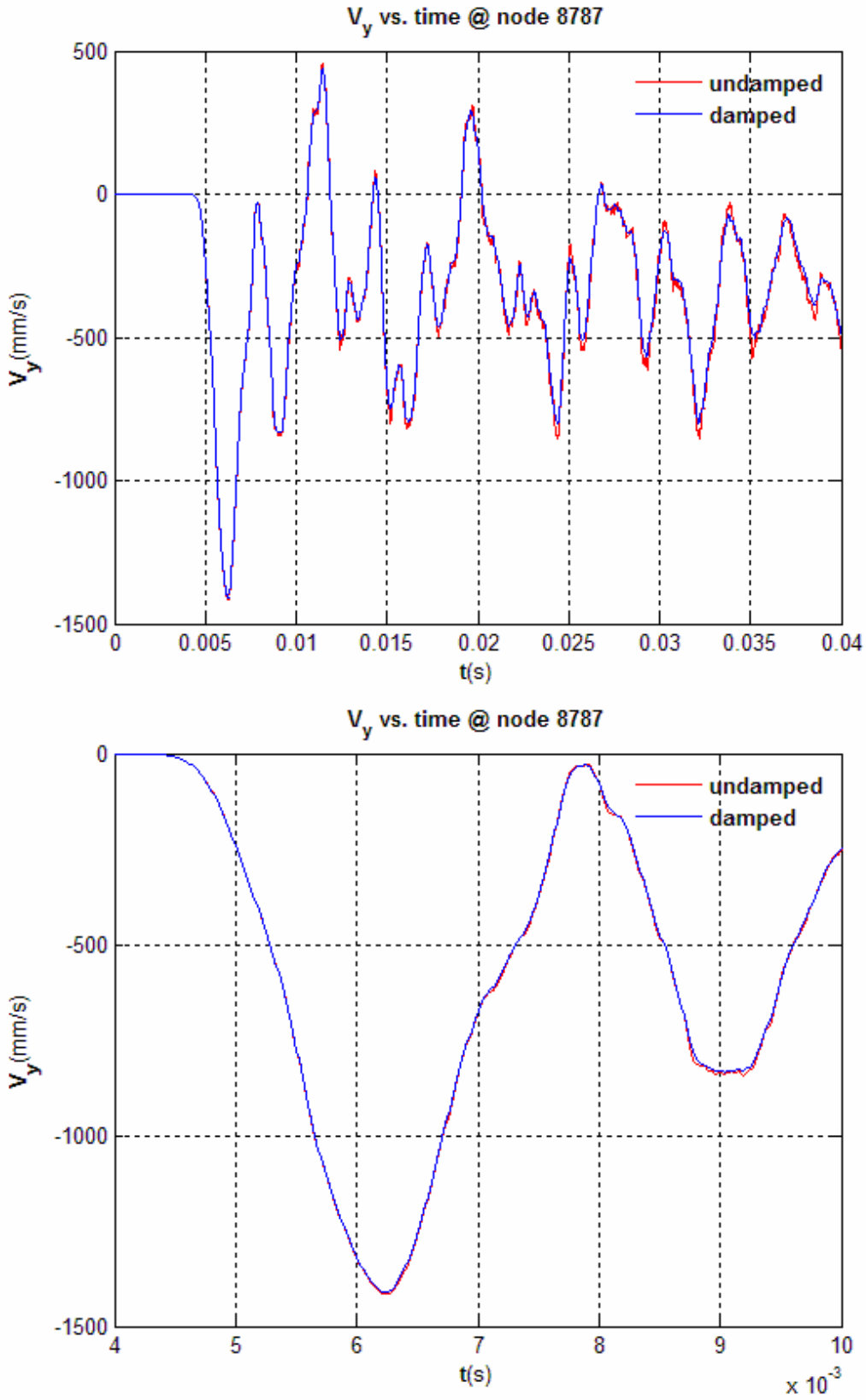

Figure G.9 : Y Direction Velocity at Node 8787.

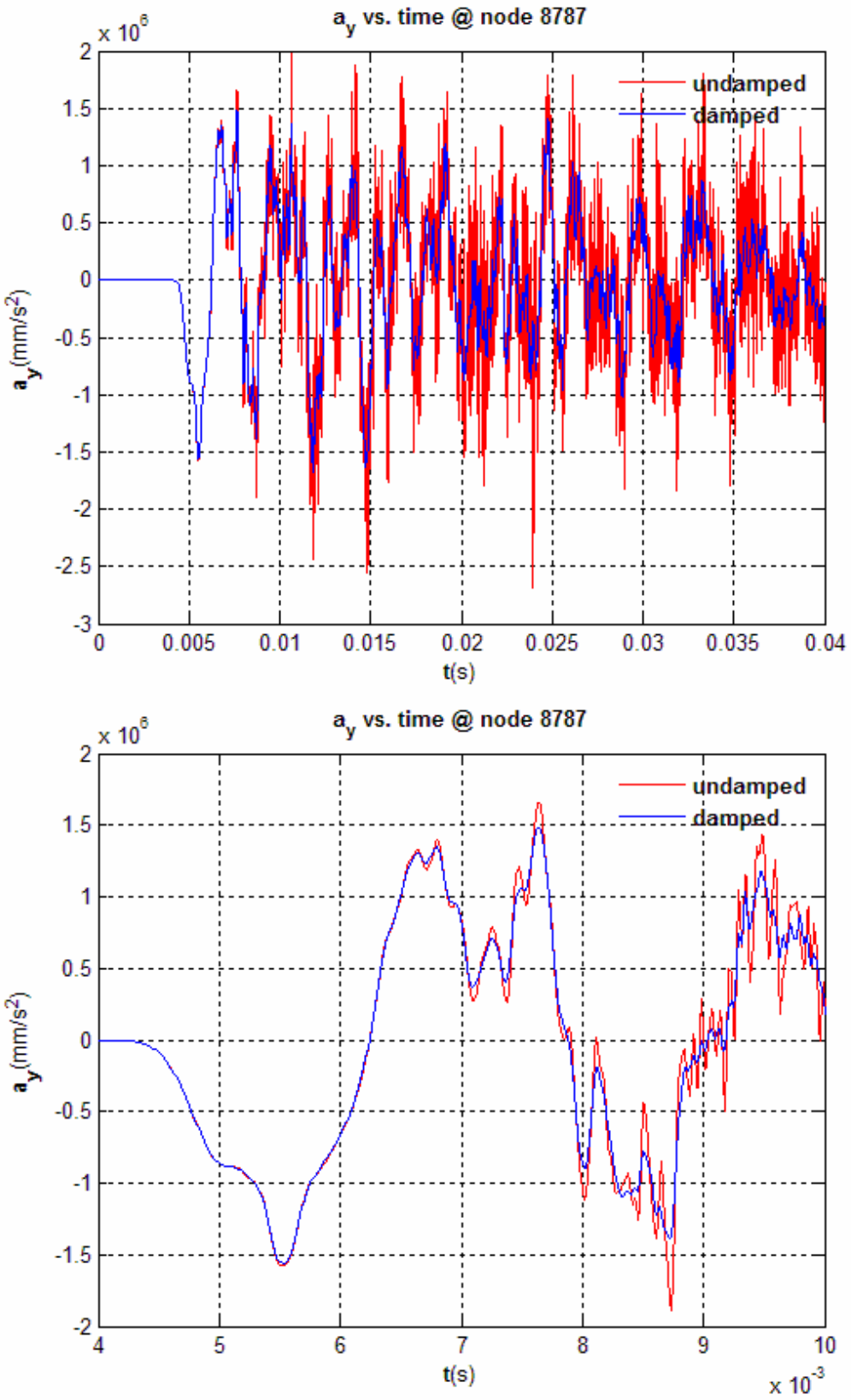

Figure G.10 : Y Direction Acceleration at Node 8787.

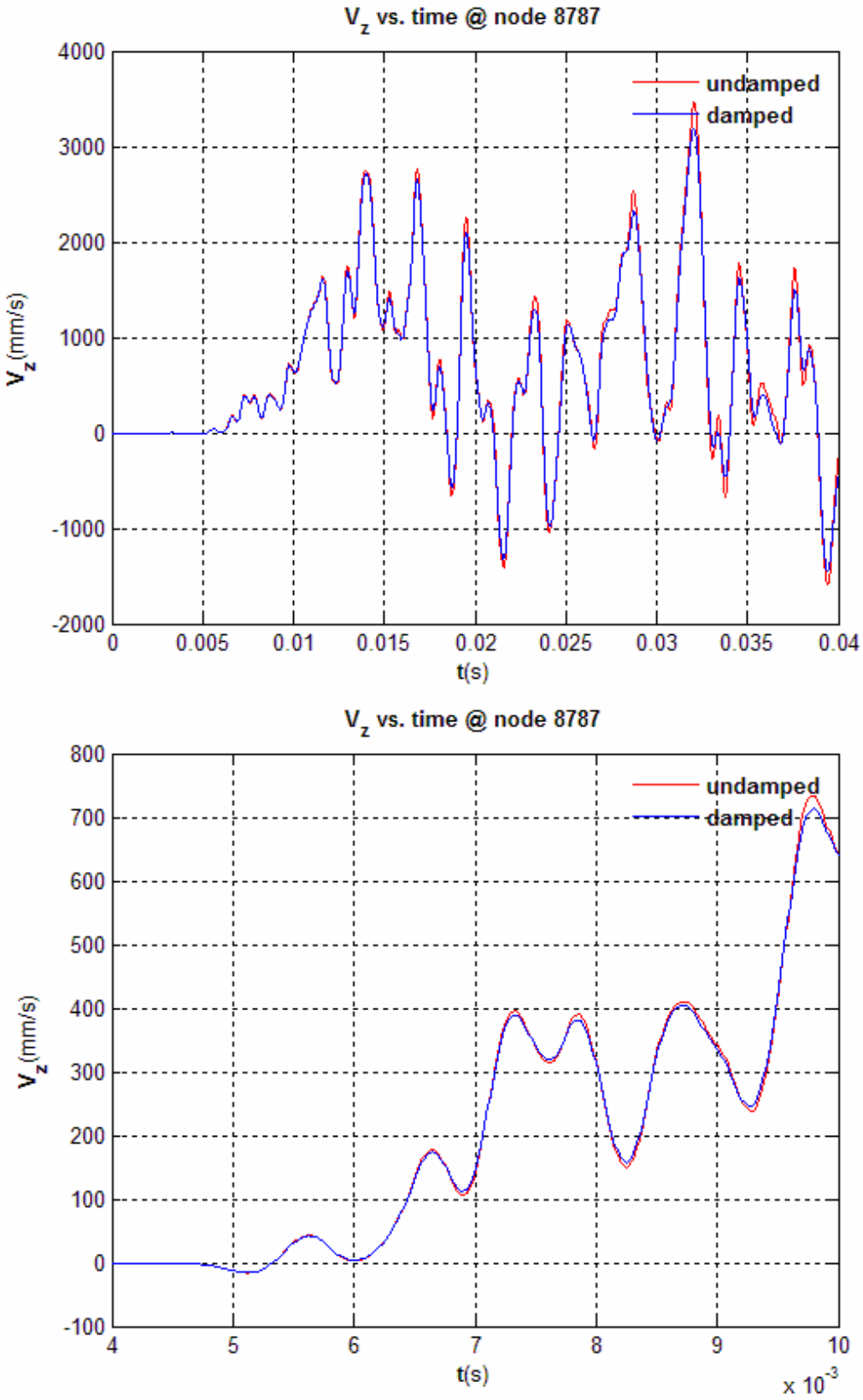

Figure G.11 : Z Direction Velocity at Node 8787.

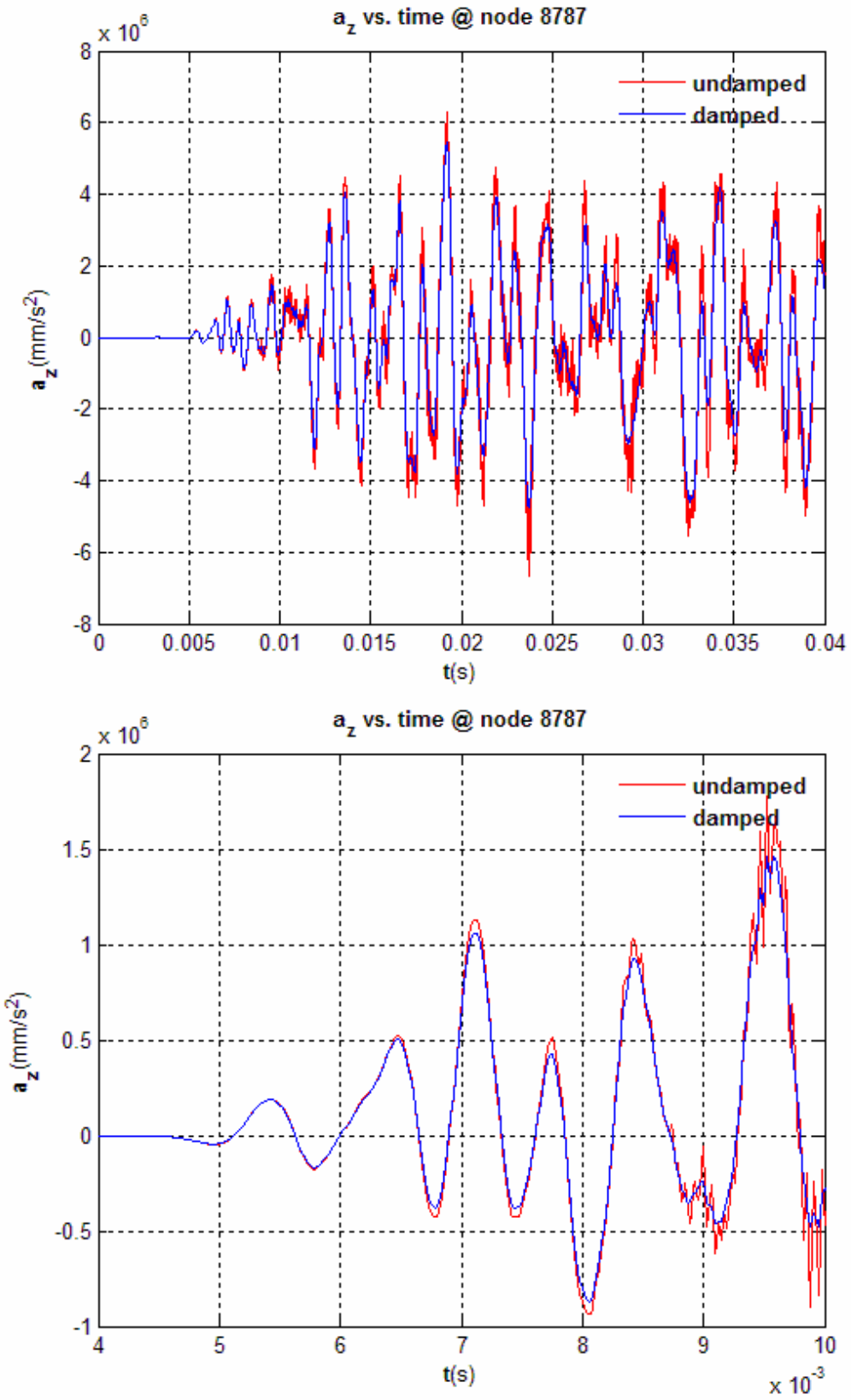

Figure G.12 : Z Direction Acceleration at Node 8787.

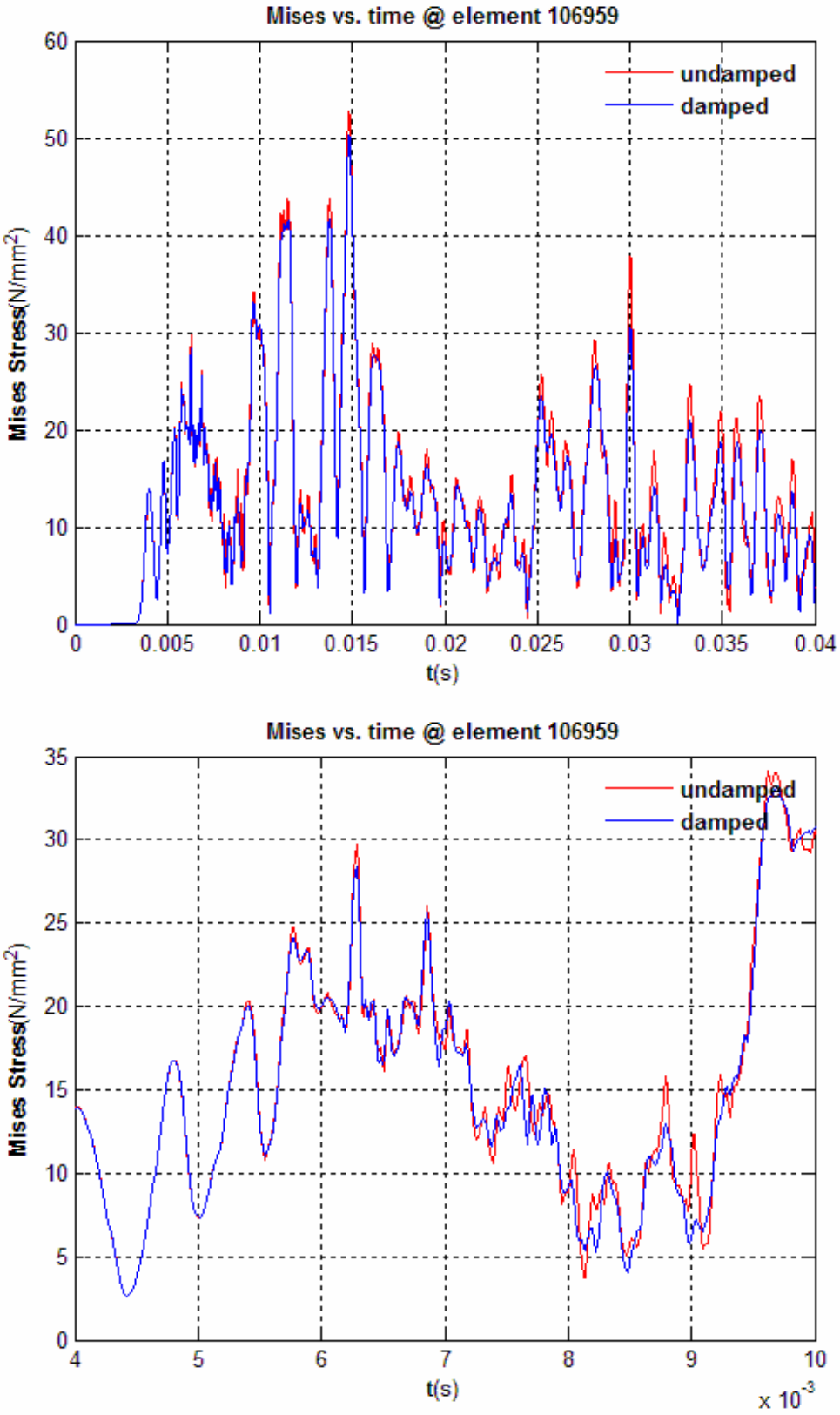

Figure G.13 : Equivalent Von Mises Stress at Element 106959.

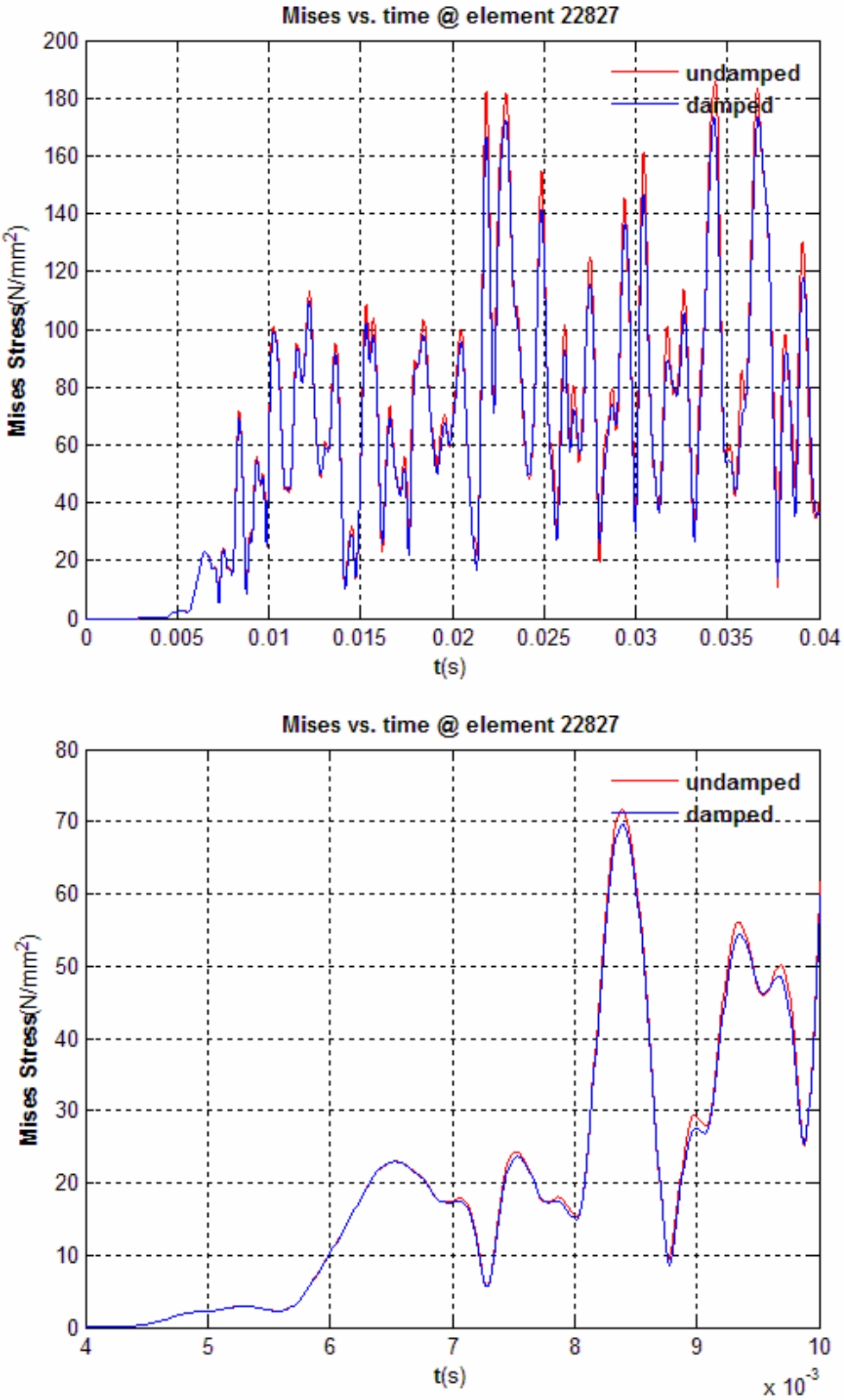

Figure G.14 : Equivalent Von Mises Stress at Element 22827.

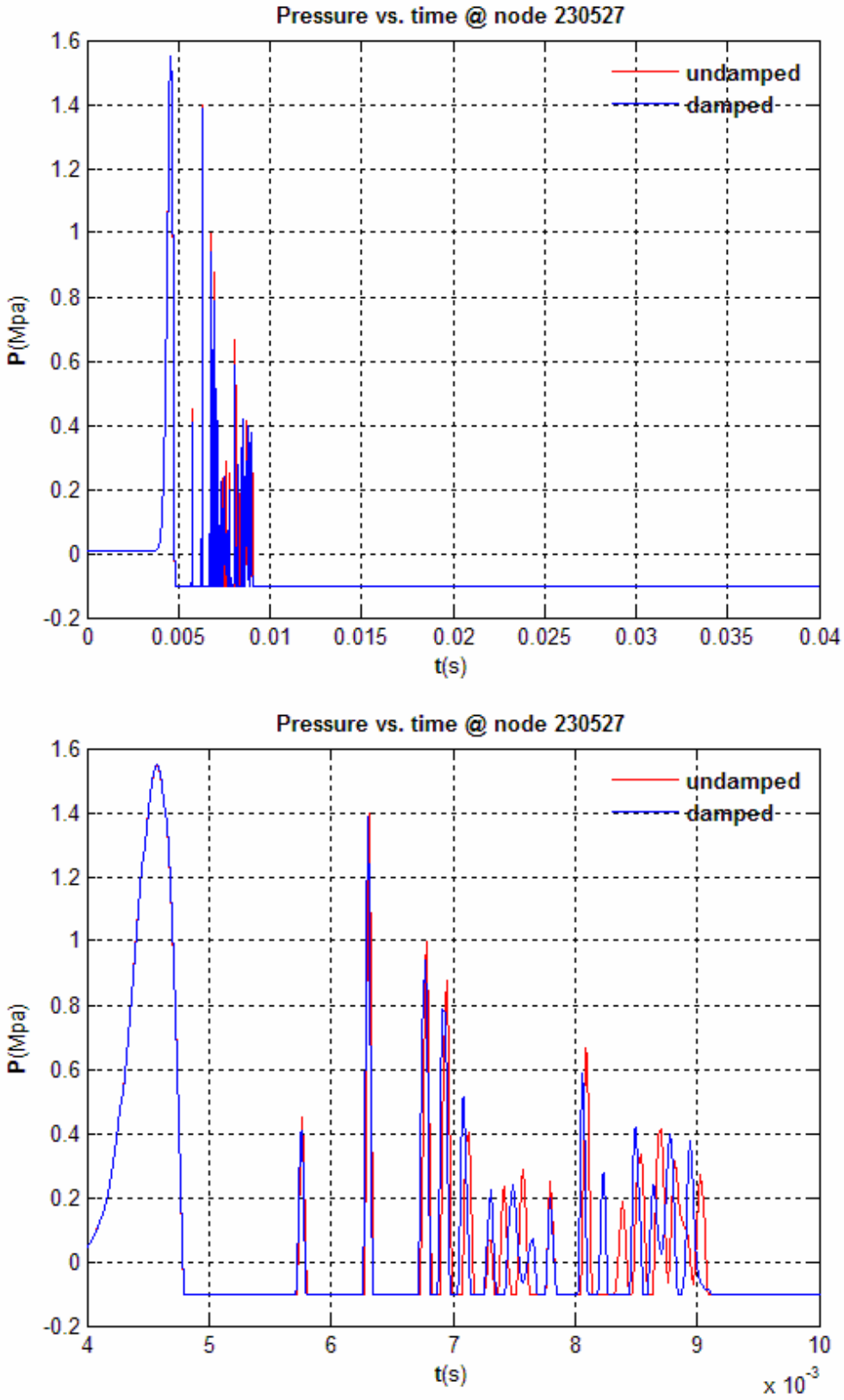

Figure G.15 : Pressure vs. Time Under Keel at Node 230527.

CIRRUCULUM VITAE

Fatih ARUK was born in Speyer, Germany in 1981. He graduated from Istanbul Technical University (İTÜ), Mechanical Engineering Faculty with Bachelor of Science, Mechanical Engineer in 2005. Same year, he started his Master of Science education at İTÜ, Construction program. He is working as a product development engineer in industry and studying his master thesis.